

ABSTRACT

In modern oil industry, it is common that a variety of data are available for reservoir modeling. These data include core and log data, seismic attributes, and conceptual geological models. Data scale, reliability, coverage and availability must be taken into account in integrating these data into numerical reservoir models. Geostatistical reservoir models can be built at different scales for different purposes, such as a large scale model for resource estimation and a fine scale model of heterogeneity for flow simulation. Different modeling techniques and different usage of the input data usually cause inconsistency between the models at different scales. It is desired that all the models are scale consistent. The scale consistent reservoir modeling scenario developed in this thesis aims to build reservoir models that are scale consistent and reproduce the data at different scales.

The basic idea is to construct a large scale model by integrating all available data, and then downscaling or upscaling for different modeling purposes. The downscaling must reproduce exactly the large scale model to ensure consistency. There are three major steps: (1) construct a large scale model over the entire lease by integrating multivariate information; Gaussian-based Bayesian updating technique can be used; local uncertainty assessment is provided, (2) perform petroleum resource estimation with global uncertainty assessment from the large scale model; a spatial/multivariate simulation approach can be used to account for the spatial and multivariate correlations among the local uncertainties, (3) construct fine scale 3-D models of

heterogeneity that are consistent with the large scale model and well data using the exact downscaling techniques.

This modeling scenario is developed from the oil sands geostatistical modeling projects for the Surmont lease, Alberta, Canada. An application of the modeling techniques to the Surmont will be presented.

ACKNOWLEDGMENTS

I would like to express my deep gratitude and appreciation to Dr. Clayton V. Deutsch for being an excellent advisor and outstanding professor, for giving me the chance to work on Surmont geostatistical modeling project, and for his constant guidance and supervision of this research work. Without his guidance, the thesis would not exist.

I would like to thank Dr. Luciane B. Cunha for being my co-supervisor and for her encouragement, support, and valuable suggestions on my study. I would also like to thank my committee members Dr. Larry W. Lake, Dr. Octavian Catuneanu, Dr. Oy Leuangthong and Dr. Marcel Polikar for their time and effort in reviewing this work.

I would like to thank Dr. Oy Leuangthong, Jason McLennan, David Garner, T.J. Wheeler, Jean-Francois Richy and Tom Trowell for the pleasant time of working together on the Surmont research project and for all the helps from them.

The financial support from the Natural Sciences and Engineering Research Council of Canada and the ConocoPhillips Canada is gratefully acknowledged.

Finally, I would like to take this opportunity to express my profound gratitude to my beloved parents, my dear wife, Jiang Bai, and my lovely son, Zachary, for their continued support and encouragement during my studies.

TABLE OF CONTENTS

ABSTRACT	I
ACKNOWLEDGEMENTS.....	III
LIST OF TABLES	IX
LIST OF FIGURES	X
NOMENCLATURE	XIX
CHAPTER 1	
INTRODUCTION	1
1.1 Proposed Modeling Method.....	4
1.2 Outline of The Thesis.....	6
CHAPTER 2	
MULTISCALE DATA AND DATA INTEGRATION	7
2.1 Data Sources.....	7
2.2 Data Availability, Coverage and Reliability.....	9
<i>2.2.1 Data availability.....</i>	<i>9</i>
<i>2.2.2 Data coverage</i>	<i>9</i>
<i>2.2.3 Data reliability</i>	<i>10</i>
2.3 Data Scale and Model Scale	10
<i>2.3.1 Data scale.....</i>	<i>11</i>

2.3.2 Model scale.....	11
2.4 Reservoir Heterogeneity at Different Scales	12
2.5 Scale Relationships of Data.....	16
2.6 Volume Averaged Covariance	17
2.7 Data Integration Techniques	18
2.7.1 Well data.....	19
2.7.1.1 Kriging for reservoir mapping.....	20
2.7.1.2 Stochastic simulation for reservoir heterogeneity.....	21
2.7.2 Seismic data.....	22
2.7.2.1 Seismic data integration for 2-D mapping	23
2.7.2.2 Seismic data integration for 3-D modeling.....	25
2.7.3 Dynamic data	26

CHAPTER 3

LARGE SCALE MODELING	29
3.1 Bayesian Updating Technique for 2-D Mapping	30
3.1.1 Theory of Bayesian Updating.....	31
3.1.2 Some interesting aspects of Bayesian Updating.....	36
3.2 Enhanced Bayesian Updating Technique.....	38
3.2.1 Locally Varying Correlation	42
3.2.2 Data impact on local correlation	45
3.2.3 Locally Varying Quality	48
3.2.4 Bayesian Updating with LVC and LVQ	49
3.2.5 Small example	52
3.3 Simulation with Bayesian Updating.....	57

CHAPTER 4

IMPLEMENTATION OF BAYESIAN UPDATING 63

4.1 Selection of Primary and Secondary Variables 63

4.2 Bayesian Updating 2-D Modeling..... 66

4.2.1 Prior models 67

4.2.2 Likelihood models..... 73

4.2.3 Updated models 78

4.2.4 Local uncertainty..... 81

4.3 Model Validation 82

CHAPTER 5

RESOURCE ESTIMATION 92

5.1 Methodology of Global Uncertainty Assessment 93

5.1.1 Local resource estimation and joint uncertainty..... 93

5.1.2 Resource estimation and global uncertainty..... 95

5.2 Example 99

CHAPTER 6

EXACT DOWNSCALING TECHNIQUES..... 105

6.1 Background 106

6.2 Theory of Exact Downscaling with Direct Kriging 109

6.2.1 Proof of Theorem I 111

6.2.2 Small example..... 113

6.3 Theory of Exact Downscaling with Direct Sequential Simulation 115

6.3.1 Proof of Theorem II..... 116

6.3.2 <i>Small example</i>	119
----------------------------------	-----

CHAPTER 7

IMPLEMENTATION OF EXACT DOWNSCALING TECHNIQUES 121

7.1 Some Interesting Aspects of EDDK 121

7.1.1 <i>Kriging weights of block and point data</i>	121
--	-----

7.1.2 <i>Number of block data used in EDDK</i>	123
--	-----

7.1.3 <i>Screen effect with multiple block data</i>	125
---	-----

7.2 Some interesting aspects of EDDSS 127

7.3 Implementation Details 129

7.3.1 <i>Global mean</i>	129
--------------------------------	-----

7.3.2 <i>Discretization level</i>	129
---	-----

7.3.3 <i>Last cell correction in EDDSS</i>	130
--	-----

7.3.4 <i>Simulation path</i>	130
------------------------------------	-----

7.3.5 <i>Search strategies</i>	131
--------------------------------------	-----

7.4 Histogram Reproduction and Proportional Effect in EDDSS..... 131

7.4.1 <i>The CCDF Look-up table method</i>	132
--	-----

7.4.2 <i>Proportional effect</i>	134
--	-----

7.4.3 <i>Discussion on the CCDF table method</i>	137
--	-----

7.5 A Large Example 141

7.5.1 <i>Data assembly</i>	141
----------------------------------	-----

7.5.2 <i>Variogram modeling</i>	142
---------------------------------------	-----

7.5.3 <i>Exact downscaling</i>	143
--------------------------------------	-----

7.5.4 <i>Checking results</i>	147
-------------------------------------	-----

7.6 Comparison Between Exact Downscaling and Approximate Downscaling Methods	148
 CHAPTER 8	
CASE STUDY: RESERVOIR MODELING IN THE SURMONT LEASE	155
8.1 2-D Mapping with Bayesian Updating.....	158
<i>8.1.1 Trend maps</i>	<i>159</i>
<i>8.1.2 Prior maps.....</i>	<i>159</i>
<i>8.1.3 Correlation matrix and likelihood maps</i>	<i>160</i>
<i>8.1.4 Updated maps and final maps.....</i>	<i>162</i>
<i>8.1.5 Model validation.....</i>	<i>165</i>
8.2 Global Resource Assessment	167
<i>8.2.1 Uncertainty in global SAGD OOIP.....</i>	<i>168</i>
8.3 Fine Scale 3-D Models	171
 CHAPTER 9	
CONCLUSIONS AND RECOMMENDATIONS	176
9.1 Large Scale Modeling.....	176
9.2 Global Resource Uncertainty Assessment.....	178
9.3 Exact Downscaling Technique.....	179
 APPENDIX	 182
 BIBLIOGRAPHY	 186

LIST OF TABLES

Table 2-1: Different data sources for reservoir modeling (summarized based on Satter <i>et al.</i> , 1994 and Reza, 2003)	8
Table 2-2: The common data for reservoir characterization (based on Kelkar and Perez, 2002 and Wen <i>et al.</i> , 2005).....	8
Table 2-3: Scales of reservoir heterogeneities (from Kelkar and Perez, 2002).....	15
Table 3-1: The Bayesian updating calculation showing the changes of updated mean (4th row) with increasing prior mean (second row). The variances of prior and likelihood are 0.4 for all cases	37
Table 3-2: The Bayesian updating calculation showing the increasing of updated variance (last row) with increasing of prior variance (second row)	38
Table 5-1: A tabulated illustration of joint uncertainty calculation for OOIP	94
Table 6-1: The table of EDDK results with different cases. The collocated block values are given in the first row. The estimated values in 8 small cells are listed in the middle, and the block averages of the estimates are listed in the last row.....	114
Table 6-2: The table of EDDSS results for the small example. The data are given on the left: type b is for block, p is for point and s is for previously simulated values. The simulated values and variances are listed in the last two rows	119
Table 7-1: The kriging weights of block and point data with different variogram ranges.....	121
Table 7-2: The weights of block and point data in the three cells with increasing block sizes	123
Table 8-1: The Surmont Lease resource estimation and uncertainty assessment: the blue shaded boxes are proportions and the others are barrels – standardized to “1.000” for the lease	171

LIST OF FIGURES

Figure 1-1: Schematic illustrations of the data and model scales for reservoir modeling. The modeling objects are taken from a heavy oil scenario in Northern Alberta.....	3
Figure 1-2: The cross plot of 2-D model versus the vertical averages of 3-D model of net pay thickness in meters (from Ren <i>et al.</i> , 2004)	4
Figure 2-1: Classifications of reservoir heterogeneity types (from Weber, 1986)	13
Figure 2-2: Schematic illustration of the scales of data, heterogeneity and model. The data and model scales are same as in Figure 1-1; they are related to the heterogeneity in the middle column.....	15
Figure 2-3: The volume averaged covariance models	18
Figure 3-1: Schematic illustration of the Bayesian Updating technique. The block dots are data, and the yellow square is a location being estimated	36
Figure 3-2: Schematic illustration of the location of updated distributions in Bayesian Updating technique	37
Figure 3-3: Cross plot of two variables that have a non-linear bivariate relationship....	40
Figure 3-4: Cross plot of two variables with two outliers in the blue circle gives a correlation of 0.590 (left). And cross plot of two variables without the two outliers gives a correlation of 0.728 (right).....	40
Figure 3-5: The maps of primary (left) and secondary (middle) variables and their cross plot (right) which indicates a global correlation coefficient of 0.533.....	41
Figure 3-6: The data locations and the cross plots for the upper-left corner (upper row) and the lower-right corner (lower row). The middle column shows the cross plots of the nine data shown in the location map. The right column shows the cross plots of exhaustive data in these corners	42
Figure 3-7: The locally varying correlation map of the two variables in Figure 3-5.....	43
Figure 3-8: The maps of two variables (left and middle) and their locally varying correlation (right) for the case of two pairs of extreme values shown in Figure 3-4	44

Figure 3-9: The locally varying correlation (LVC) maps with different powers	46
Figure 3-10: The histogram and kriged map of ACD for the two variables shown in Figure 3-5.....	47
Figure 3-11: The histogram and kriged map of ACD for the two variables shown in Figure 3-8. The two wells are the two outliers shown in the cross plot in Figure 3-4.....	47
Figure 3-12: The curve of data quality versus kriging variance when the maximum quality C is 1	49
Figure 3-13: The map of amplitude and its local varying quality (LVQ). The upper-left area is the 3-D seismic area, and the rest of the area is modeled by kriging using 2-D seismic lines	53
Figure 3-14: The global correlation and the map of locally varying correlation (LVC) between primary and amplitude (left column) and between secondary and amplitude (right column)	53
Figure 3-15: The results of Bayesian updating using global correlation coefficients	54
Figure 3-16: The results of enhanced Bayesian updating using LVC and LVQ	55
Figure 3-17: The maps of the difference between the Bayesian Updating (BU) results and the reference (left) and the difference between the Enhanced Bayesian updating (EBU) results and the reference (right).....	56
Figure 3-18: The cross validation of simple kriging (left), Bayesian updating (middle) and enhanced Bayesian updating (right).....	56
Figure 3-19: The cross plots of the estimates versus the reference for simple kriging (left), Bayesian Updating (middle), and the Enhanced Bayesian Updating (right)	57
Figure 3-20: The primary variable (reference) and secondary variable used for Bayesian updating are in the top row. The Bayesian updated estimates and P-field simulation realizations are shown in the middle and bottom rows	59
Figure 3-21: The cross plots of the reference versus the P-field simulation realizations #1, #5 and #10.....	60
Figure 3-22: The primary variable (reference, up-left) and the SGS with Bayesian updating simulation realizations	60
Figure 3-23: The cross plots of the reference versus the SGS with Bayesian updating simulation realizations #1, #5 and #10.....	61

Figure 3-24: The primary variable (reference, up-left) and the collocated co-simulation realizations	61
Figure 3-25: The cross plots of the reference versus the collocated co-simulation realizations #1, #5 and #10	62
Figure 4-1: The well locations and histograms of the primary data from the wells	65
Figure 4-2: The maps of the secondary variables: top and bottom surfaces are depth in meter, and the vertical averaged amplitude is standardized value	66
Figure 4-3: The work flow for Bayesian updating 2-D mapping techniques	67
Figure 4-4: The trend maps of the primary variables	68
Figure 4-5: The declustering results of the three primary variables. The left column row shows the declustered mean at different cell size range from 0 to 3000 m. The right column is the declustered distributions	70
Figure 4-6: The major and minor directional variograms of SBT (top), porosity (middle) and water saturation (bottom)	71
Figure 4-7: The prior maps of the primary variables	72
Figure 4-8: The cross plots of each pair of variables	73
Figure 4-9: The ACD maps of each pair of variables	74
Figure 4-10: The correlation matrix of all the variables	75
Figure 4-11: The locally varying correlations between primary variables and secondary variables	76
Figure 4-12: The likelihood maps of the primary variables from the global correlations. The variances are constant over the model area	77
Figure 4-13: The likelihood maps of the primary variables from the locally varying correlations. The variances are varying over the model area	78
Figure 4-14: The updated maps of the primary variables from Bayesian Updating method. The map of updated mean is on the left and the map of updated variance is on the right	79
Figure 4-15: The updated maps of the primary variables from Enhanced Bayesian Updating method. The map of updated mean is on the left and the map of updated variance is on the right	80

Figure 4-16: The P10/P50/P90 maps of SBT (top), porosity (middle) and water saturation (bottom).....	82
Figure 4-17: The cross validation of Bayesian Updating results for SBT	85
Figure 4-18: The cross validation of Bayesian Updating results for porosity	86
Figure 4-19: The cross validation of Bayesian Updating results for water saturation....	87
Figure 4-20: The cross validation of Enhanced Bayesian Updating results for SBT	88
Figure 4-21: The cross validation of Enhanced Bayesian Updating results for porosity	89
Figure 4-22: The cross validation of Enhanced Bayesian Updating results for water saturation.....	90
Figure 4-23: The accuracy plots of the SBT (left), porosity (middle) and water saturation (right) from Bayesian Updating method	91
Figure 4-24: The accuracy plots of the SBT (left), porosity (middle) and water saturation (right) from Enhanced Bayesian Updating method	91
Figure 5-1: A schematic illustration of joint uncertainty of OOIP from local uncertainty models of constituent variables. The square with black line is the estimated location.....	94
Figure 5-2: Work flow of the spatial/multivariate decomposition simulation approach for assessment of the global uncertainty from local uncertainty	98
Figure 5-3: The location map of the 64 wells with the colour scale showing the net pay thickness (left), and histograms of Net Pay thickness (centre) and ϕ_{So} (right)	99
Figure 5-4: Maps of three secondary variables: sequence boundary 1 (left), sequence boundary 2 (centre) and sequence boundary 3 (right)	99
Figure 5-5: Variogram for two primary data (left and centre) and the correlation matrix between the primary and secondary variables (right)	100
Figure 5-6: Prior (left), likelihood (centre) and updated (right) maps for NP (top) and ϕ_{So} (bottom).....	101
Figure 5-7: Final maps of uncertainty for Net Pay thickness (top row) and ϕ_{So} (bottom row): P10 (left), P50 (centre) and P90 (right). Note the east-west section lines in the Net Pay thickness final maps are plotted in Figure 5 8, and the black circles represent well locations	101

Figure 5-8: Uncertainty of Net Pay thickness in an east-west section: P10 (bottom line), P50 (middle line), and P90 (top line).....	102
Figure 5-9: Realizations 5, 50 and 95 of the spatial/multivariate simulation. In each realization, all values are spatially correlated over the model area and the Net Pay thickness (top) and ϕ So (bottom) are also correlated.....	103
Figure 5-10: Calculated OOIP from the two variables shown in Figure 5-9. Two areas of interest (in black line) and the whole model area were selected to estimate the OOIP. The OOIP in the three areas are shown below the maps for each realization.....	103
Figure 5-11: Distributions of global uncertainty in OOIP in Area 1 (left), Area 2 (centre), and the Whole Model Area (right).....	104
Figure 7-1: The kriging weights of block and point data with different variogram ranges	122
Figure 7-2: The weights of block and point data in the cells “1-3” with different block sizes. At the well location, the weights are constant (dash lines). Away from the well, the weights change with block size (solid lines).....	123
Figure 7-3: The large scale data (upper left) and the downscaled results in the three cases	125
Figure 7-4: The weight of collocated block in each small cell in case 1	126
Figure 7-5: The weights of blocks in each small cell in case 2	126
Figure 7-6: The weights of blocks in the small cell in case 3.....	127
Figure 7-7: The kriging weight of block datum changes with simulation path	128
Figure 7-8: The Kriging weights of point data changes with simulation path.....	128
Figure 7-9: The kriging variance changes with simulation path.....	129
Figure 7-10: The graphical representation of the transformations applied to calculate the local distributions of uncertainty. The illustrated transformation is repeated for a sufficient number of quantiles to describe the local distribution (from Pyrcz and Deutsch, 2003)	134
Figure 7-11: The proportional effect shown at different moving window sizes (50m, 100m and 200m). The two sets of lognormal data are used (the first row): a set of well data (left) and the sgsim realization using the well data (right). The correlations are different with different window sizes.....	135

Figure 7-12: The local distribution and variance are affected by the data values	136
Figure 7-13: The CCDF lookup-table method results with a lognormal global distribution (top). The proportional effect is accounted in the DSS (second row). The CCDF table of means and variances does not cover all the kriging mean and variances (third row). The results of matching mean and variance are shown in bottom row	139
Figure 7-14: The CCDF lookup-table method results with a global distribution (top row). The proportional effect is not clear (second right). The CCDF table of means and variances does not cover all the kriging mean and variances (third row). The results of matching means and variances are shown in bottom row...	140
Figure 7-15: 2-D map of porosity block data at scale of 50m x 50m x 10 m.....	141
Figure 7-16: The location map of the 16 wells and the histogram of the well log data	142
Figure 7-17: The horizontal and vertical variograms and variogram models.....	142
Figure 7-18: The 3-D porosity model from EDDK	143
Figure 7-19: The 2-D porosity map and all odd numbered x-y view slices of the 3-D model from EDDK. The 3-D porosity is at scale of 50x50x1m. The dashed lines in the porosity map (the top left) indicate the locations of the x-z and y-z cross sections.....	144
Figure 7-20: The x-z and y-z cross sections of the 3-D porosity model from EDDK. The 3-D porosity is at scale of 50x50x1m. The dashed lines in the x-z and y-z cross sections indicate the wells. The horizontal continuity matches the well data.....	145
Figure 7-21: A 3-D porosity realization from EDDSS	145
Figure 7-22: The 2-D porosity map and all odd numbered x-y view slices of the 3-D model from EDDSS. The 3-D porosity is at scale of 50x50x1m. The dashed lines in the porosity map (the top left) indicate the locations of the x-z and y-z cross sections.....	146
Figure 7-23: The x-z and y-z cross sections of the 3-D porosity model from EDDSS. The 3-D porosity is at scale of 50x50x1m. The dashed lines in the x-z and y-z cross sections indicate the wells. The horizontal continuity matches the well data.....	147
Figure 7-24: The block 2-D porosity map (left), the map of the column averaged porosity from the 3D model (middle), and the cross plot of the two grids	148

Figure 7-25: The histogram of fine scale porosity estimates from EDDK (left) and EDDSS (right).....	148
Figure 7-26: The block data and well data used for downscaling	149
Figure 7-27: The exact downscaling results in plane view (first row), y-z (left) and x-z (right) cross sections	150
Figure 7-28: The approximate downscaling results in plane view (first row), y-z (left) and x-z (right) cross sections	151
Figure 7-29: The map of original porosity block data (top), the map of vertical averages porosity from the exact downscaled 3-D model (left) and the map of vertical averages porosity from the approximate downscaled 3-D model (right)...	152
Figure 7-30: The cross plots of porosity block data vs. block average of fine scale model for the exact downscaling method (left) and the approximate downscaling method (right)	152
Figure 7-31: The steam chambers after 5 years of steam injection. The model by exact downscaling gives a better developed steam chamber.....	153
Figure 7-32: The results of flow simulation using the models generated by the two methods: the top plot is the cumulative oil production curves, and the bottom plot is the steam oil ratio (SOR) curves. The gray solid line is for the approximate downscaling method, and the black dash line is for the exact downscaling method	154
Figure 8-1: The location of the Surmont lease in the map of Alberta, Canada	155
Figure 8-2: The Surmont lease map with well locations	156
Figure 8-3: The trend maps of NCB and BOW are shown on the top, and the Prior maps are shown on the bottom	159
Figure 8-4: Directional variograms and fitted models for NCB (left) and BOW (right)....	160
Figure 8-5: The correlation matrix of the 8 variables	161
Figure 8-6: The maps of the four secondary data	162
Figure 8-7: The prior (top left), likelihood (top right) and updated maps (bottom) of NCB	163
Figure 8-8: The prior (top left), likelihood (top right) and updated maps (bottom) of BOW	164

Figure 8-9: Maps summarizing uncertainty in NCB (top row) and BOW (bottom row). The P10 low values are shown on the left, the P50 values are shown in the middle and the P90 high values are shown on the right.....	165
Figure 8-10: The accuracy plots of cross validation results for NCB and BOW	166
Figure 8-11: Accuracy plot of 2-D model vs. new wells of 2004.....	166
Figure 8-12: The Bayesian Updating with P-Field simulation realization#1(middle left) is exact downscaled from 50m by 50m to 10m by 10m (bottom left). The histograms of point data (top right), block data (middle right), and downscaled values are shown on the right.....	172
Figure 8-13: The stratigraphic surfaces used for the 3-D modeling: WabMCM is the top surface, and DevUnc is the bottom surface. Parallel to top is used for the vertical stratigraphic coordinate.....	173
Figure 8-14: The histograms of point data (top left), block data (top right), and 3-D downscaled values (bottom).....	174
Figure 8-15: The 3D porosity realization #1. The model has a grid resolution of 10 x 10m aerially and 1m vertically. The field spans 1,400m, 1,000m and 91m in the Easting, Northing and Elevation directions, respectively. The vertical direction is exaggerated by 5 times.....	175
Figure A-1: An example parameter file for EDSK.....	183
Figure A-2: An example parameter file for EDDSS.....	184

NOMENCLATURE

A	Area or volume of interest
ACD	Average Correlation Difference
APL	vertically averaged amplitude over the bitumen-bearing zone
BOT	bottom surface
BOW	bulk oil weight (fraction of the bitumen mass to the total rock mass)
BSM	bottom surface of the McMurray formation
BU	Bayesian updating
\bar{C}	volume averaged covariances
C	covariance between two variables
CCDF	conditional cumulative density function
CC-SGS	collocated co-simulation
CSOR	cumulative steam oil ratio
DSS	direct sequential simulation
EBU	enhanced Bayesian updating
EDDK	exact downscaling with direct kriging
EDDSS	exact downscaling with direct sequential simulation
EGT	effective gas thickness
EOR	enhanced oil recovery
EWT	effective water thickness
GTM	gross thickness of the McMurray formation

GOR	gas oil ratio
LVC	locally varying correlation
LVQ	locally varying quality
NCB	net continuous bitumen thickness
NP	Net Pay thickness
OOIP	original oil in place
PFBU	P-field simulation with Bayesian updating
SAGD	steam assisted gravity drainage process
SBT	SAGD recoverable bitumen thickness
SGS	sequential Gaussian simulation
SGSBU	SGS with Bayesian updating
SSC	Sequential Self-Calibration method
TOP	top surface
TSM	top surface of the McMurray formation
TZ	thief zone
TZPT	thief zone protection factor
WMS	Wabiskaw-McMurray surface
ϕ	porosity
λ	weight of data
m	mean of data
σ^2	variance of data
σ_{sk}^2	kriging variance
ρ	correlation between different variables

$R(\mathbf{u})$	the random residual at the simulated location \mathbf{u}
\mathbf{L}	the lower matrix
S_o	oil saturation
S_w	water saturation
\mathbf{U}	the upper matrix
\mathbf{u}	location vector in A
\mathbf{w}	A vector of uncorrelated standard normal values
V_{pV}	pore volume
V_{bV}	bulk volume of the rock
Z_V	block value
Z_v	value in the model cells.
Z_{vs}	previously simulated data in the model cells
Z_{\bullet}	point data

CHAPTER 1

INTRODUCTION

Reservoir management and development planning rely on accurate reservoir description. Heterogeneous reservoirs are difficult to model accurately with limited well data and geological information. It is impossible to exactly describe subsurface formations with available data. Uncertainty exists at unsampled locations. The uncertainty and heterogeneity of a reservoir are often modeled by geostatistical techniques. Geostatistical techniques are practical tools that are used to construct reservoir models by statistical inference from available data. Realistic heterogeneities are introduced in the reservoir models that reproduce input data and their spatial correlations. A measurement of uncertainty in the models is generated for the quantification of risks in making decisions. Modern reservoir management requires an assessment of these uncertainties and risks associated with heterogeneity.

Generally, a realistic assessment of uncertainty can be established by numerical modeling that integrates all available data and expert knowledge into reservoir models. Geostatistical techniques and numerical modeling continue to be developed for improved reservoir modeling. Data integration is a challenging task because there are different types of data from different sources at different times. These data have variable reliability, coverage and measurement scale.

Geostatistical reservoir models are commonly built for static reservoir properties such as porosity, permeability, initial fluid saturations, and lithofacies. Other geological properties such as structural surfaces and net pay thickness are sometimes modeled (Deutsch, 2002). The data used for modeling come from a variety of sources including core, well logs, seismic, well testing, production history and conceptual geological models. Well data are generally sparse laterally and dense vertically. Seismic data have extensive lateral coverage but with less vertical resolution than well data. Dynamic data

such as well testing and production data may provide information in the interwell regions at a large scale. Seismic and dynamic data do not directly measure the reservoir properties of interest. Often, the seismic data are used as secondary data while the well data are used as primary data in reservoir modeling. Then, the dynamic data are used to verify or update the model by inversion techniques with history matching (Wen *et al.*, 2005).

A difficult problem in data integration is that the scales of different data types are very different (see the left part in Figure 1-1). Core data are usually measured in laboratory at a scale of a few centimeters. Well log data usually represent properties at a decimeter scale. Seismic data represent a much larger scale. Well test and production data have an even larger scale. They usually are all different from the model scale. Accounting for the different data scales greatly increases the complexity of reservoir modeling. Pre-processing to bring all the data to the model scale can simplify the multiscale modeling to single scale modeling. Upscaling is relatively straightforward, but downscaling does not give a unique solution. Practitioners tend to ignore scale differences or use approximate methods to simplify the scale problem; however, using well data to represent grid blocks that are hundreds or thousands times bigger than the data scale, or assigning large scale data to small grid blocks greatly reduces the accuracy of the reservoir model. A quantitative approach to relate different scales must be established. A scale consistent modeling technique that appropriately accounts for all scales is required for more accurate reservoir description.

A reservoir sometimes is modeled at more than one scale. Consistency of models at different scales is important. The model scale is usually chosen based on the different modeling purposes, the area to be modeled, available techniques and computational cost (see the right part in Figure 1-1). In Canada's heavy oil reservoirs, it is common to build a full reservoir model at a large scale for reserve estimation and build a detailed 3-D model at a fine scale for flow simulation. The two models rarely reconcile with each other when the fine scale model is scaled up to the large scale (Ren *et al.* 2004a; Ren *et al.*, 2005c). As an example, a cross plot of 2-D model versus the vertical averages of 3-D model of porosity is shown in Figure 1-2. A poor correlation coefficient of 0.011

indicates an inconsistency between the 2-D and 3-D models. Different modeling techniques and different usages of the input data contribute to such inconsistency between models. To avoid this situation, a scale consistent modeling scenario is proposed for more accurate reservoir modeling.

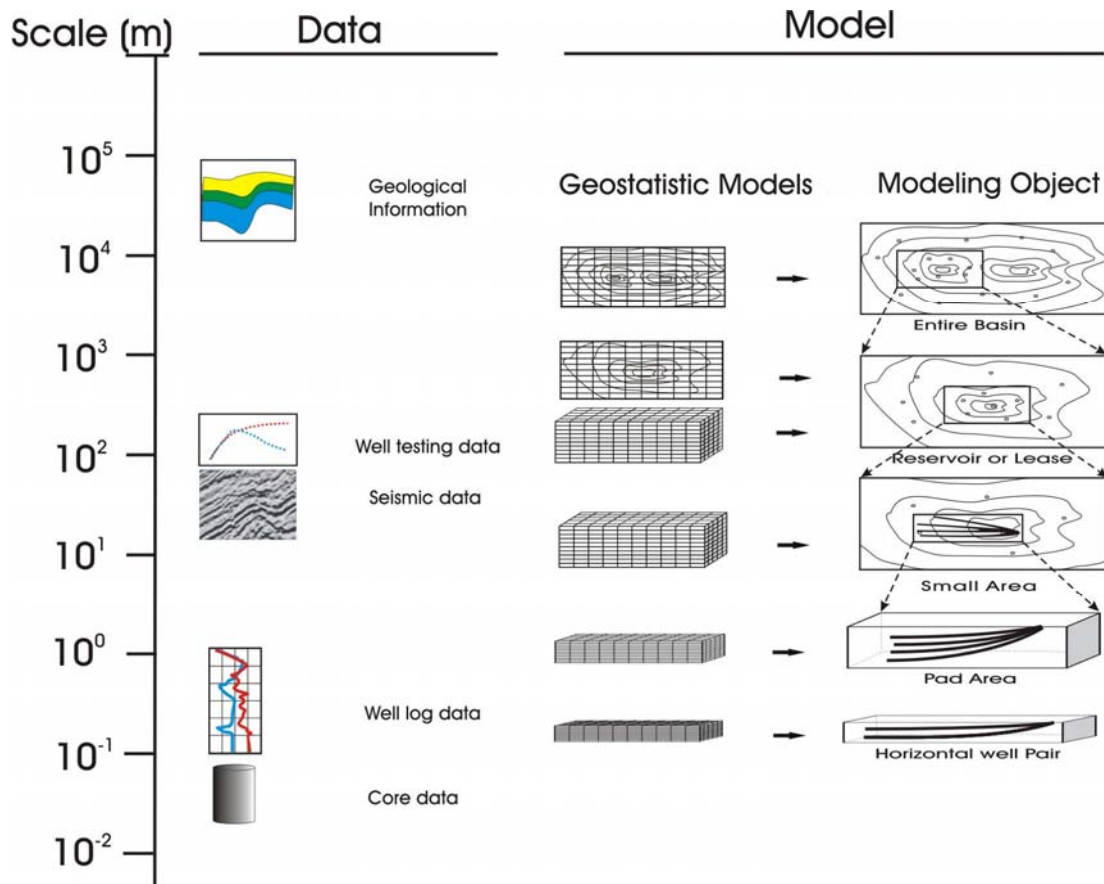


Figure 1-1: Schematic illustrations of the data and model scales for reservoir modeling. The modeling objects are taken from a heavy oil scenario in Northern Alberta.

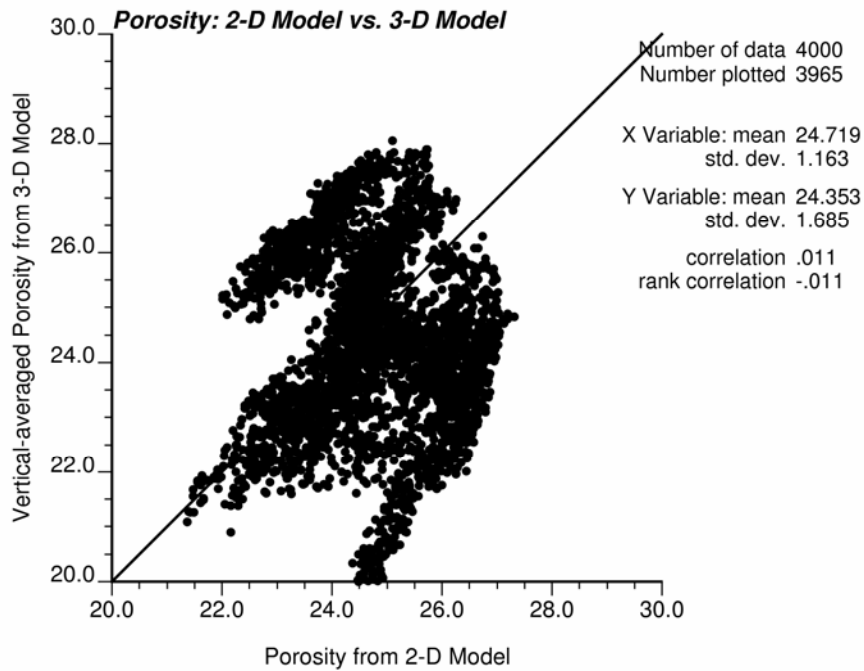


Figure 1-2: The cross plot of 2-D model versus the vertical averages of 3-D model of porosity in % (from Ren *et al.*, 2005c).

1.1. Proposed Modeling Method

The proposed scale consistent reservoir modeling scenario consists of three main steps: (1) build a full reservoir model at a large scale to account for geological trends, large scale seismic information and upscaled well data, (2) assess global resource uncertainty from the large scale reservoir model, and (3) exactly downscale the large scale model to the target scale using small scale well data.

A field scale reservoir model can help to understand the entire reservoir, to provide resource estimation and to identify the areas of interest where have the most potential to develop. Building a model at a large scale is relatively straightforward because all data can be upscaled to the model scale or converted to 2-D. The advantage of large scale modeling is that geologic trends can be easily captured. It is important to capture the large scale trends in a reservoir model because they have significant influence on flow performance (Lasseter *et al.*, 1986; Weber, 1986; Kelkar and Perez, 2002). Large scale data such as seismic data and production data also provide information on large scale

variability. The key aspect of large scale modeling is to integrate all available data to reduce the uncertainty at each location. Bayesian updating technique will be introduced for this purpose. A non-stationary Bayesian updating technique is developed by accounting for locally varying correlation and data quality. The theory and implementation will be presented.

Petroleum resource over an entire lease or a large area always associates with a large uncertainty, or in geostatistical term: *global uncertainty*. Assessing global uncertainty on resource estimation is important for reservoir management and decision making. Upscaling the local uncertainties from the large scale models to the large area provides a global uncertainty that is consistent with the local uncertainties. A spatial/multivariate simulation approach is proposed for the assessment of global uncertainty.

Once the areas of interest are defined from the large scale model, a fine scale 3-D model is normally required for flow simulation or horizontal well placement. There are many techniques for using large scale data to construct fine scale models including co-kriging, collocated co-kriging, and using the large scale data as locally varying mean (Goovaerts, 1997; Deutsch, 2002). Although these methods constrain the fine scale model with the large scale data, they do not exactly match the large scale data. To avoid any biases in the downscaling, and to ensure consistency in the models at different scales, an exact downscaling technique is needed so that the large scale data can be exactly reproduced. An exact downscaling technique is developed in the thesis. The large scale model can be exactly downscaled to smaller scales so that the reservoir models at all scales are linked together and completely consistent. The exact downscaling technique is developed based on direct block kriging and direct sequential simulation (DSS). The theory and implementation will be presented.

Application of the techniques to the Surmont lease of the McMurray Formation will be used to demonstrate the applicability and usefulness of the proposed technique.

1.2. Outline of The Thesis

The scale consistent modeling for reservoir characterization relies on integration of multiscale data. The second chapter presents a brief review of multiscale data and important data features, such as different sources, availability, coverage, reliability, and scales. Data integration techniques for the most common data: well, seismic, and dynamic data are also reviewed. Chapters 3 and 4 focus on large scale modeling. The theory of the Bayesian updating technique and the enhanced Bayesian updating technique with locally varying correlation and locally varying quality are presented in Chapter 3. In addition, simulation approaches with Bayesian updating are also introduced in Chapter 3. The implementation details of the Bayesian updating techniques for large scale 2-D mapping are presented in Chapter 4. The technique of resource estimation with assessment of global uncertainty from the mapping results is provided in Chapter 5. Chapters 6 and 7 focus on the exact downscaling techniques. The theory of the exact downscaling with direct kriging and the exact downscaling with direct sequential simulation are presented in Chapter 6. Chapter 7 shows the implementation details of the exact downscaling techniques. Some issues related to histogram reproduction and accounting for the proportional effect in DSS are addressed. A case study of scale consistent modeling for the McMurray Formation in the Surmont lease is presented in Chapter 8. Conclusions and recommendations are provided in the last Chapter.

CHAPTER 2

MULTISCALE DATA AND DATA INTEGRATION

There are a variety of data available for reservoir modeling. Accounting for all of the data simultaneously in a reservoir model is a big challenge because of different data features. This chapter reviews some important data features and data integration techniques.

2.1 Data Sources

The data for reservoir modeling are normally classified into three categories: geological, geophysical and engineering data. Most of the data are listed in Table 2-1. The table is built based on the information from Satter *et al.* (1994) and Reza (2003). All of these data will not be available for any particular reservoir modeling exercise. Because core, well logs, seismic, well test and production data (Table 2-2) are the most commonly used data for reservoir modeling, these data are considered in this thesis.

These common data may be a complex combination of different data sources. Well log data, for example, can be obtained from a variety of logging measurements including Gamma ray, resistivity, or a combination of different logs (see the partial list in Table 2-2). The resolution of each data source is potentially different. Other data features such as data availability, coverage, and reliability are also different. The data coverage is the proportion of a reservoir that is actually measured by the same type of data. Data reliability relates to the precision of the data measurement.

Geological Data	Geophysical Data	Engineering Data
Core description	2D seismic	Well logging analysis
Thin-sections	3D seismic	Conventional core analysis
Microscopes image analysis	4D or time-lapse 3D seismic	Special core analysis
X-ray	4C or multicomponent seismic	Pressure transient well tests
Stable isotope analysis	Cross-well tomography	Production history
Depositional models	Vertical seismic profile	Well tracer test
Diagenetic models	Shear-wave logging	Computed tomography scan
Structural modeling	Isochrons for structure tops	Nuclear magnetic resonance
Maps, cross sections		
Remote sensing		

Table 2-1: Different data sources for reservoir modeling (summarized based on Satter *et al.*, 1994 and Reza, 2003)

Data Types	Data Sources	Vertical Resolution	Data Description
core	Unaided human eye on a 1/3 slab of 4-in core from a distance of 24 in.	0.2 in.	Direct measurements of porosity, permeability, fluid saturations, and lithofacies
	1 ft of 4-in. core	12 in.	
	1x2-in. plug	1 in.	
logs	Density	15 in.	Recorded logs, need interpretation to get porosity, permeability, fluid saturations, and lithofacies
	Neutron	24 in.	
	Microelectrical log	2 in.	
	Gamma ray	20 in.	
	MWD resistivity	6 in.	
	MWD bit resistivity (oil-based mud)	1 in.	
seismic	2D seismic	function of depth > 10 m	Recorded seismic waves contains travel time and amplitudes. Structures, velocity, impedance, density can be inferred by inversion techniques
	3D seismic		
	4D or time-lapse 3D seismic		
	4C or multicomponent seismic		
well test	Drawdown/buildup test	interwell	Recorded pressure curve P(t), Inversion techniques applied to get effective kh, distance to boundary, fault information.
	RFT test		
	Variable rates test		
	Gas well test		
	Multiple wells test		
production	Production well	interwell	Measured pressure P(t), flow rates q(t), and fluid samples

Table 2-2: Common data for reservoir characterization (based on Kelkar and Perez, 2002 and Wen *et al.* 2005)

2.2 Data Availability, Coverage and Reliability

2.2.1 Data availability

Data are not all available at the same time. They become available during the course of reservoir development. According to Johnston (1992), the field management of a reservoir consists of four phases. At the beginning, the predevelopment phase, delineation is the main focus to maximize the reserves. Very limited core and well log data are available in this phase. Seismic data if available will be very helpful for defining reservoir boundaries. In the second phase, the initial development phase, the placement of production wells is the main focus to maximize the oil recovery. A complete geologic model of the reservoir with description of gas cap, oil zones and aquifer is required. A fair amount of well data and seismic data should be available for this purpose. When entering the operating phase, as the production wells begin to produce, dynamic data such as well test and production data become available. The integration of the reservoir performance data into the geological model is important for reservoir surveillance. Automatic history matching (Wen *et al.*, 2005, Tran *et al.*, 1999) will improve the reservoir prediction through reservoir flow simulation, providing information for adjusting depletion strategy and applying secondary recovery processes. The last phase, the enhanced recovery phase, requires a high resolution reservoir model because reliable knowledge of small scale heterogeneity and anisotropy is critical for the success of expensive Enhanced Oil Recovery (EOR) methods. Integration of all available data with precise consideration of data scales is the key for such detailed reservoir models. New data become available at different times. Updating the reservoir model with the new data will approach a more accurate reservoir description.

2.2.2 Data coverage

Data from different sources have different coverage on a reservoir. Well data provide detailed information along the wells, but with limited lateral coverage. Wells are widely spaced compared to the scale of geologic variability. On the contrary, the 3-D seismic

data have more complete lateral coverage, but limited vertical resolution relative to well data. Well test and production data extend well coverage to the drainage volumes near the wells, and perhaps provide some information about reservoir boundaries.

2.2.3 Data reliability

Not all data are direct measurements of the reservoir properties being considered. Some data provides indirect information on these properties. They must be treated differently according to their different levels of precision. The well data (core and well logs) are very close to direct measurements. Measurement errors are often ignored. Well data are considered as the most reliable data, or *hard data*. Seismic data are acoustic measurements of formation properties. These indirect information or *soft data* are normally treated as secondary data in reservoir modeling. The seismic-derived properties such as porosity are not precise, and this imprecision needs to be explicitly accounted for (Deutsch *et al.*, 1996). The dynamic data such as production rates and bottom-hole pressure are important reservoir performance data. The static properties can not be directly inferred from the dynamic data. Inversion techniques with flow simulation must be applied. The non-uniqueness of the inversion solution and the simplifications in the flow model are such that the derived reservoir property models may not be reliable even when a good history match is reached (Wen *et al.*, 2005, Tamhane *et al.*, 1999). Nevertheless, they often provide useful information that is closely related to the reservoir performance variables being predicted.

2.3 Data Scale and Model Scale

The data scale is the size of rock volume from which the property is measured. It is different from the coverage that focuses on the whole reservoir. The model scale is the size of grid block of a model being constructed.

2.3.1 Data scale

Data from different sources have different scales. Core data are usually measured in a laboratory at the scale of a few centimeters (Table 2-2). Conventional well log data usually represent rock properties at a decimeter scale. Certain high resolution well logs could have smaller scale. Seismic data have a vertical resolution related to seismic wavelength which is a function of velocity and dominant frequency. Resolution decreases rapidly with depth (Sheriff, 1992). Even the smallest resolution is larger than the core and log data. A nominal scale is about 10 meters. Well test and production data provide average information for the drainage volume around the wells. The well test derived permeability may represent ten billion times larger than the core volume (Haldorsen, 1986). The geological description, such as a sequence stratigraphic interpretation, gives the information at a reservoir scale 100s to 1000s of meters. These scale differences must be appropriately accounted for in reservoir modeling.

2.3.2 Model scale

The model scale is normally different from any of the data scales. It is chosen based on the size of the modeled area, modeling techniques and computational cost. Geostatistical models are often constructed at a scale larger than well data and less than the reservoir model for flow simulation.

Flow simulation typically demands more CPU time than that required for geostatistical modeling. Computational efficiency requires the input reservoir models at a coarser scale than the geostatistical model. The model scale may even be larger than the seismic data (Tamhane *et al.*, 1999). The input reservoir models are usually generated by upscaling the fine scale geostatistical models; however, in some special cases, the input model for flow simulation may be required to have a very fine scale. For example, in the McMurray Formation of Alberta, Canada, where the advanced heavy oil recovery technique, Steam Assisted Gravity Drainage (SAGD) process (Butler, 1991) is commonly used for oil sands recovery, the flow simulation of horizontal well pairs or an individual SAGD pad is very important. The detailed flow simulation of selected small areas

requires input models at a very fine grid size. Downscaling of geostatistical models may be required.

The variability of reservoir properties varies by scale. Data variability usually increases as the scale decreases; extreme high and low values are more likely at fine scale. This small scale variability averages out at coarser scales. The different data variability must be accounted for in reservoir modeling at different scales.

2.4 Reservoir Heterogeneity at Different Scales

Reservoir heterogeneity is spatial variation of reservoir properties and always refers to different geological structures. If a property such as permeability is constant over the whole reservoir, it is homogeneous. Real reservoirs are seldom homogeneous. Most reservoirs have very complex patterns of heterogeneity. Figure 2-1 shows seven important reservoir heterogeneity types selected by Weber (1986). Flow performance is directly affected by reservoir heterogeneity; therefore, the accuracy of a reservoir model depends on an adequate description of reservoir heterogeneity.

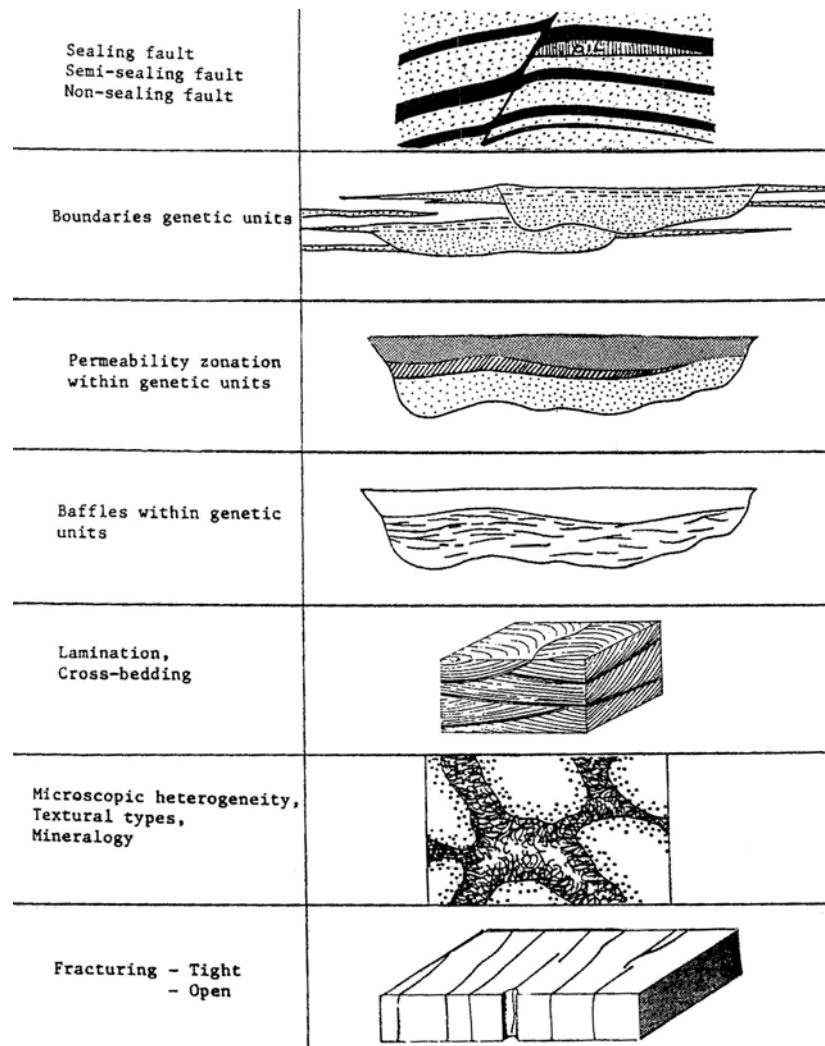


Figure 2-1: Classifications of reservoir heterogeneity types (from Weber, 1986).

Reservoir heterogeneity is scale dependent. Based on the common data scales and model scale, the heterogeneity in a reservoir can be roughly classified into four scale categories (Haldorsen, 1986; Hewett and Behrens, 1990). They are elaborated in Table 2-3 and shown in Figure 2-2. The largest heterogeneity scale is the gigascopic or reservoir scale. Heterogeneity at this scale appears as large geological trends and major faults that can be detected from seismic surveys. The data variation at the large scale normally is low. However, if large scale trends or major faults are presented, the data variation may be high. Primary oil recovery that relies on the natural energy depletion may not be affected significantly by small scale heterogeneity but certainly will be limited by a sealed fault nearby. Large scale heterogeneity has significant influence on

reservoir performance. Inaccurate modeling of large scale heterogeneity can mislead the prediction of any recovery process (Kelkar and Perez, 2002). The next scale is the megascopic or grid block scale used for a reservoir model. Heterogeneity at this scale appears as permeability zonation that can largely affect the sweep efficiency of waterflooding and is a major cause for bypassed oil. Some well logs and seismic data can measure the heterogeneity at this scale. The third scale is the macroscopic scale of core plugs and flow properties measured in a laboratory. The heterogeneity at this scale such as cross lamination is directly observed from core and should be honored in reservoir models. The smallest scale is the microscopic or pore level scale. This is the scale that fluids actually flow. Heterogeneity at this scale has to be observed through microscope to capture the connectivity of pores and the variation in rock lithology, mineralogy and grain-size distribution. This microscopic heterogeneity is a major cause for trapped oil in the reservoir. The adequate characterization of the effective behaviour of microscopic heterogeneity is critical for EOR methods.

There have been many attempts to model reservoir heterogeneity at all scales. Hewett (1986) brought Mandelbrot's fractal geometry theory into reservoir modeling and presented a methodology of using fractal geometry and fractal statistics to characterize reservoir heterogeneity. Fractal geometry can be used to describe many natural objects on all scales. Fractals are shapes or phenomena that are scale invariant. Their shapes remain unchanged if you zoom in or out; the whole looks like the parts. This character of fractal phenomena is often referred to as self-similarity. Mathematical self-similarity leads to significant numerical advantages. The variance at any scale can be determined from the variance measured at any other scale and a limited number of parameters.

Numerous studies have been conducted on fractal simulation (Hewett and Behrens, 1990, Fang *et al.*, 1992, Kentnell *et al.*, 1999, Yeten and Gumrah, 2000); however, due to important limitations, fractal simulation has not been widely used. In practice, the self-similarity of fractals only holds true for three or four scales. The reservoir model constructed by fractal simulation cannot reproduce local data. Post conditioning techniques, such as conditioning by kriging (Journel and Huijbregts, 1978, Ren *et al.*, 2004) are required.

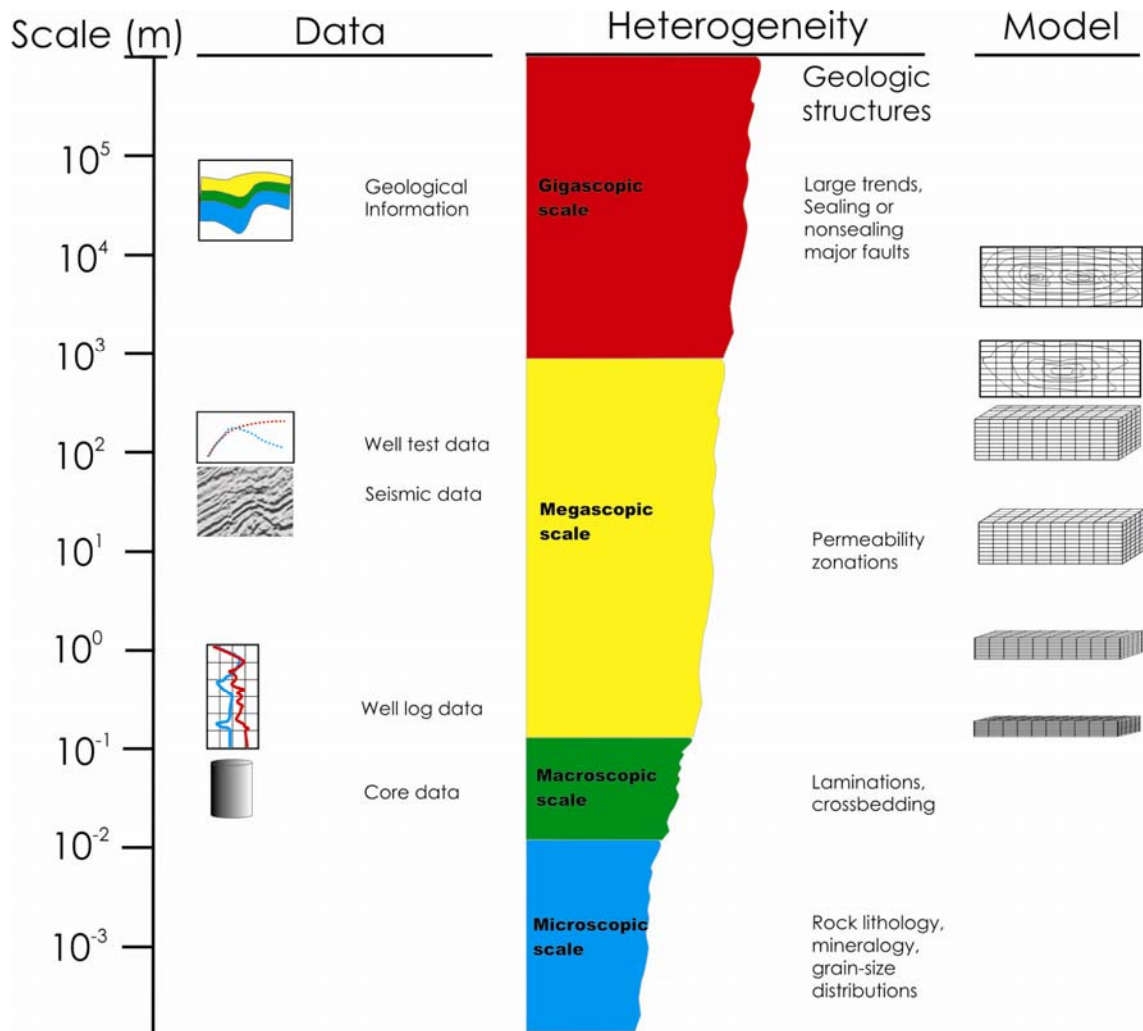


Figure 2-2: Schematic illustration of the scales of data, heterogeneity and model. The data and model scales are same as in Figure 1-1; they are related to the heterogeneity in the middle column.

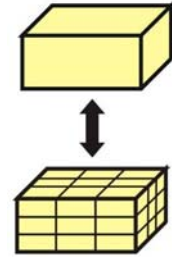
Type	Level	Measurement Scale	Measurements	Geologic Observations/Measurements	Flow Performance Effect	Flow Process Effect
Micro	Pore	$\approx \mu\text{m}$	Pore geometry Grain size Mineralogy	Texture Mineralogy Fractures	Displacement efficiency (trapped oil)	Complex EOR process
Macro	Core	$\approx \text{inch}$	k k_r ϕ P_c Wettability Saturation	Lamination Crossbedding baffles within genetic units	Sweep efficiency (bypassed oil)	Secondary recovery (waterflooding)
Mega	Gridblock	$\approx \text{foot}$	Logs RFT's Single-well tracer Seismic	Boundaries of genetic units Permeability zonation within units	Sweep efficiency (bypassed oil)	Secondary recovery (waterflooding)
Giga	Interwell	$\approx \text{mile}$	Well test Surface seismic interwell tracer tests	Sealing/nonsealing faults	Extraction efficiency (untrapped oil)	Primary recovery

Table 2-3: Scales of reservoir heterogeneities (from Kelkar and Perez, 2002)

Appropriately accounting for the scale difference of data will help the reservoir model capture the heterogeneity at all relevant scales. Multiscale data and information need to be brought to the model scale. A quantitative means must be established to relate different scales.

2.5 Scale Relationships of Data

Most static properties such as porosity, fluid saturations, layer thickness, and facies proportions scale linearly, that is, the large scale value is the arithmetic average of the small scale values. For example, porosity is the fraction of pore volume V_{pV} over the bulk volume of the rock V_{bV} . Discretizing the bulk volume into n equal-sized small volumes, V_{bv} , the block porosity value ϕ_V is exactly the average of the small scale porosities ϕ_{vi} :



$$\phi_V = \frac{V_{pV}}{V_{bV}} = \frac{\sum_{i=1}^n V_{pvi}}{n V_{bv}} = \frac{1}{n} \sum_{i=1}^n \frac{V_{pvi}}{V_{bv}} = \frac{1}{n} \sum_{i=1}^n \phi_{vi} \quad (2-1)$$

where V_{pvi} is the pore volume in the small volumes.

The same property of linear scale averaging is true for fluid saturations and layer thickness.

Lithofacies are categorical variables. This linear scaling relationship applies to their proportions. Proportions should be used carefully in lithofacies modeling because the estimated lithofacies proportions may not sum to one if the lithofacies are modeled separately.

Permeability has a complex relationship between scales. The scale relationship is linear only in an ideal case of the constant permeability layers that are parallel to the flow direction. When the layers are series to the flow direction, it is a harmonic average rather than an arithmetic average. In most cases, permeabilities vary in different directions and exhibit a strong anisotropy (Lake, 1988). The non-linear scale relationship can be expressed approximately by the incomplete layer method (Cardwell and Parsons, 1945).

A power law transformation could be used to make the arithmetic averaging applicable to the transformed permeability (Zanon *et al.* 1999, Deutsch, 2002).

The linear scale relationship can be easily handled with geostatistical modeling techniques. The linear scale relationship must be preserved in the multiscale modeling techniques. Non-linear transforms such as normal score transform or logarithmic transform do not preserve the linear scale averaging relationship; therefore, sequential Gaussian simulation (SGS) and other Gaussian-based geostatistical techniques cannot be used directly for multiscale modeling.

Upscaling and downscaling are often required to bring multiscale data to the model scale so that the Gaussian-based techniques can be used. With the linear relationship, upscaling is straightforward; but downscaling is a problem because of non-uniqueness. One can simplify the downscaling problem by using a simple duplication method that duplicates the block datum to each small cell in the large scale block; however, the small scale variation is ignored. Covariances can be used to relate all the scales together and appropriately account for data variation at different scales in the multiscale modeling.

2.6 Volume Averaged Covariance

In the common geostatistical modeling techniques such as kriging and sequential simulation, spatial correlation is defined by two-point statistics: covariance or variogram (Journel and Huijbregts, 1978; Isaaks and Srivastava, 1989; Goovaerts, 1997). The covariance (top of Figure 2-3) is used to establish how any two points relate together. A point and a block can be linked together using a point-to-block covariance (middle of Figure 2-3). The point-to-block covariance is the volume averaged covariance between any particular point and all the points in the block. The volume averaged covariance was introduced with block kriging (Journel and Huijbregts, 1978; Isaaks and Srivastava, 1989; Goovaerts, 1997). It is interesting to note that the block estimate using the point-to-block covariance is identical to the average of all the point estimates using the point-to-point covariance in the block (Isaaks and Srivastava, 1989; Goovaerts, 1997). It means the linear scale relationship can be preserved in a model when we use volume averaged covariance to relate multiscale data.

The block-to-block covariance (bottom of Figure 2-3) can also be calculated from the point-to-point covariance. Numerical discretization is required. The number of discretizing points should be larger than 4^n , where n is the dimension number, in order to get an accurate point-to-block covariance and block-to-block covariance (Isaaks and Srivastava, 1989; Goovaerts, 1997).

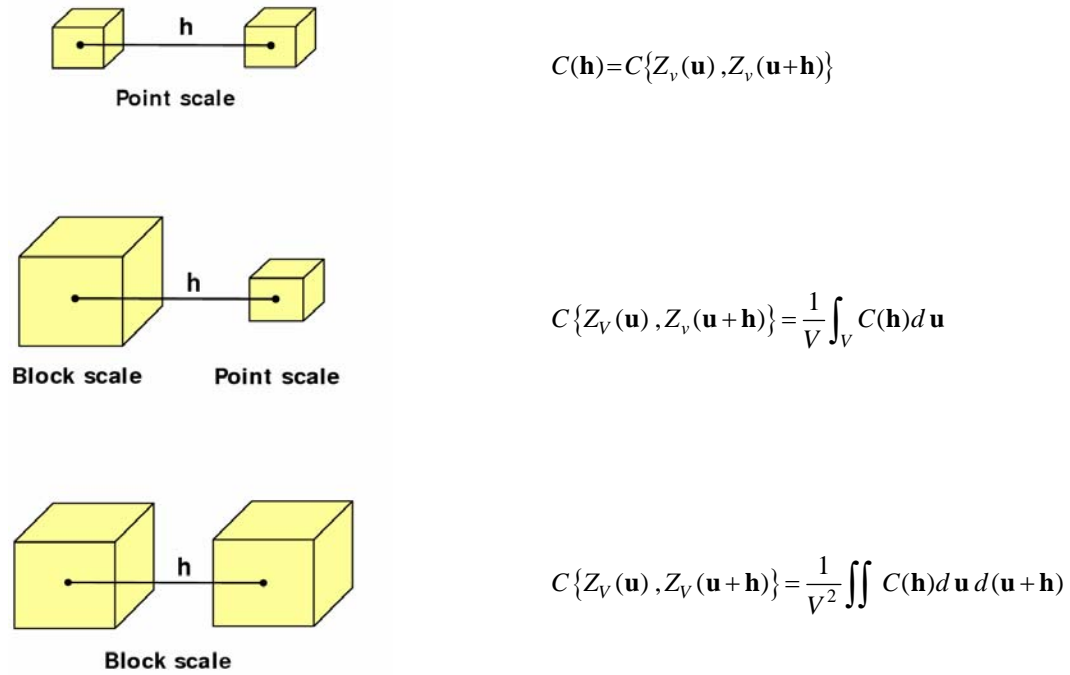


Figure 2-3: The volume averaged covariance models, where v is for the point scale volume and V is for the block scale volume.

Volume averaged covariances must be calculated from the point scale covariance. Inferring the point-to-point covariance from the block-to-block covariance does not give unique solution (Kupfersberger *et al.*, 1998).

Volume averaged covariances can be used for multiscale data to avoid explicitly scaling data. Accounting for different data scales and other data features in multiscale modeling requires advanced geostatistical techniques.

2.7 Data Integration Techniques

A number of techniques have been developed to integrate multiscale data in reservoir models. The techniques for integration of well, seismic and dynamic data are reviewed in the following sections.

2.7.1 Well data

Well data is almost always available in reservoir modeling. It includes core measurements and well logs. The core plugs used for laboratory measurement are usually a few centimeters. The measurement is normally taken at surface temperature and pressure, so the measured petrophysical properties may not be same as that in subsurface conditions. Core expansion, water evaporation and imbibition must be considered and some corrections are required (Zwicky and Eade, 1977). Despite those factors, core data are the best subsurface information available. Core data are more expensive than well logging therefore we normally have more log data. Well logs are measured at subsurface conditions, but the measurements are electrical, radioactive, acoustic and other properties of rock near the wellbore. The lithofacies and petrophysical properties are interpreted from the measurements. The wellbore condition, mineralogy and fluids will affect the interpretation. Some corrections are required. Calibration of the log and core data is also necessary. The vertical resolution of conventional logging data is larger than the core data scale. High resolution logging may match the core data scale. The core-log calibration results provide small-scale heterogeneity information for reservoir modeling (Coll *et al.*, 1999).

The well data scale is sometimes referred to as the point scale or quasi-point scale. It is smaller than the geological model scale, but in conventional geostatistical reservoir modeling, well data are used at the model scale. The missing scale difference between the well data and the model scale can be large. Scaling laws (Deutsch, 2002; Frykman and Deutsch, 1999) can be used to obtain the correct variogram and correct target histogram for geostatistical simulation when well data scale and model scale are different.

Well data are always very sparse. To model the reservoir using only well data, either an interpolation methods such as kriging or stochastic simulation methods are used. The interpolation techniques are normally used for volume calculations where the average is critically important. Simulation is mainly used for flow simulation where the extreme values are important. Kriging and sequential simulation are developed in many books (Journal and Huijbregts, 1978; Goovaerts, 1997; Deutsch, 2002). Following is a summary to show the basics.

2.7.1.1 Kriging for reservoir mapping

Kriging is a linear regression technique to provide a Best Linear Unbiased Estimate (BLUE) at unsampled locations. The “Best” means the kriging estimator has minimum error variance. The “Unbiased” means the expected value of the error is zero.

Consider a random function Z that is stationary over the volume of interest, A . With n available data $\{z(\mathbf{u}_i), i = 1 \dots n, \forall \mathbf{u}_i \in A\}$, where \mathbf{u}_i is a vector representing the locations in A . The simple kriging estimator is given for any unsampled location \mathbf{u} :

$$z^*(\mathbf{u}) - m = \sum_{i=1}^n \lambda_i(\mathbf{u}) [z(\mathbf{u}_i) - m] \quad (2-2)$$

and the weights $\lambda_i(\mathbf{u})$ are calculated from the simple kriging system that considers data closeness, redundancy and spatial correlation:

$$\sum_{i=1}^n \lambda_i(\mathbf{u}) C(\mathbf{u}_i - \mathbf{u}_j) = C(\mathbf{u} - \mathbf{u}_j), \quad j = 1, \dots, n \quad (2-3)$$

where $C(\mathbf{u}_i - \mathbf{u}_j)$ is the covariance between data $z(\mathbf{u}_i)$ and $z(\mathbf{u}_j)$, and $C(\mathbf{u} - \mathbf{u}_j)$ is the covariance between location being estimated $z(\mathbf{u})$ and data $z(\mathbf{u}_j)$. The covariance function is usually inferred from a variogram model that describes the spatial structure of the data.

The kriging variance or minimum error variance is calculated by

$$\sigma_{sk}^2(\mathbf{u}) = \sigma^2 - \sum_{i=1}^n \lambda_i(\mathbf{u}) C(\mathbf{u} - \mathbf{u}_i) \quad (2-4)$$

where σ^2 is the data variance.

With the mean of $z^*(\mathbf{u})$ and variance of $\sigma_{s_k}^2$, a distribution of uncertainty can be defined in a multivariate Gaussian context.

Ordinary kriging is slightly different from the simple kriging shown above. It constrains the sum of the weights equal to 1.

$$\sum_{i=1}^n \lambda_i(\mathbf{u}) = 1 \quad (2-5)$$

Although kriging provides estimates with minimum error-variance, the variability of the kriging estimates is less than the data. Therefore, kriging maps are smooth with less detailed variations and extreme values compared to the original data. Stochastic simulation is needed to generate realistic realizations.

2.7.1.2 Stochastic simulation for reservoir heterogeneity

Sequential simulation corrects the smoothing problem. It adds a random component to the kriging estimate to reproduce the variation at the model scale. Multiple equally-probable realizations, or stochastic images, of reservoir heterogeneity can be produced by drawing a set of random components. Moreover, the set of realizations provide a directly usable visualization of the uncertainty about the reservoir properties (Journel, 1990).

The most popular simulation technique is sequential Gaussian simulation (SGS). It adopts a multivariate Gaussian distribution for simplified calculation and global histogram reproduction. The normal transform of data is required before the simulation, and the simulation realizations are transformed back to real units at the end. When dealing with multiscale data, the normal transform is problematic because the non-linear transform does not preserve the linear scale relationship of data (Tran *et al.*, 2001). Multiscale modeling has to be done in original units. The direct sequential simulation (DSS) algorithm could be considered.

A model of covariance can be reproduced without using the Gaussian model (Journel, 1994; Leuangthong, 2005). Sequential simulation can be performed in direct space (original units). Numerous studies have been conducted on DSS (Bourgault, 1997; Caers, 2000; Soares, 2001; Deutsch *et al.*, 2001). Simple kriging is the heart of DSS.

However, the kriging estimate and variance are insufficient to describe local distributions because the distribution shapes are not known and the data values dependent nature of conditional variances is not considered. Two major challenges with the direct approach for simulation are histogram reproduction and the proportional effect. Deutsch *et al.* (2001) proposed a method of building a look-up table of local distributions for histogram reproduction in DSS. Local conditional cumulative distribution functions (CCDF) were determined by using the Gaussian transform of global histogram under a multivariate Gaussian distribution. Manchuk *et al.* (2005) proposed an analytical method for histogram reproduction using the lognormal distribution. Both methods showed some promising results for histogram reproduction. Natural data always show a relationship between the data mean and variance. This phenomenon is commonly referred to as the proportional effect (Journel and Huijbregts, 1978). Because the kriging variance is independent of kriging estimate, reproducing the proportional effect becomes an issue. This remains a big challenge for DSS.

2.7.2 Seismic Data

Seismic data are records of sound energy reflected back from subsurface rock layers. Two-way travel time and amplitude are two basic components in seismic records. Computer processing is applied to remove noise and provide a realistic image of subsurface. Inversion techniques may be applied to extract useful information. Seismic interpretation techniques based on the travel time are mainly for determining the geometry of a reservoir unit, such as reservoir limits and thickness. The amplitude-based stratigraphic inversion techniques are used for inferring the stratigraphic surfaces, and reservoir properties. Other seismic data such as acoustic impedance, velocity, and density are inverted from travel time and amplitude (Laurence and Rachel, 2004). The seismic data are band-limited and inversion techniques are inherently non-unique. Seismic data is often calibrated to well data that have both high and low frequency components.

Seismic data contain indirect information about reservoir properties. For example, the amplitude values often relate to lithology, abnormal pressure, fluid content and temperature. The lateral changes in amplitude measurements relate to the locations of

hydrocarbon accumulations and changes in stratigraphy, porosity and thickness (Sheriff, 1992). Although the information is indirect, it is very useful to improve the accuracy of reservoir models.

3-D seismic data provide dense and regular spaced information. It is an important supplement to sparse well data. Several geostatistical techniques have been introduced or developed for the integration of different types of data. Based on their applications, these geostatistical techniques are reviewed in the following sections in two groups: one group is 2-D mapping; another group focuses on 3-D modeling. 4-D (time-lapse) seismic data are usually treated as dynamic data, and will be addressed in the dynamic data section.

2.7.2.1 Seismic data integration for 2-D mapping

Due to the poor vertical resolution of seismic data relative to well log data, it is convenient to use the seismic data over a stratigraphic layer and the vertical well average data for mapping reservoir parameters. These maps could be used for reserve estimation and well placement where the details of 3-D heterogeneity are not necessarily required.

The traditional geostatistical technique of cokriging was first introduced for the integration of 3-D seismic data by Doyen (1988) for mapping porosity. Before that, conventional regression methods were commonly used for estimating porosity from seismic data. Doyen (1988) showed the porosity mapping using three different methods. One was kriging with well data. The other two methods were conventional linear regression and cokriging using the seismic transit time and well data. The results showed that the kriged map was smooth between wells and failed to predict the porosity far away from wells. The porosity map from the linear regression was better than the kriged map, but the well data were not honored and the data were treated as spatially independent. The cokriged map showed a great improvement from the kriged map, especially in the sparsely drilled area. The cokriging estimates were also much better than the porosity estimates from the linear regression. The well data were honored and the spatial correlations were accounted for. The cokriging technique was applied in the Taber-Turin reservoir, Alberta, Canada. Cross validation at the wells indicated that the cokriged model was 20% more accurate (in mean square error) than a standard regression model.

However, the tedious cross covariance/variogram inference and the computational burden of solving big cokriging matrices kept the cokriging algorithm from being widely used. A linear model of coregionalization is required and problems of matrix stability exist (Xu *et al.* 1992) in the implementation of cokriging. Many methods were developed from the cokriging technique to overcome these shortcomings.

Xu *et al.* (1992) demonstrated two geostatistical techniques: kriging with external draft and collocated cokriging for seismic data integration. In the external draft method, the seismic data is assumed to be linearly related to the local average of the primary data. The property map closely resembles the map of seismic data. The reliability of the estimates largely depends on the reliability of the linear relationship obtained from the collocated primary and secondary data; however, the linear relationship is hard to justify with the limited well data.

Collocated cokriging uses only the collocated secondary datum in estimation. It is a good approximation of full cokriging because the collocated datum screens out the influence of the secondary data away from the estimated location. Collocated cokriging significantly simplifies the cokriging matrix. Moreover, the cross covariance is also simplified by applying another Markov screening rule, that is, the collocated primary datum screens out the influence of any other data on the secondary datum. The correlation coefficient of the collocated primary and secondary data is used to scale the primary covariance to the cross covariance. Kriging with external draft and collocated cokriging were used for mapping a salt dome structure with dense 3-D seismic data (traveltime) and sparse well data. Both methods work well although the validation showed that collocated cokriging performed slightly better.

Doyen *et al.* (1996) proposed a simplified implementation of collocated cokriging using a Bayesian Updating technique. The kriging estimates are linearly updated with collocated secondary data to get the cokriging estimate. The technique eliminates the inference of cross-covariance and no need for solving the cokriging system. The advantage of the Bayesian Updating technique is separating the influences of primary data and secondary data. This allows the analysis of interwell regions more straightforwardly. The technique was demonstrated to integrate seismic impedance and

well data for mapping the porosity for the Ekofisk Field, North Sea. There was a high correlation between the acoustic impedance and the well porosity data so that additional information was revealed in the vast interwell region. They also mentioned the need to be further constrained by another secondary variable such as structural elevation. Deutsch and Zanon (2004) showed the Bayesian Updating technique in a new format that is much easier to use multiple secondary variables simultaneously to constrain the final estimates. The technique will be expanded on in the next chapter.

2.7.2.2 Seismic data integration for 3-D modeling

Dynamic flow simulation requires a 3-D model with an adequate description of heterogeneity. 3-D modeling is more complex than 2-D mapping because the vertical scale difference between well data and seismic data has to be appropriately accounted for. Several techniques have been proposed to build 3-D models based on the techniques successfully applied for 2-D mapping or directly using the 2-D maps.

Yang *et al.* (1996) demonstrate building 3-D reservoir models by integration of 3-D seismic amplitude, or the inverted seismic impedance with well logs. Sequential Gaussian Co-simulation (SGS with collocated cokriging) was used. The data were brought to a common scale but did not mention which method was used. Gorell (1995) proposed a method to build 3-D models given areal maps of seismic-derived average petrophysical properties. The 3-D reservoir was divided into a series of layers. In each layer, cokriging was applied with the average of well logs in the layer and the seismic derived 2-D maps. After all layers were mapped, a linear rescaling was applied to ensure the summary of all layers were consistent with the given 2-D maps. This method honors the wells and 2-D average maps, but not the deviated wells, and the data histogram was distorted.

Deutsch *et al.* (1996) reviewed the conventional geostatistical techniques for seismic data integration, and pointed out that the precision and scale of seismic data must be simultaneously accounted for. They proposed a simulated annealing-based technique to construct a 3-D model. The misfit between the vertical average of 3-D model and the seismic derived 2-D maps was reduced to below a user-defined tolerance to account for

precision of seismic data. But this technique requires significant CPU time and experience with the simulated annealing technique.

Behrens *et al.* (1998) proposed a sequential Gaussian simulation with block kriging to build 3-D model. Seismic-derived 2-D maps were used as direct measurement of the arithmetic average of the primary data at the scale of seismic data. Well data were used as quasi-point data to construct the 3-D model. Conventional block kriging was used to account for the difference in scale between well data and seismic derived data. The well data were honored and the seismic derived map reproduced exactly; however, the low precision of the seismic derived data was ignored. Moreover, non-linear Gaussian transform of multiscale data cannot preserve the linear scale relationship.

Doyen *et al.* (1997) proposed a Bayesian updating technique to build seismically constrained 3-D models. The simple kriging estimates were updated with seismic average likelihood estimates. The Bayesian updating is equivalent to the block kriging. A small change was applied to the updated function to make the 3-D model vertical averages approximately match the seismic derived average porosity map. The conventional Bayesian updating technique requires a Gaussian environment and a Gaussian transform of the data.

Yao and Journel (2000) proposed a method to build 3-D models by addressing both the scale and precision problem. This method was developed from sequential Gaussian simulation (SGS) with block kriging (Behrens *et al.*, 1998). Direct sequential simulation (DSS) was used instead of SGS to preserve the linear scale relationship between the block data (seismic-derived vertical averaged values) and the point data (well log). Block kriging was used to account for the scale difference. The seismic-derived 2-D porosity maps were generated by cokriging. The error variance of cokriging estimates was added in the block kriging to account for precision of the seismic derived data. They used a lognormal distribution for the “unknown shape” of the kriged local distributions in DSS. The histogram of simulated values matched the lognormal well data histogram reasonably well. The proportional effect was not addressed.

2.7.3 *Dynamic data*

Dynamic data are time dependent data. They include well test, production and 4-D seismic data. Well test and production data are wellbore pressure, flow rates or fractional flow rates such as water cut and gas oil ratio (GOR) measured at production wells. These data provide valuable information about the drainage volume around wells; however, they are not linearly related to the static reservoir properties. Flow simulations are necessary to link them together. Correct input models of reservoir properties should have output production matching real production history. History matching is an inversion problem. Good history match does not mean the input models are correct because the inversion solutions are non-unique. However, a history match is considered necessary.

Many people have studied and developed inverse techniques for dynamic data. The classical manual iteration method can be replaced by automatic history matching that estimates reservoir properties from dynamic data. Production data can be divided into three main groups: single well test, multiple well test, and production history data (Wen *et al.*, 2005). For each group, the inversion techniques are very different. A thorough review of the dynamic data inversion techniques can be found in the monograph by Wen *et al.* (2005) and the PhD thesis by Reza (2003). Among the techniques, the authors particularly illustrated the Sequential Self-Calibration (SSC) method for multiple well data. It is a geostatistics-based iterative method. Multiple coarse grid 2-D permeability realizations can be generated by closely matching the production data. Then, the 2-D coarse grid permeability maps can be used as constrains in generating fine scale 3-D reservoir models. Tran *et al.* (1999) demonstrated the construction of coarse scale 3-D models using 3-D SSC with streamline simulation. Then, the coarse grid models were downscaled using SGS with block kriging or SGS with Bayesian Updating. The downscaling technique was modified to use DSS instead of SGS in a later paper by Tran *et al.* (2001). They did not address two major problems with DSS: histogram reproduction and proportional effect. And the exactness of downscaling using DSS was not considered.

4-D seismic data can indicate pressure and saturation changes. It is particularly useful to locate bypassed oil and undrained compartments. Like production data, it can be

used for checking the accuracy of the reservoir model through flow simulation and it can assist modeling porosity and saturations (Waggoner, 1998; Tran *et al.*, 1999; Phan and Horne, 2002).

CHAPTER 3

LARGE SCALE MODELING

Large scale models are required for modeling large areas such as an entire lease or reservoir. Building fine scale models for such large areas is neither practical nor necessary. For example, 100 realizations of one variable for the Surmont lease at a scale of 20 m by 1 m by 1m would require over 1000 GB storage. This is a significant amount of storage and it takes time to process and understand the resulting models. A 2-D model for the Surmont lease at a scale of 100m by 100m only takes a few MB. Furthermore, as described in Chapter 1, it is difficult to generate fine scale models consistent with all large scale data.

Large scale models are useful for resource estimation at the early phases of field development. Resource estimation focuses on volume averages rather than detailed heterogeneity. Fine scale 3-D models of heterogeneity are useful for flow simulation but not necessary for resource estimation. Reliable large scale models are appropriate for resource estimation and selecting areas of interested. Fine scale 3-D models can be constructed in these areas when they are needed.

The advantage of modeling at a large scale is that smaller scale data can be upscaled to the model scale so that the multiscale modeling is converted to single scale modeling. Gaussian-based techniques can be used without concern for non-linear averaging. Converting data to 2-D summaries further simplifies multiscale modeling. 2-D mapping is the most common approach to large scale modeling, and will be used for the first step in the scale consistent modeling approach.

For scale consistent modeling, an important step is to construct a large scale model as accurate as possible by integrating all available data. There are several geostatistical techniques that can be used to integrate different data into a geological model including Gaussian-based Bayesian updating, indicator cokriging, and full cokriging. The Bayesian

updating approach will be presented in detail due to its reliability and simplicity in data integration. The contribution of the primary and secondary information on the updated results can be easily understood. In this method, well data including core and well log data are considered as primary data that we have the most confidence. The seismic data, geologic trends, structural information, geological interpretations and other indirectly measured data are used as secondary data to reduce the uncertainty at unsampled locations.

Bayesian updating uses all related information to generate local distributions of uncertainty. For large areas or areas have complex heterogeneity, the modeling may be improved by accounting for non-stationarity in correlations and data precision. This chapter focuses on the theory of Bayesian updating, and provides the methodologies of (1) Bayesian updating using locally varying correlation and locally varying quality, and (2) simulation with Bayesian updating. The implementation details of the Bayesian updating technique are presented in the next chapter.

3.1. Bayesian Updating Technique for 2-D Mapping

Conventional geostatistical 2-D mapping is done by kriging the well data to interpolate between the well locations. Under a multivariate Gaussian model, local uncertainty in the estimates is given by the kriging variance that accounts for the closeness and redundancy of the well data. Sparse well data lead to significant uncertainty in the interwell regions. It is necessary to integrate secondary information such as seismic and geological data to improve the 2-D modeling. Cokriging and collocated cokriging (Xu *et al.*, 1992) are common to integrate different types of data; however, inference of the cross-covariance model(s) is demanding from the perspective of professional effort and computational time.

Recently, the Bayesian updating technique (Doyen *et al.*, 1996) was introduced for data integration. The technique decomposes the collocated cokriging estimate into two models: prior and likelihood. The prior model is built from well data, and the likelihood model is built from all secondary information. The definition could be reversed with a

different interpretation. The prior model is then updated with the likelihood model to build the final posterior or updated model. Deutsch and Zanon (2004) applied the Bayesian updating technique to predict reservoir performance. They showed the approach in a new format that has the advantage of easy implementation in mapping multiple primary variables using multiple secondary variables. It has been successfully applied in the McMurray formation (Ren *et al.*, 2006a and Ren *et al.*, 2006c), and a non-stationary Bayesian updating approach was developed to account for locally varying correlations and data quality in Bayesian updating 2-D mapping (Ren *et al.*, 2006b).

3.1.1. Theory of Bayesian Updating

Consider a random function Y that is stationary over the area of interest, A . It is the primary variable of interest. There are m random functions X_j , $j = 1 \dots m$ over the same model area. They are the secondary variables. Assume Y and X_j ($j = 1 \dots m$) are jointly multi-Gaussian after univariate transformation.

Suppose there are n data of the primary variable available in the area of interest: $\{y(\mathbf{u}_i), i = 1 \dots n\}$, where \mathbf{u}_i is the location vector in A . In the context of this thesis, the results of simple kriging using only the primary data are considered as a *prior* distribution of uncertainty parameterized by the kriging mean and variance. The kriging mean is calculated by:

$$\bar{y}_p(\mathbf{u}) = \sum_{i=1}^n \lambda_i y(\mathbf{u}_i) \quad (3-1)$$

where \mathbf{u} is the location being estimated and the weights λ_i , ($i = 1 \dots n$) are calculated from the well known normal equations:

$$\sum_{i=1}^n \lambda_i C(\mathbf{u}_i - \mathbf{u}_k) = C(\mathbf{u} - \mathbf{u}_k), \quad k = 1, \dots, n \quad (3-2)$$

where $C(\mathbf{u}_i - \mathbf{u}_k)$ is the covariance between the two primary data $y(\mathbf{u}_i)$ and $y(\mathbf{u}_k)$, and $C(\mathbf{u} - \mathbf{u}_k)$ is the covariance between estimated location $y(\mathbf{u})$ and primary data $y(\mathbf{u}_k)$. The kriging variance is given by

$$\sigma_p^2(\mathbf{u}) = 1 - \sum_{i=1}^n \lambda_i C(\mathbf{u} - \mathbf{u}_i) \quad (3-3)$$

The simple kriging leads to the parameters of a Gaussian conditional distribution conditioning to the primary data. A conditional distribution is predicted at each unsampled location.

In general, secondary data are available at every location in the modeled area: $\{x_j(\mathbf{u}), j=1, \dots, m, \forall \mathbf{u} \in A\}$. The results of prediction with all collocated secondary data provide another conditional distribution. This distribution is related to the likelihood distribution in a Bayesian context. It has been called the *likelihood* distribution; this thesis retains that name. The non-standard Gaussian likelihood distribution is fully defined by a mean and variance.

The likelihood mean is calculated by:

$$\bar{y}_L(\mathbf{u}) = \sum_{j=1}^m \lambda_j x_j(\mathbf{u}) \quad (3-4)$$

Here, the weights λ_j ($j=1, \dots, m$) are also given by the well-known normal equations:

$$\sum_{j=1}^m \lambda_j \rho_{j,k} = \rho_{j,0}, \quad k=1, \dots, m \quad (3-5)$$

where $\rho_{j,k}$ is the correlation between different types of secondary data, and $\rho_{j,0}$ is the correlation between the secondary data and primary data. The likelihood variance is then given by:

$$\sigma_L^2(\mathbf{u}) = 1 - \sum_{j=1}^m \lambda_j \rho_{j,0} \quad (3-6)$$

The two conditional distributions (prior and likelihood) can be merged together to get the updated distribution. The mathematic combination is derived from the Bayesian statistical analysis of the posterior distribution. The posterior distribution of uncertainty at estimated location \mathbf{u} is a conditional distribution conditioning to both primary and secondary data:

$$P\{y(\mathbf{u}) | X(\mathbf{u}), y(\mathbf{u}_1), \dots, y(\mathbf{u}_n)\} \quad (3-7)$$

where $X(\mathbf{u}) = (x_1(\mathbf{u}) \quad x_2(\mathbf{u}) \quad \dots \quad x_m(\mathbf{u}))^T$ is a vector of the collocated secondary data. Under the assumption that collocated secondary data screen the influence of other secondary data that are further away (Journel, 1999), only collocated secondary data are considered. This distribution is equivalent to the results of collocated cokriging.

In the context of Bayesian statistical analysis, the posterior distribution can be decomposed into a product of two distributions (Doyen *et al.*, 1996; Besag, 1986):

$$P\{y(\mathbf{u}) | X(\mathbf{u}), y(\mathbf{u}_1), \dots, y(\mathbf{u}_n)\} \propto f\{X(\mathbf{u}) | y(\mathbf{u})\} P\{y(\mathbf{u}) | y(\mathbf{u}_1), \dots, y(\mathbf{u}_n)\} \quad (3-8)$$

where $P\{y(\mathbf{u}) | y(\mathbf{u}_1), \dots, y(\mathbf{u}_n)\}$ is the prior distribution only conditioning to primary data. As shown before, the prior distribution is a non-standard Gaussian distribution with simple kriging mean $\bar{y}_p(\mathbf{u})$ and variance $\sigma_p^2(\mathbf{u})$. We have

$$P\{y(\mathbf{u}) | y(\mathbf{u}_1), \dots, y(\mathbf{u}_n)\} \propto \exp\left(-\frac{[y(\mathbf{u}) - \bar{y}_p(\mathbf{u})]^2}{2\sigma_p^2(\mathbf{u})}\right)$$

$$\text{where } \exp\left(-\frac{[y(\mathbf{u}) - \bar{y}_p(\mathbf{u})]^2}{2\sigma_p^2(\mathbf{u})}\right) = \exp\left(-\frac{y^2(\mathbf{u})}{2\sigma_p^2(\mathbf{u})} + \frac{y(\mathbf{u})\bar{y}_p(\mathbf{u})}{\sigma_p^2(\mathbf{u})} - \frac{\bar{y}_p^2(\mathbf{u})}{2\sigma_p^2(\mathbf{u})}\right)$$

$$\text{Thus, } P\{y(\mathbf{u}) | y(\mathbf{u}_1), \dots, y(\mathbf{u}_n)\} \propto \exp\left(-\frac{y^2(\mathbf{u})}{2\sigma_p^2(\mathbf{u})} + \frac{y(\mathbf{u})\bar{y}_p(\mathbf{u})}{\sigma_p^2(\mathbf{u})}\right) \quad (3-9)$$

The proportionality constants that are independent of $y(\mathbf{u})$ are eliminated.

The $f\{X(\mathbf{u}) | y(\mathbf{u})\}$ in Equation (3-8) is the likelihood function that is simplified by only conditioning to the collocated primary data under the assumption of a Markov model that the collocated primary data screen the influence of other primary data that are further away (Journel, 1999). Under the assumption of a multivariate Gaussian model, it is the density function of a multivariate Gaussian distribution parameterized by the conditional mean vector $E\{X(\mathbf{u}) | y(\mathbf{u})\} = \boldsymbol{\rho} y(\mathbf{u})$ and $m \times m$ conditional covariance matrix

Σ , where $\boldsymbol{\rho} = (\rho_{10} \ \rho_{20} \ \dots \ \rho_{n0})^T$ is the vector of correlation coefficients between the primary variable and secondary data. The location \mathbf{u} is dropped from the notation for simplicity. The covariance matrix can be converted to the matrix of correlation coefficients:

$$\Sigma = \begin{pmatrix} \rho_{11} & \dots & \rho_{1n} \\ \vdots & \ddots & \vdots \\ \rho_{n1} & \dots & \rho_{nn} \end{pmatrix} - \begin{pmatrix} \rho_{10}\rho_{10} & \dots & \rho_{10}\rho_{n0} \\ \vdots & \ddots & \vdots \\ \rho_{n0}\rho_{10} & \dots & \rho_{n0}\rho_{n0} \end{pmatrix} = \boldsymbol{\rho}_{ij} - \boldsymbol{\rho} \boldsymbol{\rho}^t$$

Since the secondary data are known, the likelihood function is actually a function of $y(\mathbf{u})$. Eliminating the proportionality constants that are independent of $y(\mathbf{u})$, we have:

$$f\{X(\mathbf{u}) | y(\mathbf{u})\} \propto \exp\left(-\frac{1}{2}[X(\mathbf{u}) - \boldsymbol{\rho} y(\mathbf{u})]^t \Sigma^{-1} [X(\mathbf{u}) - \boldsymbol{\rho} y(\mathbf{u})]\right)$$

where

$$\begin{aligned} & \exp\left(-\frac{1}{2}[X(\mathbf{u}) - \boldsymbol{\rho} y(\mathbf{u})]^t \Sigma^{-1} [X(\mathbf{u}) - \boldsymbol{\rho} y(\mathbf{u})]\right) \\ &= \exp\left(-\frac{1}{2}[X^t(\mathbf{u}) - \boldsymbol{\rho}^t y(\mathbf{u})] \Sigma^{-1} [X(\mathbf{u}) - \boldsymbol{\rho} y(\mathbf{u})]\right) \\ &= \exp\left(-\frac{1}{2}[X^t(\mathbf{u}) \Sigma^{-1} X(\mathbf{u}) - 2\boldsymbol{\rho}^t \Sigma^{-1} X(\mathbf{u}) y(\mathbf{u}) + \boldsymbol{\rho}^t \Sigma^{-1} \boldsymbol{\rho} y^2(\mathbf{u})]\right) \end{aligned}$$

$$\text{Thus, } f\{X(\mathbf{u}) | y(\mathbf{u})\} \propto \exp\left(\boldsymbol{\rho}^t \Sigma^{-1} X(\mathbf{u}) y(\mathbf{u}) - \frac{1}{2} \boldsymbol{\rho}^t \Sigma^{-1} \boldsymbol{\rho} y^2(\mathbf{u})\right) \quad (3-10)$$

Multiplying the equations (3-9) and (3-10) gives the posterior distribution:

$$P\{y(\mathbf{u}) | X(\mathbf{u}), y(\mathbf{u}_1), \dots, y(\mathbf{u}_n)\} \propto \exp\left(-\frac{1}{2}[\boldsymbol{\rho}^t \Sigma^{-1} \boldsymbol{\rho} + \frac{1}{\sigma_p^2(\mathbf{u})}] y^2(\mathbf{u}) + [X^t(\mathbf{u}) \Sigma^{-1} \boldsymbol{\rho} + \frac{\bar{y}_p(\mathbf{u})}{\sigma_p^2(\mathbf{u})}] y(\mathbf{u})\right)$$

This equation is in the form of $\exp(-Ax^2 + Bx)$, where the constants A and B define the mean and variance of a Gaussian kernel:

$$\begin{aligned}
\bar{y}_U(\mathbf{u}) &= \frac{B}{2A} = \frac{\boldsymbol{\rho}^t \boldsymbol{\Sigma}^{-1} X(\mathbf{u}) + \frac{\bar{y}_P(\mathbf{u})}{\sigma_P^2(\mathbf{u})}}{\boldsymbol{\rho}^t \boldsymbol{\Sigma}^{-1} \boldsymbol{\rho} + \frac{1}{\sigma_P^2(\mathbf{u})}} = \frac{\frac{\boldsymbol{\rho}^t \boldsymbol{\rho}_{ij}^{-1} X(\mathbf{u})}{(\boldsymbol{\rho}_{ij} - \boldsymbol{\rho} \boldsymbol{\rho}^t) \boldsymbol{\rho}_{ij}^{-1}} + \frac{\bar{y}_P(\mathbf{u})}{\sigma_P^2(\mathbf{u})}}{\frac{\boldsymbol{\rho}^t \boldsymbol{\rho}_{ij}^{-1} \boldsymbol{\rho}}{(\boldsymbol{\rho}_{ij} - \boldsymbol{\rho} \boldsymbol{\rho}^t) \boldsymbol{\rho}_{ij}^{-1}} + \frac{1}{\sigma_P^2(\mathbf{u})}} \\
&= \frac{\boldsymbol{\rho}^t \boldsymbol{\rho}_{ij}^{-1} X(\mathbf{u}) \sigma_P^2(\mathbf{u}) + \bar{y}_P(\mathbf{u}) (1 - \boldsymbol{\rho} \boldsymbol{\rho}_{ij}^{-1} \boldsymbol{\rho}^t)}{\boldsymbol{\rho}^t \boldsymbol{\rho}_{ij}^{-1} \boldsymbol{\rho} \sigma_P^2(\mathbf{u}) + (1 - \boldsymbol{\rho} \boldsymbol{\rho}_{ij}^{-1} \boldsymbol{\rho}^t)}
\end{aligned} \tag{3-11}$$

From Equation (3-5), the vector of weights can be expressed as: $\boldsymbol{\lambda} = \boldsymbol{\rho}^t \boldsymbol{\rho}_{ij}^{-1}$. Thus, the likelihood mean and variance are: $\bar{y}_L(\mathbf{u}) = \boldsymbol{\rho}^t \boldsymbol{\rho}_{ij}^{-1} X(\mathbf{u})$ and $\sigma_L^2(\mathbf{u}) = 1 - \boldsymbol{\rho}^t \boldsymbol{\rho}_{ij}^{-1} \boldsymbol{\rho}$. Then, the updated mean is

$$\bar{y}_U(\mathbf{u}) = \frac{\boldsymbol{\rho}^t \boldsymbol{\rho}_{ij}^{-1} X(\mathbf{u}) \sigma_P^2(\mathbf{u}) + \bar{y}_P(\mathbf{u}) (1 - \boldsymbol{\rho} \boldsymbol{\rho}_{ij}^{-1} \boldsymbol{\rho}^t)}{\boldsymbol{\rho}^t \boldsymbol{\rho}_{ij}^{-1} \boldsymbol{\rho} \sigma_P^2(\mathbf{u}) + (1 - \boldsymbol{\rho} \boldsymbol{\rho}_{ij}^{-1} \boldsymbol{\rho}^t)} = \frac{\bar{y}_L(\mathbf{u}) \sigma_P^2(\mathbf{u}) + \bar{y}_P(\mathbf{u}) \sigma_L^2(\mathbf{u})}{\sigma_P^2(\mathbf{u}) - \sigma_P^2(\mathbf{u}) \sigma_L^2(\mathbf{u}) + \sigma_L^2(\mathbf{u})} \tag{3-12}$$

And the updated variance is:

$$\begin{aligned}
\sigma_U^2(\mathbf{u}) &= \frac{1}{2A} = \frac{1}{\boldsymbol{\rho}^t \boldsymbol{\Sigma}^{-1} \boldsymbol{\rho} + \frac{1}{\sigma_P^2(\mathbf{u})}} = \frac{(1 - \boldsymbol{\rho} \boldsymbol{\rho}_{ij}^{-1} \boldsymbol{\rho}^t) \sigma_P^2(\mathbf{u})}{\boldsymbol{\rho}^t \boldsymbol{\rho}_{ij}^{-1} \boldsymbol{\rho} \sigma_P^2(\mathbf{u}) + (1 - \boldsymbol{\rho} \boldsymbol{\rho}_{ij}^{-1} \boldsymbol{\rho}^t)} \\
&= \frac{\sigma_L^2(\mathbf{u}) \sigma_P^2(\mathbf{u})}{\sigma_P^2(\mathbf{u}) - \sigma_P^2(\mathbf{u}) \sigma_L^2(\mathbf{u}) + \sigma_L^2(\mathbf{u})}
\end{aligned} \tag{3-13}$$

These results give the parameters of a posterior non-standard Gaussian distribution called the **updated** distribution of uncertainty.

A schematic illustration of the Bayesian updating technique is given in Figure 3-1.

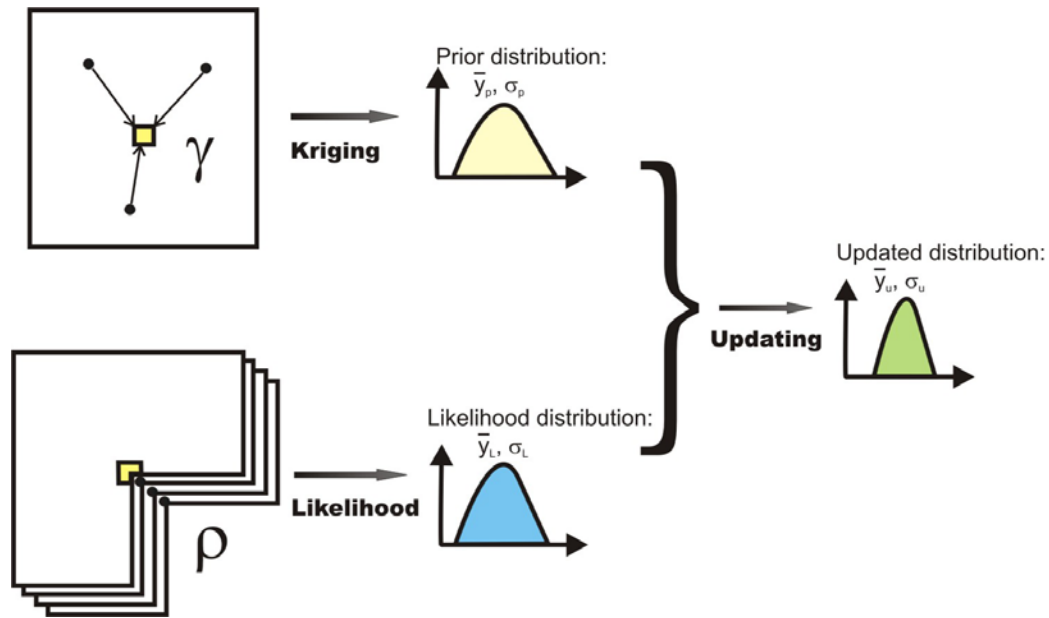


Figure 3-1: Schematic illustration of the Bayesian updating technique. The block dots are data, and the yellow square is a location being estimated.

3.1.2. *Some interesting aspects of Bayesian Updating*

The updated distribution obtained by merging the prior and likelihood distributions is non-convex because it does not always fall between the two distributions. Table 3-1 shows the updated mean changes with increasing of prior means. The global distribution, a standard Gaussian distribution $N(0,1)$ has an effect on whether the updated distribution falls between the two distributions. If the prior and likelihood distributions are on each side of the global distribution, the updated distribution will always fall in between. If the two distributions are both above the global distribution or both below the global distribution, the updated mean fall in between only when the means of the prior and likelihood distributions are far away enough (see cases 6 and 9 in Table 3-1). When the two distributions are very close, the updated mean will not fall in between (see cases 7 and 8 in Table 3-1). The updated distribution tends to be close to the distribution further away from the global mean (Figure 3-2).

Case	1	2	3	4	5	6	7	8	9
Prior Mean \bar{y}_P	-2.00	-1.50	-1.00	-0.50	0.00	0.50	1.00	1.50	2.00
Likelihood Mean \bar{y}_L	1.00	1.00	1.00	1.00	1.00	1.00	1.00	1.00	1.00
Updated Mean \bar{y}_U	-0.63	-0.31	0.00	0.31	0.63	0.94	1.25	1.56	1.88

Table 3-1: The Bayesian updating calculation showing the changes of updated mean (4th row) with increasing prior mean (second row). The variances of prior and likelihood are 0.4 for all cases.

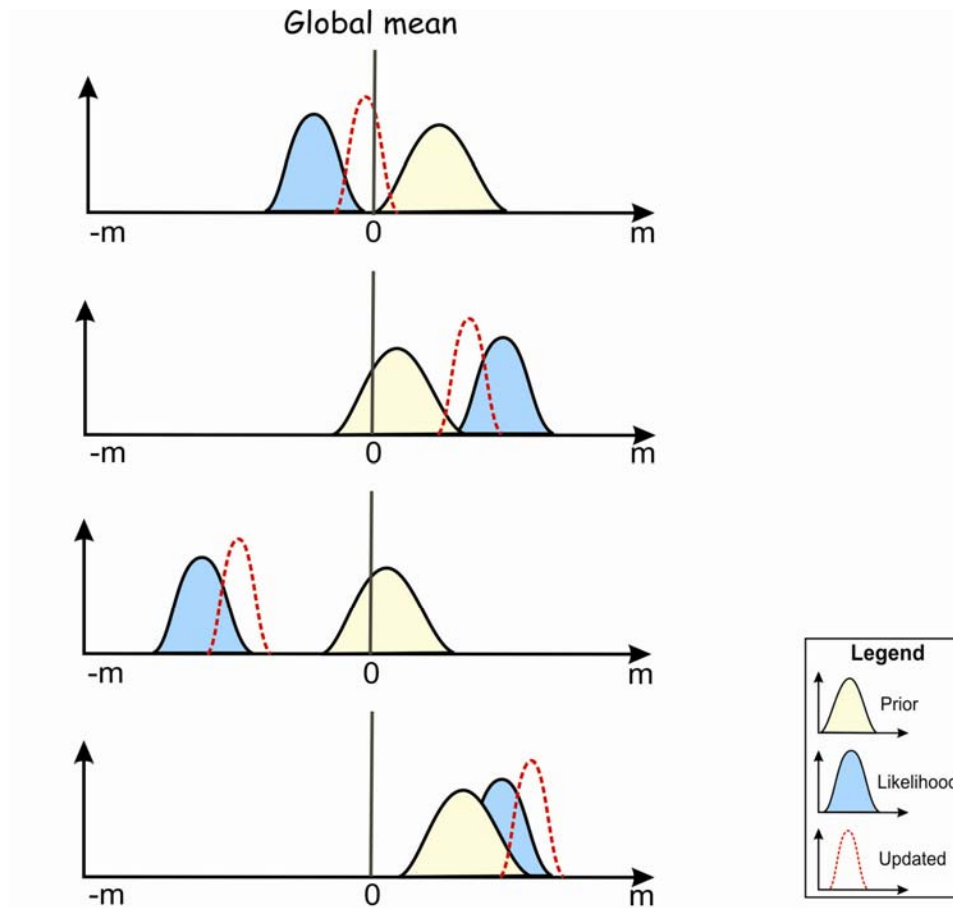


Figure 3-2: Schematic illustration of the location of updated distributions in Bayesian updating technique.

The updated variance is only affected by the prior and likelihood variances. It has the characteristic Gaussian property of homoscedasticity. Table 3-2 shows the updated variance increases with increasing of prior variances. The updated variance is always the smallest variance among the three distributions. As shown in Figure 3-2: Schematic illustration of the location of updated distributions in Bayesian updating technique., the

width of the updated distribution is always the narrowest, which indicates the uncertainty is reduced after Bayesian updating.

Case	1	2	3	4	5	6	7
Prior Variance σ_P^2	0.10	0.30	0.40	0.50	0.60	0.70	0.90
Likelihood Variance σ_L^2	0.40	0.40	0.40	0.40	0.40	0.40	0.40
Updated Variance σ_U^2	0.09	0.21	0.25	0.29	0.32	0.34	0.38

Table 3-2: The Bayesian updating calculation showing the increasing of updated variance (last row) with increasing of prior variance (second row).

The Bayesian updating technique relies on the multivariate Gaussian assumption. Under this assumption, all marginal and conditional distributions are Gaussian, and can be fully defined by an appropriate mean and variance. Therefore, the updated mean and variance provide a non-standard Gaussian distribution of uncertainty at the estimated location. Natural data may not follow Gaussian distribution. Normal score transformation is required to transform all the variables into normal scores at the beginning. The normal scores that have the most of values between 3 and -3 are referred as in *Gaussian units* in this thesis. After Bayesian updating, the local conditional distribution of uncertainty must be back transformed to original units. This will be shown in the next chapter.

The multivariate Gaussian assumption also provides that all multivariate relationships are linear and can be characterized by correlation coefficients. The correlation coefficients obtained from the wells are considered to measure the true relationship of each pair of variables over the model area and applicable to the interwell regions under the assumption of stationary. However, in practice, the multivariate relationships may not be linear or stationary. Thus, the global correlation coefficient may not be representative of the true relationship. The reliability of secondary data should also be considered in the correlation with the primary data. Modifications are introduced to account for possible non-stationarity, complex multivariate relationships and quality of the secondary data in local uncertainty assessment.

3.2. Enhanced Bayesian Updating Technique

In the Bayesian updating technique, a representative correlation coefficient is critical for integration of secondary information. To obtain a representative correlation coefficient, we must consider that: (1) it is a measure of linear dependence; (2) it is sensitive to outliers and sparse data; and (3) it is location dependent.

Consider a primary variable Y and a secondary variable X, the correlation coefficient is calculated using all data at n well locations:

$$\rho_{xy} = \frac{\frac{1}{n} \sum_{i=1}^n (x(\mathbf{u}_i) - m_x)(y(\mathbf{u}_i) - m_y)}{\sigma_x \cdot \sigma_y} \in [-1, 1] \quad (3-14)$$

where m and σ are the mean and standard deviation calculated by:

$$\begin{aligned} m_x &= \frac{1}{n} \sum_{i=1}^n x(\mathbf{u}_i) & i = 1, \dots, n \\ \sigma_x^2 &= \frac{1}{n} \sum_{i=1}^n (x(\mathbf{u}_i) - m_x)^2 & i = 1, \dots, n \end{aligned} \quad (3-15)$$

Because all variables are standard normal distributions ($m = 0$, $\sigma = 1$) after normal score transform, the equation can be simplified to:

$$\rho_{xy} = \frac{1}{n} \sum_{i=1}^n x(\mathbf{u}_i)y(\mathbf{u}_i) \in [-1, 1] \quad (3-16)$$

The correlation coefficient measures the linear relationship between two variables. Cross plots show all of the information between two variables. The correlation coefficient is a summary statistic and extracts the linear information. If the bivariate relationship is non-linear, the correlation coefficient is not representative (Figure 3-3). It is more reasonable to assume the local relationship is linear rather than the global relationship.

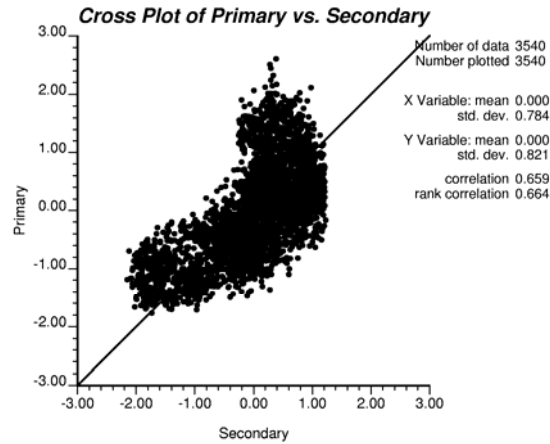


Figure 3-3: Cross plot of two variables that have a non-linear bivariate relationship.

A second well-known problem with the correlation coefficient is that it is sensitive to outliers. Figure 3-4 shows that two outliers make a big difference (from 0.590 to 0.728) in the correlation coefficient. The two extreme values are possibly caused by local geological features or errors in the measurement. If it is local geological features, the assumption of stationary is questionable; a local correlation coefficient would be more representative.

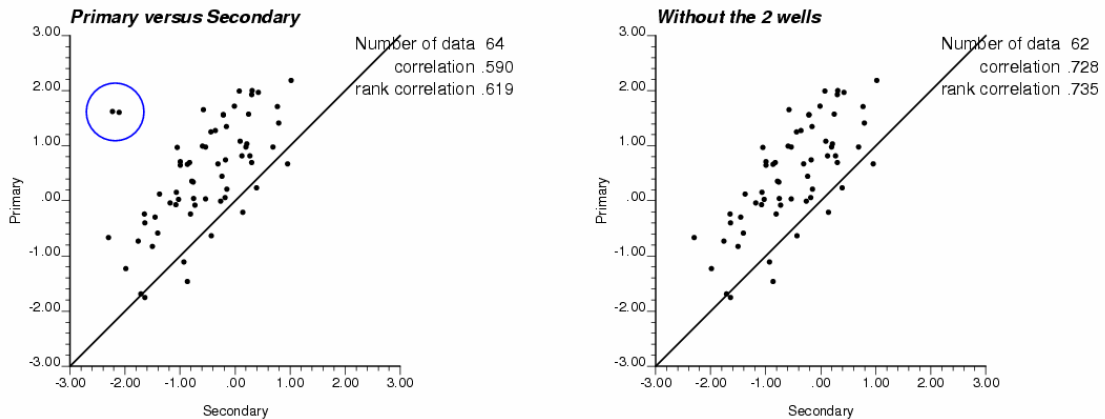


Figure 3-4: Cross plot of two variables with two outliers in the blue circle gives a correlation of 0.590 (left). And cross plot of two variables without the two outliers gives a correlation of 0.728 (right).

The correlation coefficient may be location dependent and sensitive to sparse data. Even in cases with no outliers, the correlation coefficient may be varying locally. An example is given in Figure 3-5 and 3-6. The maps of two variables and the cross plot of 64 pairs of data are shown in Figure 3-5. A global correlation coefficient of 0.533 is calculated from the 64 pairs of data extracted from the locations shown in block circles.

However, using 9 data at the upper-left and lower-right corners, the local correlation coefficients are -0.555 and 0.775, respectively (middle column in Figure 3-6). Of course, only 9 sparse data may not provide the true correlation coefficient. The cross plots of exhaustive data in the two areas indicate that the upper-left area actually has a correlation coefficient of about 0.16, and the lower-right area is about 0.64 (right column in Figure 3-6). The local correlations are different from the global correlation coefficient. Non-stationarity or local geological features cause the difference. In practice, we may not know whether non-stationary features exist in the model area with limited information available. The local correlations allow accounting for the local non-stationary features and non-linear relationship. Therefore, using local correlations will be more representative for multivariate correlations, especially for large areas.

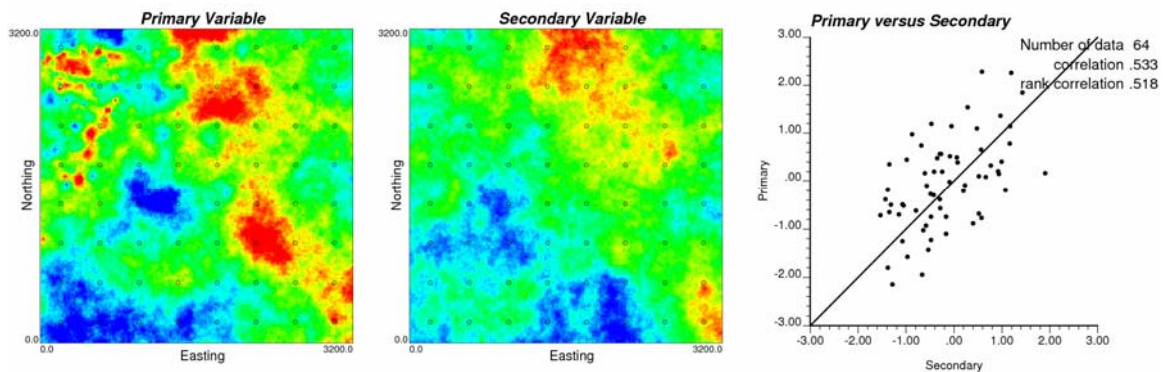


Figure 3-5: The maps of primary (left) and secondary (middle) variables and their cross plot (right) which indicates a global correlation coefficient of 0.533.

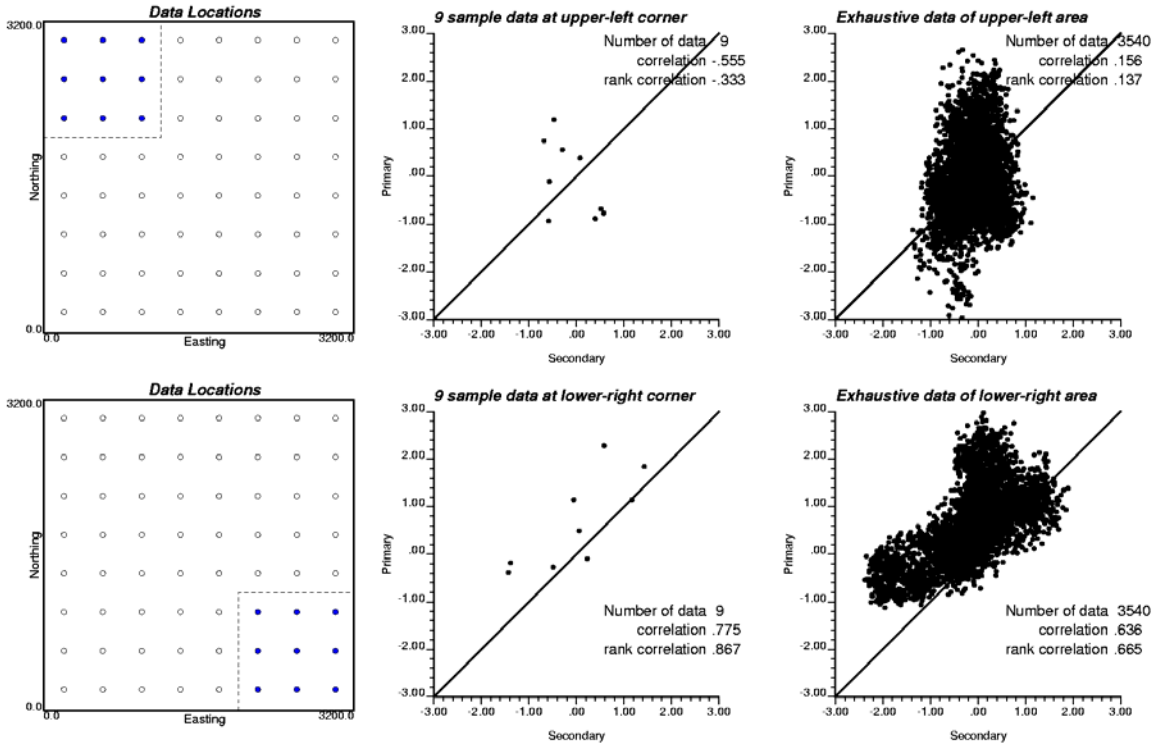


Figure 3-6: The data locations and the cross plots for the upper-left corner (upper row) and the lower-right corner (lower row). The middle column shows the cross plots of the nine data shown in the location map. The right column shows the cross plots of exhaustive data in these corners.

3.2.1. Locally Varying Correlation (LVC)

To calculate locally varying correlation coefficients, it is important to have sufficient data pairs to calculate a representative correlation. Using a moving window method with a large window size may suffice; however, there will be artifact discontinuities caused by the windows. To avoid the artifacts, a weighted correlation coefficient is proposed. Inverse distance weighting is a simple and robust method for weighting data pairs. All data pairs are weighted based on their distance from the location of interest.

The inverse distance weights are calculated by the equation below:

$$w_i = \frac{1}{(d_i + c)^p} \bigg/ \sum_{i=1}^n \frac{1}{(d_i + c)^p} \tag{3-17}$$

where d is the distance between a datum and the estimated location. The c is a constant value used to avoid computational problems when estimating at data locations. And the p is the power of the distance. The inverse distance weights are non-negative and sum to one:

$$\sum_{i=1}^n w_i = 1, \quad w_i \geq 0, \quad i = 1, \dots, n.$$

Using the inverse distance weights, the locally varying correlation coefficient can be calculated by:

$$\rho_{xy} = \frac{C_{xy}}{\sigma_x \cdot \sigma_y} = \frac{\sum_{i=1}^n w_i x(\mathbf{u}_i) y(\mathbf{u}_i) - m_x m_y}{\sigma_x \cdot \sigma_y} \in [-1, 1] \quad (3-18)$$

where the weighted mean and variance of variable X are given by:

$$m_x = \sum_{i=1}^n w_i x(\mathbf{u}_i) \quad i = 1, \dots, n$$

$$\sigma_x^2 = \sum_{i=1}^n (w_i x(\mathbf{u}_i) - m_x)^2 \quad i = 1, \dots, n \quad (3-19)$$

It is same for the variable Y. Figure 3-7 shows the locally varying correlation map for these two variables shown in Figure 3-5. The local correlations are low in the upper-left corner and high at the lower-right corner. This is consistent with the local correlations in Figure 3-6.

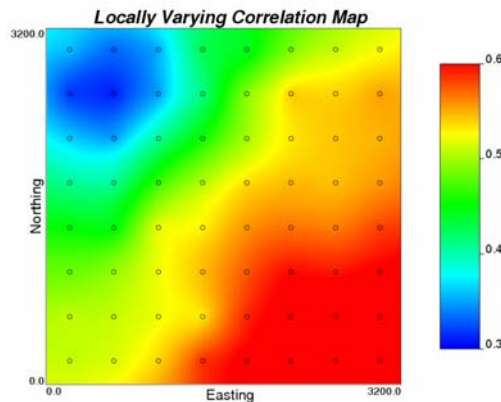


Figure 3-7: The locally varying correlation map of the two variables in Figure 3-5.

The locally varying correlation map for the case of two pairs of extreme values (Figure 3-4) is shown in Figure 3-8. The maps of the two variables are shown on the left of the figure. The two outliers are from a channel in the secondary data. The locally varying correlation captures the two data. It also shows that the correlation is high in the upper-left of the area, which is a low-valued area in both maps.

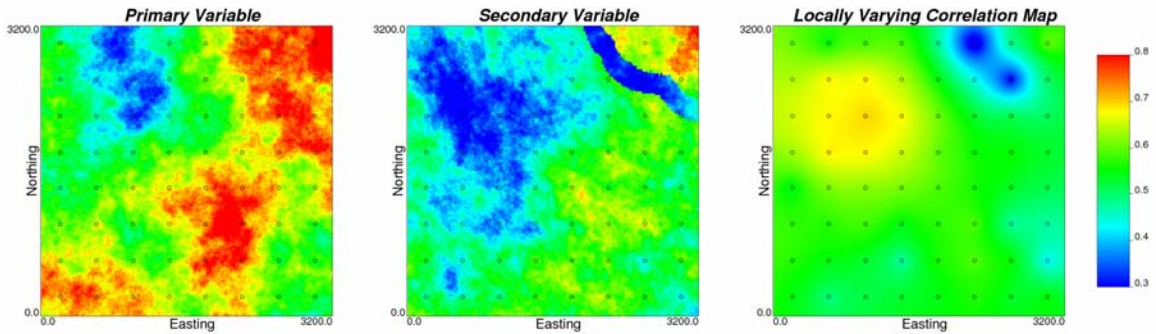


Figure 3-8: The maps of two variables (left and middle) and their locally varying correlation (right) for the case of two pairs of extreme values shown in Figure 3-4.

The locally varying correlations are highly dependent on the weights from the inverse distance method. The weights, in turn, are dependent on the values used for the power p and the constant c in Equation 3-10. Firstly, with the constant c fixed, as the power increases, the weights become more dissimilar; the data far away will have less weight (Isaaks and Srivastava, 1989), and the variation of local correlations will increase. As the power decreases, the weights are more similar, and the variation of local correlations becomes smaller. When the power reaches zero, the local correlations become the global correlation. Now, consider the power as fixed. As the constant increases, the weights are more similar, and the variation of the local correlations is less.

In calculation of locally varying correlations, all of the data need to be taken into account. To avoid giving too much weight to the closest datum, the constant is normally fixed at the average well spacing. Then, the power is adjusted to generate locally varying correlations that change smoothly. Figure 3-9 shows the maps of locally varying correlations calculated with constant of 400 m and different powers. The well spacing is 400m. The power of 0.8 gives a very smooth map of locally varying correlations. The

maps using powers larger than 1.0 are showing some bull-eye shapes around wells that are considered unreliable.

3.2.2. *Data impact on local correlation*

Outliers can dramatically affect the correlation between two variables. Although those outliers can be revealed in the local correlations, it would be convenient to automatically identify those data pairs and investigate. To identify them, a measure of the impact of each data pair on the local correlation is introduced here. This measure is named *Average Correlation Difference (ACD)*.

The calculation of the ACD is based on a jackknife type method. Firstly, a base locally varying correlation (LVC) map is generated using all data pairs. Then, a data pair is taken out and the rest of data pairs are used to generate a new locally varying correlation map. The difference between the two locally varying correlation maps is averaged over the entire model area:

$$ACD = \frac{100}{n} \sum_{i=1}^n |\rho_{Bi} - \rho_{JKi}| \quad (3-20)$$

where the ρ_B is the base local correlation, the ρ_{JK} is the new local correlation, and the n is the number of cells in the model area. Repeat this for another data pair at a time until the ACD for each data pair is calculated. Data with high differences can be investigated. A map of ACD may be useful to identify the data pairs with large impact.

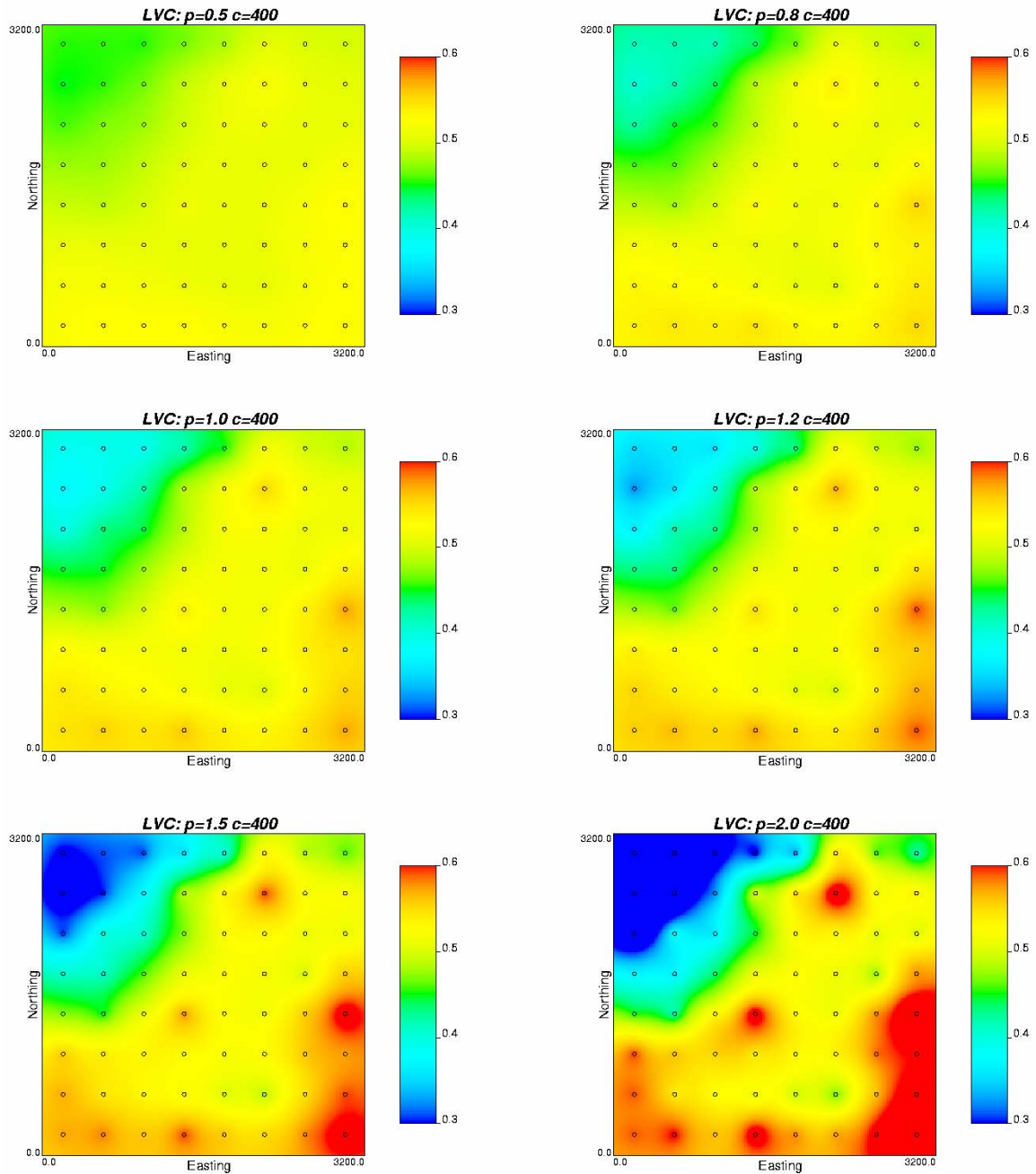


Figure 3-9: The locally varying correlation (LVC) maps with different powers.

Figure 3-10 shows the histogram and kriged map of the ACD for the 64 data pairs of the two variables in Figure 3-5. The ACDs are very small with a maximum of 3.04. No outliers exist. Figure 3-11 shows the histogram and kriged map of the ACD for the 64 data pairs of the two variables in Figure 3-8. The two extreme high ACDs are the outliers shown in Figure 3-4.

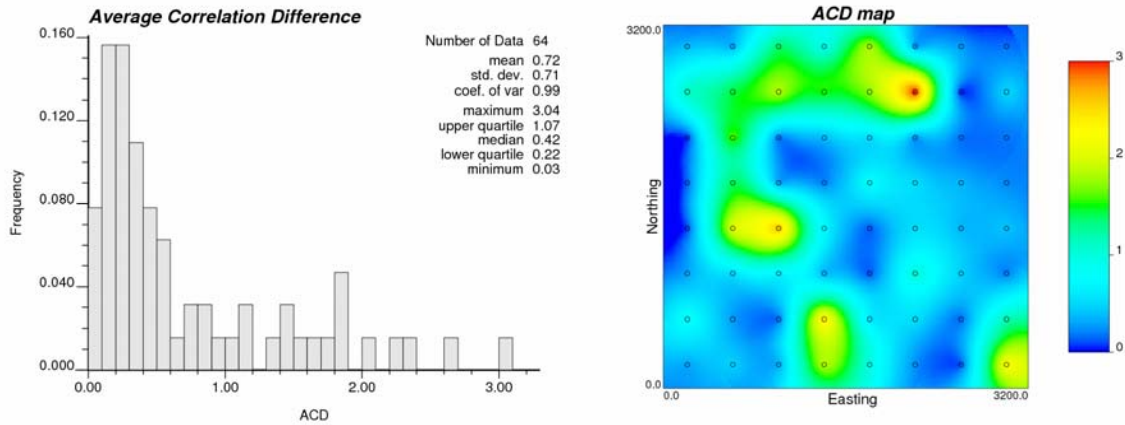


Figure 3-10: The histogram and kriged map of ACD for the two variables shown in Figure 3-5.

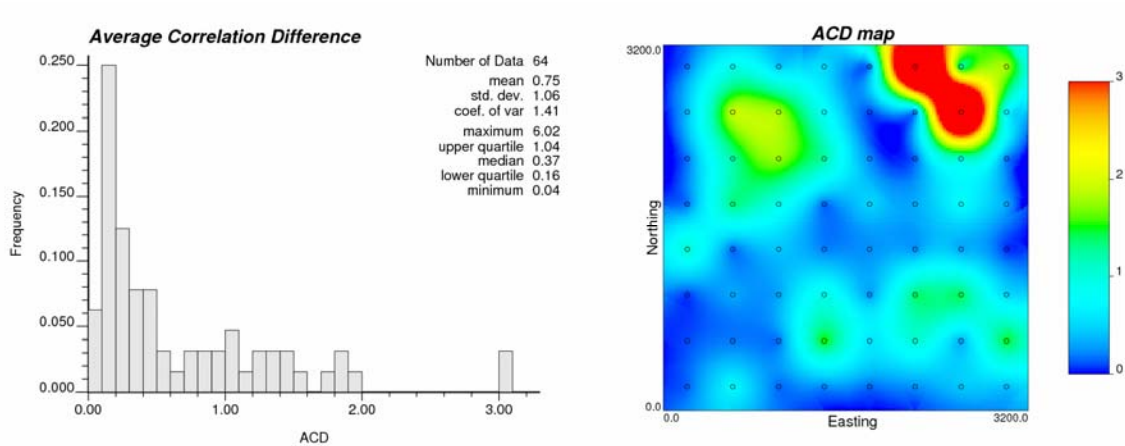


Figure 3-11: The histogram and kriged map of ACD for the two variables shown in Figure 3-8. The two wells are the two outliers shown in the cross plot in Figure 3-4.

In the Bayesian updating technique, secondary data are required over the entire model area. The correlations calculated from the wells are applied in the interwell regions based on the assumption that the secondary data are equally accurate over the entire area. However, in practice, the qualities of secondary data are not always the same. This locally varying quality must be accounted for explicitly to improve the estimation and uncertainty assessment.

3.2.3. *Local Varying Quality (LVQ)*

The quality of secondary data is different when they come from different sources. Dense secondary data may come from different 3-D seismic surveys or from kriged 2-D seismic lines or geologic mapping. The secondary data at well locations have the best quality if they are calibrated with well picks. The quality will almost always be less away from the wells. Different 3-D seismic surveys may have different qualities depending on different survey techniques and conditions. 2-D seismic data usually has less quality than 3-D seismic data. 2-D seismic lines should have better quality than the estimated locations. Treating them all the same could mislead the final updated estimate and local uncertainty results. The locally varying quality of secondary data must be appropriately accounted for.

The locally varying quality defines our confidence in the data. 3-D seismic data can be assumed to have the same quality in the same survey area. The different qualities for different 3-D surveys must be defined based on expert knowledge. When the secondary data is generated from a kriging-type method, the local varying quality can be calculated using kriging variance as below:

$$Q(\mathbf{u}) = C \cdot \sqrt{1 - \sigma_k^2(\mathbf{u})} \quad \in [0, 1] \quad (3-21)$$

where the C is the maximum quality, which is the quality of data used in kriging. If the data are secondary data at wells, the C is 1; if the data are 2-D seismic lines, the C is always less than 1. The σ_k^2 is the kriging variance, which is the error variance of kriging estimates.

Equation 3-21 is derived from kriging with one datum. The simple kriging system gives the following relationship between the kriging variance and the correlation ρ between the datum and the estimate:

$$\sigma_k^2 = 1 - \rho^2 \quad (3-22)$$

If the variance is low, the correlation is high, and the estimate is closer to the true datum; the quality of the estimate will be high.

Figure 3-12 shows the curve of data quality versus kriging variance. At well locations, the kriging variance is zero and the quality is 1. As the kriging variance increases, the data quality drops.

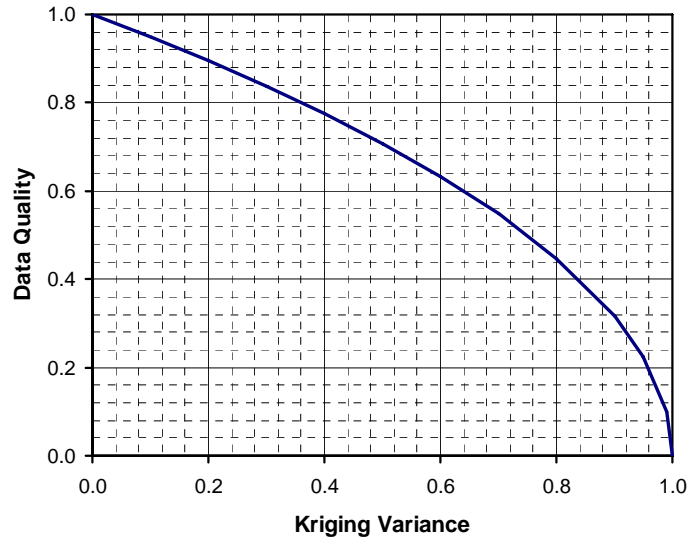


Figure 3-12: The curve of data quality versus kriging variance when the maximum quality C is 1.

3.2.4. Bayesian Updating with LVC and LVQ

The locally varying quality affects the correlation between the secondary data and primary data. Usually, secondary data are calibrated with well data so that the secondary data at wells are assumed to have 100% quality. Away from the wells, the quality is less. Assume the quality of secondary data is caused by random errors in the data, then the correlations calculated from the wells may be higher than the correlations at the estimated locations. A *locally varying effective correlation* between secondary and primary data can be used. It is calculated by multiplying the LVQ and the LVC:

$$\hat{\rho}_{i,0} = Q \cdot \rho_{i,0} \quad (3-23)$$

The data quality may also affect the correlations between different secondary variables. But the effect is less important and is difficult to quantify. The locally varying correlations calculated from wells are assumed applicable to the estimated locations.

Applying the locally varying correlations and effective correlations in Bayesian updating is straightforward. They are used in the likelihood calculation. The global correlations between secondary and primary data are replaced with the locally varying effective correlations, and the global correlations between different secondary data are replaced with the LVC in Equations 3-5 and 3-6. The new likelihood system is:

$$\sum_{j=1}^n \lambda_j \cdot \rho_{i,j} = \hat{\rho}_{i,0} \quad i=1, \dots, n \quad (3-24)$$

The likelihood variance is:

$$\sigma_L^2 = 1 - \sum_{i=1}^n \lambda_i \cdot \hat{\rho}_{i,0} \quad (3-25)$$

With the new likelihood results, the prior is updated using same Equations 3-7 and 3-8. The local uncertainty will be affected by the locally varying quality. The likelihood variance is calculated using the weights and the effective correlations that are all related to the secondary data quality. If the quality drops, the likelihood variance will increase fast. So does the updated variance.

The locally varying matrices of weighted correlations must be positive semi-definite to ensure a positive likelihood variance and a unique solution to the weights $\lambda_j, j=1, \dots, m$ in Equation 3-24. The proof of positive definiteness of the new weighted correlation matrix is given below:

For all the secondary variables $X_j, j = 1 \dots m$, the $m \times m$ LVC matrix is

$$\mathbf{\rho} = \begin{pmatrix} \rho_{x_1 x_1} & \rho_{x_1 x_2} & \cdots & \rho_{x_1 x_m} \\ \rho_{x_2 x_1} & \rho_{x_2 x_2} & \cdots & \rho_{x_2 x_m} \\ \vdots & \vdots & \ddots & \vdots \\ \rho_{x_m x_1} & \rho_{x_m x_2} & \cdots & \rho_{x_m x_m} \end{pmatrix} \quad (3-26)$$

where the weighted correlation coefficient is $\rho_{x_i x_j} = \frac{C_{x_i x_j}}{\sigma_{x_i} \cdot \sigma_{x_j}}$, where C is the weighted covariance and $\sigma_{x_i} > 0, i = 1, \dots, m$. Thus, the LVC matrix can be rewritten as

$\boldsymbol{\rho} = \mathbf{Y}^T \mathbf{C} \mathbf{Y}$, where the $m \times m$ diagonal matrix $\mathbf{Y} = \mathbf{Y}^T = \text{diag}(\mathbf{h})$ with a vector

$$\mathbf{h} = \left[\frac{1}{\sigma_{x_1}} \cdots \frac{1}{\sigma_{x_m}} \right]^T \text{ on the diagonal.}$$

We know that if \mathbf{A} is positive semi-definite matrix, so is $\mathbf{Y}^T \mathbf{A} \mathbf{Y}$, where \mathbf{Y} is arbitrary matrix. Therefore, we only need to prove the positive semi-definiteness of the weighted covariance matrix \mathbf{C} as shown below:

$$\mathbf{C} = \begin{pmatrix} C_{x_1 x_1} & C_{x_1 x_2} & \cdots & C_{x_1 x_m} \\ C_{x_2 x_1} & C_{x_2 x_2} & \cdots & C_{x_2 x_m} \\ \vdots & \vdots & \ddots & \vdots \\ C_{x_m x_1} & C_{x_m x_2} & \cdots & C_{x_m x_m} \end{pmatrix} \quad (3-27)$$

where $C_{x_i x_j} = \sum_{k=1}^n w_k x_i(\mathbf{u}_k) x_j(\mathbf{u}_k) - \sum_{k=1}^n w_k x_i(\mathbf{u}_k) \sum_{k=1}^n w_k x_j(\mathbf{u}_k)$, $i, j = 1, \dots, m$, and the weights

from inverse distance method are $\sum_{k=1}^n w_k = 1$, $w_k \geq 0$, $k = 1, \dots, n$.

For fixed $i, j = 1, \dots, m$, we have:

$$\begin{aligned} C_{x_i x_j} &= \sum_{k=1}^n w_k x_i(\mathbf{u}_k) x_j(\mathbf{u}_k) - \sum_{k=1}^n w_k x_i(\mathbf{u}_k) \sum_{k=1}^n w_k x_j(\mathbf{u}_k) \\ &= \mathbf{X}_i^T \text{diag}(\mathbf{w}) \mathbf{X}_j - \mathbf{X}_i^T \mathbf{P} \mathbf{X}_j = \mathbf{X}_i^T (\text{diag}(\mathbf{w}) - \mathbf{P}) \mathbf{X}_j \end{aligned} \quad (3-28)$$

where $\mathbf{X}_i = (x_i(\mathbf{u}_1), \dots, x_i(\mathbf{u}_n))^T$; $\mathbf{X}_j = (x_j(\mathbf{u}_1), \dots, x_j(\mathbf{u}_n))^T$; $\mathbf{w} = (w_1, \dots, w_n)^T$; $\text{diag}(\mathbf{w})$ is a diagonal matrix with the vector \mathbf{w} on the diagonal, and the matrix \mathbf{P} is given by

$$\mathbf{P} = \mathbf{w} \mathbf{w}^T = \begin{pmatrix} w_1^2 & w_1 w_2 & \cdots & w_1 w_n \\ w_1 w_2 & w_2^2 & \cdots & w_2 w_n \\ \vdots & \vdots & \ddots & \vdots \\ w_1 w_n & w_2 w_n & \cdots & w_n^2 \end{pmatrix} \quad (3-29)$$

Thus, the covariance matrix \mathbf{C} can be rewritten as $\mathbf{C} = \mathbf{X}^T (\text{diag}(\mathbf{w}) - \mathbf{w} \mathbf{w}^T) \mathbf{X}$, where $\mathbf{X} = (\mathbf{X}_1, \dots, \mathbf{X}_m)$. Again, we only need to prove that the matrix $\text{diag}(\mathbf{w}) - \mathbf{w} \mathbf{w}^T$ is positive semi-definite. Based on McCullagh and Nelder (1989), the matrix

$diag(\mathbf{w}) - \mathbf{w}\mathbf{w}^T$ is a positive semi-definite matrix if $\sum_{k=1}^n w_k = 1$, $w_k \geq 0$, $k = 1, \dots, n$.

Since the inverse distance weights meet the condition, the matrix $diag(\mathbf{w}) - \mathbf{w}\mathbf{w}^T$ is positive semi-definite. So are the covariance matrix \mathbf{C} and the locally varying correlation matrix $\boldsymbol{\rho}$.

3.2.5. *Small example*

The Bayesian updating and enhanced Bayesian updating techniques are performed using the two variables in Figure 3-5 and one additional secondary variable, seismic amplitude. The primary variable supposes to be unknown except at the 64 well locations. The image of the primary variable will be used as a reference to validate estimations from Bayesian updating techniques. The exhaustive secondary variable is used as one secondary data. Another secondary data, seismic amplitude, is generated from both 3-D and 2-D seismic. Suppose a 3-D seismic survey is conducted in the upper-left area, and a 2-D seismic survey is conducted for the rest of model area. Kriging is performed using the 2-D seismic lines to generate an amplitude model for the 2-D survey area, and then it is combined with the amplitude model from 3-D seismic results. The final map of the amplitude and the associated LVQ map are given in Figure 3-13. In generating the LVQ model, the quality of 3-D seismic area is 100%, and the quality of 2-D seismic lines is 90%. The kriged estimates have different qualities from 60% to 90%. The global correlation coefficients of amplitude to primary and secondary variables are 0.593 and 0.483, respectively (Figure 3-14). The locally varying correlations are also given in Figure 3-14. The locally varying correlation of amplitude to primary variable is high in the upper-left area and low in the rest of area, especially in the upper-right corner.

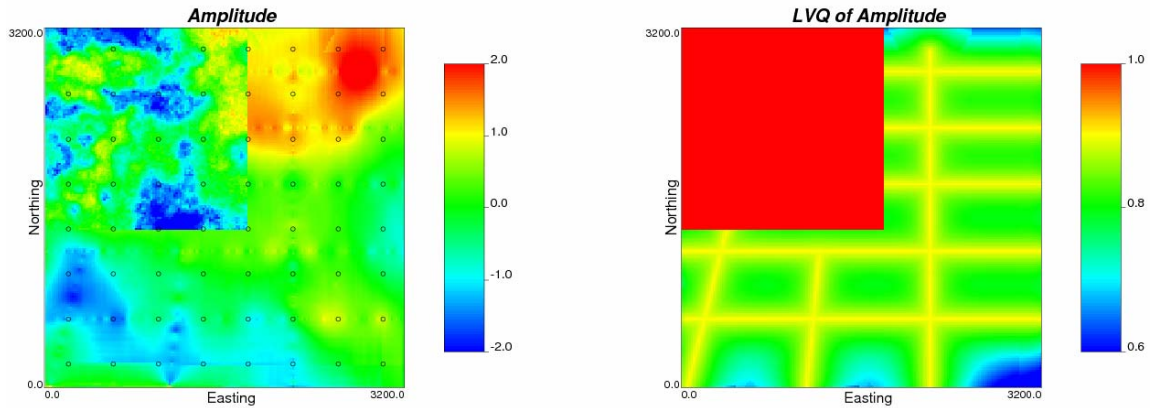


Figure 3-13: The map of amplitude and its local varying quality (LVQ). The upper-left area is the 3-D seismic area, and the rest of the area is modeled by kriging using 2-D seismic lines.

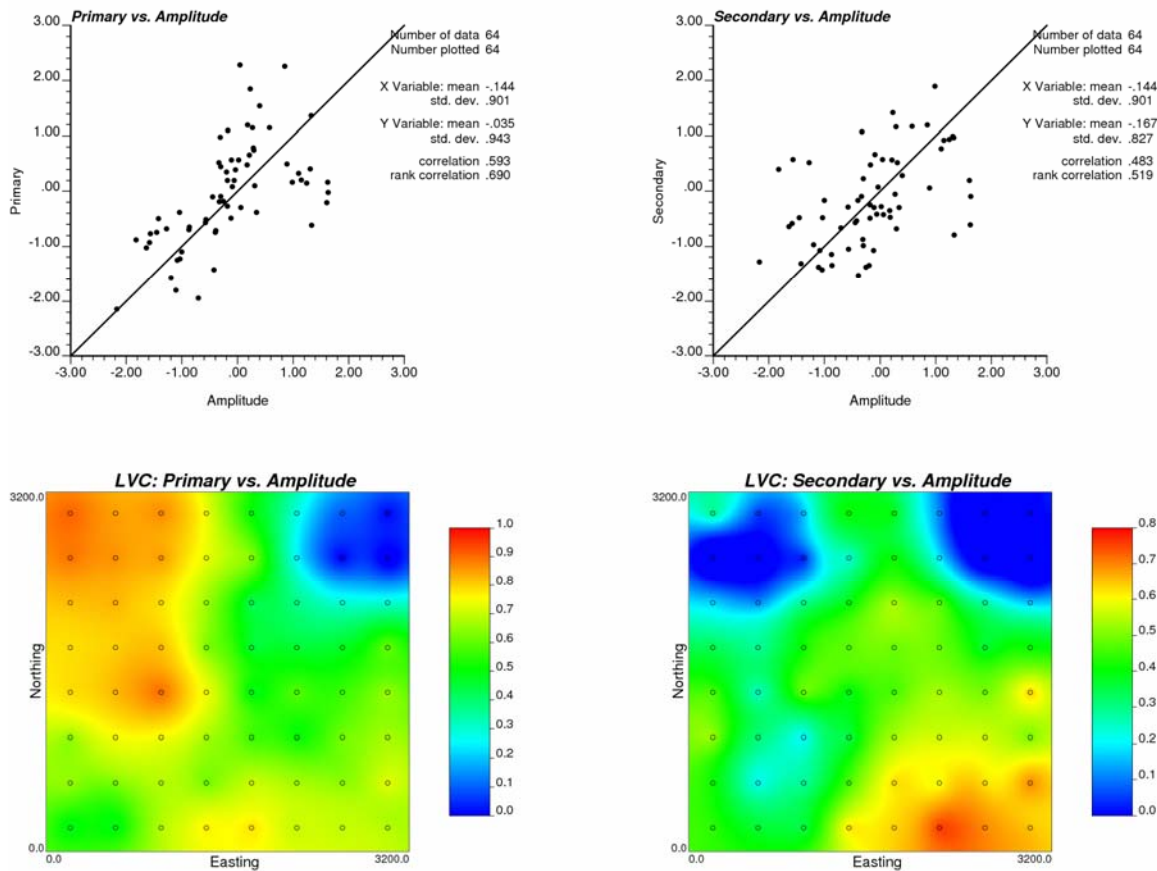


Figure 3-14: The global correlation and the map of locally varying correlation (LVC) between primary and amplitude (left column) and between secondary and amplitude (right column).

The results of Bayesian updating and enhanced Bayesian updating are given in Figure 3-15 and Figure 3-16. The left column shows the reference, prior and updated

models for visual comparison. The right column shows the secondary data, amplitude data, and likelihood model. The likelihood model of enhanced Bayesian updating fits the high and low correlated areas better, especially in the upper-left area, the enhanced Bayesian updating results show more detailed heterogeneity with more high and low values.

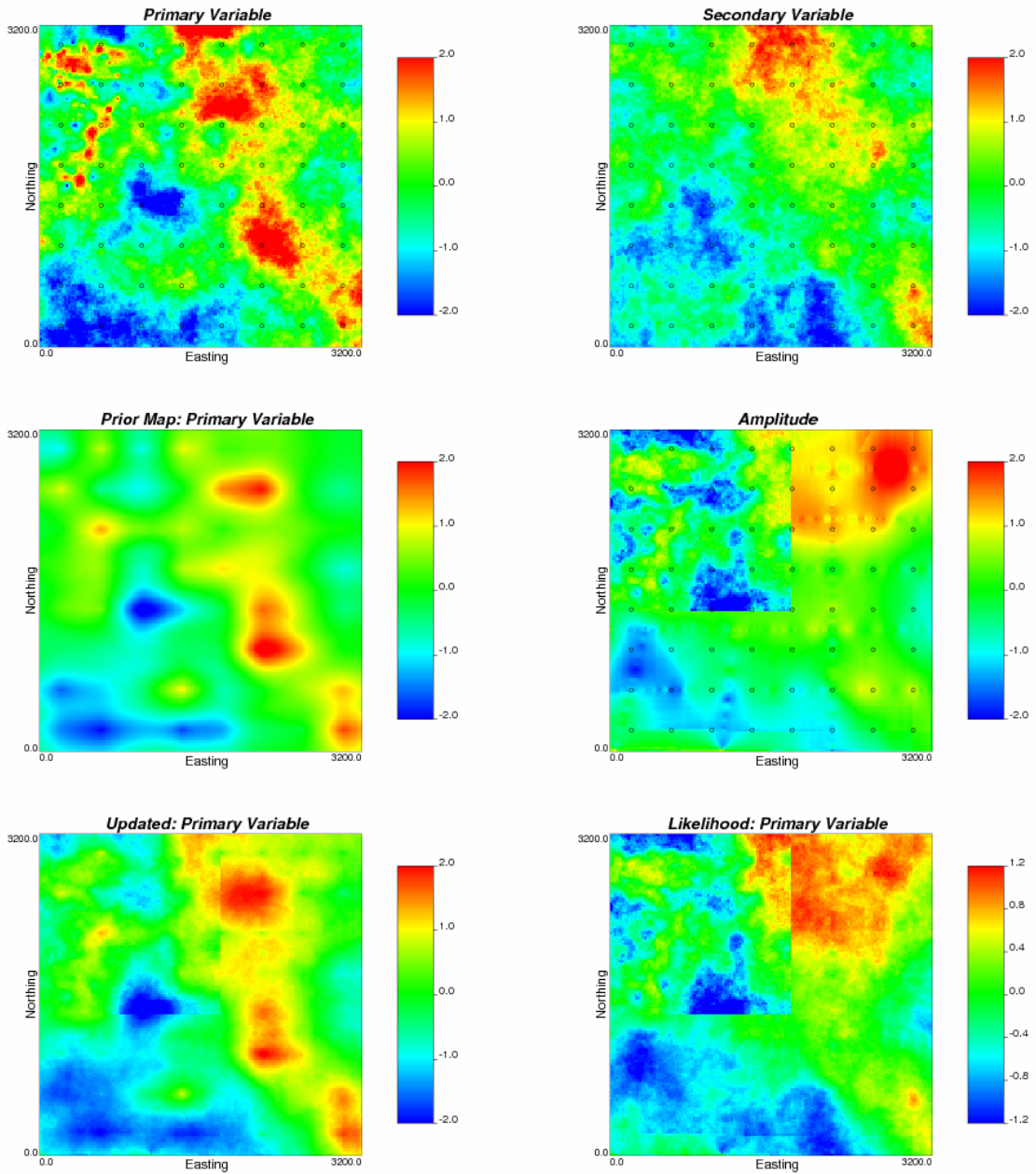


Figure 3-15: The results of Bayesian updating using global correlation coefficients.

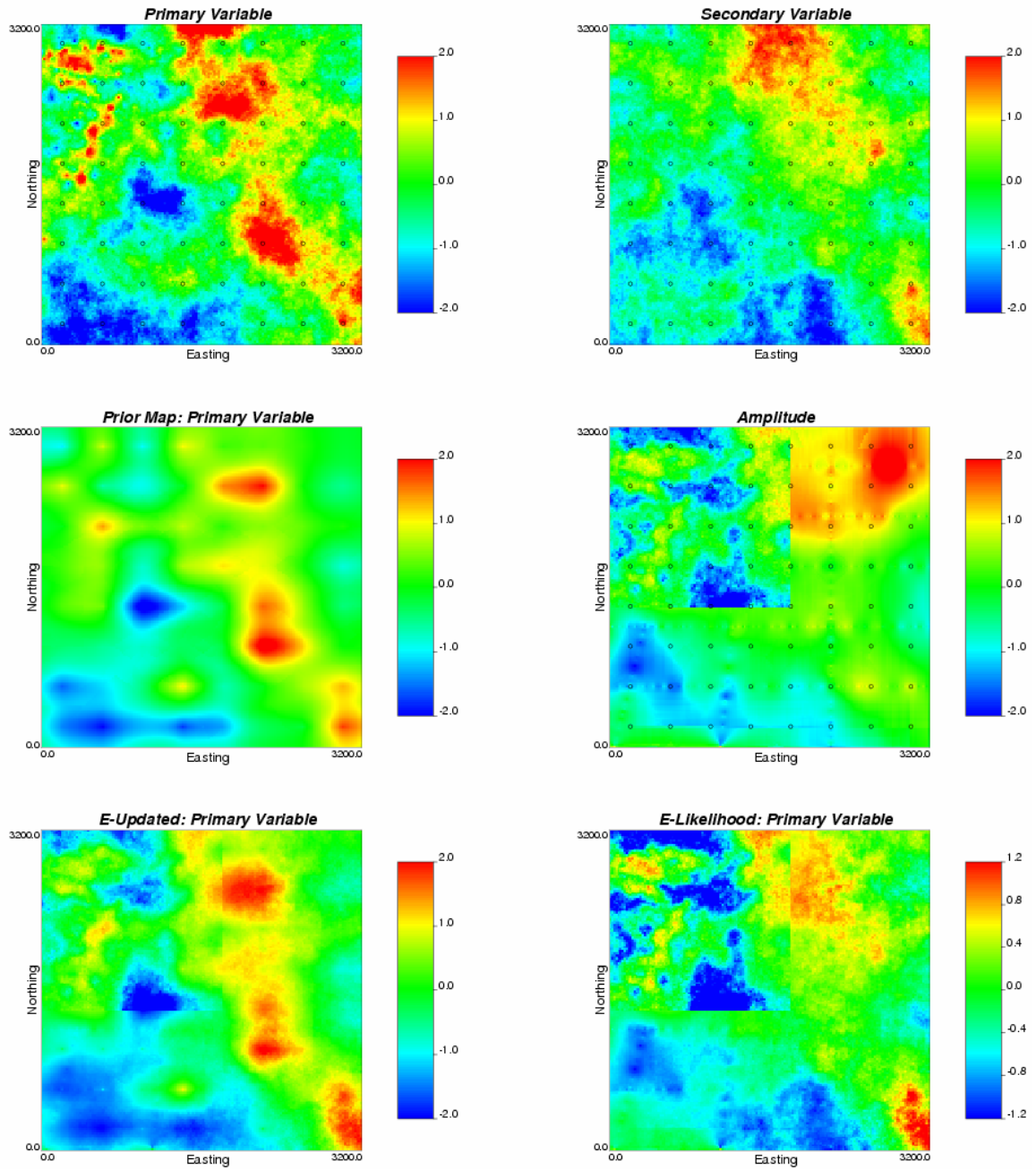


Figure 3-16: The results of enhanced Bayesian updating using LVC and LVQ.

The updated maps of Bayesian updating and enhanced Bayesian updating are compared with the reference. The maps of difference between each updated result and the reference are shown in Figure 3-17. The differences in the upper-left area are less in enhanced Bayesian updating estimates (less red and blue) because of using high local

correlations with amplitude data. The upper-right corner is also improved in enhanced Bayesian updating estimates (less yellow) because of using the lower local correlations.

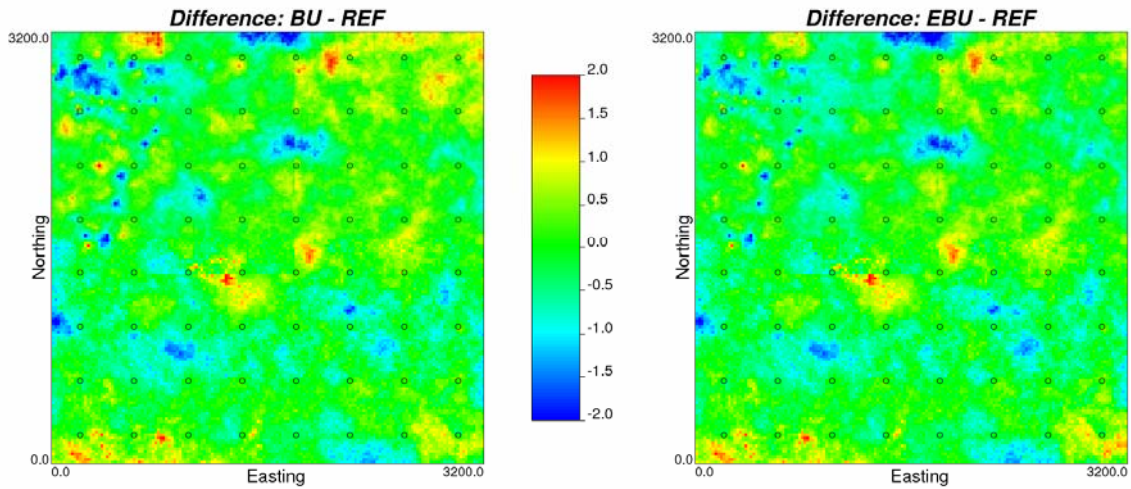


Figure 3-17: The maps of the difference between the Bayesian updating (BU) results and the reference (left) and the difference between the enhanced Bayesian updating (EBU) results and the reference (right).

Both cross validation results (Figure 3-18) and the cross plots of exhaustive estimates versus the reference (Figure 3-19) indicate that the enhanced Bayesian updating is performing better than the Bayesian updating. And the Bayesian updating is performing better than kriging. The enhanced Bayesian updating estimates are the closest to the true values.

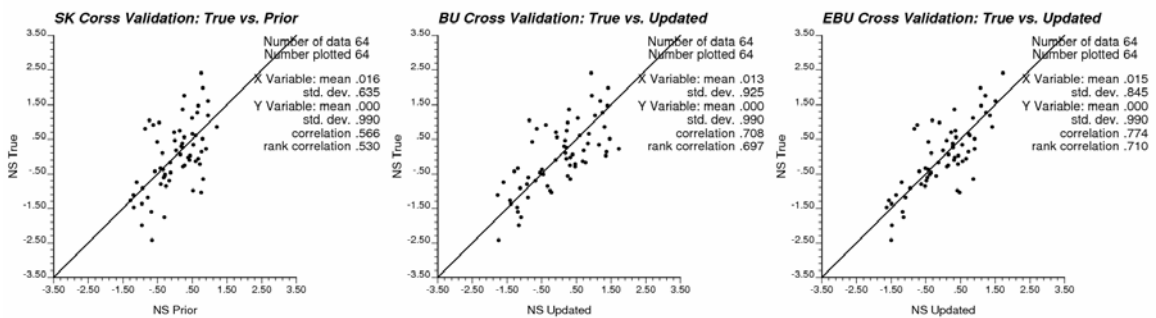


Figure 3-18: The cross validation of simple kriging (left), Bayesian updating (middle) and enhanced Bayesian updating (right).

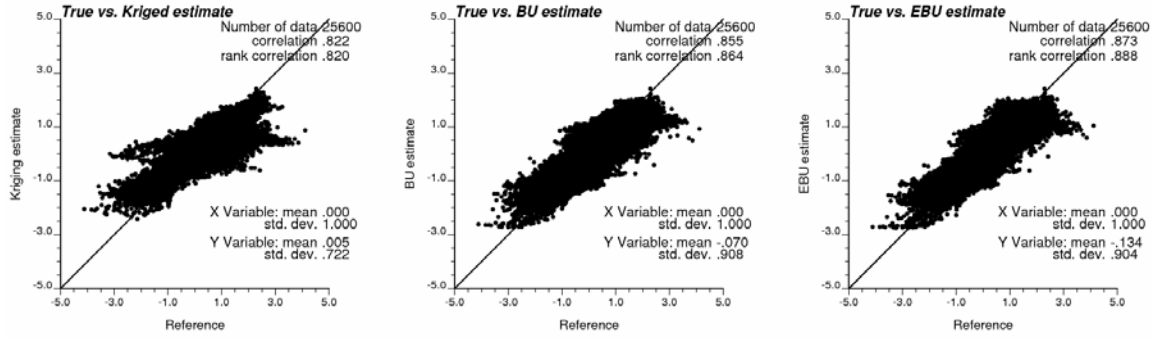


Figure 3-19: The cross plots of the estimates versus the reference for simple kriging (left), Bayesian updating (middle), and the enhanced Bayesian updating (right).

Secondary information, locally varying correlation and quality are used in Bayesian updating to improve the local estimation. However, regardless of how fine-tuned the estimates are, there are errors and uncertainties. Bayesian updating technique provides uncertainty distributions at all of locations. The mean values of updated distributions cannot be used as a realization because of smoothness. Simulated realizations are required for constructing fine scale models.

3.3. Simulation with Bayesian Updating

Under the multivariate Gaussian model, Bayesian updating can be performed within sequential Gaussian simulation (SGS). The basic procedure is to perform simple kriging sequentially using input data and previously simulated values (Equations 3-1 to 3-3) to build local prior distributions, and establish the updated distribution using the prior distribution and the likelihood distribution (Equations 3-4 to 3-6) from collocated secondary data. Then, draw randomly from the updated distribution (Equations 3-12 and 3-13) to get the simulated value:

$$y_s(\mathbf{u}) = w(\mathbf{u})\sigma_u(\mathbf{u}) + \bar{y}_u(\mathbf{u}) \quad (3-30)$$

where $w(\mathbf{u})$ is a random number drawn from a standard normal distribution, $\sigma_u(\mathbf{u})$ and $\bar{y}_u(\mathbf{u})$ are the Bayesian updated standard deviation and mean, respectively.

For computing efficiency, rather than performing Bayesian updating sequentially, we can perform Bayesian updating to build local uncertainty distributions and use a simplified simulation approach, P-field simulation (Srivastava, 1992), to generate simulated realizations. P-field simulation starts with a probability field, that is, a set of spatially correlated probability values uniformly distributed between 0 and 1. Then, simulated values are drawn by sampling the local conditional distributions using the corresponding probability values.

The implementation of P-field simulation with Bayesian updating is to draw a set of standard normal deviates that are spatially correlated within the field A , and then condition these standard normal values with the Bayesian updated mean and standard deviation to get simulated values as shown in Equation 3-30. The only difference is that the $w(\mathbf{u})$ is the spatially correlated value from standard normal distribution.

Both SGS with Bayesian updating and P-field simulation with Bayesian updating are performed using the primary and secondary data in Figure 3-5. Multiple realizations are generated. The P-field simulation realizations #1, #5 and #10 are shown together with the reference image, secondary data, and updated estimates in Figure 3-20. The SGS with Bayesian updating simulation realizations are shown in Figure 3-22. Figure 3-21 and Figure 3-23 shows the cross plots of reference versus the simulation realizations #1, #5 and #10. The collocated co-simulation (CC-SGS) is also performed to compare the two Bayesian updating simulation realizations. The collocated co-simulation is performed using the SGSim program from GSLIB (Deutsch and Journel, 1998). A variance reduction factor of 0.6 is used to correct the variance inflation. The reference and the collocated co-simulation realizations #1, #5 and #10 are shown in Figure 3-24. And the cross plots of the reference versus the CC-SGS realizations #1, #5 and #10 are shown in Figure 3-25. The variances of all simulation realizations are close to the variance of reference data. P-field simulation shows no variance inflation. SGS with Bayesian updating shows slightly higher variances. CC-SGS realizations would show much higher variances if no variance correction applied. The correlations between the reference and P-field simulation realizations are the highest among the three simulation methods. The other two simulation methods show similar correlations between reference and simulation

realizations. SGS with Bayesian updating is slightly better. The P-field simulation realizations may be used to construct fine scale 3-D models.

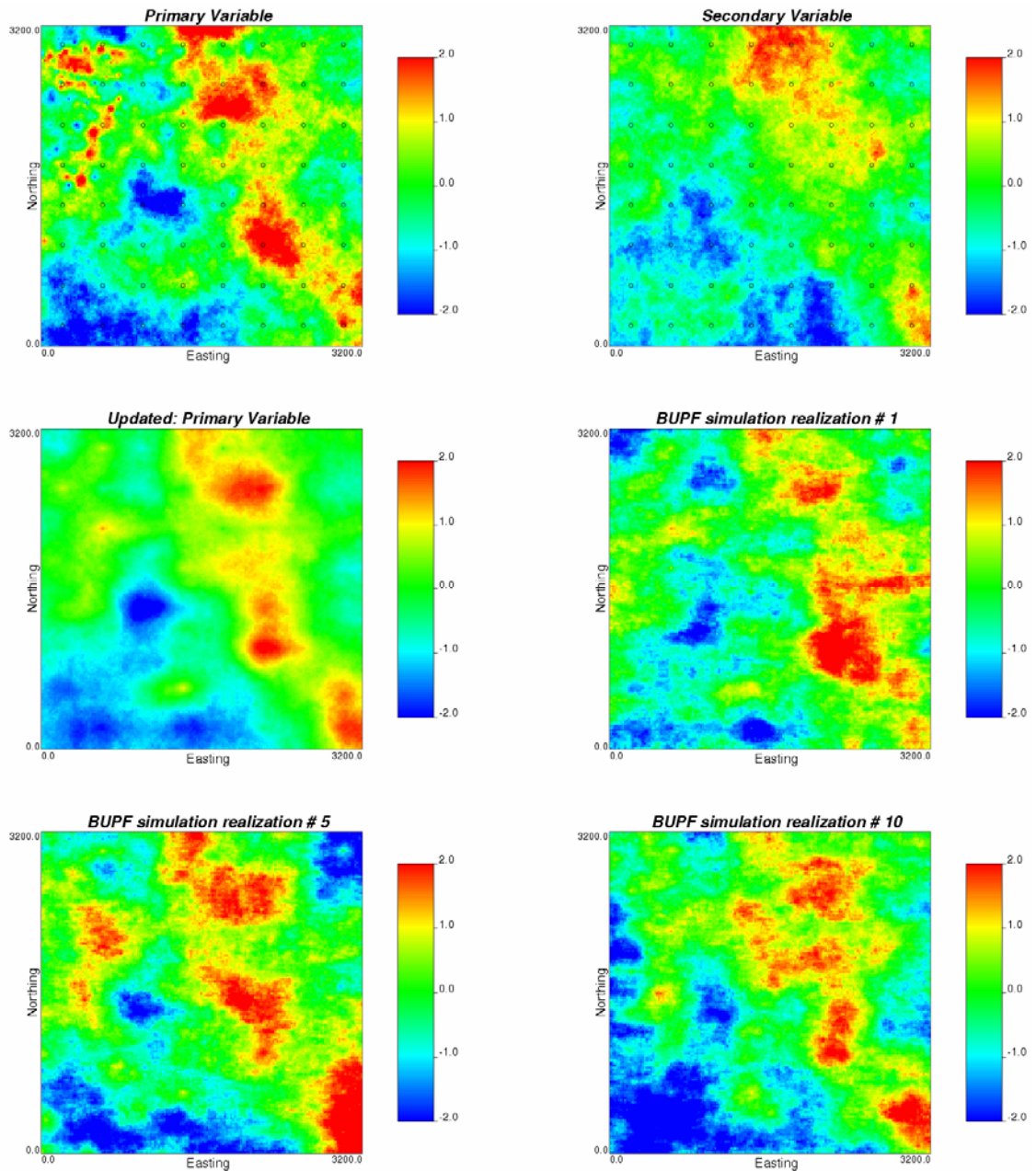


Figure 3-20: The primary variable (reference) and secondary variable used for Bayesian updating are in the top row. The Bayesian updated estimates and P-field simulation realizations are shown in the middle and bottom rows.

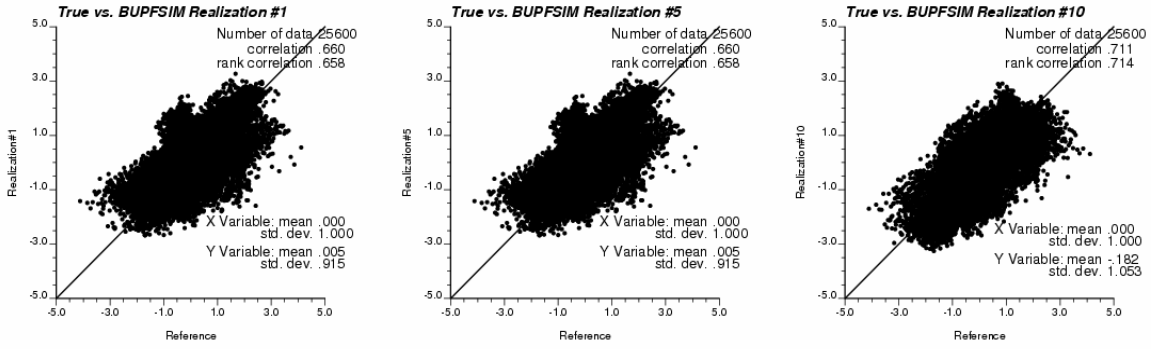


Figure 3-21: The cross plots of the reference versus the P-field simulation realizations #1, #5 and #10.

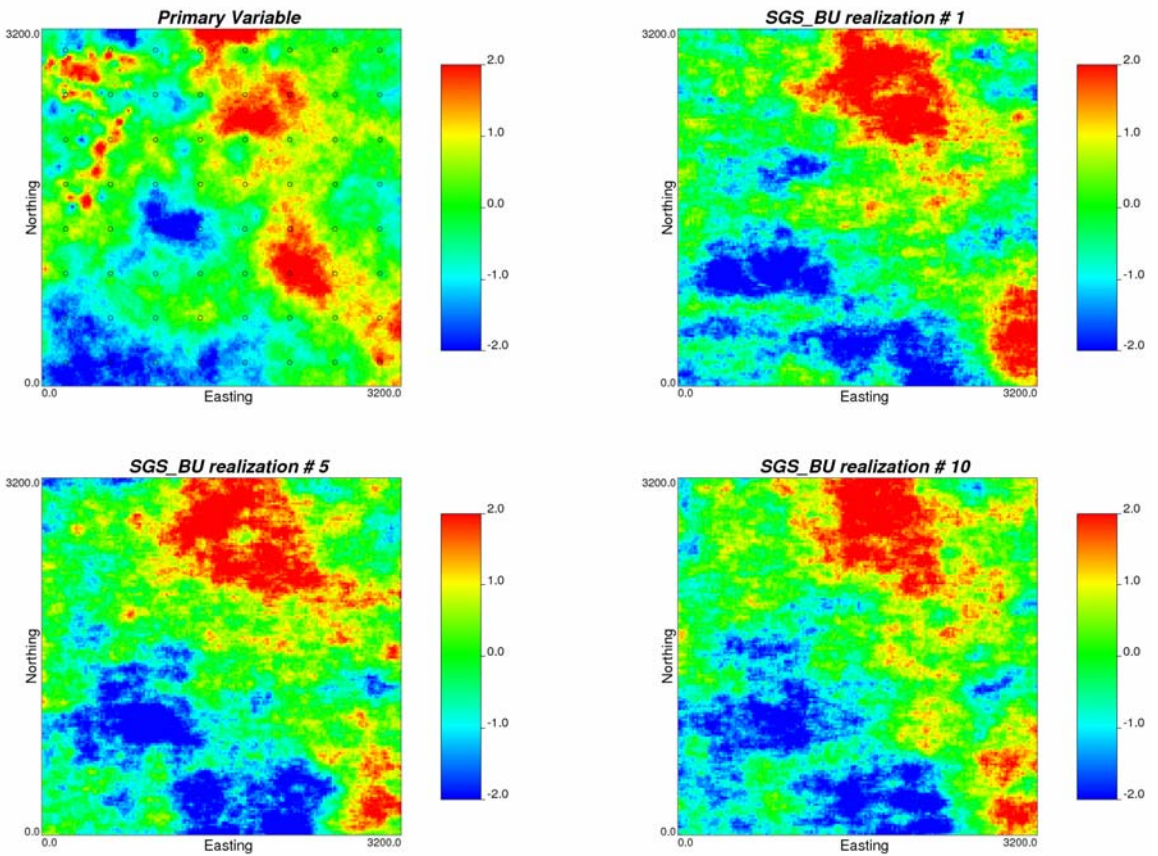


Figure 3-22: The primary variable (reference, up-left) and the SGS with Bayesian updating simulation realizations.

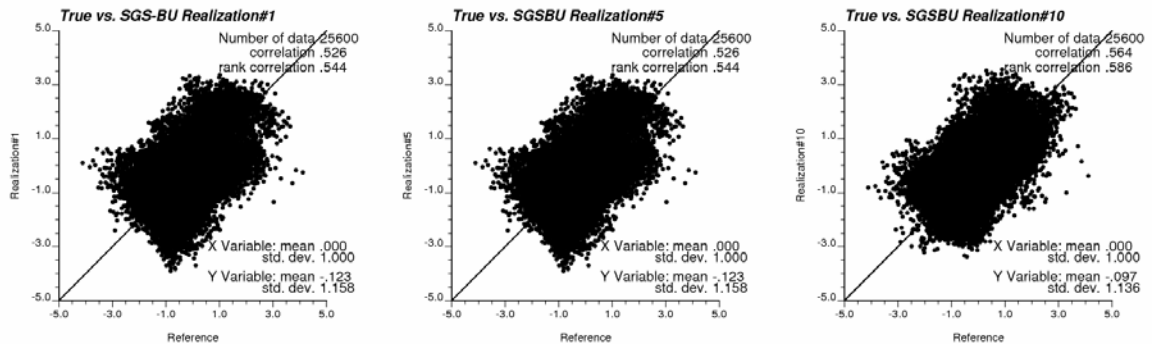


Figure 3-23: The cross plots of the reference versus the SGS with Bayesian updating simulation realizations #1, #5 and #10.

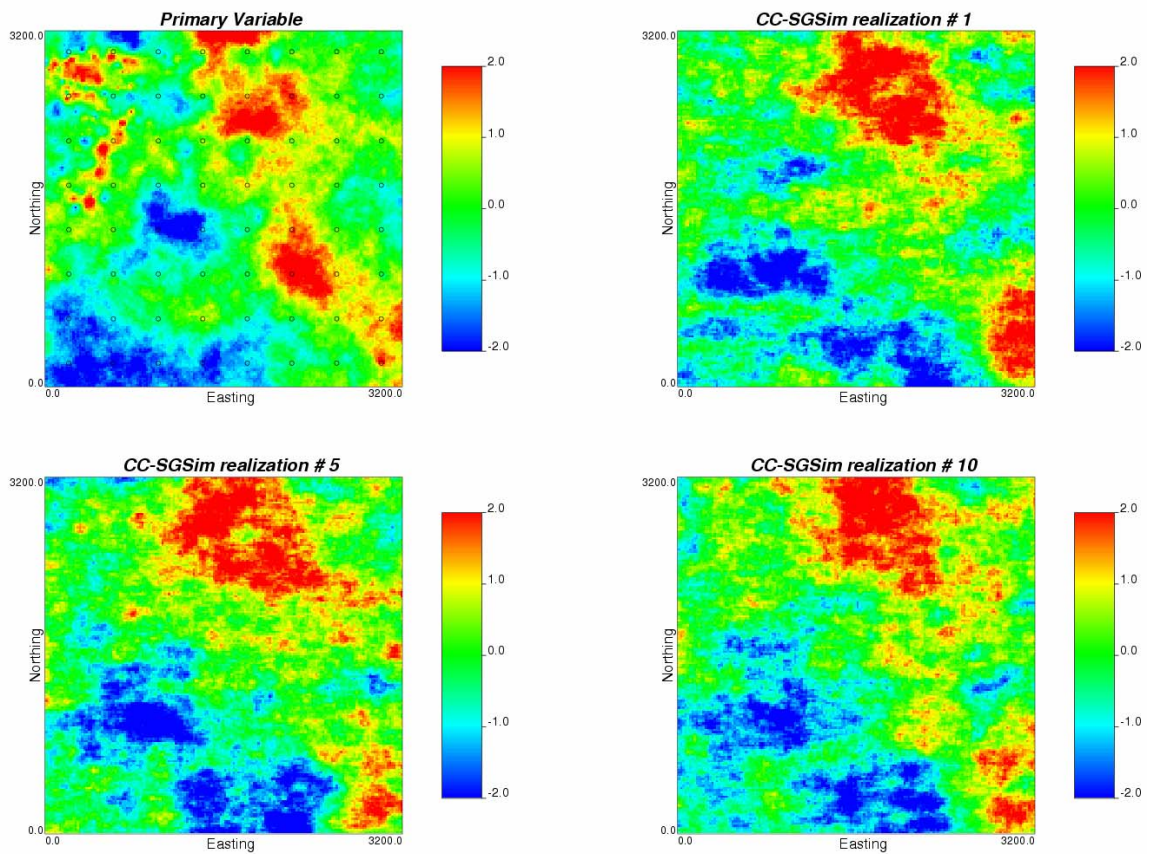


Figure 3-24: The primary variable (reference, up-left) and the collocated co-simulation realizations.

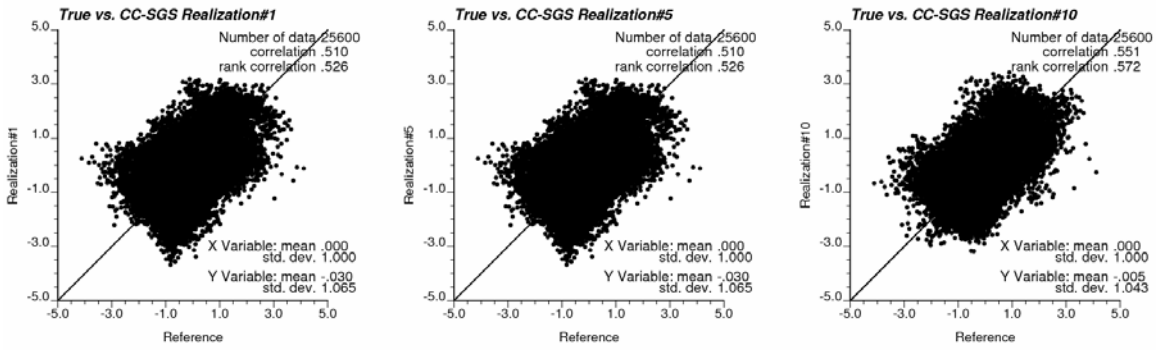


Figure 3-25: The cross plots of the reference versus the collocated co-simulation realizations #1, #5 and #10.

CHAPTER 4

IMPLEMENTATION OF BAYESIAN UPDATING

The Bayesian updating technique has been successfully applied for 2-D mapping in McMurray formation (Ren *et al.*, 2006a and Ren *et al.*, 2006c). The implementation details of Bayesian updating will be demonstrated with a large example. The example is aimed to characterize a bitumen-bearing zone for Steam Assisted Gravity Drainage (SAGD) process (Butler, 1991).

The large scale 2-D mapping using Bayesian updating techniques consists of three main steps. 1) Data assembly including careful selection of the reservoir parameters for mapping and preparation of secondary data. 2-D summaries of some reservoir parameters are calculated from wells, and secondary data are normally generated from seismic data and geological mapping. 2) 2-D mapping using the Bayesian updating or enhanced Bayesian updating techniques. The prior, likelihood, and updated models are modeled separately. 3) Validating the model results using cross validation and new wells. It is important to validate the large scale model to ensure the model is reliable for resource estimation and scale consistent modeling.

4.1. Selection of Primary and Secondary Variables

Several reservoir parameters are crucial for screening a reservoir for SAGD. The thickness of net pay or net continuous bitumen, porosity (ϕ), oil saturation (S_o), and bitumen quality over the net continuous bitumen are all related to the recoverable resources of bitumen. A complete project usually requires the mapping of 20 to 30 variables. For demonstration purposes, only three primary variables are selected.

The primary variables are 2-D summary of the reservoir parameters and are calculated at each well. The SAGD recoverable bitumen thickness (SBT) that accounts

for the basic requirements of SAGD process is an important variable. Development of steam chamber requires no thick shale barriers. Therefore, SBT is calculated for the net continuous thickness up to the top surface or a shale barrier thicker than a threshold chosen by production data or flow simulation (say 3 m). The porosity and water saturation over the SBT are also modeled. They can be combined together to calculate the recoverable resources by SAGD process.

Secondary variables should be reliable and highly correlated with the primary variables. They should have a physical connection with the primary variables, such as impedance for modeling porosity. These data are not always available. Structural data can be used as secondary data because they are usually quite reliable. They are the fundamental variables for all geological models, and they are usually derived from a variety of different sources. The secondary variables in the example are primarily structural variables that are generated from well logs, sequence stratigraphy and seismic data. Two structural surfaces are selected: (1) the bottom surface of the bitumen-bearing zone (BOT), (2) the top surface of the bitumen-bearing zone (TOP). The seismic amplitude is also added for improved porosity modeling. The amplitude data are vertical averages over the bitumen-bearing zone (APL). They are standardized by dividing the maximum value to be between 1 and -1. The selected variables for the example are listed below:

Secondary Data			Primary Data		
1	2	3	4	5	6
TOP	BOT	APL	SBT	SPhie	SSw

Some basic data analysis must be performed before modeling. Histograms are plotted to check the data distributions and assess some basic statistics. The data need to be checked to see if they are in valid data range. And the secondary data need to be checked to see if they are consistent with well data. If there are large differences in some wells, these wells need to be reviewed. If the differences are small, the secondary data may be modified by using the conditioning by kriging technique to ensure the consistency between secondary data and well data.

The model area in the example is 9660m by 9660m. A synthetic data set is created based on real data from the Surmont Project. There are 161 wells in the area. The location map of the wells is given in Figure 4-1 with the histograms of the three primary variables. The maps of three secondary data are shown in Figure 4-2. The TOP and BOT are depth in meters, and the APL is standardized value.

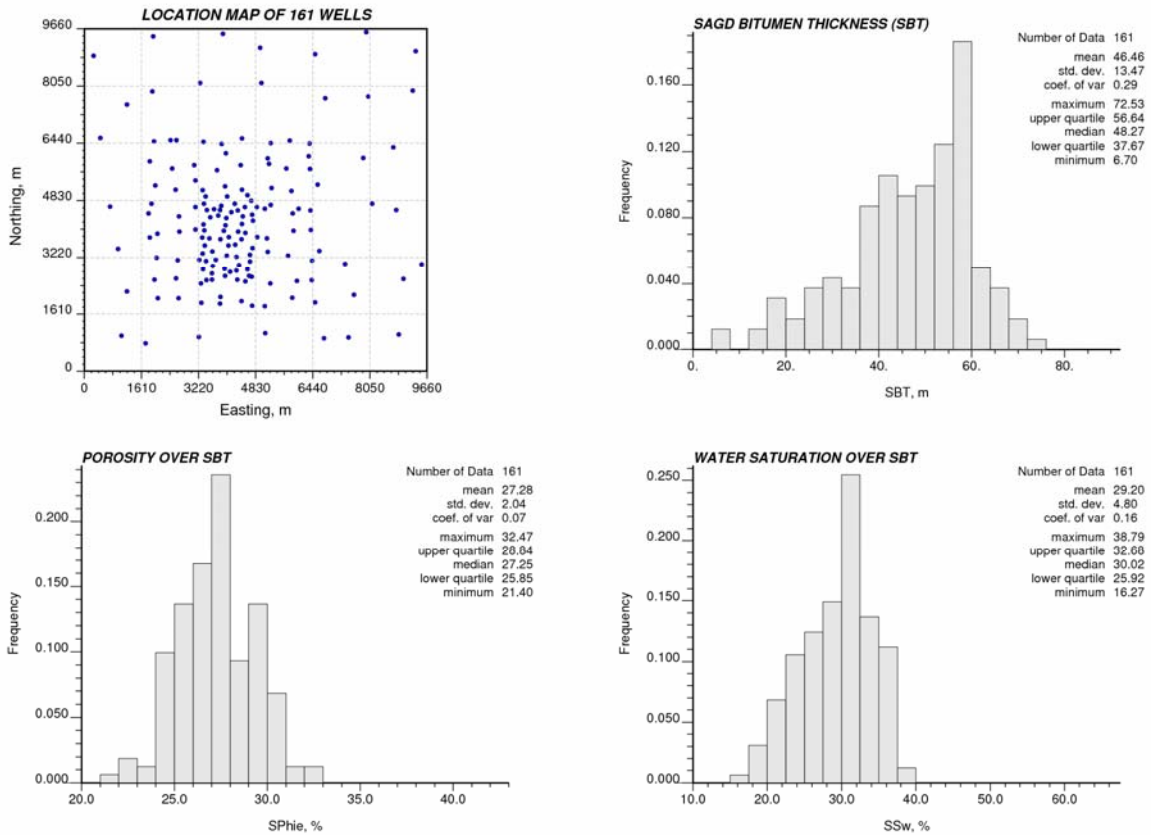


Figure 4-1: The well locations and histograms of the primary data from the wells.

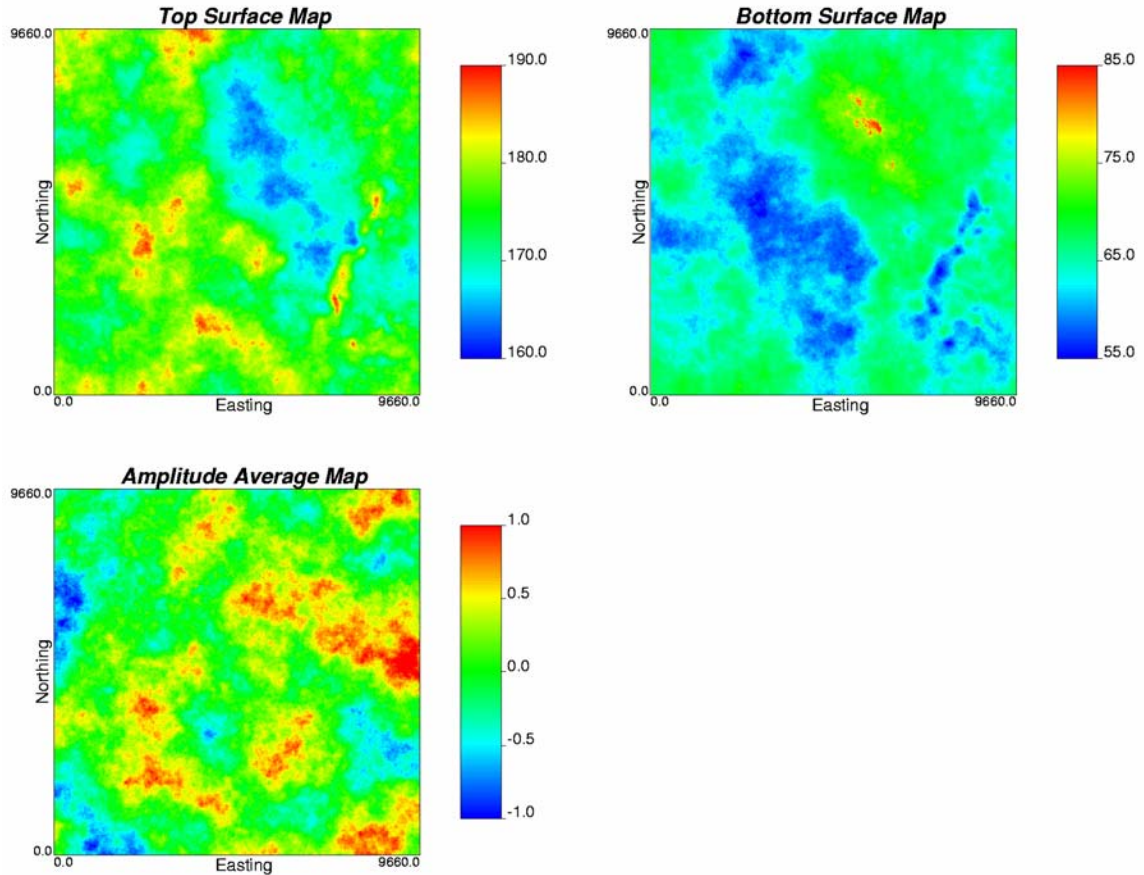


Figure 4-2: The maps of the secondary variables: top and bottom surfaces are depth in meters, and the vertical averaged amplitude is standardized to be values between 1 to -1.

4.2. Bayesian Updating 2-D Modeling

Bayesian updating is applied under a multivariate Gaussian model. All of the primary and secondary data must be transformed into normal scores at the beginning. Prior model and likelihood model will be built using these normal scores. At the end, the results are back transformed into original units. A workflow for the Bayesian updating techniques is given in Figure 4-3. The implementation details of each step are presented in the next four sections.

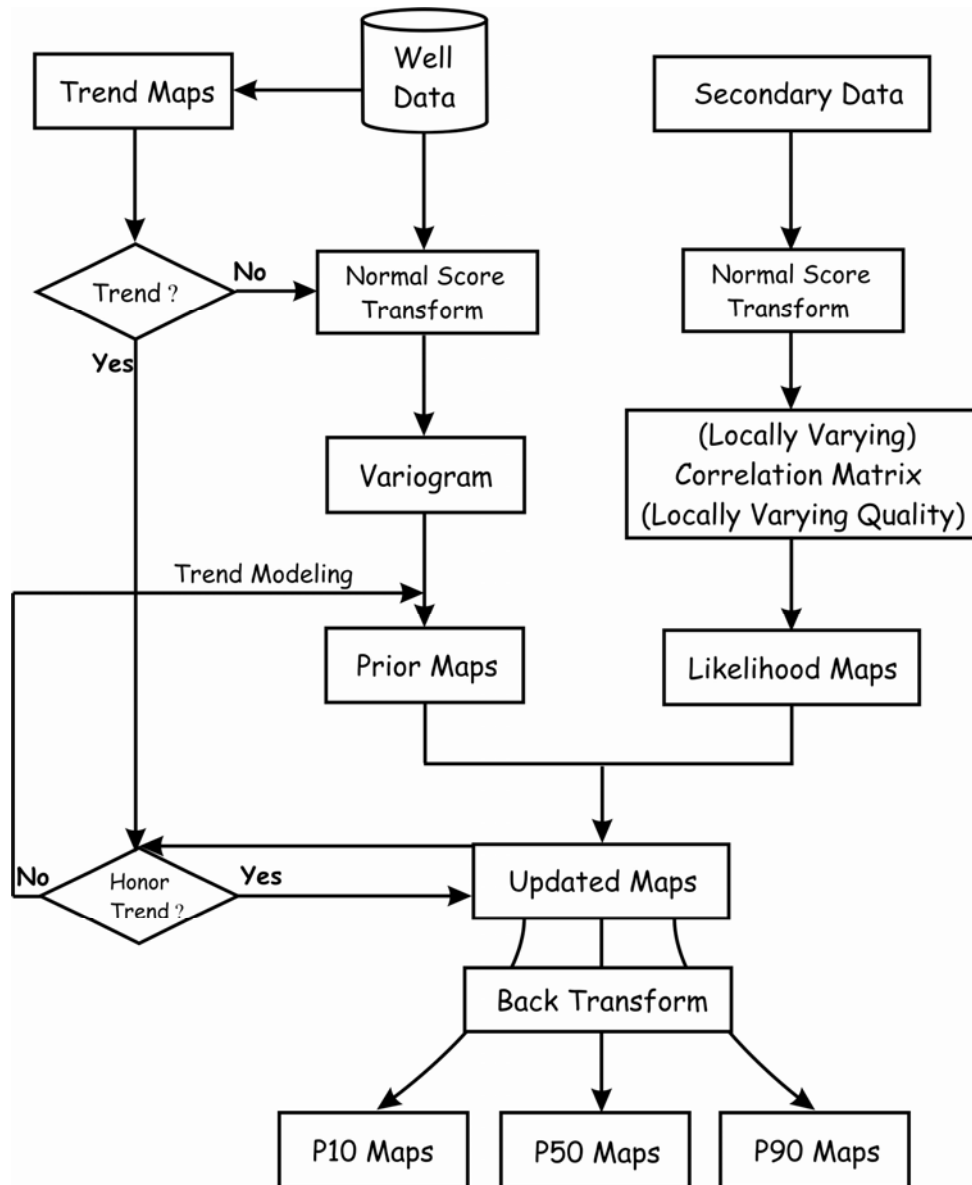


Figure 4-3: The work flow for Bayesian updating 2-D mapping techniques.

4.2.1. *Prior models*

Simple kriging is used to construct the prior models of uncertainty for each primary variable. There is an implicit assumption of stationarity in kriging and other geostatistical techniques. Stationarity means the spatial statistics are constant over the model area. Trends in the model area will require special treatment. It is important to check the trend at the beginning of the modeling. If large scale trends exist, we must make sure the trend is captured in the final updated maps. Usually a large amount of data will ensure that the

trend is reproduced in the prior model. Secondary data with a reasonable correlation will also capture trend information and ensure that it is reproduced in the likelihood model. Thus, the updated maps normally show the trend. However, if the trend is not captured in the updated maps, simple kriging with non-stationary mean (Deutsch, 2002) or other trend modeling techniques may be used to rebuild a prior model.

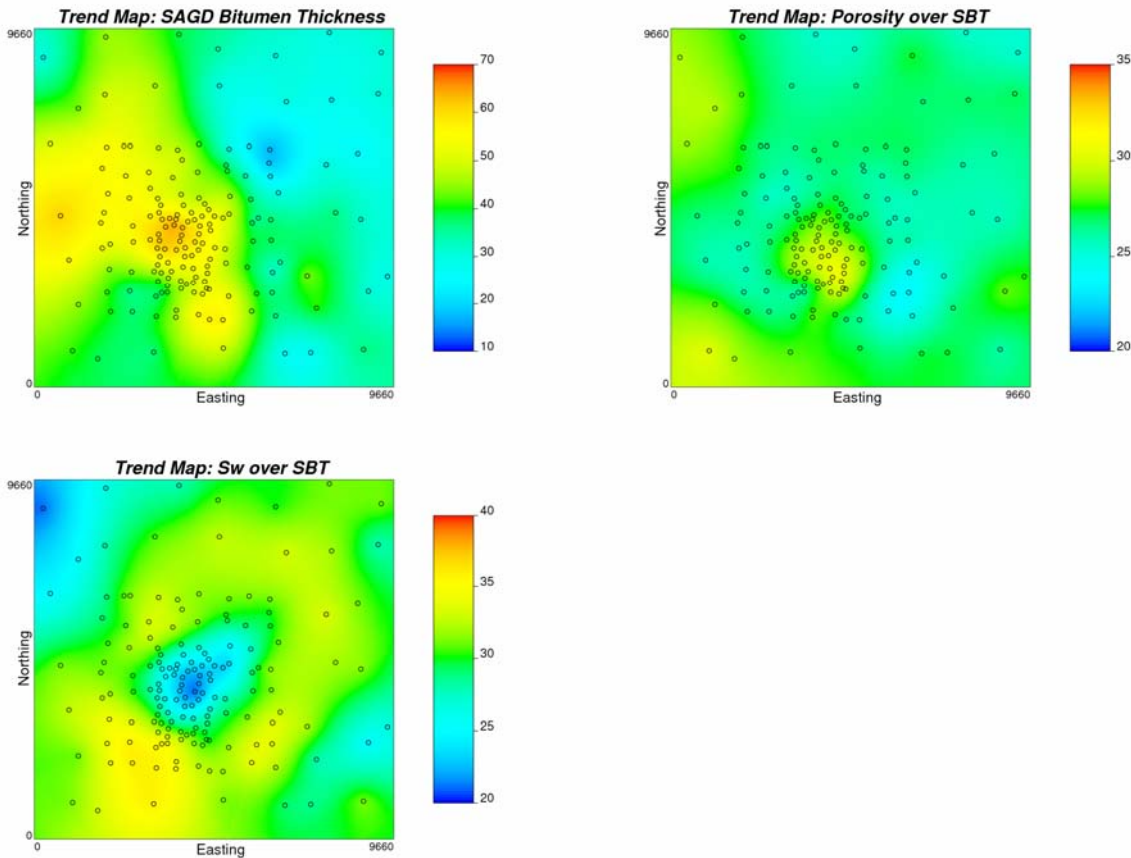


Figure 4-4: The trend maps of the primary variables: the SAGD Bitumen Thickness (SBT) is in meters, and the porosity and Sw are in percentage.

The trend map is used to determine if there are large scale trends in a primary variable over the model area. The trend map is created by simple or ordinary kriging using data in real units. A variogram with a large range of correlation and a small nugget effect is used. It allows trends shown in sparse wells area. Trends generated from a large amount of data are reliable. Trends in sparse wells area need to be adopted with care because we do not want to over constrain the model. The trend maps of the primary variables are shown in Figure 4-4. All trend maps indicate some trends in the area. They

will be compared with the updated maps to see if the trends are captured in the final models.

The well data are clustered in the center of the study area. The trend maps also indicate that the clustered wells are preferentially drilled in the high SBT, high porosity and low Sw area. The histograms of the well data (Figure 4-1) do not represent the true distributions of the primary variables in the model area. Declustering should be used to obtain more representative distributions. Cell declustering (Deutsch, 2002) is used. An appropriate cell size must be defined to generate declustering weights. The calculated declustered means at different cell sizes (100m to 3000m) are cross-plotted in the left column of Figure 4-5. The declustered mean of SBT drops at the large cell sizes. The declustered means of the other two variables change slightly. Because the clustered data in high SBT area, we expect a lower mean for SBT. The location map (Figure 4-1) indicates there is approximately one datum per section in the sparse well areas. Therefore, the cell size is fixed at 1610m to calculate declustering weights. The histograms of the declustered distributions from the weights and data are plotted in the right column of the Figure 4-5. There is a large change in the distribution of SBT. These declustered distributions are used for transforming the primary data into normal scores.

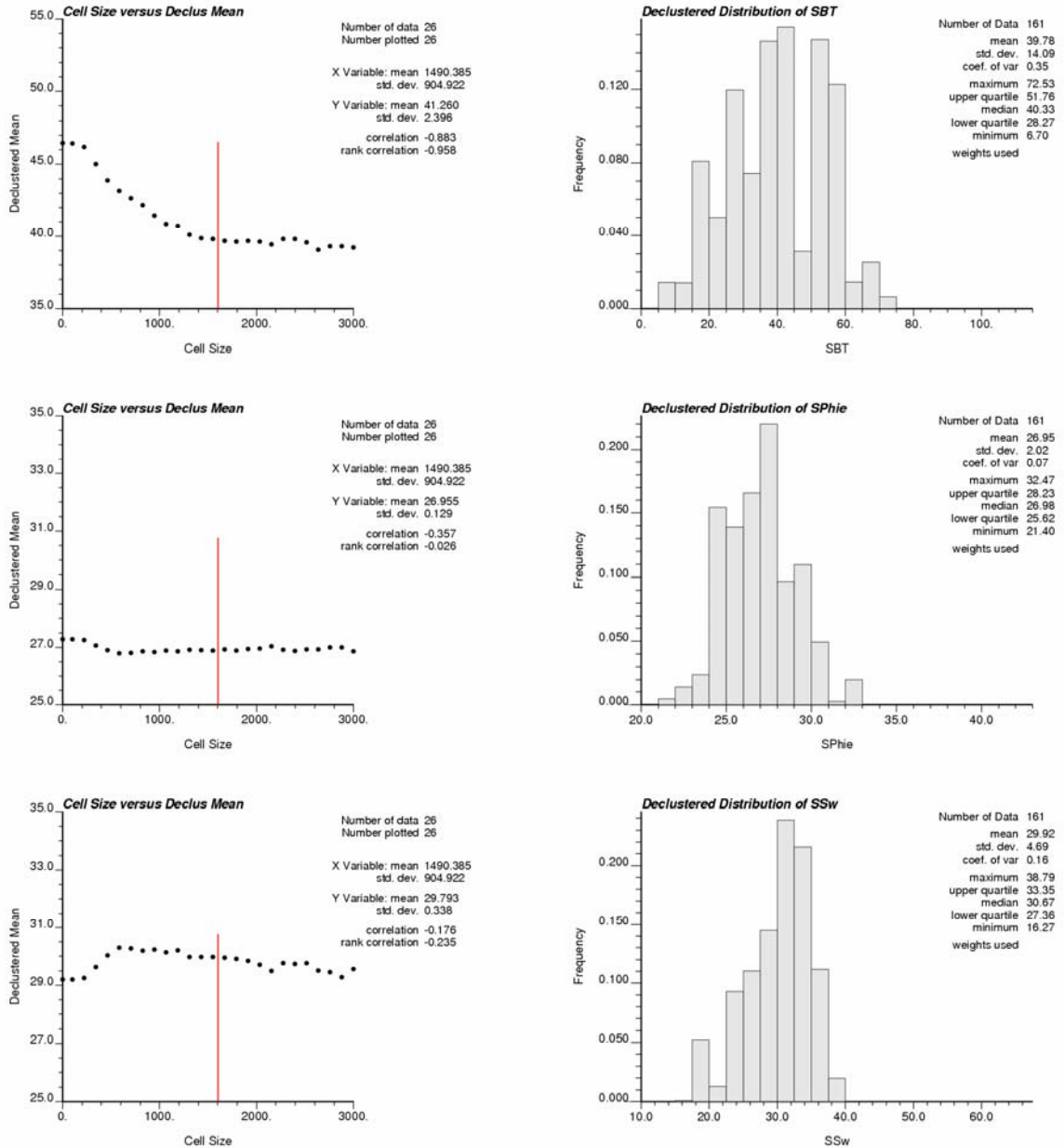


Figure 4-5: The declustering results of the three primary variables. The left column shows the declustered mean at different cell size range from 0 to 3000m. The red lines are the selected cell size at 1610m. The right column is the declustered distributions of the primary variables: the SAGD Bitumen Thickness (SBT) is in meters, and the porosity and Sw are in percentage.

The spatial correlation of a reservoir parameter is measured by the variogram model. The variogram model is generated from the experimental variogram. The experimental variogram is calculated from the normal scores. Variogram map may be used to determine the major and minor directions for variogram calculation. The experimental variograms can be modelled using a semi-automatic variogram fitting algorithm. The variogram models of the primary variables are shown in Figure 4-6.

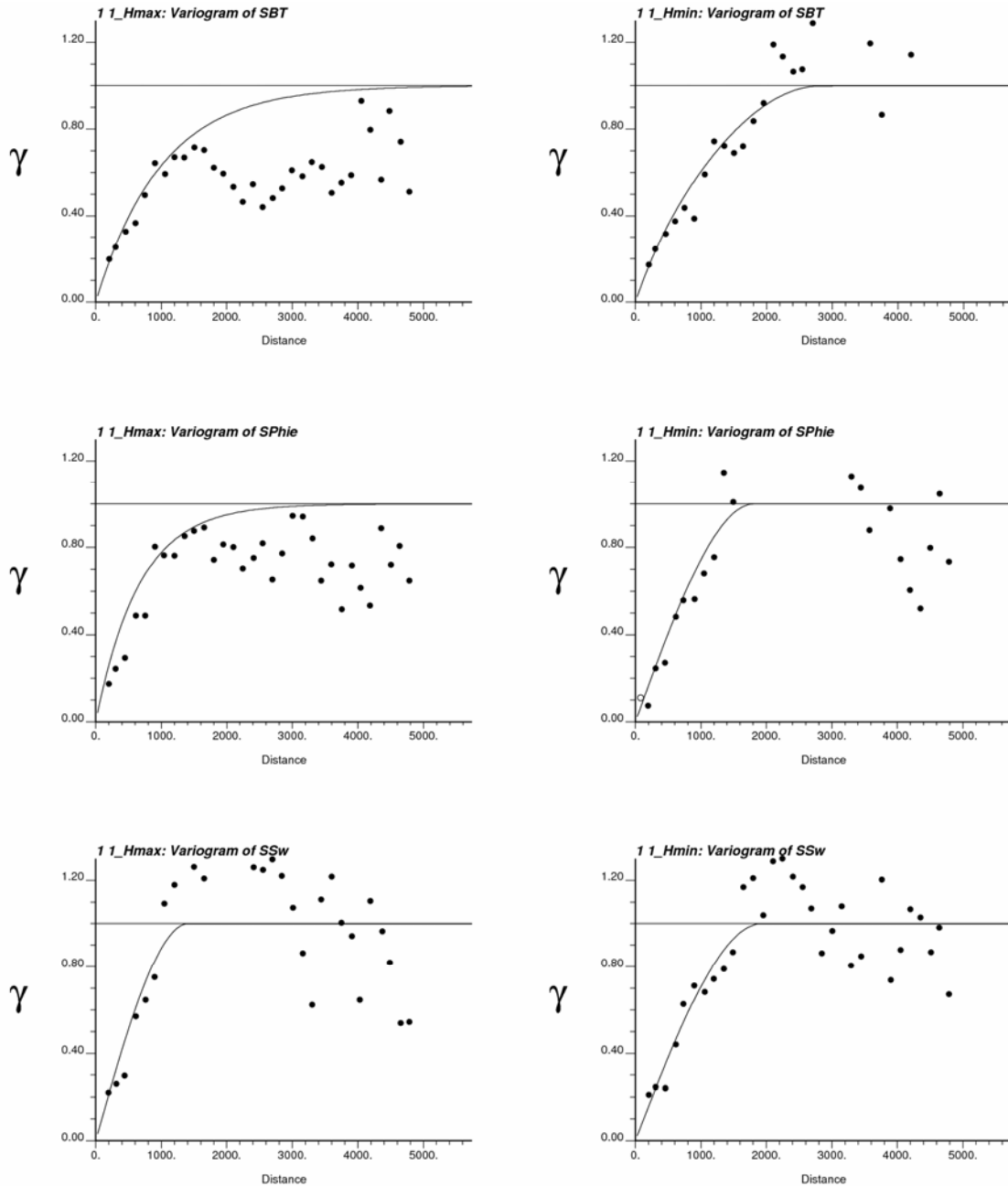


Figure 4-6: The major and minor principal directional variograms of SBT (top), porosity (middle) and water saturation (bottom).

The prior maps are the kriged maps of the primary variables (Figure 4-7). Using the normal scores and the corresponding variogram, simple kriging is performed and the result is a prior model that yields an uncertainty distribution at each location. The local uncertainty is a non-standard normal distribution defined by the kriged mean and variance. The maps of kriged mean are shown in the left column and the maps of kriging

variance are shown in the right column in Figure 4-7. The variance at wells is zero (blue dots). The trends in the prior maps match well with the trend maps (Figure 4-4). The values on these maps are only conditional to surrounding data of the same type; we must also consider the secondary data.

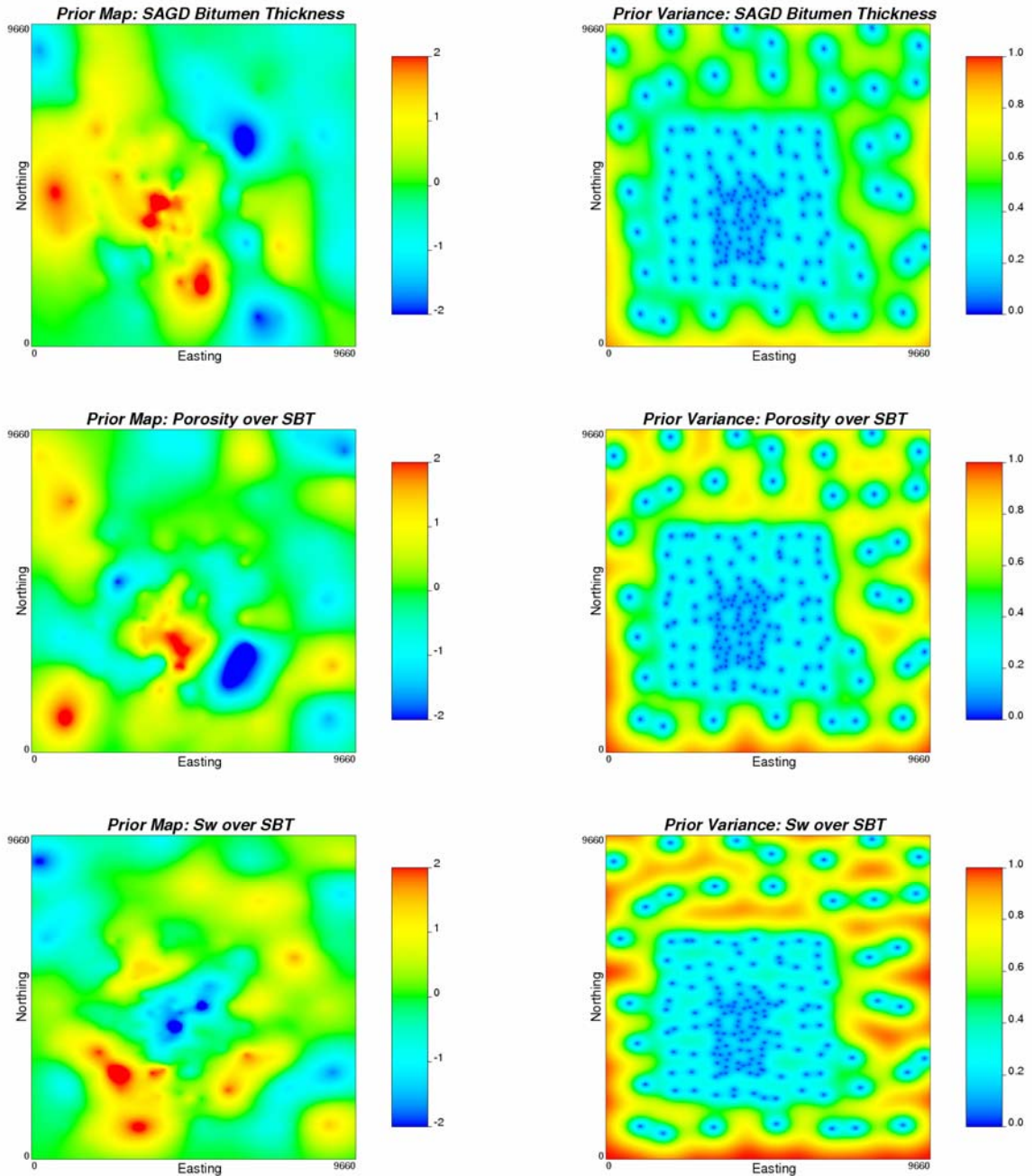


Figure 4-7: The prior maps of the primary variables. The left column is prior mean in Gaussian units and the right column is prior variance.

4.2.2. Likelihood models

Multiple secondary data are combined to generate a likelihood model for each primary variable. Representative correlations between the primary variable and the secondary variables are vital in building likelihood model. Checking the data and understanding the extreme values are important to obtain representative correlations. The cross plot and the ACD map of each pair of the variables are used to check the data. Problem data should be reviewed and perhaps eliminated to obtain a more representative correlation between the variables. Figure 4-8 shows the cross plots of all the pairs of the variables. One value in the red circle in the cross plot of porosity versus bottom surface is questionable. This extreme value is also indicated in ACD map (middle in Figure 4-9).

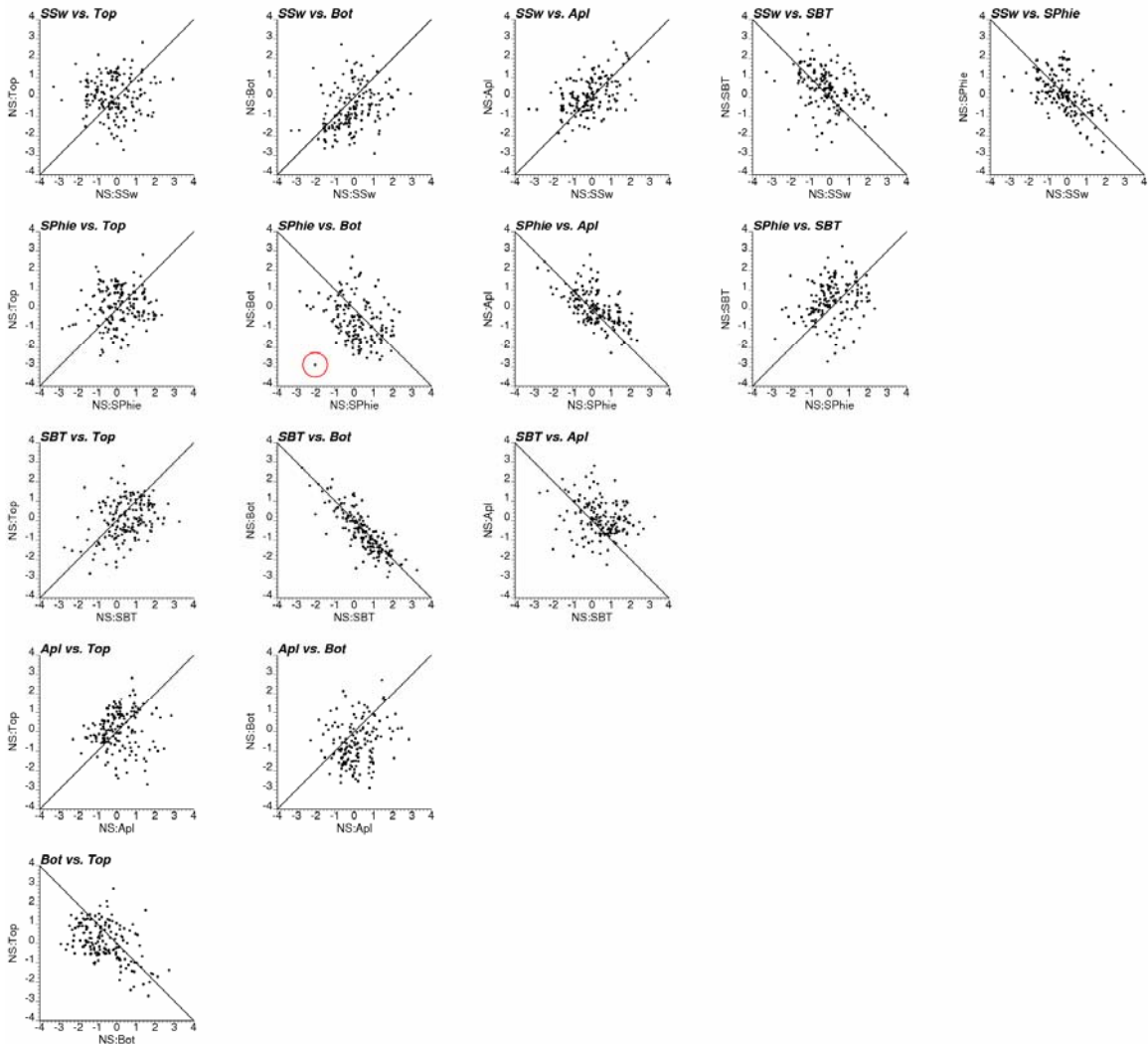


Figure 4-8: The cross plots of each pair of variables.

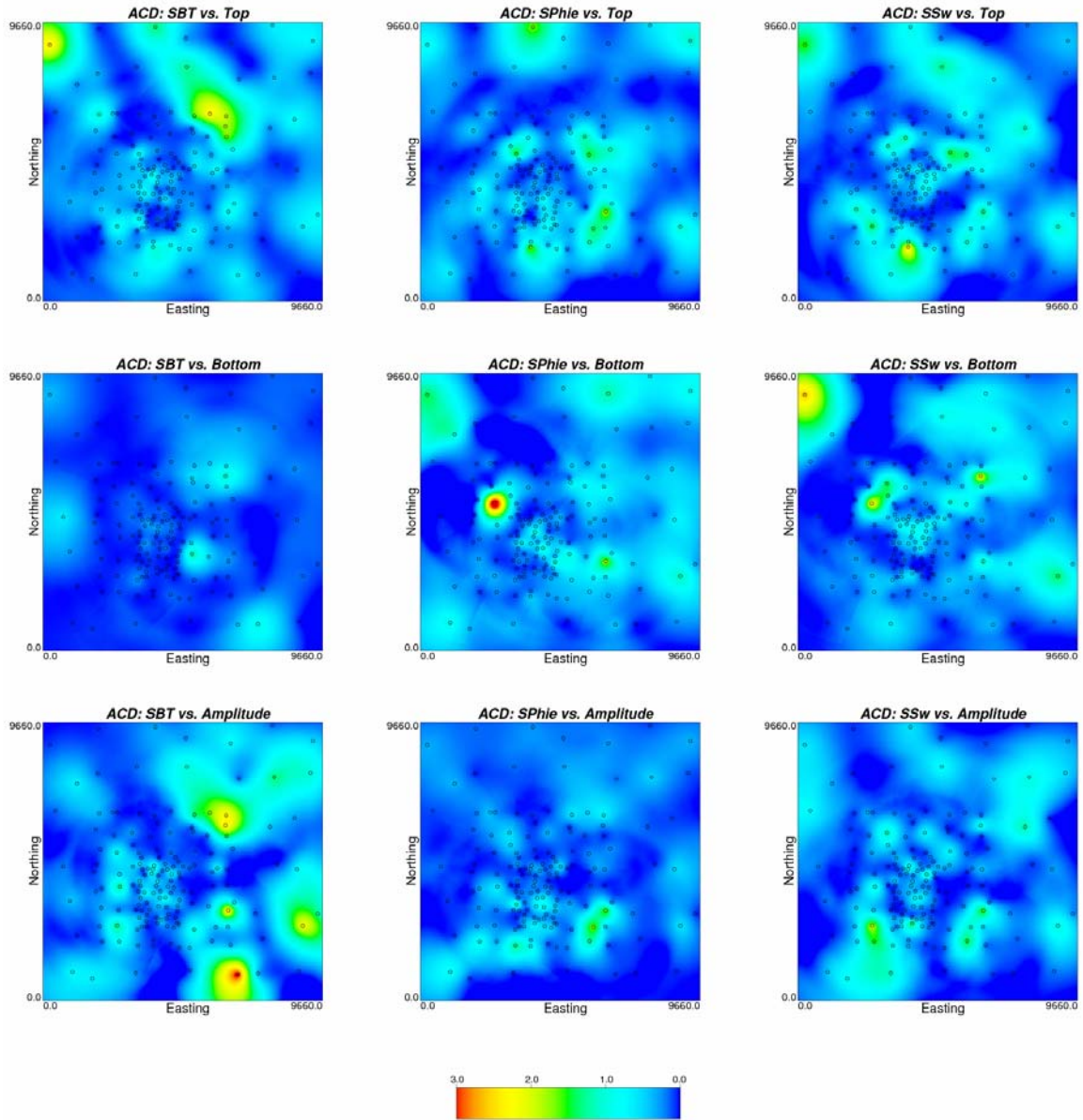


Figure 4-9: The ACD maps of each pair of variables.

The ACD map is used to identify data pairs of extreme values that can affect the local correlation between two variables. The ACD is calculated for each well by the method introduced in Section 3.2.2 of previous chapter. Then, they are mapped using kriging to identify the data pairs with large impact.

The questionable well is taken out. Thus 160 wells are actually used for the 2-D modeling. The final global correlation coefficients are summarized and shown in a correlation matrix (Figure 4-10). It is symmetric. The SBT is highly correlated with

bottom surface with a correlation of -0.83 . The porosity is highly correlated with the amplitude with a correlation of -0.61 . Water saturation is correlated with both bottom surface and amplitude. These secondary data will influence the estimation at unsampled locations. Bottom surface and amplitude will play important roles. Top surface is less important than the other secondary variables.

SSw	0.01	0.37	0.44	-0.34	-0.53	1.00
SPhie	0.09	-0.30	-0.61	0.27	1.00	-0.53
SBT	0.32	-0.83	-0.22	1.00	0.27	-0.34
APL	0.08	0.24	1.00	-0.22	-0.61	0.44
BOT	-0.48	1.00	0.24	-0.83	-0.30	0.37
TOP	1.00	-0.48	0.08	0.32	0.09	0.01
	TOP	BOT	APL	SBT	SPhie	SSw

Figure 4-10: The correlation matrix of all the variables.

Locally varying correlations are required for the enhanced Bayesian updating technique. They are calculated at each location from all the wells with the weights from inverse distance method. Figure 4-11 shows only the locally varying correlation maps of the primary variables versus the secondary variables. The locally varying correlations will be used in the likelihood calculation. Locally varying qualities are not used in this example.

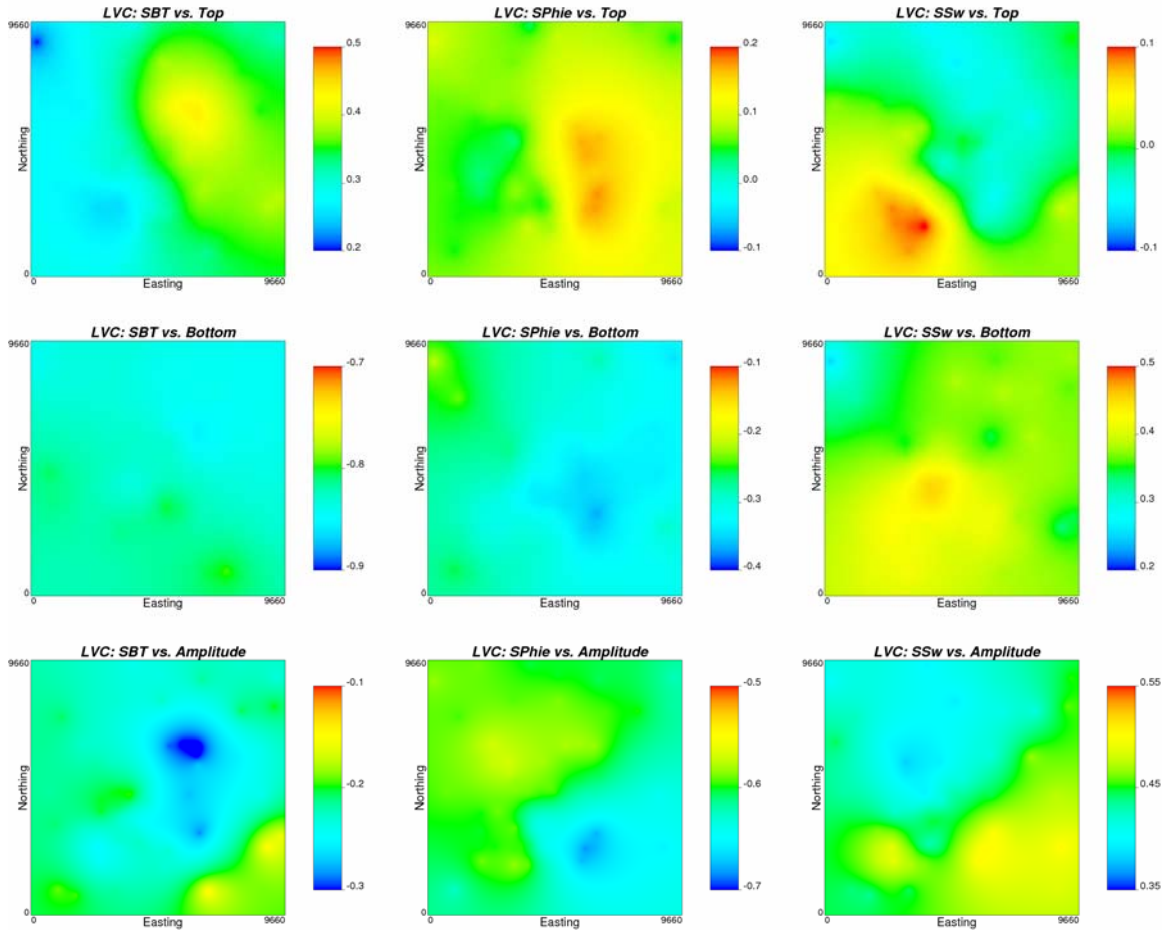


Figure 4-11: The locally varying correlations between primary variables and secondary variables.

With the correlations between a reservoir parameter and multiple secondary variables, we can use the secondary data to calculate the likelihood model for the reservoir parameter. The likelihood models provide an uncertainty distribution at each location conditional to collocated secondary data of multiple types. Both the global correlations and the locally varying correlations are used. The likelihood models from the global correlations are shown in Figure 4-12. The left column is the maps of likelihood means, and the right column is the likelihood variances. The variance is constant over the entire area. The likelihood models from the locally varying correlations are shown in Figure 4-13. The means look very similar to the means shown in Figure 4-12, but the variances are varying locally.

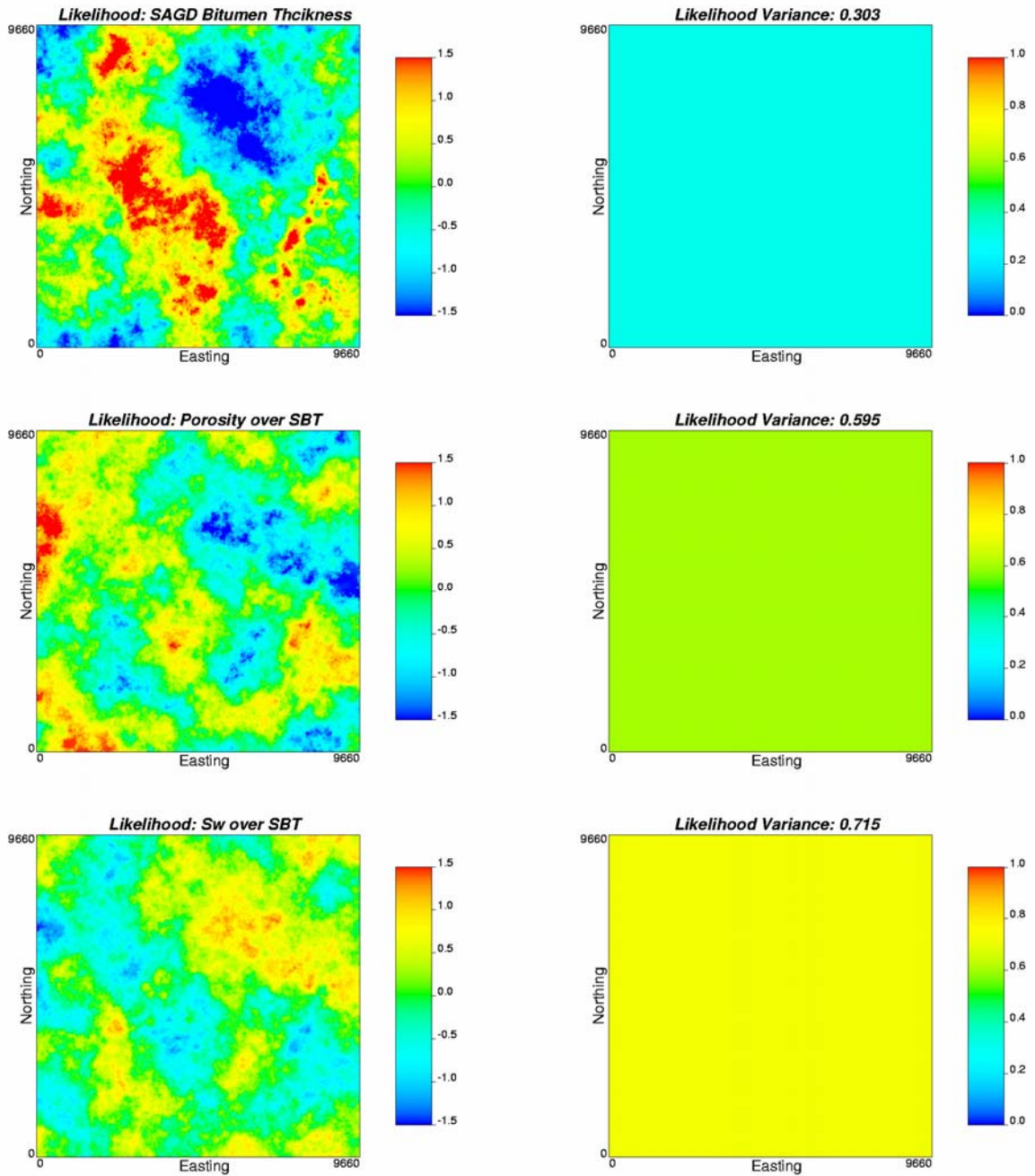


Figure 4-12: The likelihood maps of the primary variables from the global correlations. The left column is likelihood mean in Gaussian units and the right column is likelihood variance. The variances are constant over the model area.

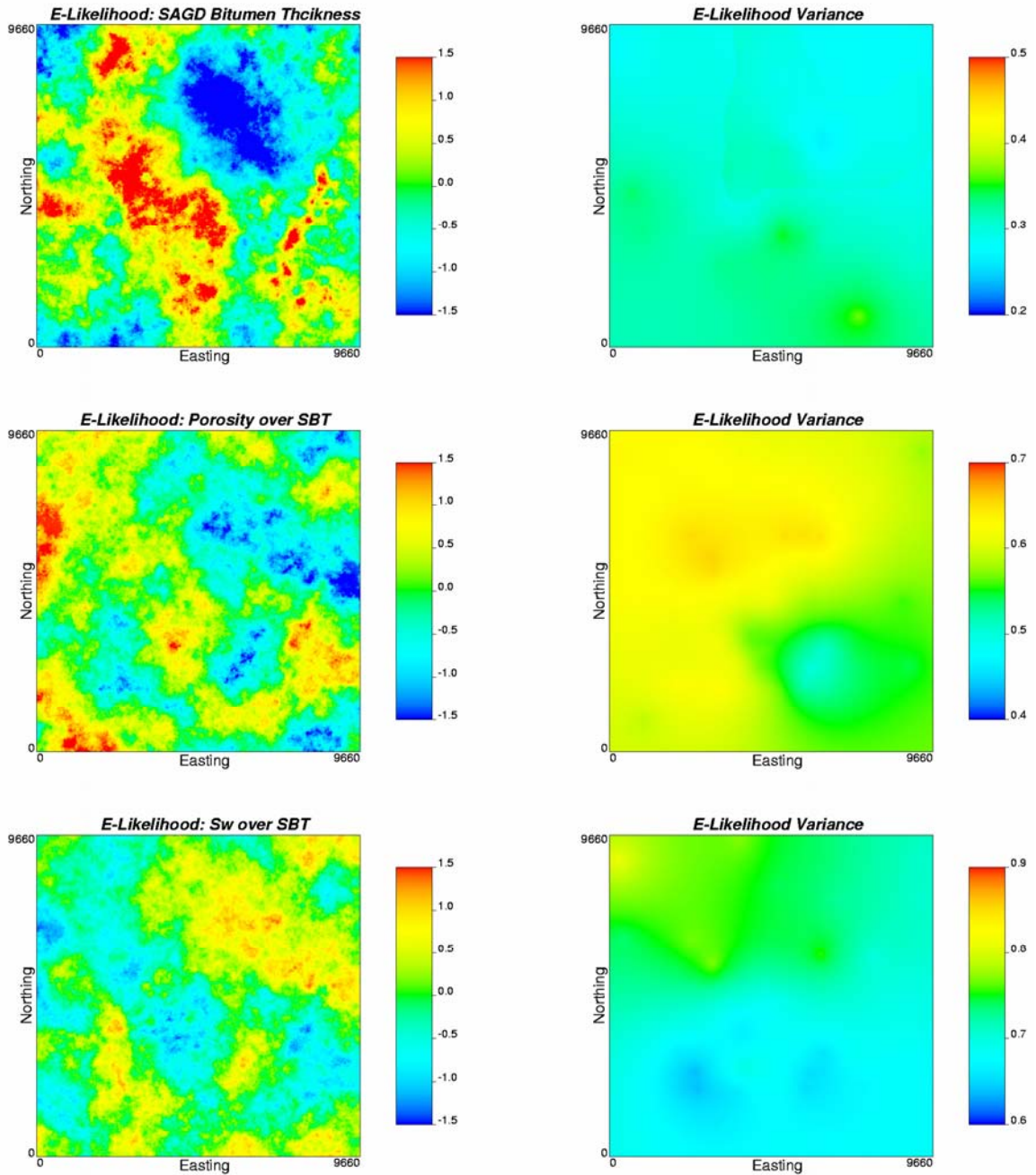


Figure 4-13: The likelihood maps of the primary variables from the locally varying correlations. The left column is likelihood mean in Gaussian units and the right column is likelihood variance. The variances are varying over the model area.

4.2.3. Updated models

Bayesian updating merges the prior models and likelihood models to generate updated models. The resulting model accounts for both primary and secondary information. The distribution of uncertainty is defined at each location in the form of a

non-standard normal distribution given by the updated mean and variance. The updated maps of primary variables using the Bayesian updating method are shown in Figure 4-14, given by the updated mean and variance in Gaussian units. The results using the enhanced Bayesian updating method are shown in Figure 4-15. The differences between the two results are very small so that they look very similar at this colour scale.

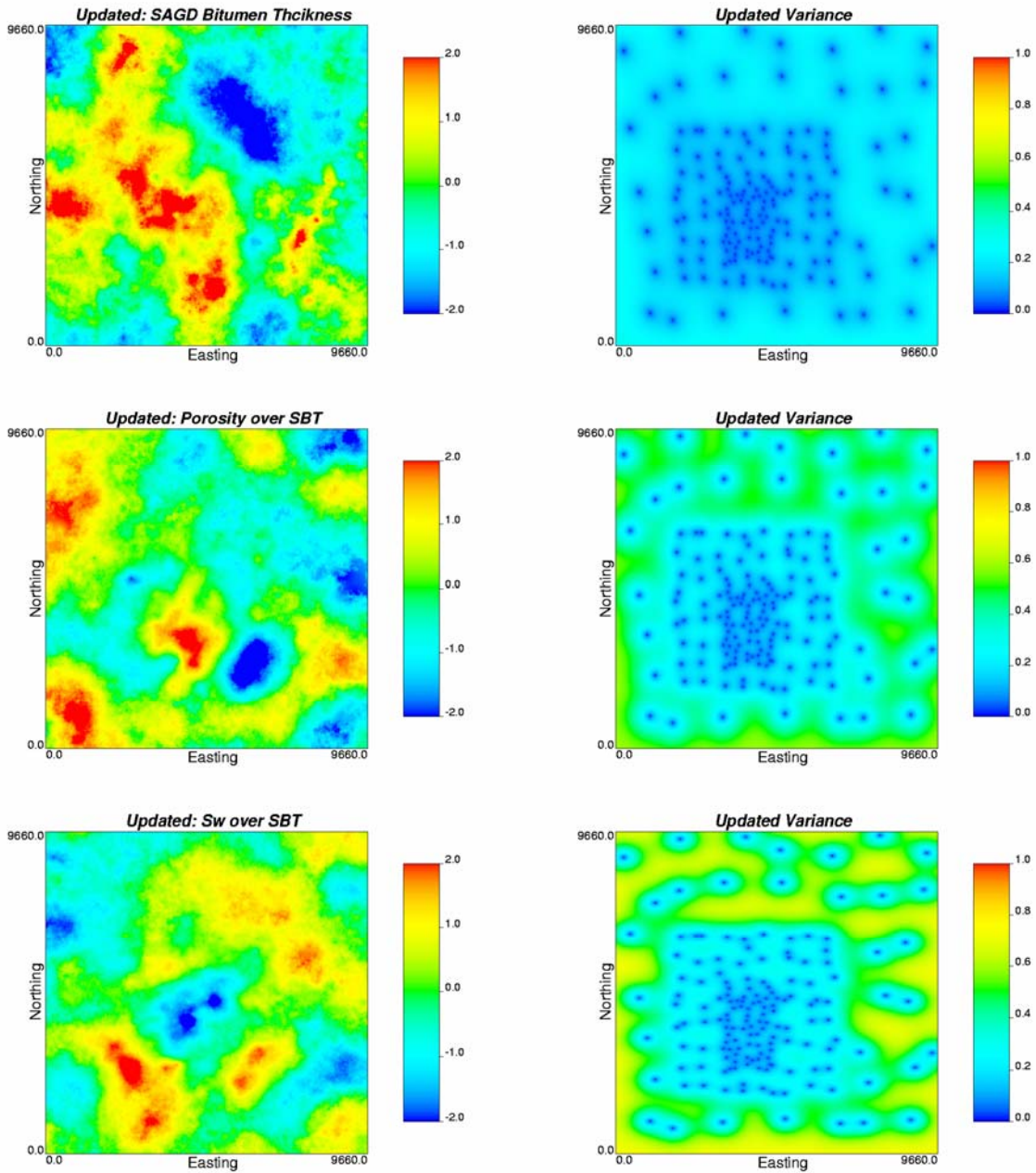


Figure 4-14: The updated maps of the primary variables from Bayesian updating method. The left column is updated mean in Gaussian units and the right column is updated variance.

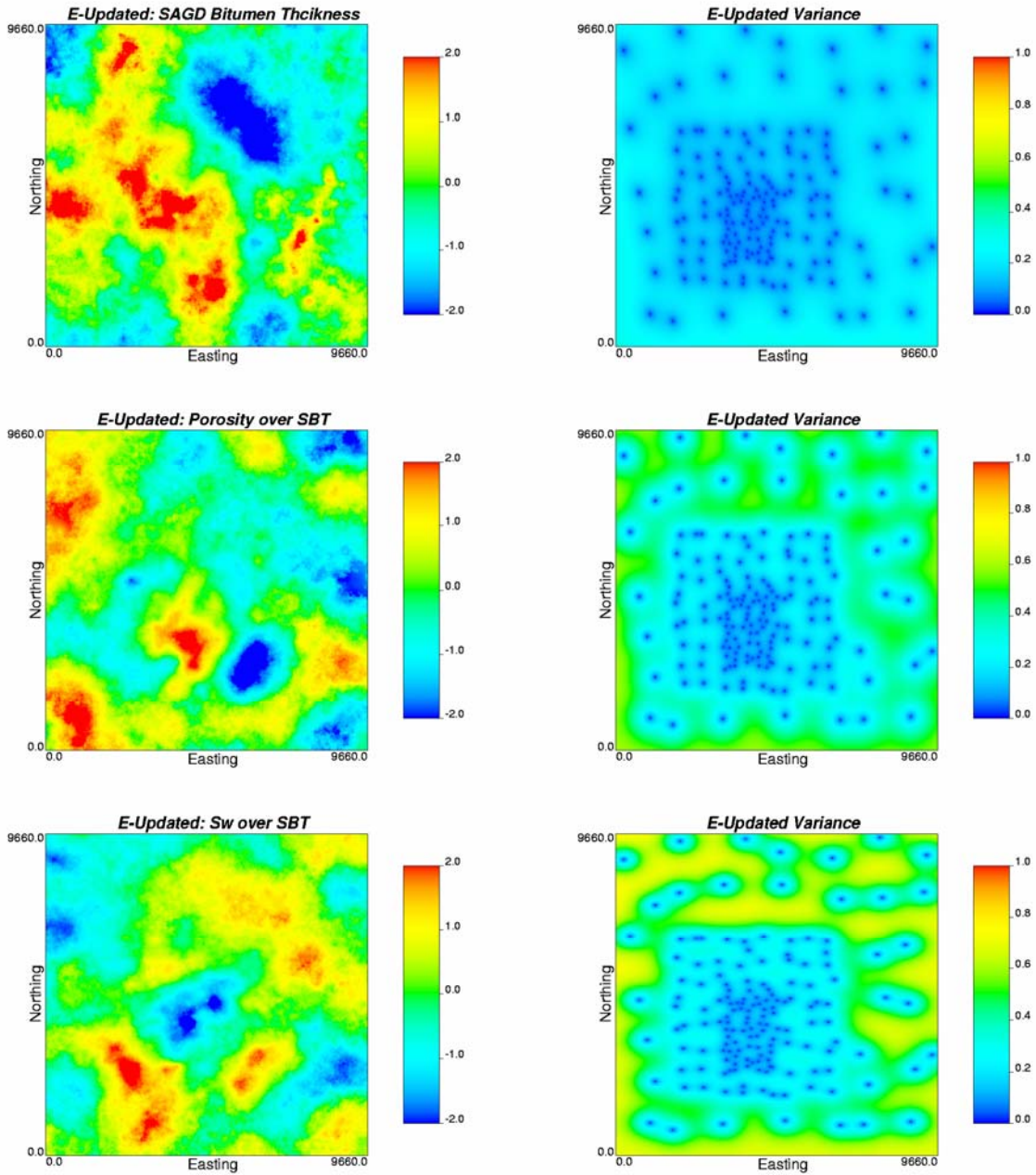


Figure 4-15: The updated maps of the primary variables from enhanced Bayesian updating method. The left column is updated mean in Gaussian units and the right column is updated variance.

The updated distributions must be back transformed to real units to show the uncertainty at each location. The back transformation of the non-standard normal distribution is accomplished using a large number of quantiles. The mean can not be back transformed directly; the back transformed value would be a biased estimate of the mean in real units because the transformation is non-linear. Quantiles can be back transformed with no bias.

4.2.4. Local uncertainty

It is common to summarize uncertainty with a set of maps that show the P_{10} , P_{50} and P_{90} values. The P_{10} values provide a conservative estimate since there is a 90% probability of being larger than this value. The P_{50} values correspond to the median estimate of the reservoir parameter at each location, and provide a measure of central tendency. The P_{90} values provide an optimistic estimate as there is a 90% probability of being less than this value. The map of local P_{10} values can be used to identify the high valued areas since the high P_{10} values reflect areas that are surely high. The map of local P_{90} values can be used to identify the low valued areas since the low P_{90} values reflect areas that are surely low.

The P_{10} , P_{50} and P_{90} maps for the primary variables from the Bayesian updating method are shown in Figure 4-16. The P_{10} , P_{50} and P_{90} maps from the enhanced Bayesian updating method are not shown because they are very similar to Figure 4-16. The yellow areas in the P_{10} map of SBT indicate where there is a 90% chance to have more than 55 meters. The P_{90} map of SBT shows there is a small area with 90% chance to be less than 10 meters. The P_{50} map shows the median value of the SBT in the model area.

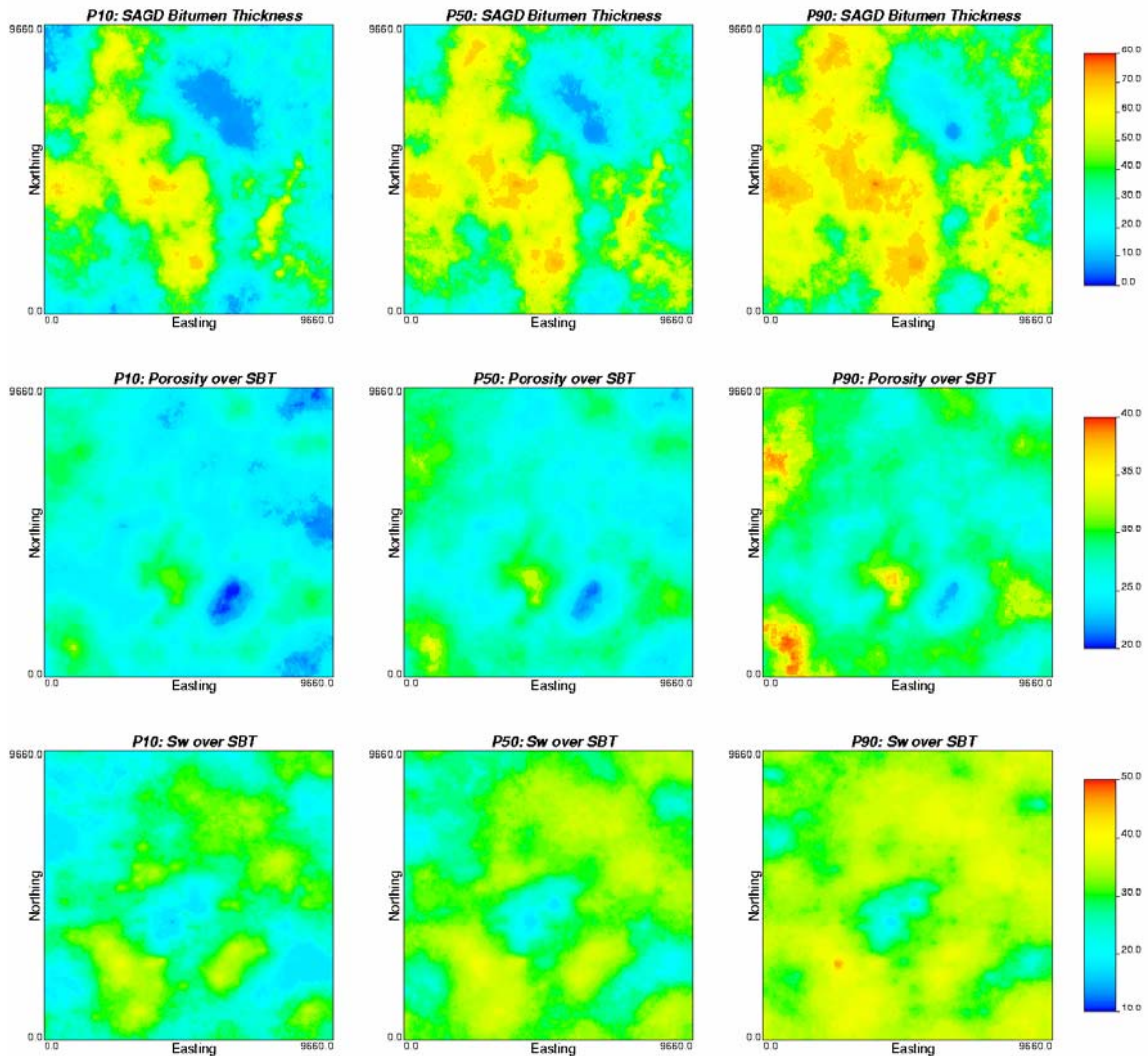


Figure 4-16: The $P_{10}/P_{50}/P_{90}$ maps of SBT in meters (top), porosity (middle) and water saturation (bottom) are in percentage.

4.3. Model Validation

Reservoir modeling consists of many interdependent modeling steps with many opportunities for mistakes or unreasonable use of erroneous data. It is impossible to completely validate models; however, there are some basic checks that can be used to identify problem data or errors in the geostatistical modeling. Cross validation is used to estimate the variables at locations where we know the true value. The actual data are deleted one at a time and re-estimated from the remaining neighbouring wells. Then, we

can check the accuracy of the estimation and the predicted distributions of uncertainty to evaluate the *goodness* of modeling parameters.

The accuracy of the estimation can be checked by the cross plots of the well data versus the estimates from cross validation. For Bayesian updating techniques, the prior, likelihood and updated results versus the true data can be used to check each step. The mean and standard deviation of the estimates should be close to the mean and standard deviation of true data. The updated results should be the best. The correlation between the updated means and true values is expected to improve if the secondary information is useful. The cross plots together with the histograms of SBT, porosity and water saturation from Bayesian updating are shown in Figures 4-17 to 4-19. The data are all in Gaussian units. The histograms of the updated means are closer to the histograms of true data than the histograms of prior and likelihood means. The standard deviations of the updated means are all very close to the standard deviation of the true data. The maximum and minimum values are improved. It indicates that the secondary information adds variation in the updated means. The correlations between the updated means and true values are all improved. The cross plots together with the histograms of SBT, porosity and water saturation from enhanced Bayesian updating are shown in Figures 4-20 to 4-22. The correlations between the updated means and true values are higher than the Bayesian updated results.

An accuracy plot is used to check the *goodness* of the uncertainty model. It shows the percentage of true data falling in symmetric probability intervals. The width of symmetric probability intervals is plotted on the abscissa axis. The fraction of true values within the interval is plotted on the ordinate axis. If the points fall on the 45° line, the uncertainty distributions are appropriate. If above the line, the uncertainty distributions are too wide. If below the line, the uncertainty distributions are too narrow. The accuracy plots of cross validation of Bayesian updating results for the primary variables are shown in Figure 4-23, and the accuracy plots for enhanced Bayesian updating results are shown in Figure 4-24. The uncertainty distributions of SBT are slightly too narrow. The uncertainty from the enhanced Bayesian updating is slightly better than Bayesian updating results for SBT. The porosity and water saturation are close to the 45° line.

Good cross validation results do not necessary mean the model is good. It is important to check the models with additional data (new wells) if available. The cross plots and accuracy plots using new data can be plotted to check the estimates and the uncertainty models.

If satisfied with the model validation results, we can use the local uncertainty results to assess global uncertainty over the entire area, which is addressed in the next chapter. We can also use them to generate simulation realizations using the P-field simulation approach that described in Section 3.3. Then, the simulation realizations will be used to construct the fine scale 3-D models using the exact downscaling techniques, which will be addressed in Chapters 7 and 8.

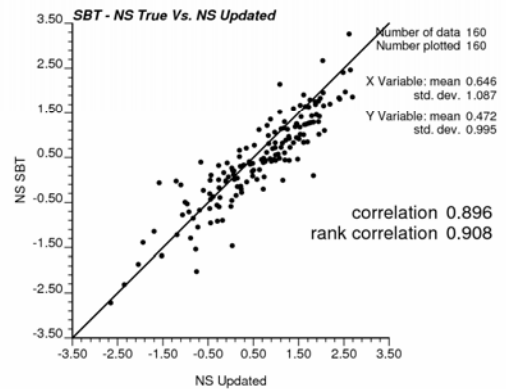
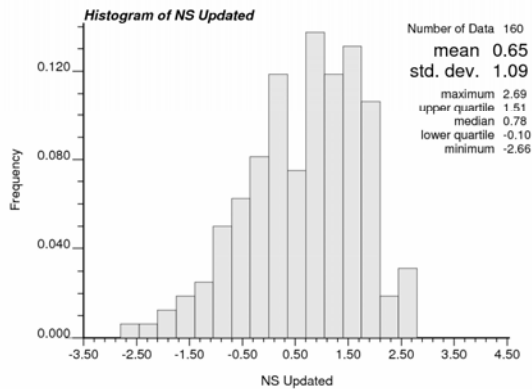
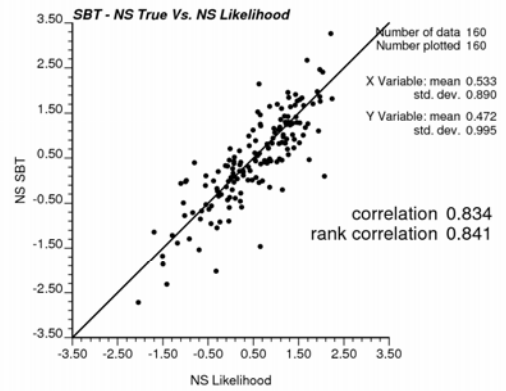
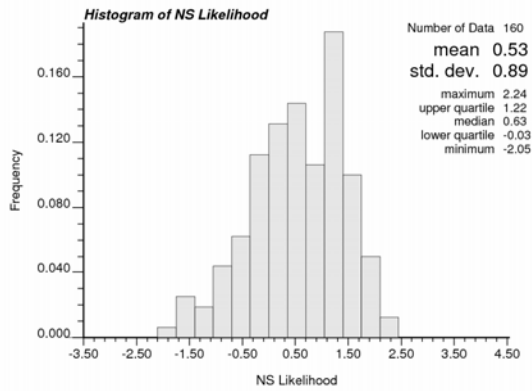
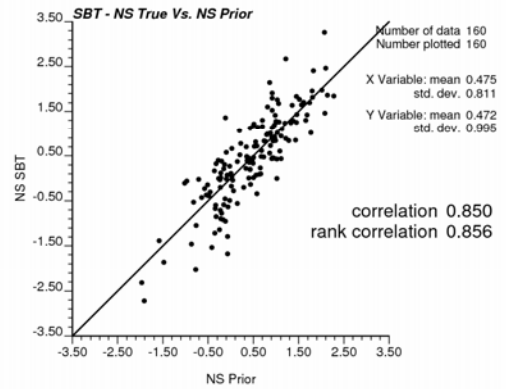
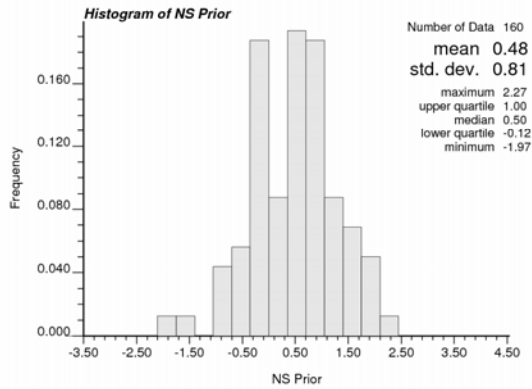
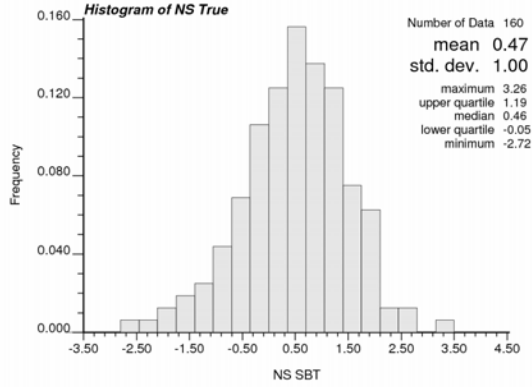


Figure 4-17: The cross validation of Bayesian updating results for SBT in Gaussian units.

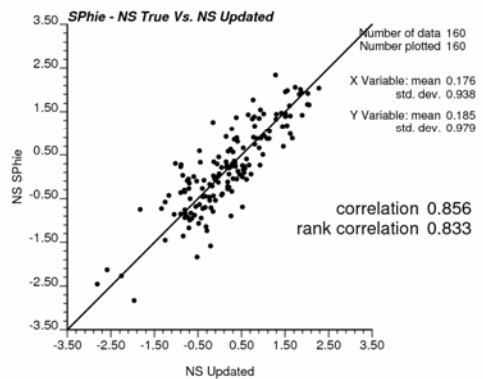
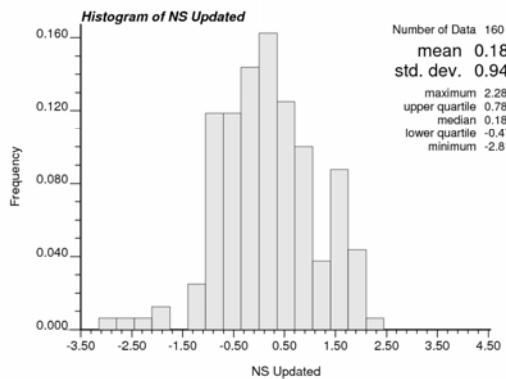
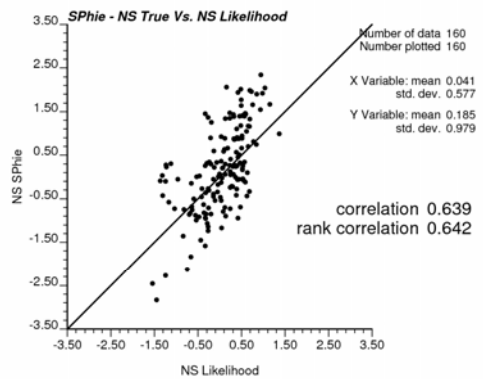
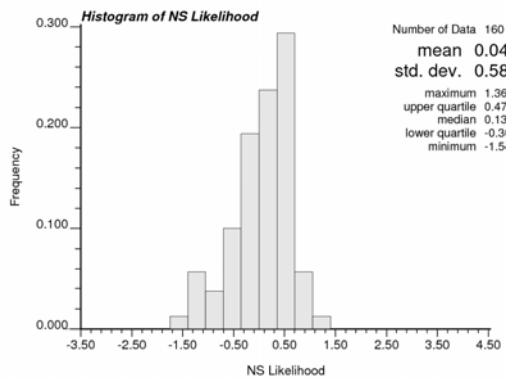
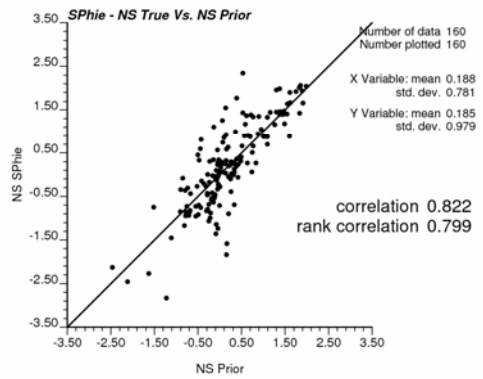
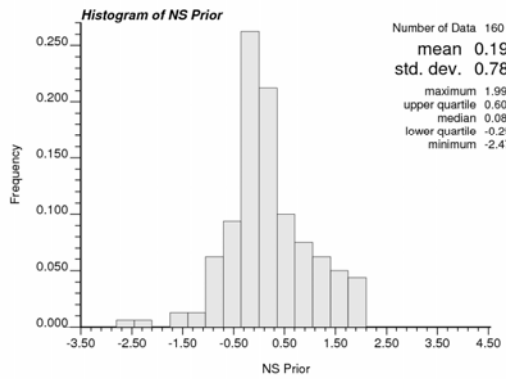
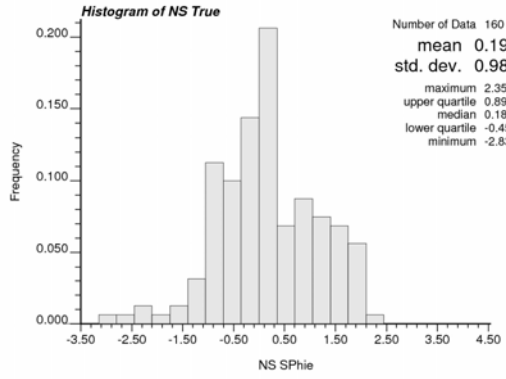


Figure 4-18: The cross validation of Bayesian updating results for porosity in Gaussian units.

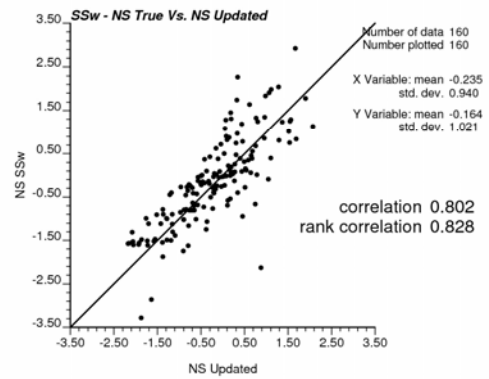
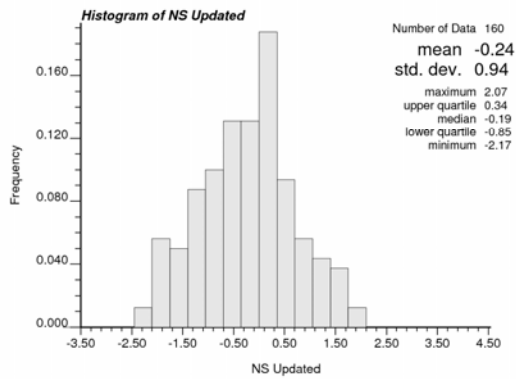
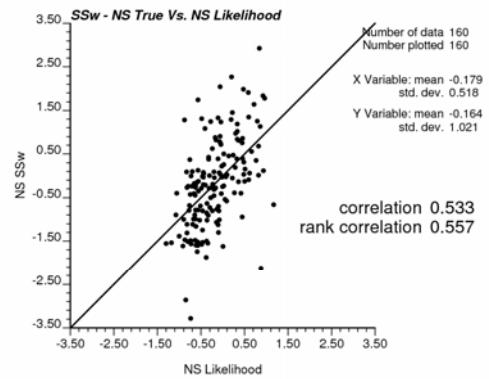
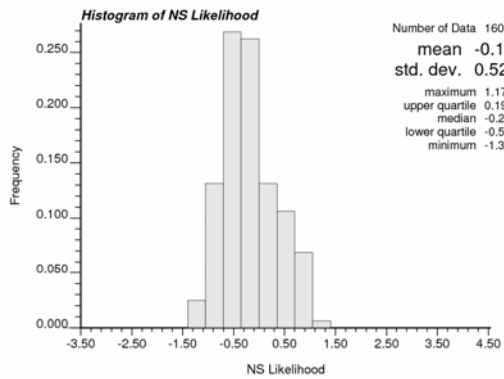
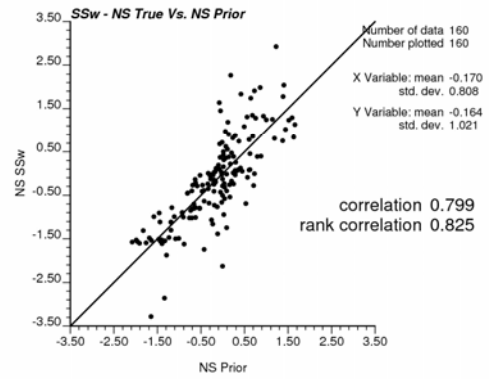
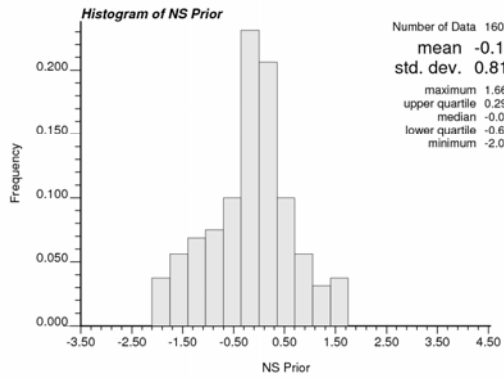
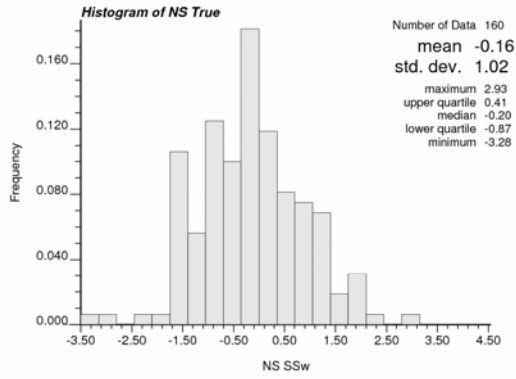


Figure 4-19: The cross validation of Bayesian updating results for water saturation in Gaussian units.

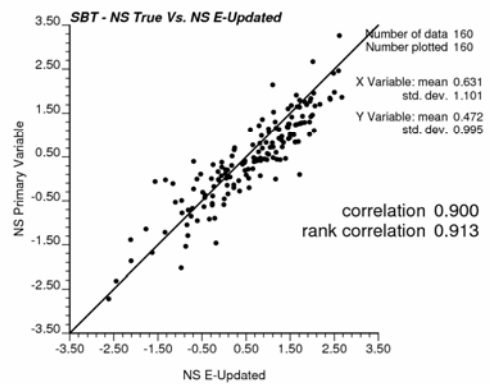
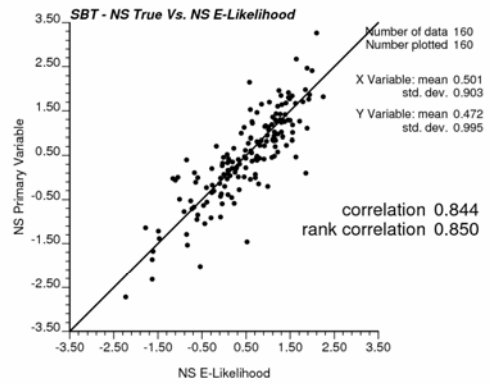
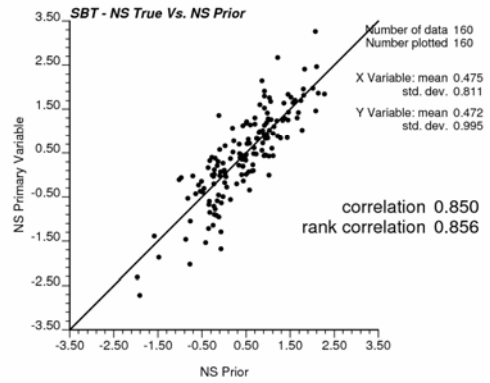
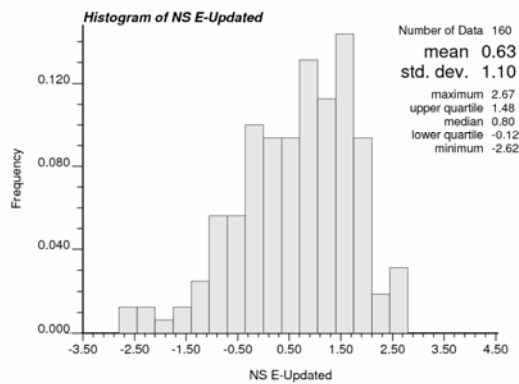
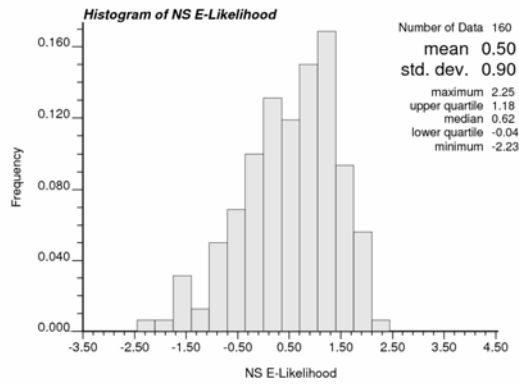
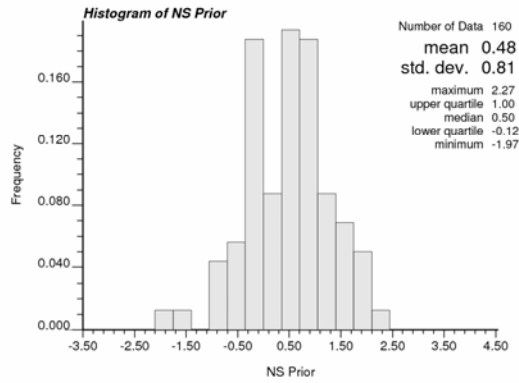
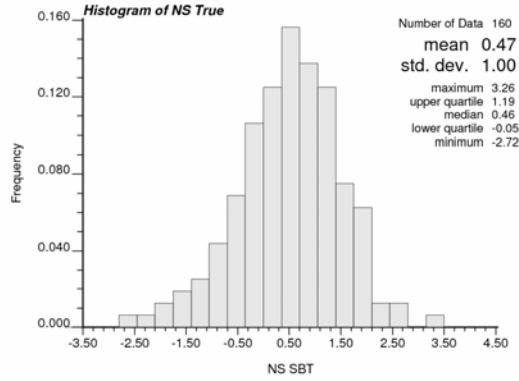


Figure 4-20: The cross validation of enhanced Bayesian updating results for SBT in Gaussian units.

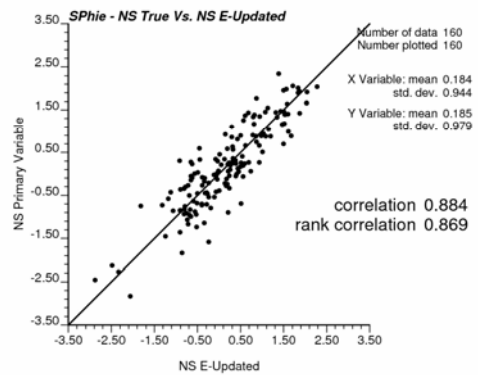
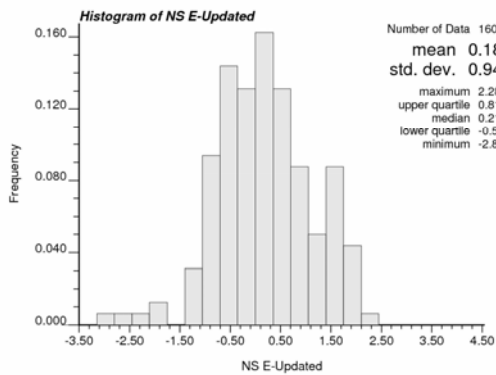
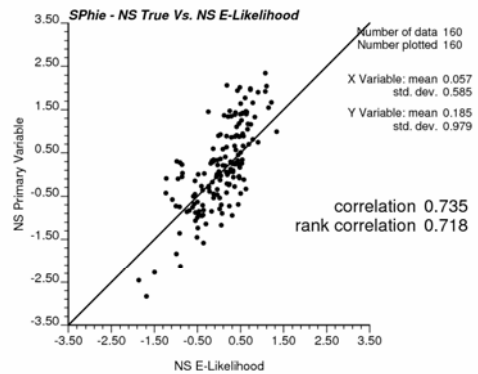
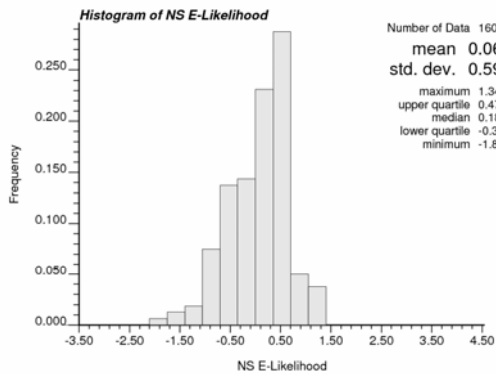
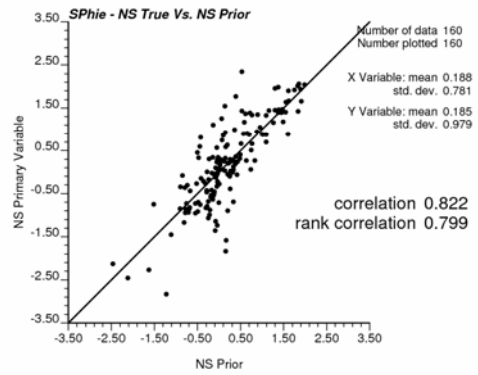
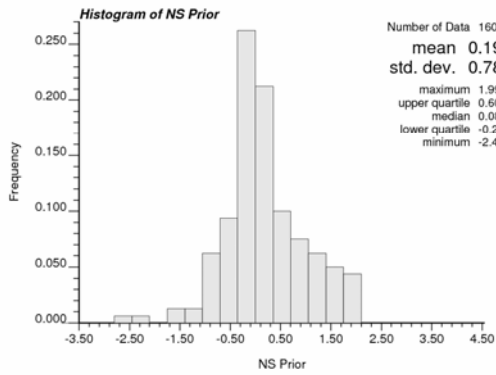
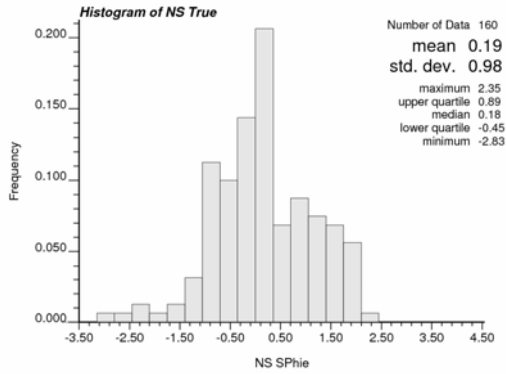


Figure 4-21: The cross validation of enhanced Bayesian updating results for porosity in Gaussian units.

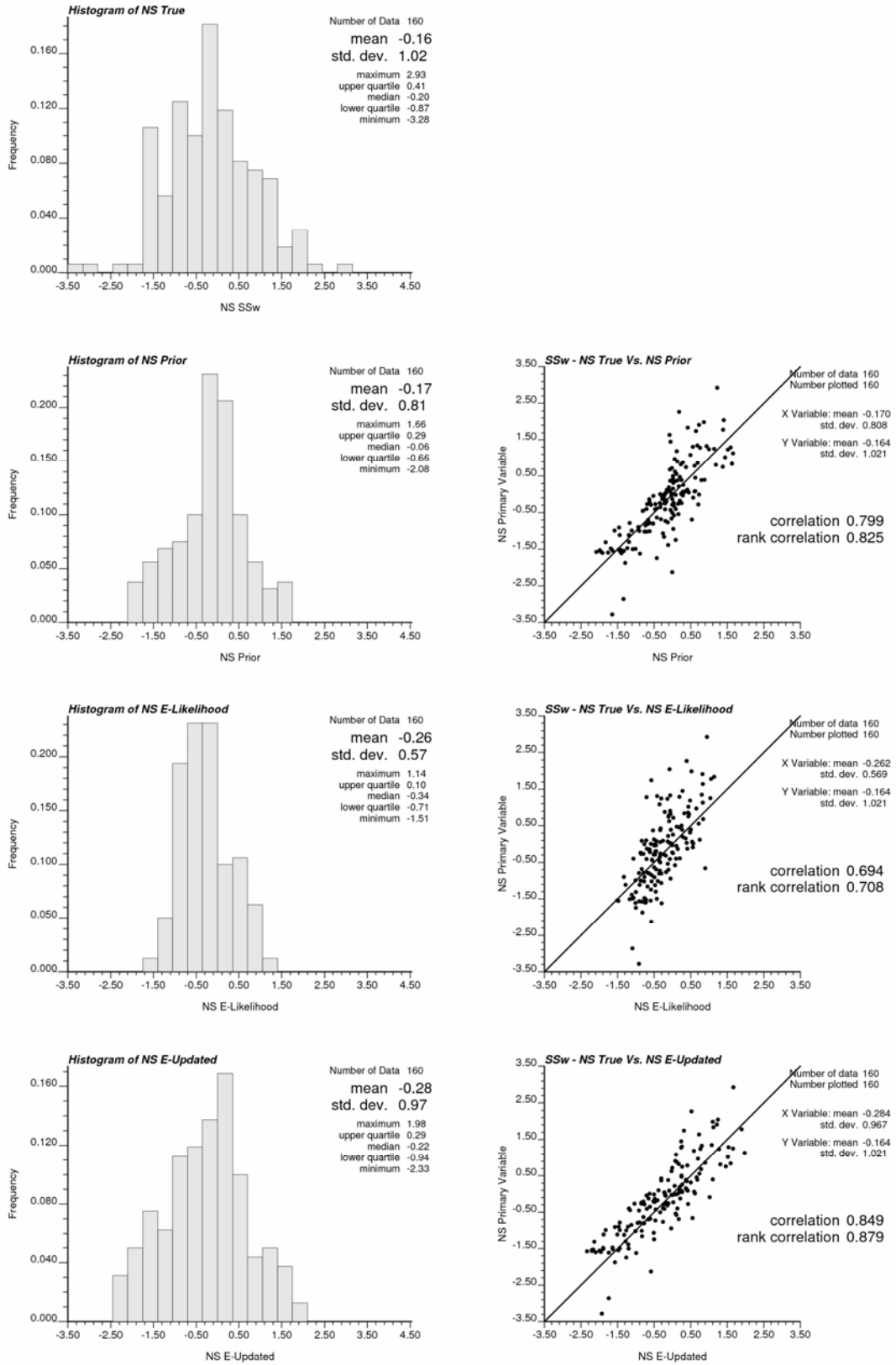


Figure 4-22: The cross validation of enhanced Bayesian updating results for water saturation in Gaussian units.

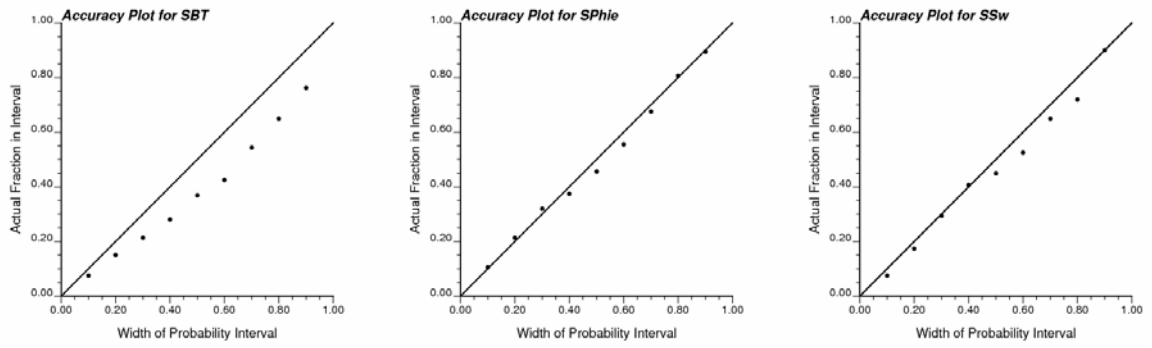


Figure 4-23: The accuracy plots of the SBT (left), porosity (middle) and water saturation (right) from Bayesian updating method.

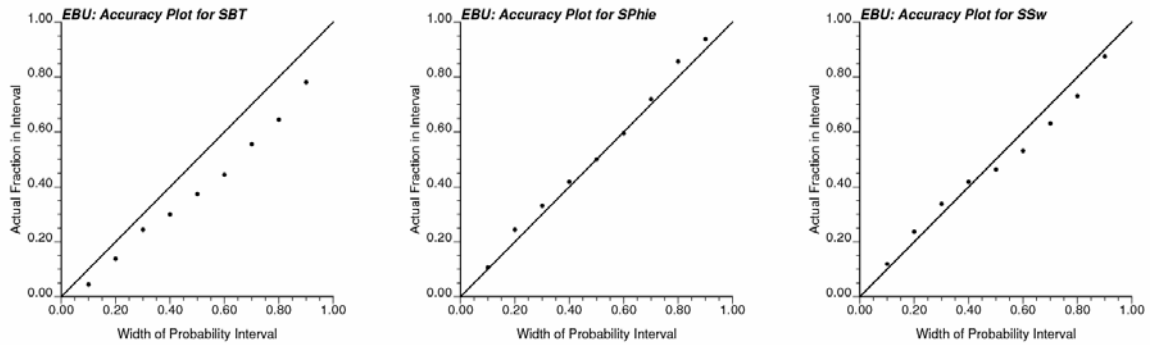


Figure 4-24: The accuracy plots of the SBT (left), porosity (middle) and water saturation (right) from enhanced Bayesian updating method.

CHAPTER 5

RESOURCE ESTIMATION

With limited data and geological information, there is always uncertainty in resource estimation. Assessing the uncertainty is important for reservoir management and decision making. The Bayesian updating techniques has been introduced in Chapter 3 to construct local uncertainty models of reservoir parameters. These local uncertainty models can be used to assess the uncertainty in petroleum resources over a large area; however, the upscaling of local uncertainties to global uncertainty is a challenge because both the spatial correlations between different locations and the multivariate correlations between the different variables that go into resource calculation must be accounted for.

Petroleum resources are calculated from several reservoir parameters. For example, the Original Oil In Place (OOIP), which is a function of three variables:

$$\text{OOIP} = A \times \text{NP} \times \phi \times (1 - S_w) \quad (5-1)$$

where A is a constant that calculated from the area of model cell, oil formation volume factor and unit converter, NP is the Net Pay thickness, and the other two variables are porosity (ϕ) and water saturation (S_w). The three variables may be correlated. When the porosity is low, the oil saturation is also often low. Treating the variables independently will lead to underestimation of the uncertainty in OOIP: high values average out with low values. The correlations between these variables must be accounted for in the resource estimation. For the resources over a large area, local uncertainty cannot simply be summed to obtain the joint uncertainty at larger scales; the spatial correlation must also be considered. Assessment of global uncertainty over a large area requires a simulation method to combine all the local uncertainties and correlations between multiple variables accounting for spatial correlation. A spatial/multivariate simulation approach is introduced for this purpose. Global uncertainty is consistent with the local uncertainty

from the large scale models. Methodology and implementation are presented in the chapter.

5.1. Methodology of Global Uncertainty Assessment

The methodology of global uncertainty assessment will be presented in two steps: (1) the joint uncertainty at each location considering only the multivariate correlations; (2) the global uncertainty over a large area considering both multivariate and spatial correlations.

5.1.1. Local resource estimation and joint uncertainty

Assessment of local uncertainty in a derived variable (such as OOIP) requires simulation to combine the uncertainties in constituent variables. Accounting for the multivariate correlation can be achieved by applying LU simulation. LU simulation has been used for many years, but popularised in geostatistics by Alabert (1987). The conventional LU simulation is applied to simulate a single variable using information from multiple locations. It is suitable when the locations are less than 5000. Here the LU simulation is used for assessing the uncertainty in a derived variable by jointly simulating multiple variables at the same location. Because the number of variables is relatively small (3 to 30) and working in a Multivariate Gaussian environment, the LU simulation is always applicable.

The implementation of the LU method to simulate multiple dependent variables is straightforward. The matrix of correlation coefficients is used instead of the spatial covariance matrix in the conventional implementation (GSLIB). The matrix of locally varying correlations could be used if the constituent variables are modeled using the enhanced Bayesian updating technique. The matrix C is decomposed by Cholesky decomposition: $C=LU$. The L is the lower matrix and the U is the upper matrix. A vector of uncorrelated standard normal values $\mathbf{w}(\mathbf{u})$ is generated by a random number generator, then the correlated values are calculated by:

$$\mathbf{Y}_{us}(\mathbf{u}) = \mathbf{L}\mathbf{w}(\mathbf{u}) \quad (5-2)$$

The unconditional simulated values y_{us} are standard Gaussian and have the correct correlation structure. Each value should follow the local conditional distribution of the corresponding variable. Therefore, the simulated value is calculated by non-standardizing with the local mean and variance:

$$y_s(\mathbf{u}) = y_{us}(\mathbf{u})\sigma_u(\mathbf{u}) + \bar{y}_u(\mathbf{u}) \quad (5-3)$$

The simulated realizations of non-standard values $y_s(\mathbf{u})$ can be back transformed to original units and calculate the derived variable.

Figure 5-1 and Table 5-1 show the multivariate LU simulation for OOIP in a single cell. The local uncertainties of the Net Pay thickness (NP), porosity (ϕ) and Water saturation (S_w) are modeled from Bayesian updating. The correlation matrix of the three variables is used for LU simulation. Multiple realizations (say 100) of the three variables are drawn using LU simulation accounting for the correlation between the variables (yellow shaded squares in Table 5-1). Then, the OOIP is calculated with each set of numbers. The local estimate and uncertainty in the OOIP (or any other derived property) can be assembled from the realizations; a histogram of the final OOIP values is created.

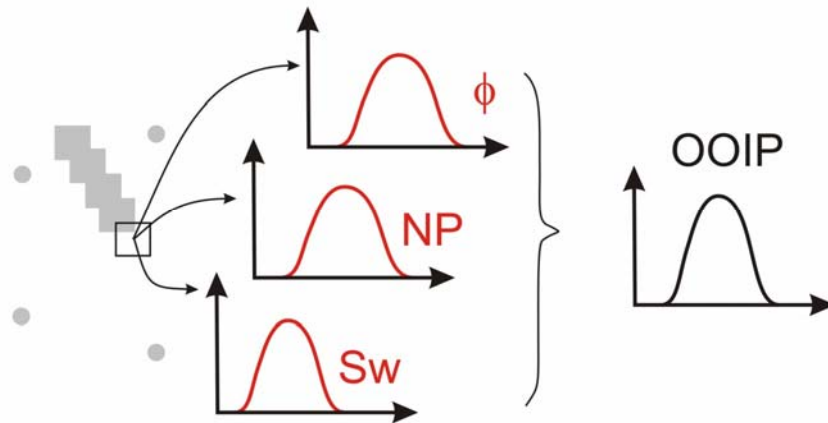


Figure 5-1: A schematic illustration of joint uncertainty of OOIP from local uncertainty models of constituent variables. The square with black line is the estimated location.

Realization Number	NP	ϕ	Sw	Calculated Local OOIP
1	10	0.30	0.25	1600 bbl
2	9	0.28	0.22	1300 bbl
...
100	11	0.27	0.23	1550 bbl

Table 5-1: A tabulated illustration of joint uncertainty calculation for local OOIP in barrels.

5.1.2. Resource estimation and global uncertainty

There is often interest in resource estimation over a large area such as a lease boundary or pad location. The global uncertainty in such estimation cannot be calculated by simply summing the local uncertainties. The spatial continuity of the variables must be considered. If the variables are very discontinuous, then the uncertainty decreases quickly with scale. If the variable is continuous, then the uncertainty decreases slowly, but fewer data are needed to constrain the uncertainty. Therefore, to estimate the resource over a large area and to assess the global uncertainty, we must account for the spatial correlation over the area of interest as well as the multivariate correlation between variables.

A full cosimulation approach could be used to assess the global uncertainty; however, this is cumbersome to implement because of the complicated cross-variograms calculation and expensive computing time.

A spatial/multivariate simulation approach is proposed for assessing the global uncertainty from the local uncertainties that has been described in Chapter 3. This approach is based on the P-field simulation technique (Srivastava, 1992) combined with the LU simulation presented in the previous section. Assessing global uncertainty over a large area requires drawing values of each variable simultaneously over many grid nodes. There is correlation between the different variables and spatial correlation between the locations of interest. The LU simulation method could also be used to model this joint multivariate and spatial correlation; however, the number of variables and locations quickly becomes large and computationally expensive. For this reason, the P-field-like simulation technique is used to account for the spatial correlation. The P-field simulation

is combined with the LU simulation to perform the spatial/multivariate simulation. Most common geostatistical assumptions also apply to this approach, such as assuming that the data are representative, and the statistical properties of the data are the same over the entire model area. An assumption of multivariate Gaussianity is critical for this approach.

The spatial/multivariate simulation for global uncertainty assessment consists of the following steps:

1. Build the local conditional distributions with the updated mean and variance for each variable.

2. Generate a set of standard normal values that are spatially correlated for each variable: $\{w_i(\mathbf{u}), \mathbf{u} \in A\}$, $i = 1, 2, \dots, n$

where \mathbf{u} is a location vector in the field A , and $w_i(\mathbf{u})$ is the standard normal value for the i^{th} variable at location \mathbf{u} .

3. Determine the global or local correlation matrix, $\boldsymbol{\rho}$, for the n variables and perform Cholesky decomposition: $\boldsymbol{\rho} = \mathbf{L}\mathbf{U} = \mathbf{L}\mathbf{L}^T$.

4. Obtain the multivariate correlated standard normal values of n variables:

$$\mathbf{Y}_{us}(\mathbf{u}) = \mathbf{L}\mathbf{w}(\mathbf{u})$$

where $\mathbf{Y}_{us}(\mathbf{u})$ is the vector of the multivariate correlated normal deviates at location \mathbf{u} . and $\mathbf{w}(\mathbf{u})$ is the vector of the standard normal values from step (2).

5. Obtain the conditional simulated values:

$$y_{si}(\mathbf{u}) = y_{usi}(\mathbf{u})\sigma_i(\mathbf{u}) + \bar{y}_i(\mathbf{u})$$

where σ_i and \bar{y}_i are the updated standard deviation and mean, respectively, for the i^{th} variable.

6. Back transform the simulated values to real units, and assemble the distribution of uncertainty over any volume using the joint spatial/multivariate realizations.

A schematic illustration of the spatial/multivariate simulation work flow is shown in Figure 5-2. Virtually all of this work must be performed in Gaussian space; this requires that all the data (primary and secondary) must first be transformed into normal scores.

Step 1 of the methodology can be achieved by Bayesian updating to generate local distributions of uncertainty. Step 2 requires running unconditional simulations using sequential Gaussian simulation with the appropriate variograms. These variograms are calculated based on the normal scores of each data. Use of the variogram ensures that the set of normal deviates for each variable is spatially correlated. Steps 4 and 5 can be implemented together; the simulation generates the spatial and multivariate correlated simulation values in Gaussian units. Finally, these simulated values are back transformed to original units. OOIP can now be determined from the n simulated values at each location. Summing them over any area of interest gives a simulated value of the global resource. With multiple realizations, we can assess the global uncertainty over any area of interest.

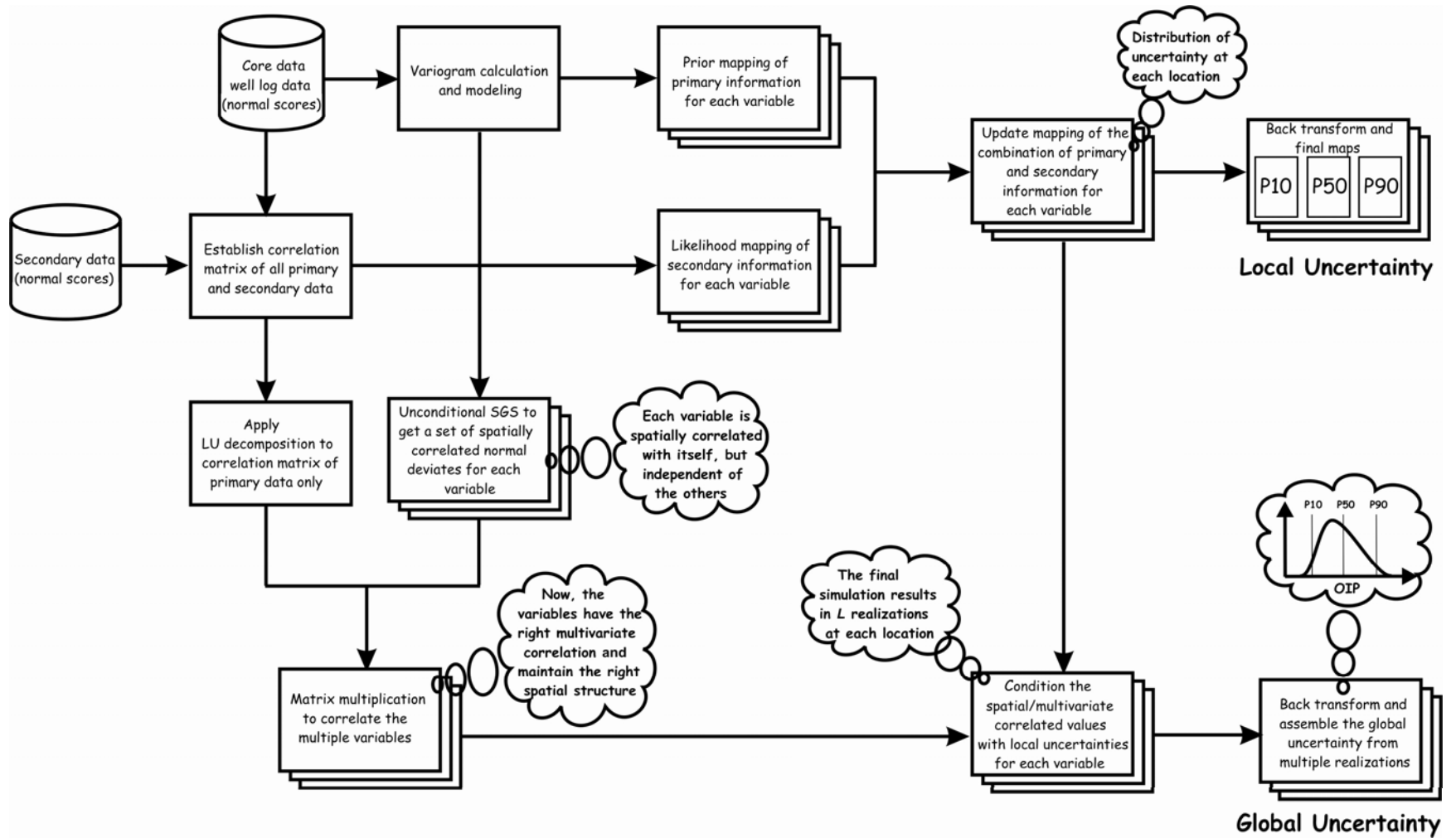


Figure 5-2: Work flow of the spatial/multivariate simulation approach for assessment of global uncertainty from local uncertainty.

5.2. Example

This approach has been applied on real reservoirs (Ren *et al.*, 2005a). This synthetic example was created to demonstrate the entire process from modeling local uncertainties to assessing global uncertainty.

In this example, the global uncertainty is for the OOIP over a study area, which is about 4 sections (each section is 1 mi²): 3200m x 3200m. The OOIP is calculated using Equation 5-1, and A is the local area of 20m x 20m. For simplification, let us consider ϕS_o as one variable.

64 well data are available at a spacing of 400 m. The well locations and the histograms of NP and ϕS_o are shown in Figure 5-3. To assess the local uncertainties of the two variables, we also have three secondary variables available (Figure 5-4): three sequence boundaries (1 to 3) from seismic data and geological interpretation.

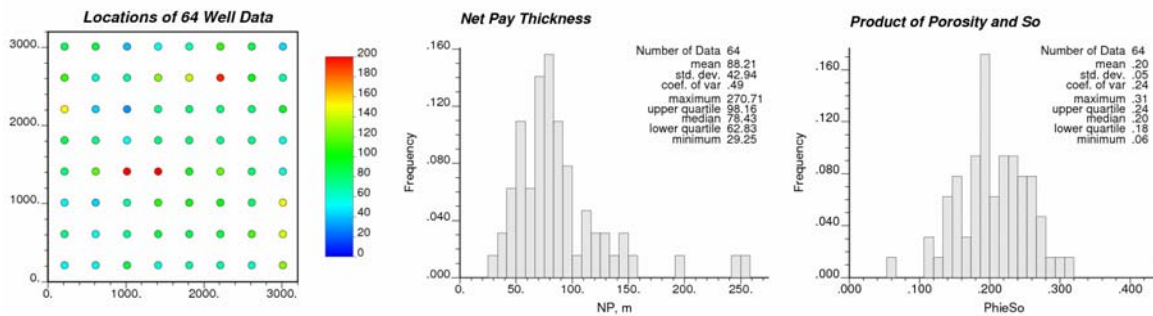


Figure 5-3: The location map of the 64 wells with the colour scale showing the net pay thickness in meters (left), and histograms of Net Pay thickness in meters (centre) and ϕS_o in fraction (right).

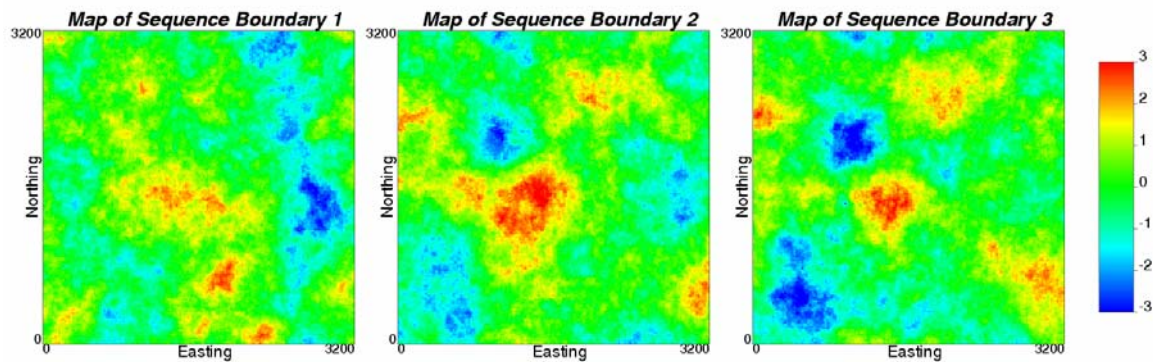


Figure 5-4: Maps of three secondary variables in Gaussian unit: sequence boundary 1 (left), sequence boundary 2 (centre) and sequence boundary 3 (right).

The correlations between each primary variable and each secondary variable are summarized in the correlation matrix in Figure 5-5. The variograms of the two primary variables, NP and ϕS_o , are also shown in Figure 5-5. The prior, likelihood and updated maps are shown in Figure 5-6. The prior maps only show the primary information from well data. The likelihood maps show the secondary information based on a combination of all secondary data. The updated maps show the combination of the primary and secondary information. After transforming the updated results back to real units, the P10, P50, P90 quantiles were plotted to show the uncertainties in NP and ϕS_o (Figure 5-7). An east-west cross-section for each quantile map was extracted and plotted together to show the uncertainty of NP thickness in 1-D (Figure 5-8). It is interesting to see that the P10 and P90 curves are not symmetric at P50. The uncertainty is varying at different locations and is zero at well locations. The P10 values are high around 1600 m so that the NP is most likely to be high. The P90 values are low between 800 m and 900 m, the NP is most likely to be low over there.

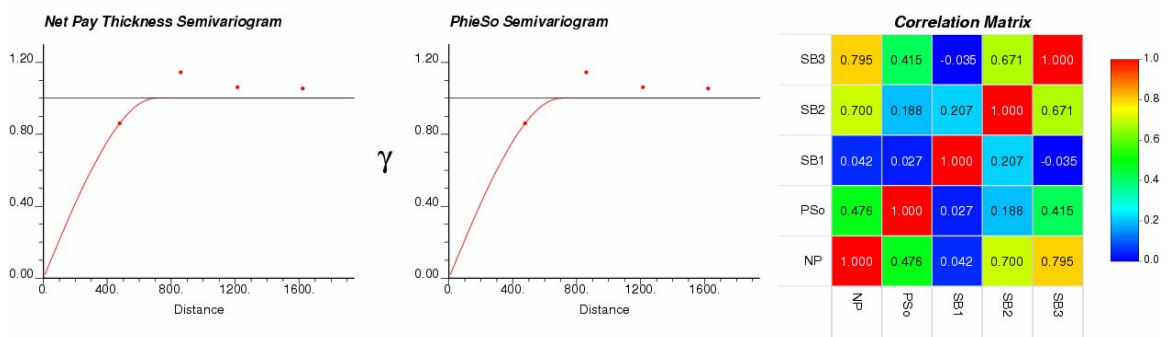


Figure 5-5: Variogram for two primary data (left and centre) and the correlation matrix between the primary and secondary variables (right).

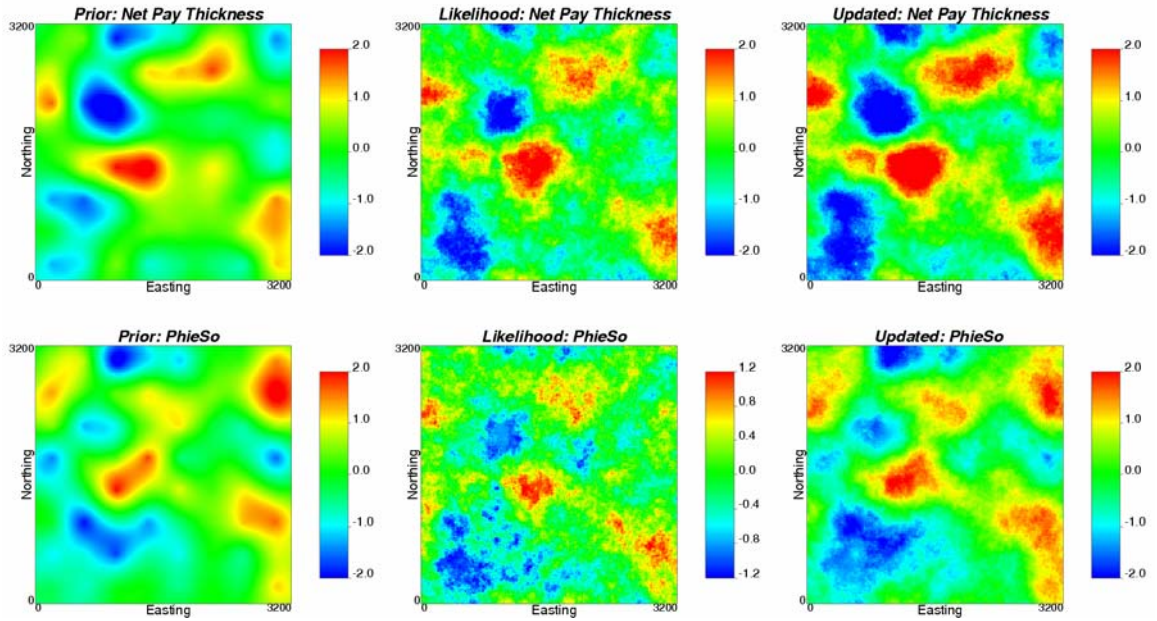


Figure 5-6: Prior (left), likelihood (centre) and updated (right) maps for NP (top) and ϕS_o (bottom) in Gaussian unit.

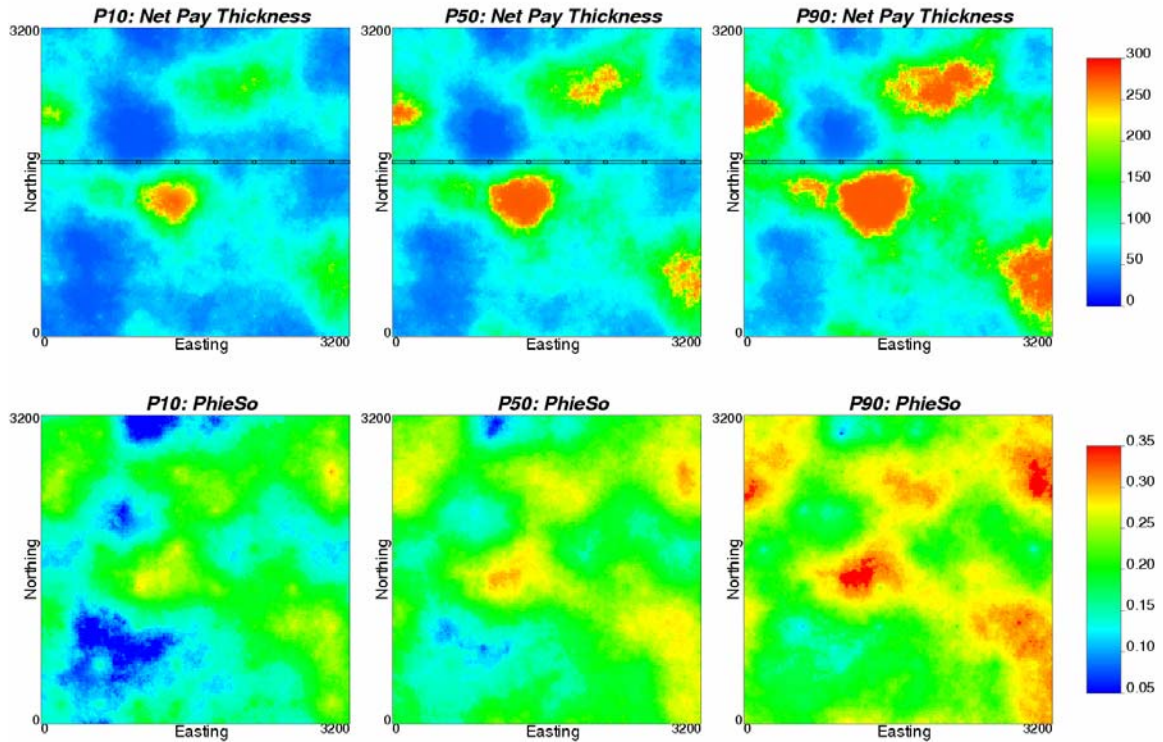


Figure 5-7: Final maps of uncertainty for Net Pay thickness in meters (top row) and ϕS_o in fraction (bottom row): P10 (left), P50 (centre) and P90 (right). Note the east-west section lines in the Net Pay thickness final maps are plotted in Figure 5-8, and the black circles represent well locations.

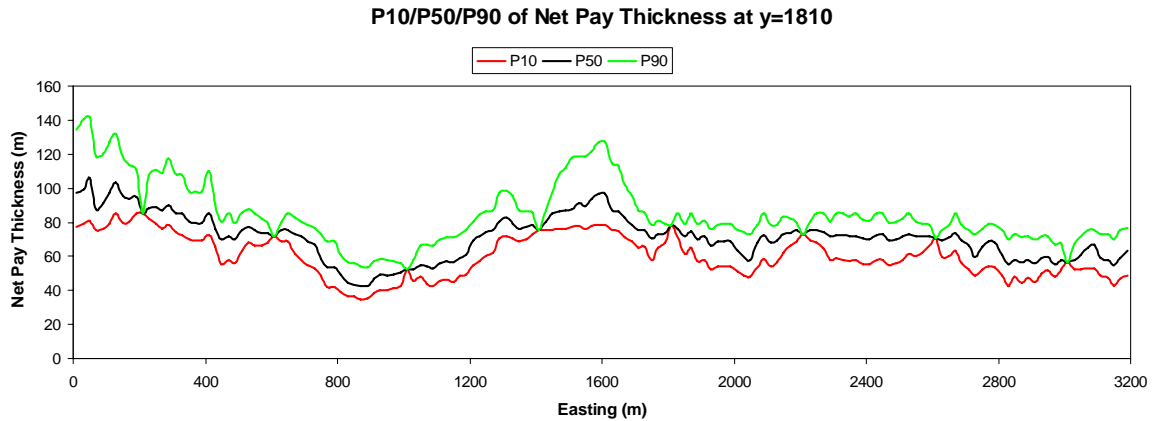


Figure 5-8: Uncertainty of Net Pay thickness in an east-west section: P10 (bottom line), P50 (middle line), and P90 (top line). The location of $y=1810\text{m}$ is shown in the top row of Figure 5-7.

Using the local uncertainties from the updated models, the spatial/multivariate decomposition simulation approach was used to generate 100 realizations. Realizations 5, 50 and 95 are arbitrarily chosen for illustration in Figure 5-9. In each realization, all values are spatially correlated over the model area. At each location, the two variables, NP and ϕS_o are statistically correlated and were used to calculate the OOIP at that location (Figure 5-10). Two areas of interest and the whole model area were selected to assess the OOIP (values are posted below the maps). Using the 100 realizations, we can assess the global uncertainties in OOIP in these three areas (Figure 5-11). These distributions of global uncertainty look similar to a normal distribution. The global uncertainty in area 1 shows a mean of 38.41 million cubic meters and a standard deviation of 4.17. The global uncertainty in area 2 shows a mean of 40.93 million cubic meters and a standard deviation of 4.93. Area 1 is smaller than area 2, but the OOIP mean and variance are very close. The global uncertainty in the whole model area shows a mean of 203.29 million cubic meters and a standard deviation of 10.23.

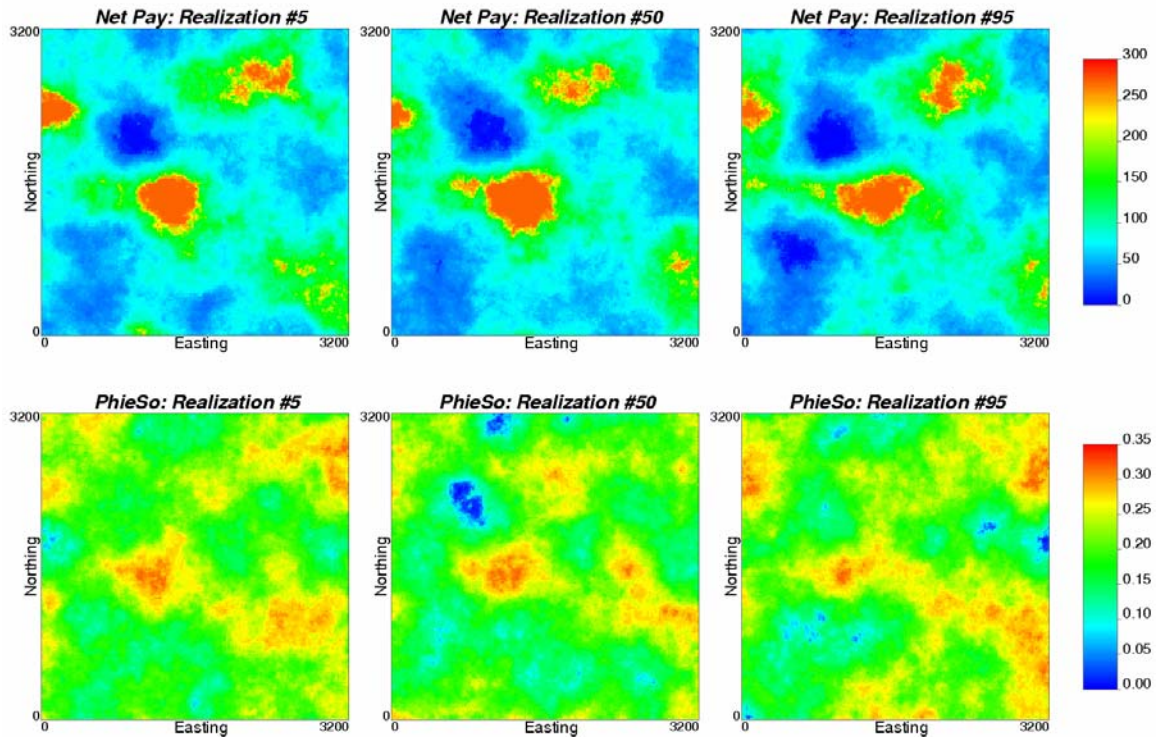


Figure 5-9: Realizations 5, 50 and 95 of the spatial/multivariate simulation. In each realization, all values are spatially correlated over the model area and the Net Pay thickness in meters (top row) and ϕS_o in fraction (bottom row) are also correlated.

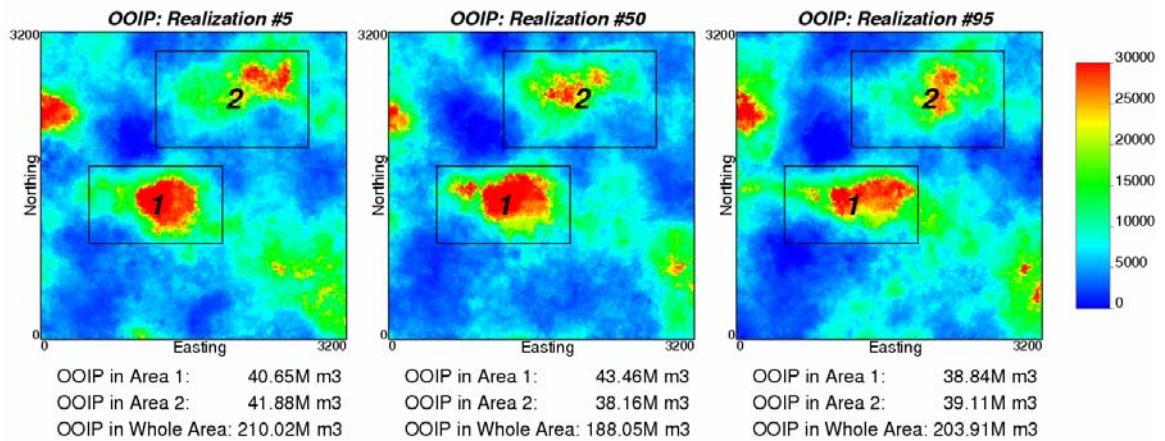


Figure 5-10: Calculated OOIP from the two variables shown in Figure 5-9. The colour scale shows the OOIP in cubic meters. Two areas of interest (in black box) and the whole model area were selected to estimate the global OOIP. The global OOIP in the three areas in million cubic meters are shown below the maps for each realization.

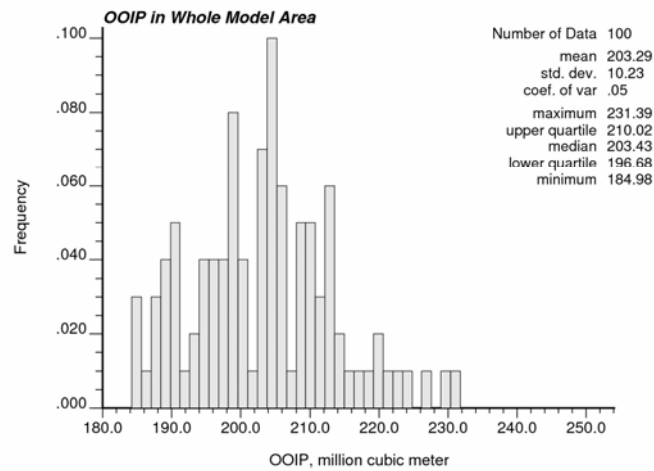
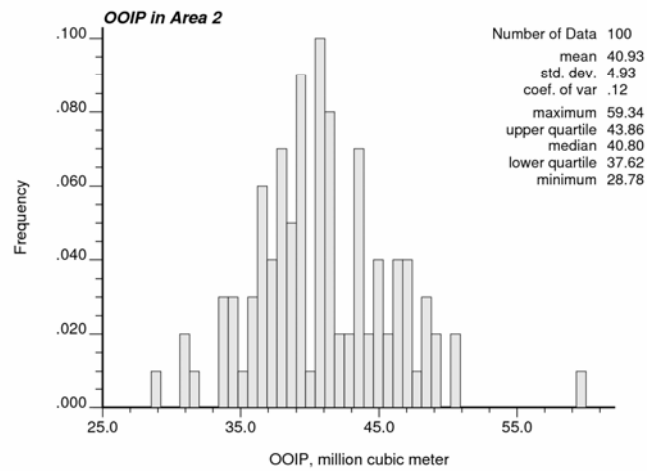
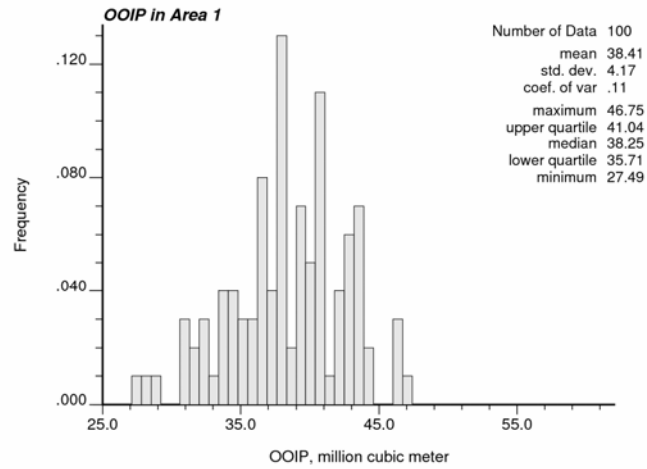


Figure 5-11: Global uncertainty distribution of the OOIP in the Area 1 (left), the Area 2 (centre), and the Whole Model Area (right).

CHAPTER 6

EXACT DOWNSCALING TECHNIQUES

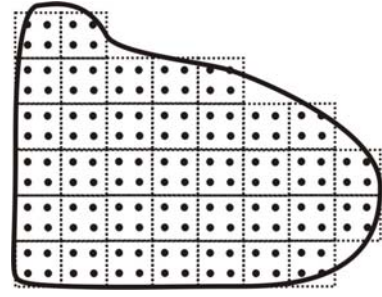
A major task of geostatistical modeling is to build reservoir models of petrophysical properties for reservoir flow simulation. When the target is the entire reservoir, upscaling of geostatistical reservoir models is often required because geostatistical models often have a finer scale than the reservoir simulation models. When the target is a small area, downscaling of geostatistical models may be required. In the McMurray Formation, where the SAGD technique is commonly used for bitumen recovery, the flow simulation of horizontal well pairs or individual SAGD pads is very important. The detailed flow simulation of selected small areas requires input models at a very fine grid size.

The previous chapters have demonstrated that reliable geostatistical models can be constructed at a large scale. Using the large scale model to generate a fine scale model is a downscaling process. Co-kriging, collocated co-kriging, and trend modeling techniques can be used to generate fine scale models; however, the fine scale model may not be completely consistent with the large scale model (Ren *et al.*, 2004a and Ren *et al.*, 2005c). Exact downscaling techniques are introduced to generate fine scale heterogeneous models. The term “exact” means the fine scale model would exactly reproduce the large scale model if it was scaled up. Exact downscaling techniques are developed using direct kriging and direct sequential simulation (DSS) techniques.

The background and theory of the two exact downscaling techniques are presented in this chapter. Theoretical and numerical proofs of exact reproduction of block data in the techniques are provided. The practical aspects and detailed implementation of the downscaling methods will be presented in the next chapter.

6.1. Background

Consider a block volume V with an arbitrary shape as shown by the solid black line in the sketch to the right. The block is composed of a great number of points (the black dots). If a property scales linearly, the block value Z_V can be calculated from the point data by this equation:



$$Z_V = \frac{1}{V} \int Z_{\bullet}(\mathbf{u}) d\mathbf{u} \quad (6-1)$$

where $Z_{\bullet}(\mathbf{u})$ is the point value at location \mathbf{u} in the block V .

If the block can be discretized into n equal-sized cells with small volume v (the squares drawn with dashed lines), the block value can be expressed as a discrete sum:

$$Z_V = \frac{1}{n} \sum_{i=1}^n Z_v(\mathbf{u}_i) \quad (6-2)$$

where $Z_v(\mathbf{u}_i)$ ($i = 1 \dots n$) are the values in the small cells. If the small volume is discretized by m points, the cell value $Z_v(\mathbf{u}_i)$ can be expressed as:

$$Z_v(\mathbf{u}_i) = \frac{1}{m} \sum_{j=1}^m Z_{\bullet}(\mathbf{u}'_j) \quad (6-3)$$

where $Z_{\bullet}(\mathbf{u}'_j)$ ($j = 1 \dots m$) are the point data in the small cell.

Now consider a large domain A (or a large model area) in which the multiscale data are stationary. Thus, the statistical properties such as mean, variance, covariance of data at each scale are constants over the entire area; and the statistical properties of data at different scales follow same relationships over the entire area. As stated in Section 2.5, most static properties have a linear scaling relationship. Under the assumption of

stationary, the mean is the same for all the scales. The data variance decreases as the scale increases. The volume averaged covariances apply to any scale.

In the large model area, the block data are exhaustively available for the entire area. A certain number of point data are also available. Statistical properties at the block and point scales can be calculated from the available data. We are interested in the statistical properties at the model scale, which can be any scale between the block and point scales. The mean at the model scale can be inferred from the block data. Because the block data covers the whole model area, the mean of block data is the true mean for all the scales:

$$\bar{Z}_V = \bar{Z}_v = \bar{Z}_\bullet \quad (6-4)$$

where the subscript V represents the block scale, v represents the model scale, and \bullet represents the point scale.

The variance of data at the model scale is the dispersion variance of the data in the large domain A , $\sigma_v^2 = D^2(v, A)$. Similarly, the variance of point data is: $\sigma_\bullet^2 = D^2(\bullet, A)$. Krige's Relation (Journel and Huijbregts, 1978) gives the variance at the model scale:

$$D^2(v, A) = D^2(\bullet, A) - D^2(\bullet, v) \quad (6-5)$$

where the dispersion variance of the point data in the model scale volume can be calculated from the Volume-Variance Relation (Journel and Huijbregts, 1978):

$$D^2(\bullet, v) = C_{\bullet\bullet}(0) - \bar{C}_{vv}(0) = \sigma_\bullet^2 - \bar{C}_{vv}(0) \quad (6-6)$$

where the $C_{\bullet\bullet}(0)$ and $\bar{C}_{vv}(0)$ are the volume averaged covariances between a datum and itself at the point and model scales. Therefore, the variance at the model scale is actually the volume-averaged covariance at the model scale:

$$\sigma_v^2 = \bar{C}_{vv} \quad (6-7)$$

As stated in Section 2.7, the covariance at the model scale can be inferred from the covariance at point data through the volume-averaged covariance relationship.

$$\begin{aligned}
\bar{C}_{vv}(\mathbf{h}) &= E\{Z_v(\mathbf{u}) \times Z_v(\mathbf{u} + \mathbf{h})\} - E\{Z_v(\mathbf{u})\}E\{Z_v(\mathbf{u} + \mathbf{h})\} \\
&= E\left\{\frac{1}{|v|} \int_{v(\mathbf{u})} Z_{\bullet}(\mathbf{x}) d\mathbf{x} \times \frac{1}{|v|} \int_{v(\mathbf{u}+\mathbf{h})} Z_{\bullet}(\mathbf{y}) d\mathbf{y}\right\} - m^2 \\
&= E\left\{\frac{1}{|v||v|} \int_{v(\mathbf{u})} \int_{v(\mathbf{u}+\mathbf{h})} Z_{\bullet}(\mathbf{x}) Z_{\bullet}(\mathbf{y}) d\mathbf{x} d\mathbf{y}\right\} - m^2 \\
&= \frac{1}{|v||v|} \int_{v(\mathbf{u})} \int_{v(\mathbf{u}+\mathbf{h})} (E\{Z_{\bullet}(\mathbf{x}) Z_{\bullet}(\mathbf{y})\} - m^2) d\mathbf{x} d\mathbf{y} \tag{6-8} \\
&= \frac{1}{|v|^2} \int_{v(\mathbf{u})} \int_{v(\mathbf{u}+\mathbf{h})} C_{\bullet\bullet}(\mathbf{x} - \mathbf{y}) d\mathbf{x} d\mathbf{y} \\
&= \frac{1}{|v|^2} \sum_{v(\mathbf{u})} \sum_{v(\mathbf{u}+\mathbf{h})} C_{\bullet\bullet}(\mathbf{h}')
\end{aligned}$$

Similarly, we can get the block scale covariance, block-to-model covariance, block-to-point covariance, and model-to-point covariance so that a total of five covariance models from the point scale covariance.

The block scale covariance:

$$\bar{C}_{VV}(\mathbf{h}) = E\{Z_V(\mathbf{u}) \times Z_V(\mathbf{u} + \mathbf{h})\} - E\{Z_V(\mathbf{u})\}E\{Z_V(\mathbf{u} + \mathbf{h})\} = \frac{1}{|V|^2} \sum_{V(\mathbf{u})} \sum_{V(\mathbf{u}+\mathbf{h})} C_{\bullet\bullet}(\mathbf{h}') \tag{6-9}$$

The block-to-model covariance:

$$\bar{C}_{Vv}(\mathbf{h}) = E\{Z_V(\mathbf{u}) \times Z_v(\mathbf{u} + \mathbf{h})\} - E\{Z_V(\mathbf{u})\}E\{Z_v(\mathbf{u} + \mathbf{h})\} = \frac{1}{|V||v|} \sum_{V(\mathbf{u})} \sum_{v(\mathbf{u}+\mathbf{h})} C_{\bullet\bullet}(\mathbf{h}') \tag{6-10}$$

The block-to-point covariance:

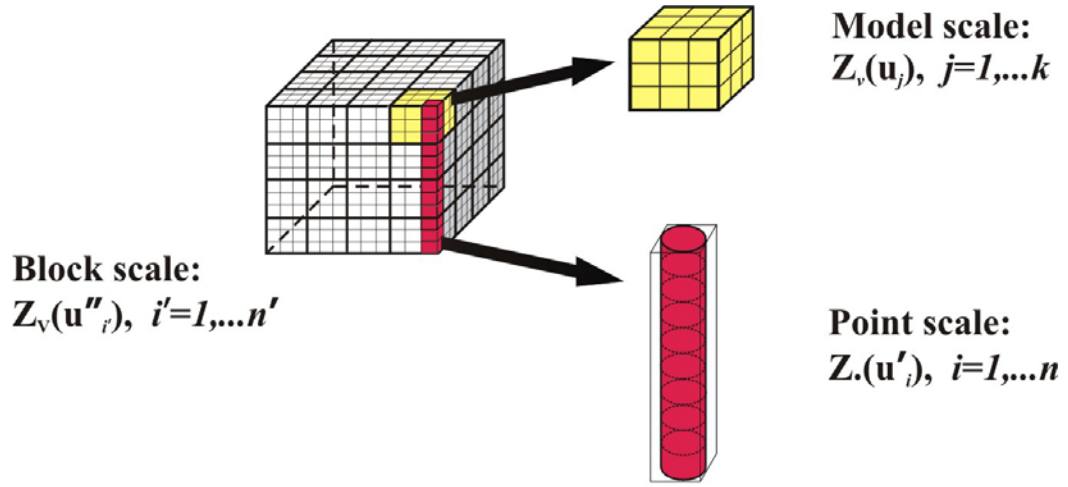
$$\bar{C}_{V\bullet}(\mathbf{h}) = E\{Z_V(\mathbf{u}) \times Z_{\bullet}(\mathbf{u} + \mathbf{h})\} - E\{Z_V(\mathbf{u})\}E\{Z_{\bullet}(\mathbf{u} + \mathbf{h})\} = \frac{1}{|V|} \sum_{V(\mathbf{u})} C_{\bullet\bullet}(\mathbf{h}') \tag{6-11}$$

And the model-to-point covariance:

$$C_{v\bullet}(\mathbf{h}) = E\{Z_v(\mathbf{u}) \times Z_{\bullet}(\mathbf{u} + \mathbf{h})\} - E\{Z_v(\mathbf{u})\}E\{Z_{\bullet}(\mathbf{u} + \mathbf{h})\} = \frac{1}{|v|} \sum_{v(\mathbf{u})} C_{\bullet\bullet}(\mathbf{h}') \tag{6-12}$$

After establishing the correlations between different scales, we can use them to account for the different volume supports of the conditioning data in the multiscale modeling using direct kriging or direct sequential simulation framework.

6.2. Theory of Exact Downscaling with Direct Kriging



Assuming a data domain A is stationary. Let $\{z_{\bullet}(\mathbf{u}'_i), i=1, \dots, n, \forall \mathbf{u}'_i \in A\}$ be the available point data, and let $\{z_V(\mathbf{u}''_j), j=1, \dots, n', \forall \mathbf{u}''_j \in A\}$ be the block data that is exhaustively available over A . The block and point data can be used with simple kriging to estimate the values at the model scale:

$$Z_v^*(\mathbf{u}) - m = \sum_{i=1}^n \lambda_{\bullet, i}(\mathbf{u})(Z_{\bullet}(\mathbf{u}'_i) - m) + \sum_{i'=1}^{n'} \lambda_{V, i'}(\mathbf{u})(Z_V(\mathbf{u}''_{i'}) - m) \quad \text{or}$$

$$Z_v^*(\mathbf{u}) = \sum_{i=1}^n \lambda_{\bullet, i}(\mathbf{u})Z_{\bullet}(\mathbf{u}'_i) + \sum_{i'=1}^{n'} \lambda_{V, i'}(\mathbf{u})Z_V(\mathbf{u}''_{i'}) + \left[1 - \sum_{i=1}^n \lambda_{\bullet, i}(\mathbf{u}) - \sum_{i'=1}^{n'} \lambda_{V, i'}(\mathbf{u}) \right] m \quad (6-13)$$

where $\lambda_{V, i'}(\mathbf{u})$ is the kriging weight for block data $Z_V(\mathbf{u}''_{i'})$, and λ_{\bullet} is the weight for point data $Z_{\bullet}(\mathbf{u}'_i)$. More precisely, this formalism can be referred to as *simple block kriging*.

By minimizing the error variance, the simple block kriging system is written as:

$$\begin{cases} \sum_{i'=1}^{n'} \lambda_{V_{i'}} \bar{C}_{V_{i'} V_j} + \sum_{i=1}^n \lambda_{\bullet_i} \bar{C}_{\bullet_i V_j} = \bar{C}_{v(\mathbf{u}) V_j} & j = 1, \dots, n' \\ \sum_{i'=1}^{n'} \lambda_{V_{i'}} \bar{C}_{V_{i'} \bullet_j} + \sum_{i=1}^n \lambda_{\bullet_i} \bar{C}_{\bullet_j \bullet_i} = \bar{C}_{v(\mathbf{u}) \bullet_j} & j' = 1, \dots, n \end{cases} \quad (6-14)$$

And the minimum error variance or the simple block kriging variance can be expressed as:

$$\sigma_{sbk}^2(\mathbf{u}) = \sigma_v^2 - \sum_{i=1}^n \lambda_{\bullet_i} \bar{C}_{\bullet_i v(\mathbf{u})} - \sum_{i'=1}^{n'} \lambda_{V_{i'}} \bar{C}_{V_{i'} v(\mathbf{u})} \quad (6-15)$$

where σ_v^2 is the variance at the model scale and can be calculated by Equation (6-7).

In the downscaling process, the block is expected to be reproduced exactly so that the fine scale model is consistent with the large scale model and no bias is introduced by the scaling process. A theorem on the exact reproduction of block data using the direct simple block kriging is developed below.

Theorem I: simple block kriging with block data and point data is an exact downscaling method:

$$Z_v^*(\mathbf{u}) = \sum_{i=1}^n \lambda_{\bullet_i}(\mathbf{u}) Z_{\bullet}(\mathbf{u}'_i) + \sum_{i'=1}^{n'} \lambda_{V_{i'}}(\mathbf{u}) Z_V(\mathbf{u}''_{i'}) + \left[1 - \sum_{i=1}^n \lambda_{\bullet_i}(\mathbf{u}) - \sum_{i'=1}^{n'} \lambda_{V_{i'}}(\mathbf{u}) \right] m$$

that is, the estimated values of the small cells in a block exactly reproduce the block value:

$$Z_v^*(\mathbf{u}) = \frac{1}{n} \sum_{i=1}^n Z^*(\mathbf{u}_i) = Z_v(\mathbf{u}) \quad (6-16)$$

6.2.1. Proof of Theorem I

Consider a block consisting of k small cells, and there are n point data available. Then, for each small cell at \mathbf{u}_j ($j=1 \dots k$), the kriging estimates are:

$$Z_v^*(\mathbf{u}_j) = \sum_{i=1}^n \lambda_{\bullet i}(\mathbf{u}_j) Z_{\bullet}(\mathbf{u}'_i) + \sum_{i'=1}^{n'} \lambda_{V i'}(\mathbf{u}_j) Z_V(\mathbf{u}''_{i'}) + \left[1 - \sum_{i=1}^n \lambda_{\bullet i}(\mathbf{u}_j) - \sum_{i'=1}^{n'} \lambda_{V i'}(\mathbf{u}_j) \right] m \quad j = 1, \dots, k$$

and the kriging system is

$\mathbf{C} \boldsymbol{\lambda}(\mathbf{u}_j) = \bar{\mathbf{C}}(\mathbf{u}_j)$ or in matrix format:

$$\begin{pmatrix} \bar{C}_{V_1 V_1} & \bar{C}_{V_1 V_2} & \cdots & \bar{C}_{V_1 V_{n'}} & \bar{C}_{V_1 \bullet_1} & \bar{C}_{V_1 \bullet_2} & \cdots & \bar{C}_{V_1 \bullet_n} \\ \bar{C}_{V_2 V_1} & \bar{C}_{V_2 V_2} & \cdots & \bar{C}_{V_2 V_{n'}} & \bar{C}_{V_2 \bullet_1} & \bar{C}_{V_2 \bullet_2} & \cdots & \bar{C}_{V_2 \bullet_n} \\ \vdots & \vdots & \ddots & \vdots & \vdots & \vdots & \ddots & \vdots \\ \bar{C}_{V_{n'} V_1} & \bar{C}_{V_{n'} V_2} & \cdots & \bar{C}_{V_{n'} V_{n'}} & \bar{C}_{V_{n'} \bullet_1} & \bar{C}_{V_{n'} \bullet_2} & \cdots & \bar{C}_{V_{n'} \bullet_n} \\ \bar{C}_{\bullet_1 V_1} & \bar{C}_{\bullet_1 V_2} & \cdots & \bar{C}_{\bullet_1 V_{n'}} & C_{\bullet_1 \bullet_1} & C_{\bullet_1 \bullet_2} & \cdots & C_{\bullet_1 \bullet_n} \\ \bar{C}_{\bullet_2 V_1} & \bar{C}_{\bullet_2 V_2} & \cdots & \bar{C}_{\bullet_2 V_{n'}} & C_{\bullet_2 \bullet_1} & C_{\bullet_2 \bullet_2} & \cdots & C_{\bullet_2 \bullet_n} \\ \vdots & \vdots & \ddots & \vdots & \vdots & \vdots & \ddots & \vdots \\ \bar{C}_{\bullet_n V_1} & \bar{C}_{\bullet_n V_2} & \cdots & \bar{C}_{\bullet_n V_{n'}} & C_{\bullet_n \bullet_1} & C_{\bullet_n \bullet_2} & \cdots & C_{\bullet_n \bullet_n} \end{pmatrix} \begin{pmatrix} \lambda_{V_1}(\mathbf{u}_j) \\ \lambda_{V_2}(\mathbf{u}_j) \\ \vdots \\ \lambda_{V_{n'}}(\mathbf{u}_j) \\ \lambda_{\bullet_1}(\mathbf{u}_j) \\ \lambda_{\bullet_2}(\mathbf{u}_j) \\ \vdots \\ \lambda_{\bullet_n}(\mathbf{u}_j) \end{pmatrix} = \begin{pmatrix} \bar{C}_{V_1 v}(\mathbf{u}_j) \\ \bar{C}_{V_2 v}(\mathbf{u}_j) \\ \vdots \\ \bar{C}_{V_{n'} v}(\mathbf{u}_j) \\ \bar{C}_{\bullet_1 v}(\mathbf{u}_j) \\ \bar{C}_{\bullet_2 v}(\mathbf{u}_j) \\ \vdots \\ \bar{C}_{\bullet_n v}(\mathbf{u}_j) \end{pmatrix}$$

Summarizing all the k kriging systems together, we get

$$\mathbf{C} \sum_{j=1}^k \boldsymbol{\lambda}(\mathbf{u}_j) = \sum_{j=1}^k \bar{\mathbf{C}}(\mathbf{u}_j)$$

From the volume averaged covariance relationship, we know that:

$$\bar{C}_{V_i V_j} = \frac{1}{k} \sum_{j=1}^k \bar{C}_{V_i v_j}(\mathbf{u}_j) \quad i = 1, 2, \dots, n'$$

$$\bar{C}_{\bullet_i v_j} = \frac{1}{k} \sum_{j=1}^k \bar{C}_{\bullet_i v_j}(\mathbf{u}_j) \quad i = 1, 2, \dots, n$$

Then, the matrix becomes:

$$\begin{pmatrix}
\bar{C}_{V_1V_1} & \bar{C}_{V_1V_2} & \cdots & \bar{C}_{V_1V_{n'}} & \bar{C}_{V_1\bullet_1} & \bar{C}_{V_1\bullet_2} & \cdots & \bar{C}_{V_1\bullet_n} \\
\bar{C}_{V_2V_1} & \bar{C}_{V_2V_2} & \cdots & \bar{C}_{V_2V_{n'}} & \bar{C}_{V_2\bullet_1} & \bar{C}_{V_2\bullet_2} & \cdots & \bar{C}_{V_2\bullet_n} \\
\vdots & \vdots & \ddots & \vdots & \vdots & \vdots & \ddots & \vdots \\
\bar{C}_{V_{n'}V_1} & \bar{C}_{V_{n'}V_2} & \cdots & \bar{C}_{V_{n'}V_{n'}} & \bar{C}_{V_{n'}\bullet_1} & \bar{C}_{V_{n'}\bullet_2} & \cdots & \bar{C}_{V_{n'}\bullet_n} \\
\bar{C}_{\bullet_1V_1} & \bar{C}_{\bullet_1V_2} & \cdots & \bar{C}_{\bullet_1V_{n'}} & C_{\bullet_1\bullet_1} & C_{\bullet_1\bullet_2} & \cdots & C_{\bullet_1\bullet_n} \\
\bar{C}_{\bullet_2V_1} & \bar{C}_{\bullet_2V_2} & \cdots & \bar{C}_{\bullet_2V_{n'}} & C_{\bullet_2\bullet_1} & C_{\bullet_2\bullet_2} & \cdots & C_{\bullet_2\bullet_n} \\
\vdots & \vdots & \ddots & \vdots & \vdots & \vdots & \ddots & \vdots \\
\bar{C}_{\bullet_nV_1} & \bar{C}_{\bullet_nV_2} & \cdots & \bar{C}_{\bullet_nV_{n'}} & C_{\bullet_n\bullet_1} & C_{\bullet_n\bullet_2} & \cdots & C_{\bullet_n\bullet_n}
\end{pmatrix}
\begin{pmatrix}
\sum_{j=1}^k \lambda_{V_1}(\mathbf{u}_j) \\
\sum_{j=1}^k \lambda_{V_2}(\mathbf{u}_j) \\
\vdots \\
\sum_{j=1}^k \lambda_{V_{n'}}(\mathbf{u}_j) \\
\sum_{j=1}^k \lambda_{\bullet_1}(\mathbf{u}_j) \\
\sum_{j=1}^k \lambda_{\bullet_2}(\mathbf{u}_j) \\
\vdots \\
\sum_{j=1}^k \lambda_{\bullet_n}(\mathbf{u}_j)
\end{pmatrix}
=
\begin{pmatrix}
k\bar{C}_{V_1V_1} \\
k\bar{C}_{V_2V_1} \\
\vdots \\
k\bar{C}_{V_{n'}V_1} \\
k\bar{C}_{\bullet_1V_1} \\
k\bar{C}_{\bullet_2V_1} \\
\vdots \\
k\bar{C}_{\bullet_nV_1}
\end{pmatrix}$$

The right side is k multiplied by the first column of the covariance matrix. Thus, the solution is:

$$\begin{cases}
\sum_{j=1}^k \lambda_{V_1} = k \\
\sum_{j=1}^k \lambda_{V_2} = \sum_{j=1}^k \lambda_{V_3} = \cdots = \sum_{j=1}^k \lambda_{V_{n'}} = 0 \\
\sum_{j=1}^k \lambda_{\bullet_1} = \sum_{j=1}^k \lambda_{\bullet_2} = \cdots = \sum_{j=1}^k \lambda_{\bullet_n} = 0
\end{cases} \quad (6-17)$$

This solution is unique because it is a kriging system. This solution indicates that the total weight to the collocated block is the number of cells in the block, and the total weights to the point data and other block data are zero.

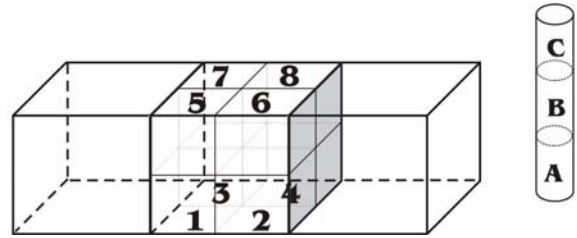
Using this solution, the block value calculated from all the estimates is:

$$\begin{aligned}
z_V^* &= \frac{1}{k} \sum_{j=1}^k z_V^*(\mathbf{u}_j) \\
&= \frac{1}{k} \sum_{j=1}^k \left\{ \sum_{i=1}^n \lambda_{\bullet i}(\mathbf{u}_j) Z_{\bullet}(\mathbf{u}'_i) + \sum_{i'=1}^{n'} \lambda_{V i'}(\mathbf{u}_j) Z_V(\mathbf{u}''_{i'}) + \left[1 - \sum_{i=1}^n \lambda_{\bullet i}(\mathbf{u}_j) - \sum_{i'=1}^{n'} \lambda_{V i'}(\mathbf{u}_j) \right] m \right\} \\
&= \frac{1}{k} \left\{ \sum_{j=1}^k \lambda_{V 1}(\mathbf{u}_j) Z_{V 1} + k m - \sum_{j=1}^k \lambda_{V 1}(\mathbf{u}_j) m \right\} \\
&= Z_V
\end{aligned}$$

Therefore, the block data is always reproduced exactly with the simple block kriging. It can be referred to as *exact downscaling with direct kriging (EDDK)* from a downscaling point view. A small example is given in the next section to demonstrate the exact reproduction of block data.

6.2.2. Small example

Consider three block data at scale of 4m x 4m x 4m in a row, and three point data in a vertical well close to the blocks. The center block is downscaled into 8 small cells at scale of 2m x 2m x 2m.



Three sets of block and well data used for the downscaling are listed in the table below. The center block datum is changed in all three sets. The two adjacent block data change in sets 1 and 2, while the well data are kept same. Then, the well data change in sets 2 and 3, while the two adjacent block data are kept same.

	Location	Set 1	Set 2	Set 3
Block	Left	0.50	0.80	0.80
	Center	0.25	1.00	4.00
	Right	0.10	1.20	1.20
Well	A	0.70	0.70	0.50
	B	0.50	0.50	1.20
	C	2.00	2.00	3.00

An exponential variogram model is used for the downscaling: $\gamma(h) = 1 - e^{-\frac{h}{a}}$, where h is the distance between two data locations. To check the block datum reproduction under different variograms, three different variogram ranges are used as shown in the table below.

Variogram	$\gamma_1(h)$	$\gamma_2(h)$	$\gamma_3(h)$
Range, a	4	9	16

The results of kriging using the three sets of data with different variogram models are given in Table 6-1. The center block values are given in the first row. The estimated values in 8 small cells are listed in the middle, and the block average of the small cells is calculated in the last row for each case. The block datum is exactly reproduced in all cases, which numerically confirms the theorem presented above. The changes in block data, well data and variogram models affect estimates in small cells, but do not affect the exact reproduction of block datum.

	Set 1: Zcb = 0.25			Set 2: Zcb = 1.00			Set 3: Zcb = 4.00		
Cell	γ_1	γ_2	γ_3	γ_1	γ_2	γ_3	γ_1	γ_2	γ_3
1	0.18	0.15	0.14	0.95	0.93	0.93	3.99	4.06	4.11
2	0.28	0.26	0.25	1.01	0.98	0.95	3.96	3.83	3.75
3	0.17	0.14	0.13	0.94	0.93	0.93	3.99	4.09	4.15
4	0.26	0.24	0.23	1.00	0.97	0.95	3.97	3.88	3.82
5	0.22	0.24	0.25	0.98	1.01	1.04	4.02	4.12	4.18
6	0.35	0.39	0.40	1.08	1.10	1.09	4.02	3.92	3.86
7	0.21	0.22	0.23	0.97	1.00	1.03	4.02	4.14	4.22
8	0.32	0.36	0.38	1.06	1.08	1.08	4.02	3.96	3.91
Zavg	0.25	0.25	0.25	1.00	1.00	1.00	4.00	4.00	4.00

Table 6-1: The table of EDDK results with different cases. The collocated block values are given in the first row. The estimated values in 8 small cells are listed in rows 1-8, and the block averages of the estimates are listed in the last row.

Kriging estimates are smooth. A simulation approach is needed to generate realizations with the correct variability.

6.3. Theory of Exact Downscaling with Direct Sequential Simulation

Considering the same data domain A is stationary. Let $\{z_{\bullet}(\mathbf{u}'_i), i=1, \dots, n, \forall \mathbf{u}'_i \in A\}$ be the available point data, and let $\{z_V(\mathbf{u}''_j), j=1, \dots, n', \forall \mathbf{u}''_j \in A\}$ be the block data that are exhaustively available over A . Direct sequential simulation uses the block, point data and previously simulated data to simulate the values at the model scale:

$$Z_{v,s}(\mathbf{u}) = \lambda_V Z_V(\mathbf{u}') + \sum_{i=1}^n \lambda_{v_i} Z_{v,s}(\mathbf{u}_i) + \sum_{i'=1}^{n'} \lambda_{\bullet i'} Z_{\bullet}(\mathbf{u}''_{i'}) + \left[1 - \lambda_V - \sum_{i=1}^n \lambda_{v_i} - \sum_{i'=1}^{n'} \lambda_{\bullet i'} \right] m + R(\mathbf{u}) \quad (6-18)$$

where $Z_V(\mathbf{u}')$ is the collocated block value. Note only the collocated block datum is used because the previously simulated data are used. And $Z_{\bullet}(\mathbf{u}'')$ is the point data, $Z_{v,s}(\mathbf{u}_i)$ is the previously simulated data, $R(\mathbf{u})$ is the random residual at the simulated location \mathbf{u} .

The kriging system is written as:

$$\begin{cases} \lambda_V \bar{C}_{VV} + \sum_{i=1}^n \lambda_{v_i} \bar{C}_{Vv_i} + \sum_{i'=1}^{n'} \lambda_{\bullet i'} \bar{C}_{V\bullet i'} = \bar{C}_{Vv(\mathbf{u})} \\ \lambda_V \bar{C}_{Vv_j} + \sum_{i=1}^n \lambda_{v_i} \bar{C}_{v_i v_j} + \sum_{i'=1}^{n'} \lambda_{\bullet i'} \bar{C}_{\bullet i' v_j} = \bar{C}_{v_j v(\mathbf{u})}, \quad j=1, \dots, n \\ \lambda_V \bar{C}_{V\bullet j'} + \sum_{i=1}^n \lambda_{v_i} \bar{C}_{v_i \bullet j'} + \sum_{i'=1}^{n'} \lambda_{\bullet i'} \bar{C}_{\bullet i' \bullet j'} = \bar{C}_{\bullet j' v(\mathbf{u})}, \quad j'=1, \dots, n' \end{cases} \quad (6-19)$$

And the simple block kriging variance is

$$\sigma_{s,bk}^2(\mathbf{u}) = \sigma_v^2 - \lambda_V \bar{C}_{Vv(\mathbf{u})} - \sum_{i=1}^n \lambda_{v_i} \bar{C}_{v_i v(\mathbf{u})} - \sum_{i'=1}^{n'} \lambda_{\bullet i'} \bar{C}_{\bullet i' v(\mathbf{u})} \quad (6-20)$$

where σ_v^2 is the variance at model scale.

Theorem II: Direct sequential simulation with block data and point data is an exact downscaling method:

$$Z_{v,s}(\mathbf{u}) = \lambda_V Z_V(\mathbf{u}') + \sum_{i=1}^n \lambda_{v,i} Z_{v,s}(\mathbf{u}_i) + \sum_{i'=1}^{n'} \lambda_{\bullet,i'} Z_{\bullet}(\mathbf{u}''_{i'}) + \left[1 - \lambda_V - \sum_{i=1}^n \lambda_{v,i} - \sum_{i'=1}^{n'} \lambda_{\bullet,i'} \right] m + R(\mathbf{u})$$

that is, the simulated values of the small cells in a block can exactly reproduce the block value:

$$Z_{v,s}(\mathbf{u}) = \frac{1}{n} \sum_{i=1}^n Z_{v,s}(\mathbf{u}'_i) = Z_V(\mathbf{u}) \quad (6-21)$$

6.3.1. Proof of Theorem II

Consider a block consisting of k small cells, and there are n point data are available. Perform DSS to simulate the cells in the block following a random path; the previously simulated cells are added into the conditioning data for simulating the next cell, until reach the last cell at \mathbf{u}_k , the simulated value is:

$$Z_{v,s}(\mathbf{u}_k) = \lambda_V Z_V(\mathbf{u}') + \sum_{i=1}^n \lambda_{v,i} Z_{v,s}(\mathbf{u}_i) + \sum_{i'=1}^{n'} \lambda_{\bullet,i'} Z_{\bullet}(\mathbf{u}''_{i'}) + \left[1 - \lambda_V - \sum_{i=1}^n \lambda_{v,i} - \sum_{i'=1}^{n'} \lambda_{\bullet,i'} \right] m + R(\mathbf{u}_k)$$

$k = 1, \dots, k$

where among the n previously simulated cells, there are $k-1$ of them inside the block. The kriging system in matrix format:

$$\begin{pmatrix} \bar{C}_{VV} & \bar{C}_{Vv_1} & \cdots & \bar{C}_{Vv_n} & \bar{C}_{V\bullet_1} & \bar{C}_{V\bullet_2} & \cdots & \bar{C}_{V\bullet_{n'}} \\ \bar{C}_{v_1V} & \bar{C}_{v_1v_1} & \cdots & \bar{C}_{v_1v_n} & \bar{C}_{v_1\bullet_1} & \bar{C}_{v_2\bullet_2} & \cdots & \bar{C}_{v_2\bullet_{n'}} \\ \vdots & \vdots & \ddots & \vdots & \vdots & \vdots & \ddots & \vdots \\ \bar{C}_{v_nV} & \bar{C}_{v_nv_1} & \cdots & \bar{C}_{v_nv_n} & \bar{C}_{v_n\bullet_1} & \bar{C}_{v_n\bullet_2} & \cdots & \bar{C}_{v_n\bullet_{n'}} \\ \bar{C}_{\bullet_1V} & \bar{C}_{\bullet_1v_1} & \cdots & \bar{C}_{\bullet_1v_n} & C_{\bullet_1\bullet_1} & C_{\bullet_1\bullet_2} & \cdots & C_{\bullet_1\bullet_{n'}} \\ \bar{C}_{\bullet_2V} & \bar{C}_{\bullet_2v_1} & \cdots & \bar{C}_{\bullet_2v_n} & C_{\bullet_2\bullet_1} & C_{\bullet_2\bullet_2} & \cdots & C_{\bullet_2\bullet_{n'}} \\ \vdots & \vdots & \ddots & \vdots & \vdots & \vdots & \ddots & \vdots \\ \bar{C}_{\bullet_{n'}V} & \bar{C}_{\bullet_{n'}v_1} & \cdots & \bar{C}_{\bullet_{n'}v_n} & C_{\bullet_{n'}\bullet_1} & C_{\bullet_{n'}\bullet_2} & \cdots & C_{\bullet_{n'}\bullet_{n'}} \end{pmatrix} \begin{pmatrix} \lambda_V(\mathbf{u}_k) \\ \lambda_{v_1}(\mathbf{u}_k) \\ \vdots \\ \lambda_{v_n}(\mathbf{u}_k) \\ \lambda_{\bullet_1}(\mathbf{u}_k) \\ \lambda_{\bullet_2}(\mathbf{u}_k) \\ \vdots \\ \lambda_{\bullet_{n'}}(\mathbf{u}_k) \end{pmatrix} = \begin{pmatrix} \bar{C}_{Vv(\mathbf{u}_k)} \\ \bar{C}_{v_1v(\mathbf{u}_k)} \\ \vdots \\ \bar{C}_{v_nv(\mathbf{u}_k)} \\ \bar{C}_{\bullet_1v(\mathbf{u}_k)} \\ \bar{C}_{\bullet_2v(\mathbf{u}_k)} \\ \vdots \\ \bar{C}_{\bullet_{n'}v(\mathbf{u}_k)} \end{pmatrix}$$

From the volume averaged correlations, we can get:

$$\bar{C}_{VV} = \frac{1}{k} \sum_{i=1}^k \bar{C}_{Vv_i} \quad \text{or} \quad k\bar{C}_{VV} - \sum_{i=1}^{k-1} \bar{C}_{Vv_i} = \bar{C}_{Vv(\mathbf{u}_k)}$$

$$\bar{C}_{Vv_j} = \frac{1}{k} \sum_{i=1}^k \bar{C}_{v_jv_i}, \quad j=1, \dots, n \Rightarrow k\bar{C}_{Vv_j} - \sum_{i=1}^{k-1} \bar{C}_{v_jv_i} = \bar{C}_{v_jv(\mathbf{u}_k)}, \quad j=1, \dots, n$$

$$\bar{C}_{V\bullet_{j'}} = \frac{1}{k} \sum_{i=1}^k C_{v_i\bullet_{j'}}, \quad j'=1, \dots, n' \Rightarrow k\bar{C}_{V\bullet_{j'}} - \sum_{i=1}^{k-1} \bar{C}_{v_i\bullet_{j'}} = \bar{C}_{v_n\bullet_{j'}}, \quad j'=1, \dots, n'$$

Then, the kriging system becomes:

$$\begin{pmatrix} \bar{C}_{VV} & \bar{C}_{Vv_1} & \cdots & \bar{C}_{Vv_n} & \bar{C}_{V\bullet_1} & \bar{C}_{V\bullet_2} & \cdots & \bar{C}_{V\bullet_{n'}} \\ \bar{C}_{v_1V} & \bar{C}_{v_1v_1} & \cdots & \bar{C}_{v_1v_n} & \bar{C}_{v_1\bullet_1} & \bar{C}_{v_2\bullet_2} & \cdots & \bar{C}_{v_2\bullet_{n'}} \\ \vdots & \vdots & \ddots & \vdots & \vdots & \vdots & \ddots & \vdots \\ \bar{C}_{v_nV} & \bar{C}_{v_nv_1} & \cdots & \bar{C}_{v_nv_n} & \bar{C}_{v_n\bullet_1} & \bar{C}_{v_n\bullet_2} & \cdots & \bar{C}_{v_n\bullet_{n'}} \\ \bar{C}_{\bullet_1V} & \bar{C}_{\bullet_1v_1} & \cdots & \bar{C}_{\bullet_1v_n} & C_{\bullet_1\bullet_1} & C_{\bullet_1\bullet_2} & \cdots & C_{\bullet_1\bullet_{n'}} \\ \bar{C}_{\bullet_2V} & \bar{C}_{\bullet_2v_1} & \cdots & \bar{C}_{\bullet_2v_n} & C_{\bullet_2\bullet_1} & C_{\bullet_2\bullet_2} & \cdots & C_{\bullet_2\bullet_{n'}} \\ \vdots & \vdots & \ddots & \vdots & \vdots & \vdots & \ddots & \vdots \\ \bar{C}_{\bullet_{n'}V} & \bar{C}_{\bullet_{n'}v_1} & \cdots & \bar{C}_{\bullet_{n'}v_n} & C_{\bullet_{n'}\bullet_1} & C_{\bullet_{n'}\bullet_2} & \cdots & C_{\bullet_{n'}\bullet_{n'}} \end{pmatrix} \begin{pmatrix} \lambda_V(\mathbf{u}_k) \\ \lambda_{v_1}(\mathbf{u}_k) \\ \vdots \\ \lambda_{v_n}(\mathbf{u}_k) \\ \lambda_{\bullet_1}(\mathbf{u}_k) \\ \lambda_{\bullet_2}(\mathbf{u}_k) \\ \vdots \\ \lambda_{\bullet_{n'}}(\mathbf{u}_k) \end{pmatrix} = \begin{pmatrix} k\bar{C}_{VV} - \sum_{i=1}^{k-1} \bar{C}_{Vv_i} \\ k\bar{C}_{Vv_1} - \sum_{i=1}^{k-1} \bar{C}_{v_1v_i} \\ \vdots \\ k\bar{C}_{Vv_n} - \sum_{i=1}^{k-1} \bar{C}_{v_nv_{k-1}} \\ k\bar{C}_{V\bullet_1} - \sum_{i=1}^{k-1} \bar{C}_{v_i\bullet_1} \\ k\bar{C}_{V\bullet_2} - \sum_{i=1}^{k-1} \bar{C}_{v_i\bullet_2} \\ \vdots \\ k\bar{C}_{V\bullet_{n'}} - \sum_{i=1}^{k-1} \bar{C}_{v_i\bullet_{n'}} \end{pmatrix}$$

This kriging system gives a unique solution:

$$\begin{cases} \lambda_V = k \\ \lambda_{v_i} = -1, & i = 1, \dots, k-1 \\ \lambda_{v_i} = 0, & i = k, \dots, n \\ \lambda_{\bullet i'} = 0, & i' = 1, \dots, n' \end{cases} \quad (6-22)$$

Now, let's check the variance:

$$\begin{aligned} \sigma_{sbc k}^2(\mathbf{u}_k) &= \sigma_V^2 - \lambda_V \bar{C}_{Vv}(\mathbf{u}) - \sum_{i=1}^n \lambda_{v_i} \bar{C}_{v_i v}(\mathbf{u}) - \sum_{i'=1}^{n'} \lambda_{\bullet i'} \bar{C}_{\bullet i' v}(\mathbf{u}) = \bar{C}_{v_k v_k} - k \bar{C}_{Vv}(\mathbf{u}) + \sum_{i=1}^{k-1} \bar{C}_{v_i v_k} \\ &= \sum_{i=1}^k \bar{C}_{v_i v_k} - k \bar{C}_{Vv}(\mathbf{u}) = 0 \end{aligned} \quad (6-23)$$

Thus, the random residual at the last cell $R(\mathbf{u}_k) \equiv 0$ because it follows a distribution with zero mean and zero variance. Then, the simulated value at the last location is

$$Z_{v_s}(\mathbf{u}_k) = k Z_V - \sum_{i=1}^{k-1} Z_{v_s}(\mathbf{u}_i) \quad (6-24)$$

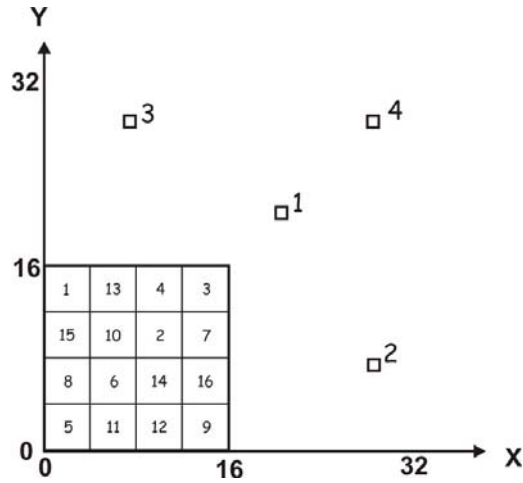
This equation indicates that the simulated value in the last cell is actually the block value multiplied by the number of cells in the block and subtracted by all the previously simulated cells in the block. Therefore, the block average of simulated values is always the block value:

$$Z_{V_s} = \frac{1}{k} \left[\sum_{i=1}^{k-1} Z_{v_s}(\mathbf{u}_i) + Z_{v_s}(\mathbf{u}_k) \right] = \frac{1}{k} \left[\sum_{i=1}^{k-1} Z_{v_s}(\mathbf{u}_i) + k Z_V - \sum_{i=1}^{k-1} Z_{v_s}(\mathbf{u}_i) \right] = Z_V$$

The block data is always exactly reproduced in direct sequential simulation. This exact downscaling technique is named *exact downscaling with direct sequential simulation* (EDDSS). Again, a small example is given to show the exact reproduction of block data in EDDSS numerically.

6.3.2. Small example

Consider downscaling a block at scale of 16 m by 16 m into 16 small cells at scale of 4 m by 4 m as shown in the figure below. There are also four point data at scale of 1 m by 1 m close to the block.



EDDSS is performed using the block and point data. The results are shown in Table 6-2. The 16 small cells are simulated with a random path. The weights of data in each cell are given in the 16 columns. The kriged estimate and variance are listed in the last two rows. The table shows the block value is exactly reproduced.

Data				Kriging weights in each cell																Summary		
type	x	y	z	value	1	2	3	4	5	6	7	8	9	10	11	12	13	14	15	16	/average	
block	8	8	0.5	48.10	0.88	1.23	0.03	-0.20	2.21	1.49	1.33	0.13	4.68	1.80	3.55	3.76	2.86	5.58	8.10	16.37	53.80	
point	20.5	20.5	0.5	58	-0.04	0.01	0.32	-0.03	0.05	0.01	-0.03	0.01	0.00	-0.01	0.01	0.01	0.00	-0.01	0.01	0.00	0.30	
point	28.5	7.5	0.5	28	0.00	-0.04	0.04	-0.03	-0.02	-0.04	0.03	0.00	0.03	0.02	0.00	-0.02	0.00	-0.01	-0.01	0.00	-0.04	
point	7.5	28.5	0.5	48	0.09	-0.03	0.05	0.04	0.01	-0.02	-0.01	-0.02	0.02	-0.02	-0.01	0.00	0.02	0.01	-0.01	0.00	0.12	
point	28.5	28.5	0.5	38	0.03	-0.02	-0.06	0.00	0.00	-0.02	0.00	-0.01	0.01	0.00	0.00	0.00	0.00	0.00	0.00	0.00	-0.05	
simulate	2	10	0.5	47.41																	-1.02	
simulate	10	6	0.5	49.29																	-0.74	
simulate	6	14	0.5	51.86														-0.28	-0.59	-1.02	-1.90	
simulate	10	2	0.5	50.35													-0.25	-0.11	-0.42	-1.02	-1.79	
simulate	6	2	0.5	47.30												0.23	-0.12	-0.43	-0.51	-1.02	-1.85	
simulate	6	10	0.5	48.13											-0.48	-0.42	0.11	-0.58	-0.27	-1.02	-2.66	
simulate	14	2	0.5	48.84										-0.32	-0.37	-0.03	-0.28	-0.49	-0.74	-1.03	-3.27	
simulate	2	6	0.5	47.17									-0.41	0.04	-0.46	-0.35	-0.34	-0.61	-0.24	-1.02	-3.40	
simulate	14	10	0.5	46.45								-0.07	-0.23	-0.30	-0.42	-0.46	-0.31	-0.50	-0.78	-1.04	-4.11	
simulate	6	6	0.5	48.25							-0.40	0.42	-0.81	0.02	0.10	-0.27	-0.34	-0.02	-0.52	-1.02	-2.84	
simulate	2	2	0.5	47.76						0.08	-0.19	0.44	-0.38	-0.30	0.21	-0.31	-0.14	-0.30	-0.57	-1.02	-2.47	
simulate	10	14	0.5	48.08					-0.07	-0.09	-0.38	-0.03	-0.48	-0.06	-0.27	-0.33	0.35	-0.42	-0.51	-1.02	-3.31	
simulate	14	14	0.5	48.43				0.50	-0.23	-0.27	0.48	0.01	-0.23	-0.11	-0.16	-0.16	-0.26	-0.32	-0.44	-1.02	-2.22	
simulate	10	10	0.5	48.42			0.63	0.47	-0.75	0.02	0.36	-0.08	-0.64	0.24	-0.33	-0.24	-0.37	-0.02	-0.49	-1.02	-2.21	
simulate	2	14	0.5	46.75																	-1.02	
simulated values					47.41	49.29	51.86	50.35	47.30	48.13	48.84	47.17	46.45	48.25	47.76	48.08	48.43	48.42	46.75	45.06		48.10
kriging variance					0.32	0.12	0.21	0.09	0.19	0.08	0.07	0.09	0.08	0.05	0.05	0.04	0.04	0.04	0.02	0.02	0.00	

Table 6-2: The table of EDDSS results for the small example. The simulated values and variances are listed in the last two rows.

The exact downscaling with direct kriging and the exact downscaling with direct sequential simulation honor the data scales and can exactly reproduce the block data. Using them to construct fine scale 3-D models will ensure the fine scale models are consistent with the large scale data. The detailed implementation is presented in the next Chapter.

CHAPTER 7

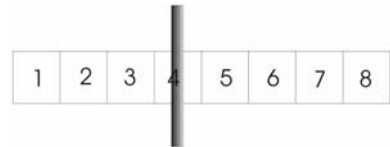
IMPLEMENTATION OF EXACT DOWNSCALING TECHNIQUES

Exact downscaling techniques are applied to construct fine scale models using both large scale and point scale data. The practical aspects of the exact downscaling techniques are illustrated with some small examples. Implementation is further demonstrated with a large example. Comparison between exact downscaling and approximate downscaling is presented at the end of the chapter to show that the exact downscaled model is consistent with the large scale data and the downscaling method have a big impact on flow simulation result.

7.1 Some Interesting Aspects of EDDK

7.1.1 Kriging weights of block and point data

Kriging weights indicate the influence of block and point data in the estimation. Consider a single block discretized into 8 finer cells and a well located at the center of cell 4.



Three different variogram ranges are used: (1) small range: $a_h=a_v= 10$, (2) median range: $a_h=a_v= 100$, and (3) long range: $a_h=a_v=1000$. The weights of block and point data in each cell are listed in Table 7-1 and plotted in Figure 7-1.

Cell	ah = av = 10		ah = av = 100		ah = av = 1000	
	block	point	block	point	block	point
1	1.09	-0.26	1.10	-0.14	1.09	-0.10
2	1.16	-0.15	0.95	0.05	0.91	0.09
3	0.84	0.22	0.58	0.43	0.55	0.45
4	0.00	1.00	0.00	1.00	0.00	1.00
5	0.91	0.19	0.75	0.27	0.73	0.27
6	1.34	-0.22	1.29	-0.26	1.27	-0.27
7	1.43	-0.39	1.61	-0.60	1.63	-0.63
8	1.24	-0.39	1.72	-0.75	1.81	-0.81

Table 7-1: The kriging weights of block and point data with different variogram ranges.

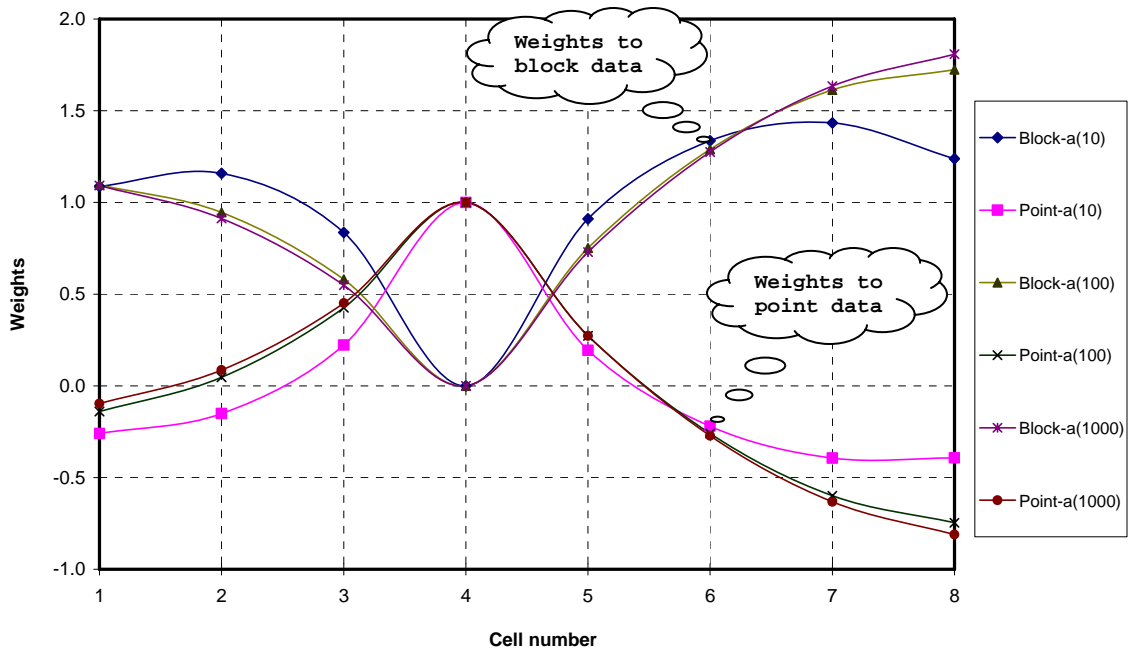
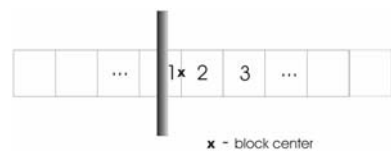


Figure 7-1: The kriging weights of block and point data with different variogram ranges.

Because of the large volume support, the weight of block datum is always larger than the weight of point datum except at the well location. At the well location, the well gets all the weights so the well datum is reproduced. Moving away from the well, the weight of the block is increasing until it reaches a maximum, then, it will decrease. The maximum is related to the variogram range. The longer the variogram range the maximum will be further away from the well.

Consider another small example with increasing block sizes: from 4 cells to 100 cells. The well is located at the cell 1. The weights of block and point data in the cells close to the well are listed in Table 7-2 and plotted in Figure 7-2. As the block size increases, the weight of block becomes smaller; and the influence of the well increases.



Cell No.	block size	4	6	8	10	20	50	100
1	block weight	0	0	0	0	0	0	0
	point weight	1	1	1	1	1	1	1
2	block weight	1.41	1.09	0.91	0.80	0.60	0.50	0.47
	point weight	-0.30	0.03	0.19	0.29	0.45	0.51	0.53
3	block weight	1.68	1.51	1.34	1.21	0.93	0.78	0.74
	point weight	-0.71	-0.42	-0.22	-0.09	0.14	0.25	0.28

Table 7-2: The weights of block and point data in the three cells with increasing block sizes.

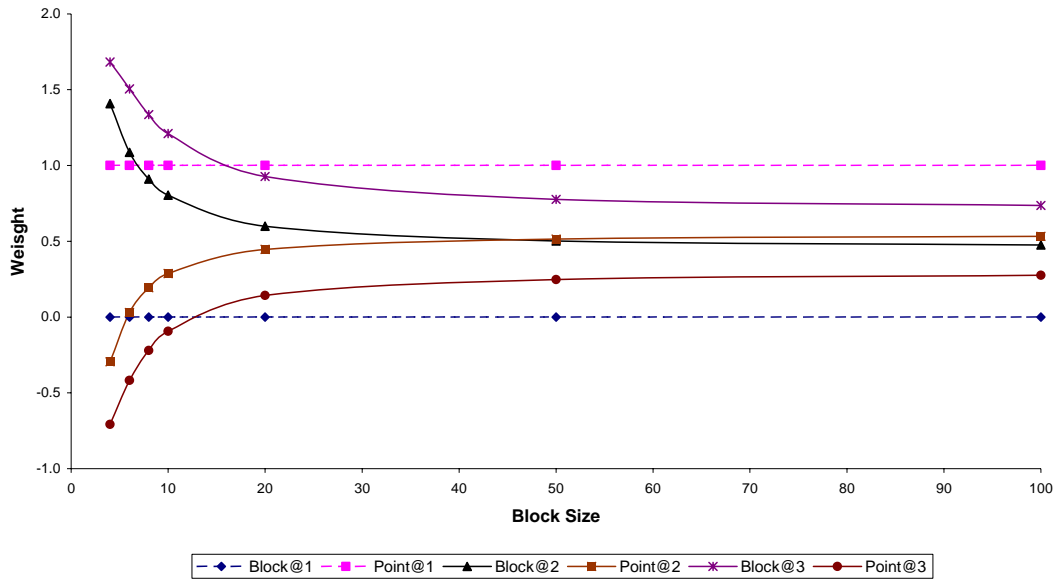
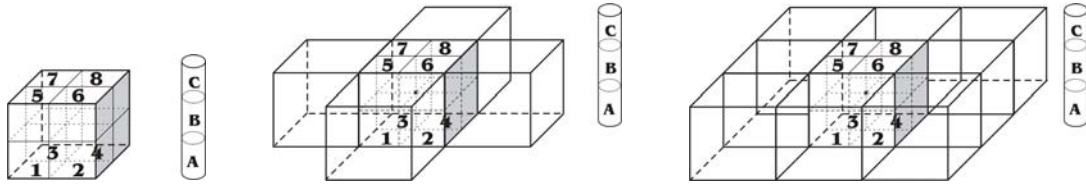


Figure 7-2: The weights of block and point data in the cells “1-3” with different block sizes. At the well location, the weights are constant (dash lines). Away from the well, the weights change with block size (solid lines).

7.1.2 Number of block data used in EDDK

Although many block data are available, not all of them are necessarily required for downscaling. Some blocks are redundant and computer requirements will increase when many blocks are used. Three cases will be shown below: (1) collocated block case, which uses only the collocated block datum. (2) directly connected blocks case, which uses the

collocated block and all directly connected blocks data, 5 blocks in 2-D and 7 blocks in 3-D. (3) corner connected blocks case, which uses the collocated block and all the directly and corner connected blocks data, 9 blocks in 2-D and 27 blocks in 3-D.



collocated block directly connected blocks(2-D) corner connected blocks(2-D)

A 2-D downscaling example for the three cases is shown in Figure 7-3. The upper left image is a 2-D grid of large scale data. The single collocated block case (upper right) indicates that using the collocated block alone does not provide any information on the spatial arrangement of small scale estimates. The multiple block cases show more fine scale spatial continuity. Using the collocated block and all the directly and corner connected blocks provides all surrounding information. The example in the next section shows the weights of the blocks in the three cases.

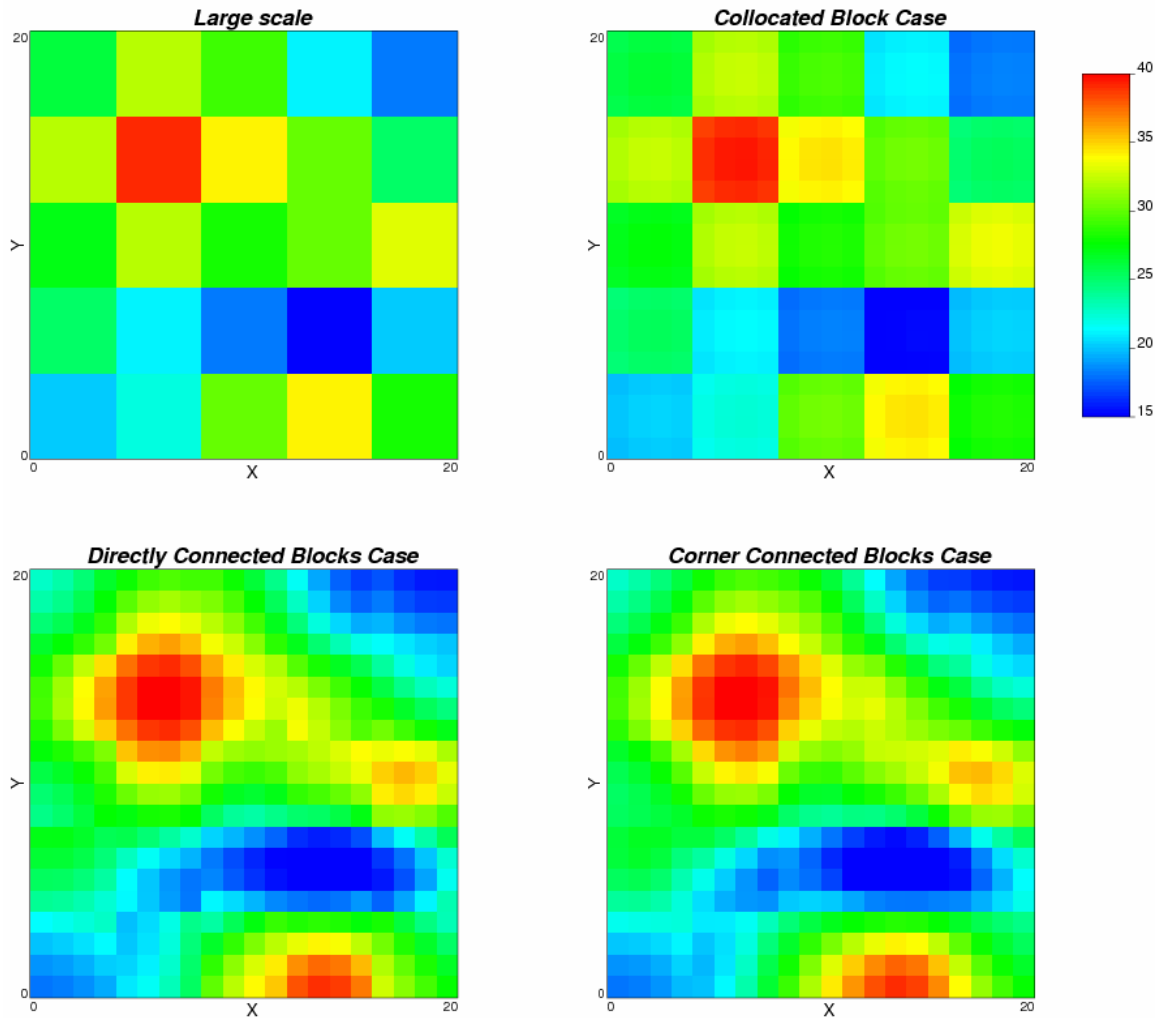


Figure 7-3: The large scale data (upper left) and the downscaled results in the three cases.

7.1.3 Screen effect with multiple block data

The center block is discretized to 9 small cells. The surrounding large blocks are used in estimation. Blocks 1-4 are directly connected, and blocks 5-8 are corner connected.

The weights of the block data in the three cases are plotted in Figure 7-6. The collocated block always has the highest weight. The weights of the directly connected blocks

5	2	6		
1	6	3	7	3
	2	1	4	
	9	5	8	
8	4	7		

depend on the closeness and redundancy. For example, at cell 2, the weight of the block 1 is at the peak, and the weight of block 3 is negative. The weights of the corner connected blocks are always close to zero.

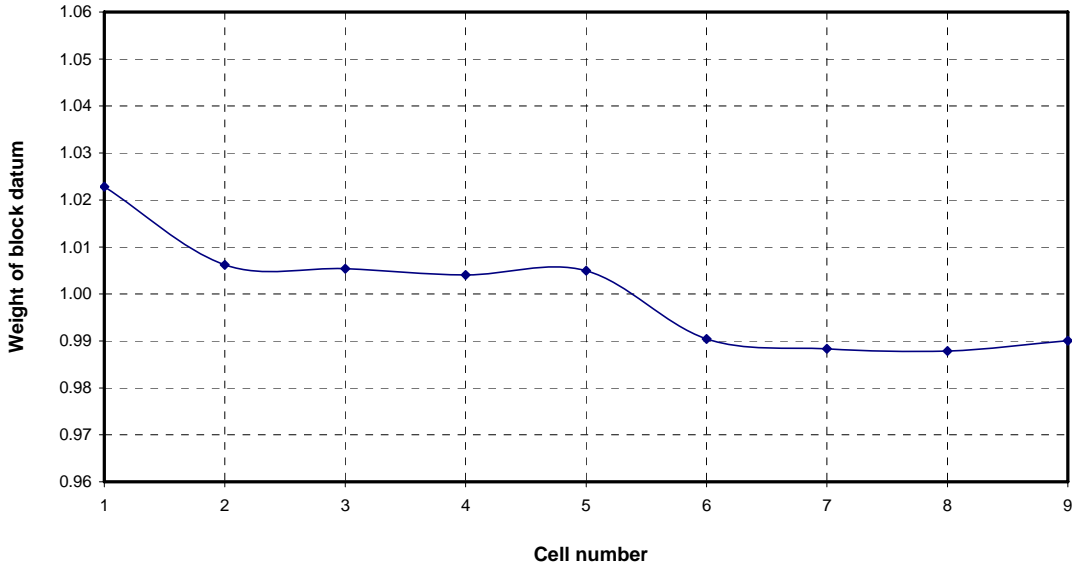


Figure 7-4: The weight of collocated block in each small cell in case 1.

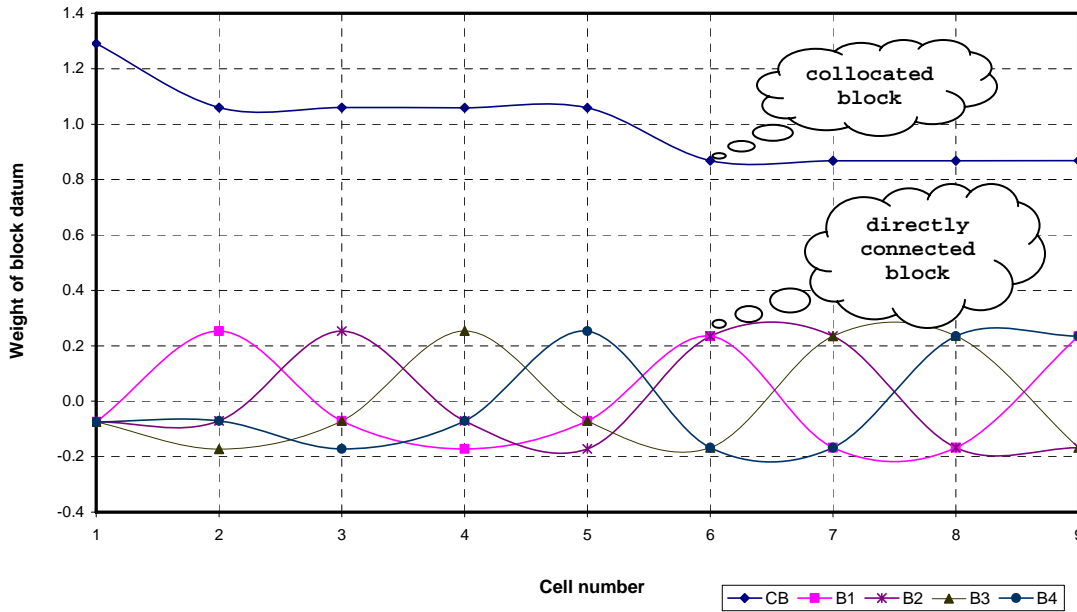


Figure 7-5: The weights of blocks in each small cell in case 2.

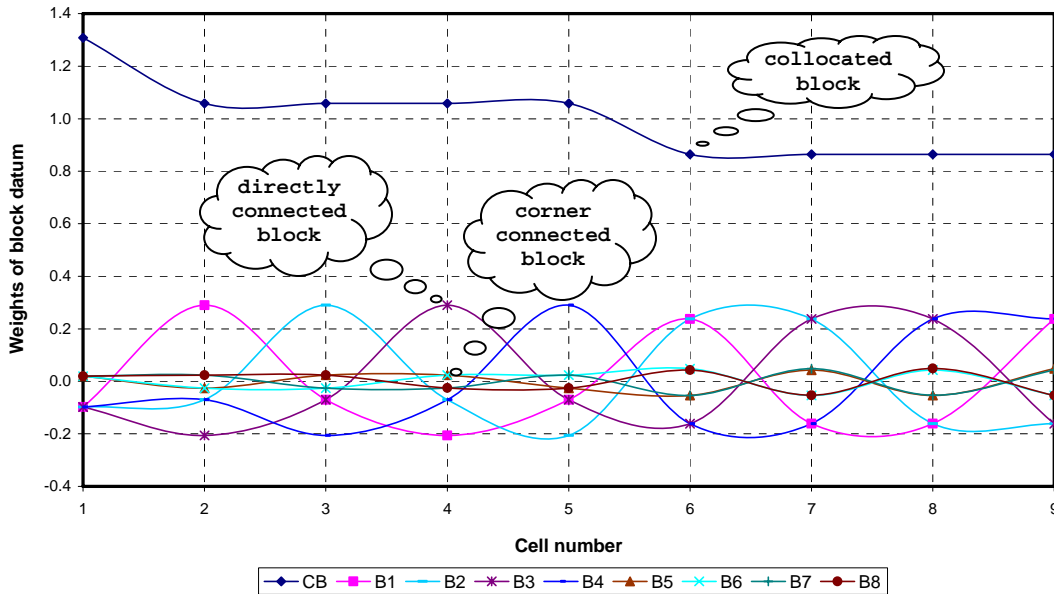


Figure 7-6: The weights of blocks in the small cell in case 3.

7.2 Some Interesting Aspects of EDDSS

Because previously simulated cells are used, the spatial structure at model scale is enforced in simulation. Thus, the collocated block case works much better with DSS than EDDK. The directly and corner connected blocks are not necessary for the spatial structure. For computing efficiency, only the collocated block is used in EDDSS. Kriging weights of block and point data will be affected by the previously simulated data.

The kriging weights accounts for the data closeness, redundancy, and support volume. The weight of the block datum is not always higher than the weights of the point data. As shown in the EDDSS result (Table 6-2) of the small example in previous chapter, at the cells 3, 4, and 8, the weight of the block datum is small or negative due to the screen effect of adjacent simulated cells. The weights of the point data are always low due to their small volume and long distance from the simulated cell. When simulating the last few cells (14, 15 and 16 in this example), the weight of the block datum is going up fast (Figure 7-7), while the weights of the point data become close to zero (Figure 7-8), and the weights of previously simulated cells become negative. In the last cell, the weight

to block datum is the discretization number; the weights of the point data are zero; and the weights of the previously simulated cells are all -1. Following the simulation sequence, the kriging variance is going down, at the last cell, the variance is zero (Figure 7-9). This matches the proof of Theorem II.

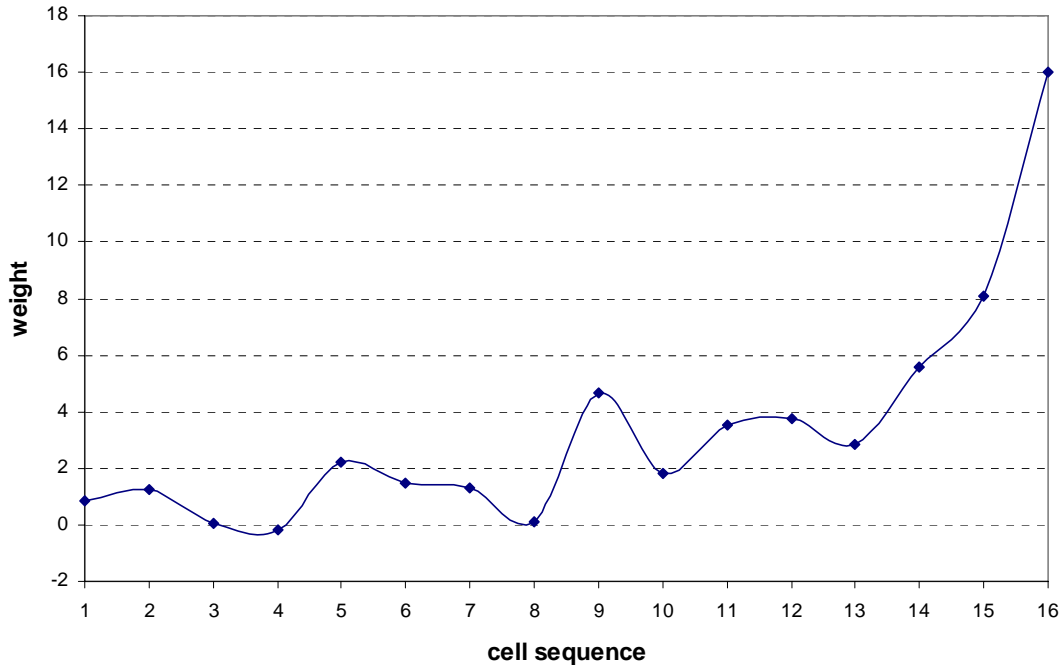


Figure 7-7: The kriging weight of block datum changes with simulation path

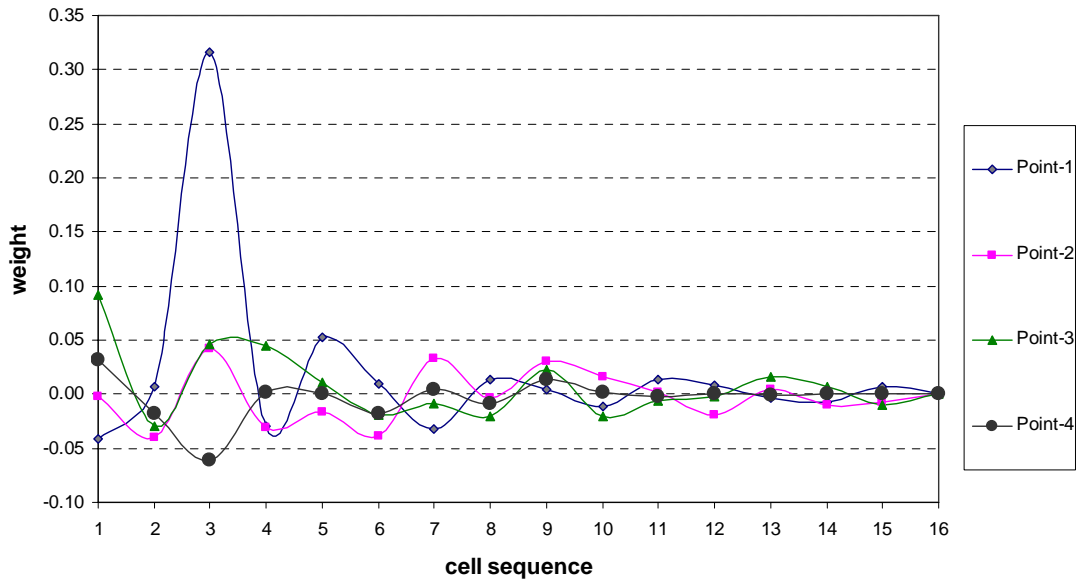


Figure 7-8: The kriging weights of point data changes with simulation path.

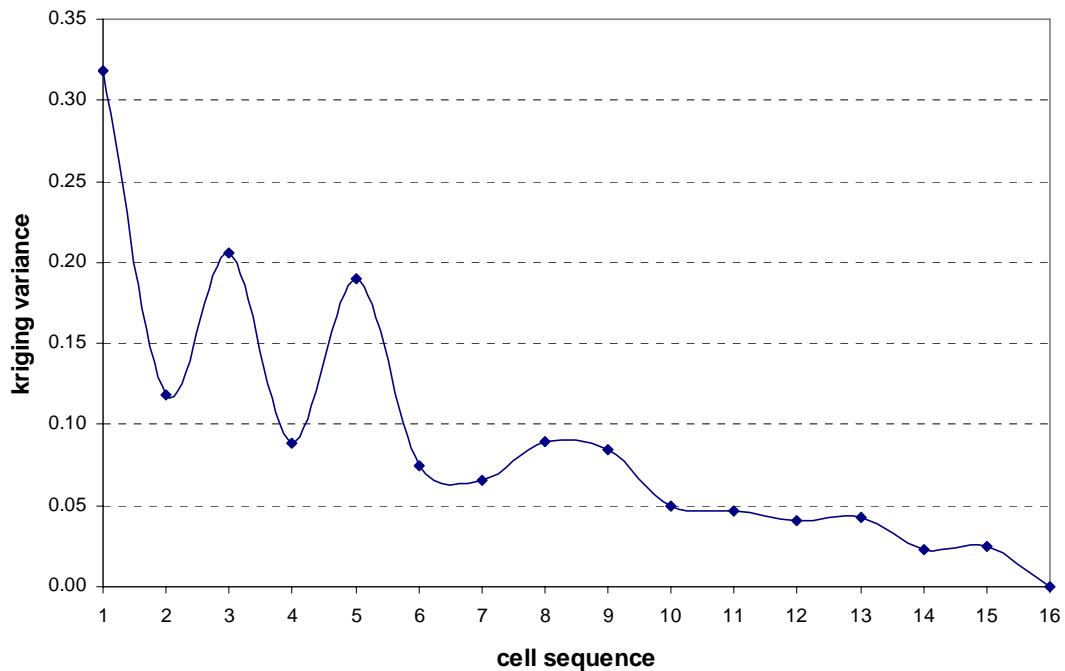


Figure 7-9: The kriging variance changes with simulation path

7.3 Implementation Details

7.3.1 Global mean

The mean of the block data should be used as the global mean because the block data are exhaustive over the entire model area. The mean of sampled point data may be different from the block data mean. Declustering of point data would reduce the difference; however, this is accounted for when modeling at the large scale and not during downscaling.

7.3.2 Discretization level

A large level of discretization between block scale and point scale can cause a very high computational time and low precision of simulated results. To downscale a 3-D model in three directions with a discretization number of 4, we require 4,096 point scale

covariance calculations for the block covariance when model at the point scale. If the discretization number between the model scale and point scale is 4 in three directions, 16,777,216 point scale covariance calculations are required. Such a large number could cause round off error and the block data may not be exactly reproduced. Increasing the data precision will require even more computational space and time. Covariance lookup tables for all three scales are necessary to reduce the computational time.

The EDDSS requires all the previously simulated cells in the block to be used. The kriging system includes the collocated block datum, the nearby point data and the nearby previously simulated cells. A large discretization number will give a large kriging system. Solving a large system requires significant computational cost. To avoid using a large discretization number, it is recommended to construct a fine scale 3-D model by building a 2-D model at the fine scale and downscaling only in vertical direction.

7.3.3 Last cell correction in EDDSS

As stated in Section 7.2, the block datum starts to take control and screens out the previously simulated cells in the last few cells, and forces the block data to be exactly reproduced at the last cell in EDDSS. The good side of the block value control is the block data are exactly reproduced; the bad side is that the simulated value of last cell may be out of the valid data range. Some post corrections or re-simulation in such blocks may be required. Actually, an invalid value in the last cell indicates an error in the values of the previously simulated cells. Re-simulation of all the cells in the block with a new random path would be more appropriate than directly modifying the simulated values of those cells.

7.3.4 Simulation path

In Sequential Gaussian Simulation, it is preferred to use a random simulation path for all the cells of the model. However, if used in EDDSS, such a simulation path results more invalid values in the last cells because it does not emphasize the local block data control. It also makes the corrections or re-simulation of a block difficult to apply during

the simulation process. To emphasize the local block data control, the simulation path in EDDSS consists of two sets of random orders: one random order is assigned to all the blocks in the model; another random order is assigned to all the cells in a block. The simulation is to randomly simulate each cell in a block, then cycle over all blocks. One advantage of this simulation path is easy to apply re-simulation of a block during the simulation process.

7.3.5 Search strategies

Exact downscaling methods require a search for nearby block data, point data, (and previously simulated data in EDDSS). Different data scales require different search strategies. There is no need for a block data search for EDDSS because only the collocated block is used. The super block search (Deutsch and Journel, 1998; Zanon, 2004) could be used for point data because well (point) data are normally non-gridded data. The spiral search (Deutsch and Journel, 1998; Zanon, 2004) could be used for the previously simulated nodes because they are regularly gridded. There are two parts of previously simulated nodes: inside the block and outside the block. All the simulated nodes inside the block need to be included according to the theory. A maximum number of nodes outside the block need to be specified. An octant search (Deutsch and Journel, 1998; Zanon, 2004) could be used to restrict the number of nodes from any one nearby block. This avoids all of the nodes coming from one closest block.

7.4 Histogram Reproduction and Proportional Effect in EDDSS

Histogram reproduction and proportional effect are two major challenges with direct sequential simulation (DSS). When performing sequential Gaussian simulation (SGS), the kriging mean and variance fully characterize Gaussian distributions of uncertainty at each location. The simulated values are drawn from the distributions and back transformed into original units using the input global histogram. The global histogram is always reproduced with minor fluctuations. In direct space, the kriging mean and variance are not adequate to describe the local distributions because the shapes of the

distributions are not known. Without multivariate Gaussian model, DSS requires some means to determine the local distributions and to reproduce the global histogram.

Several approaches have been proposed to solve the problem. The post processing methods (Journel and Xu, 1994; Caers, 2000) can exactly reproduce the global histogram. However, they remove the variability or uncertainty caused by ergodic fluctuations from the final realizations. Nowak and Srivastava (1997) proposed a method to build local distributions by extracting subsets of values from a large amount of data that follow the global distribution. This approach is not really successful because of lack of suitable subset at the end of simulation. Soares (2001) proposed a method that follows the idea behind SGS. The local distributions are Gaussian distributions defined by the mean that normal score transformed from the SK estimate, and the standardized SK variance. The simulated values are drawn from these Gaussian distributions and back transformed using the global histogram. However, normal score transform of the mean does not necessarily give the mean in Gaussian unit. It is biased to transform directly the mean using the non-linear transformation. Quantiles can be transformed without biases. Deutsch *et al.* (2001) proposed a method to use Gaussian transformation of a series of quantiles of local Gaussian distributions into direct space to build a lookup table of local distributions. This method has been established with program coding and detailed explanation (Oz *et al.*, 2003; Pyrcz and Deutsch, 2002). However, the proportional effect does not take into account, and the influence of minimum and maximum values is not addressed. The look-up table method is modified to account for the proportional effect and added in the EDDSS program for histogram reproduction.

7.4.1 The CCDF Look-up table method

There are three main steps in this approach. The first step is to build a complete list of all possible local Gaussian distributions. In SGS, the kriged mean is normally between -3 and 3, and the kriged variance is between 0 and 1. Therefore, all Gaussian distributions with mean between -3 and 3 and variance between 0 and 1 should be included in the list. However, there are some distributions affected by the minimum and maximum values should never being used. The discussion on this will be presented later.

The second step is that, for each local Gaussian distribution, a series of quantiles are transformed into original units to build the conditional cumulative density function (CCDF) of a local distribution. This can be defined by the following equation and the graphical representation of the transformation is shown in Figure 7-10.

$$Z_L(q) = F^{-1}[G_{\{0,1\}}[G_{\{m,\sigma\}}^{-1}(q)]]$$

where q is a quantile; $G_{\{m,\sigma\}}^{-1}(q)$ is inverse of Gaussian distribution with mean of m and standard derivation of σ , which gives “Val1” in Figure 7-10; $G_{\{0,1\}}[]$ is standard Gaussian distribution, which gives “Val2” in Figure 7-10; $F^{-1}[]$ is inverse of global distribution, which gives “Val3” in Figure 7-10.

The third step is to calculate mean and variance of each local distribution and use them as the index of the look up table of local distributions. In the progress of DSS, the local kriging mean and variance are matched with the index to find the CCDF of the local distribution. Then, the simulated value is drawn randomly from the distribution.

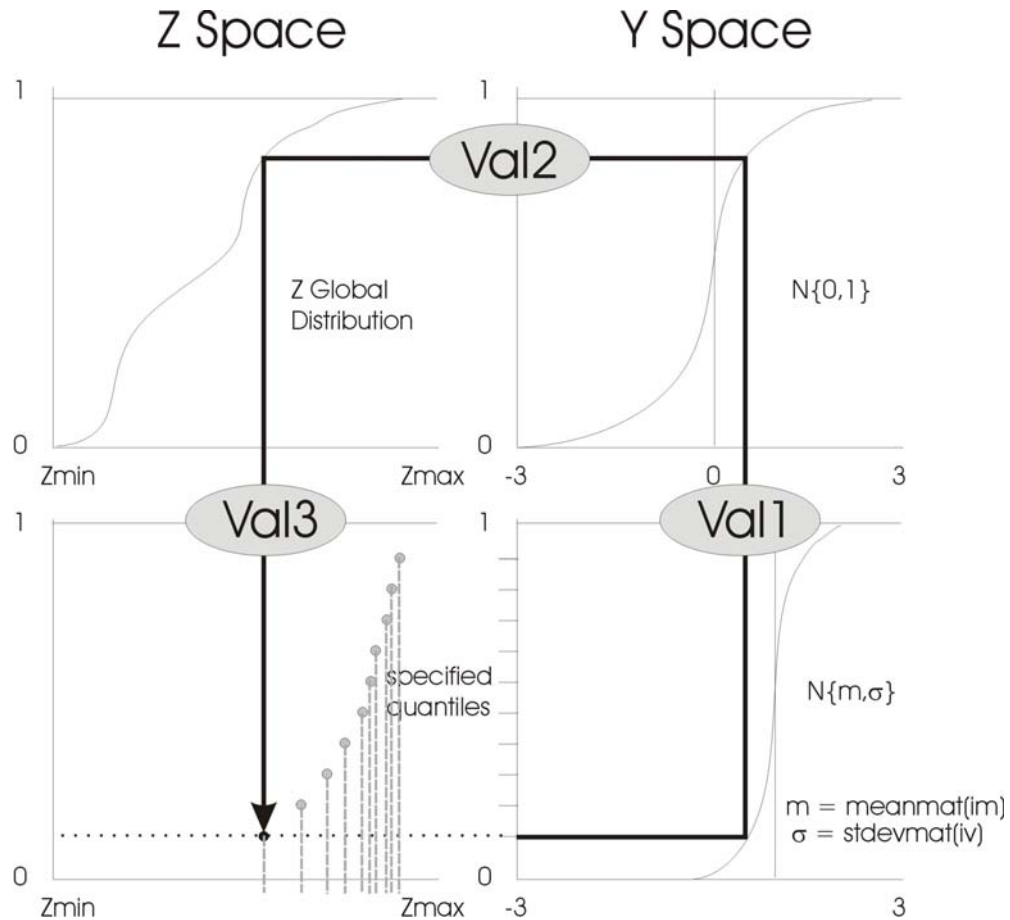


Figure 7-10: The graphical representation of the transformations applied to calculate the local distributions of uncertainty. The illustrated transformation is repeated for a sufficient number of quantiles to describe the local distribution (from Pyrcz and Deutsch, 2003).

7.4.2 Proportional effect

Natural data always show a relationship between the mean and variance. A low variance is normally found in a low valued area, and a high variance is found in a high valued area. The variance is proportional to the mean value, thus it is commonly referred to as the proportional effect (Journel and Huijbregts, 1978) or in statistical terms called *heteroscedastic*. The proportional effect is normally identified from a cross plot of means and standard deviations calculated from a moving window method. The cone shape is the most common shape of the points in cross plots. The points are more spread when the mean is high. For simplicity, the relationship is always assumed to be linear, and linear regression is commonly used to characterize the relationship.

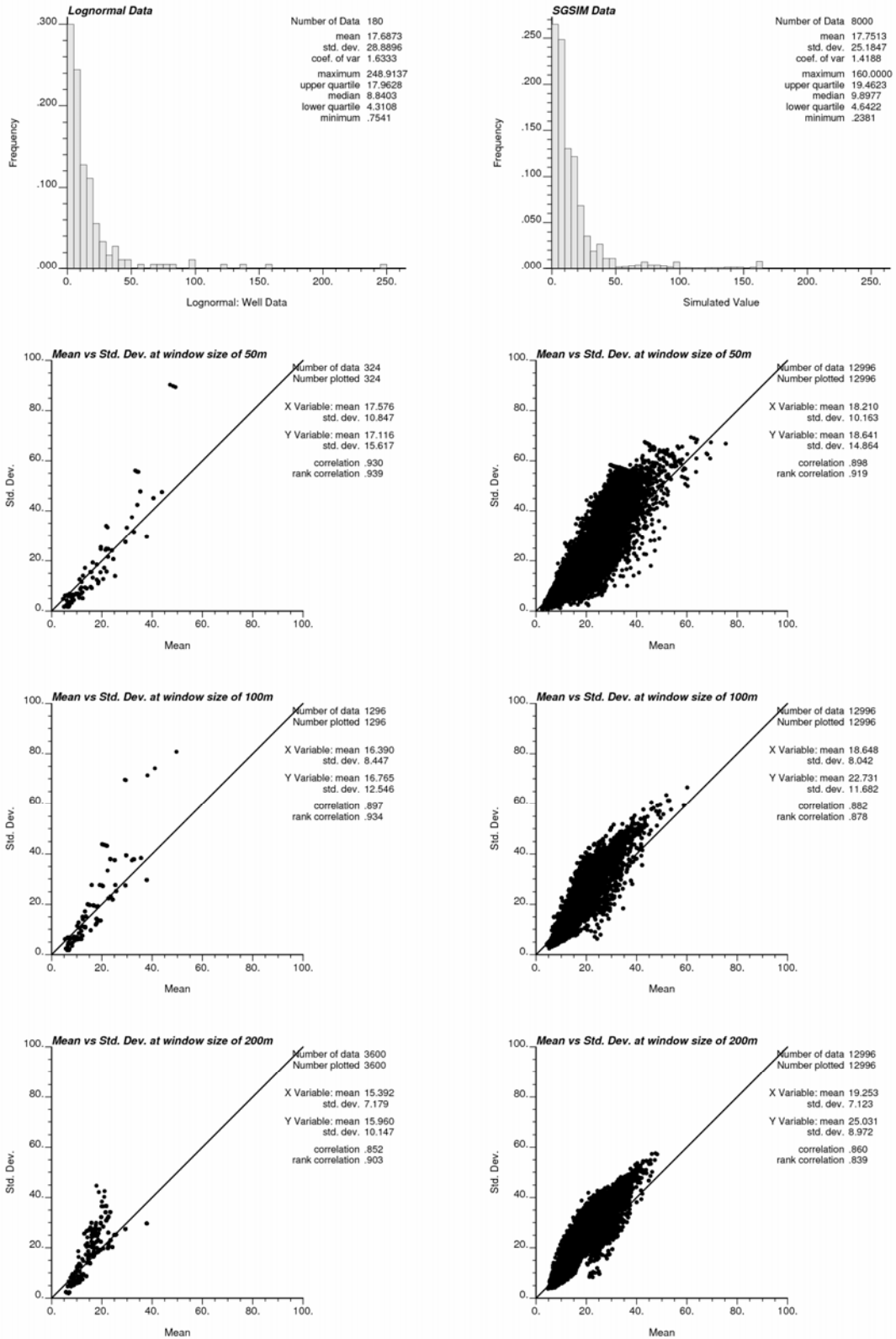


Figure 7-11: The proportional effect shown at different moving window sizes (50m, 100m and 200m). The two sets of data are used (the first row): a set of well data (left) and the sgsim realization using the well data (right). The correlations are different with different window sizes.

Figure 7-11 shows some cross plots of mean vs. variance calculated at different window sizes. It appears that the relationship is also dependent on window size. The correlation decreases as the window size increases. Thus, the correlation must be established at the correct window size that consistent with the support volume of data. In EDDSS, because the block data are exhaustively available, a block size window will be appropriate.

Kriging variance is calculated basing on the data configuration and spatial correlations (Isaaks and Srivastara, 1996). It is independent from data values and the kriging mean. This feature is named *homoscedastic*. For example, Figure 7-12 shows two blocks that have four points. The only difference between the two blocks is the lower right point values (one is 20 and another is 200). The kriging estimates are different at the estimate location; the kriging variances are same. Based on the surrounding data values, we would expect a short-range local distribution for the left block and a long-range local distribution for the right block (Figure 7-12). Thus, kriging variance does not reflect the variance of local distribution. The proportional effect must be accounted for to get the correct local variance.

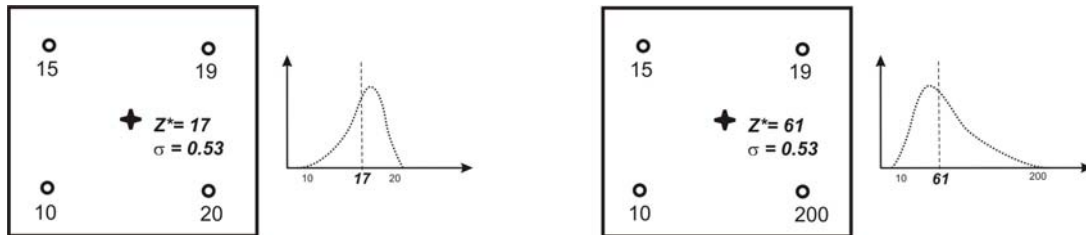


Figure 7-12: The local distribution and variance are affected by the data values.

The proportional effect at the block scale can be calculated using available point data. If there is a strong linear relationship between the calculated variances and block values, we can fit a linear relationship between them:

$$\sigma_b = a + bm_b$$

where the σ_b is the standard derivation at the block scale; a and b are constants; and the m_b is the block value.

Using this relationship, we can calculate the local standard derivation at any block because the block values are known. According to Isaaks and Srivastara (1996), the proportional effect can be taken into account by multiplying the calculated variance with the kriging variance to get the modified local variance for each cell in a block: $\sigma' = \sigma_b \times \sigma_{sbck}$. The multiplication will not affect the exact downscaling because the modified variance is zero at the last cell. Thus, the global mean can be reproduced. However, accounting for the proportional effect makes it difficult to reproduce the global variance. The proportional effect may not be fully described by a simple linear function. The fitted linear function may over modify the local variances resulting in the final global variance being too high or too low. Further research is needed for a better way to characterize proportional effect.

7.4.3 Discussion on the CCDF table method

The CCDF table method provides local distributions for DSS and may produce histograms that are close to the input histogram (Deutsch *et al.*, 2001; Oz *et al.*, 2003). However, the method still has not been fully understood. One problem is the CCDF table can not provide all the local distributions required by the kriging mean and variance. There are always some kriging means and variances that fall outside of the CCDF table (Figure 7-13 and Figure 7-14). It requires a matching method to choose a CCDF from the table that closely matches those kriging means and variances. Different matching methods will affect the simulation results and give different final histograms.

The mean and variance from CCDF table are bounded by maximum and minimum values. The cross plots of the mean and variance are always shown in a bell shape (third row left in Figure 7-13 and Figure 7-14). The points in the middle show that same mean may have very different variances. When mean is close to the maximum and minimum values, it always has a low variance. The distributions with high mean and low variance should not be used if proportional effect presents in the data. The kriging mean sometimes can be very high or very low, even below the minimum or above the maximum. These kriging means are difficult to be considered as means of local distributions. They must be adjusted to be a valid value. The adjustment can be

performed with a matching method by taking a close pair of mean and variance from CCDF table. Figure 7-13 shows the CCDF lookup-table method results with a lognormal global distribution. The proportional effect (second row right in Figure 7-13) is accounted for in the DSS. The CCDF table of means and variances does not cover all the kriging mean and variances (third row in Figure 7-13). The results of matching mean and variance are shown in the bottom row. The high variances are adjusted to match the CCDF table variances. Figure 7-14 shows the CCDF lookup-table method results with a distribution shown in the top row. The proportional effect is not taken into account because it is not clearly shown in the cross plot (second row right). The CCDF table of means and variances does not cover all the kriging mean and variances. The results of matching means and variances are shown in the bottom row. The high and low mean and variances are adjusted to match the mean and variance from the CCDF table.

Although there are so many adjustments involved in the CCDF table method, this method works fine to reproduce symmetric distribution approximately. For highly skewed distributions, the analytical method based on lognormal distribution works better than the CCDF table method (Manchuk *et al.*, 2005). An a-posteriori histogram correction can be used to achieve histogram reproduction (Deutsch, 2005; Journel and Xu, 1994). However, there is a trade-off that the linear scale relationship can not be preserved and the block data can not be reproduced exactly.

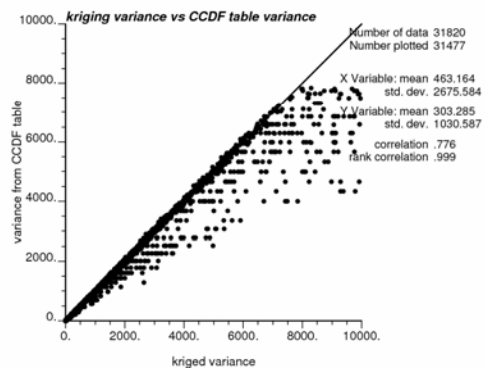
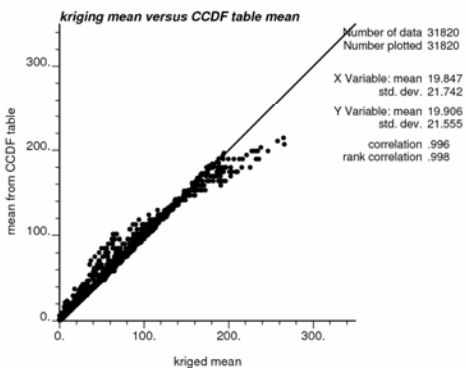
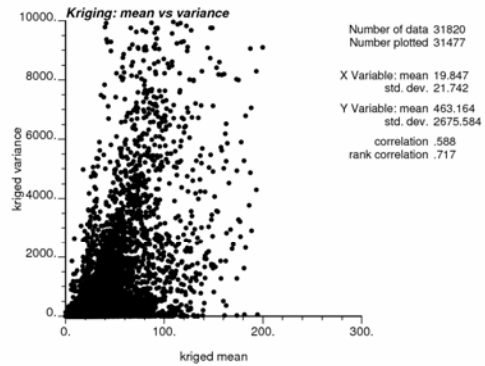
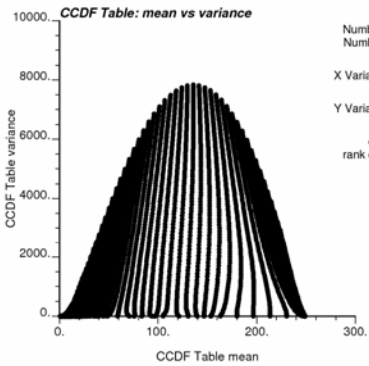
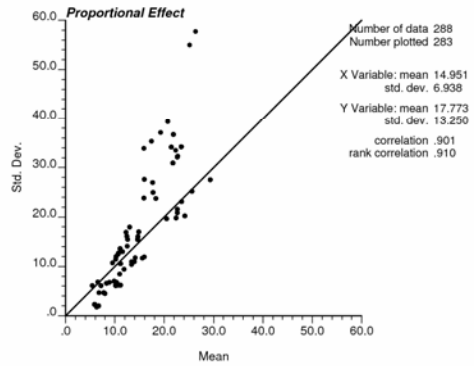
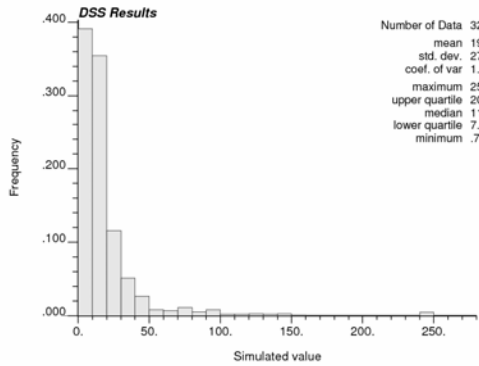
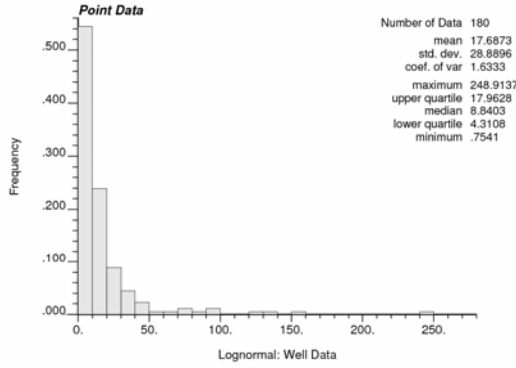


Figure 7-13: The CCDF lookup-table method results with a lognormal global distribution (top). The proportional effect is accounted in the DSS (second row). The CCDF table of means and variances does not cover all the kriging mean and variances (third row). The results of matching mean and variance are shown in bottom row.

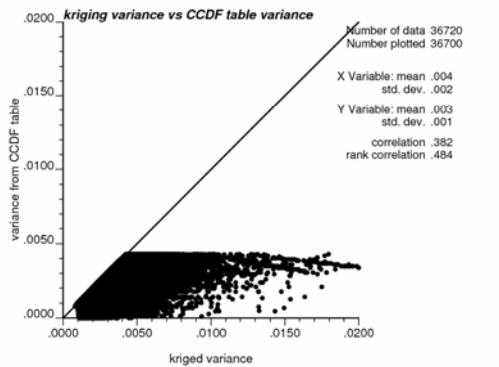
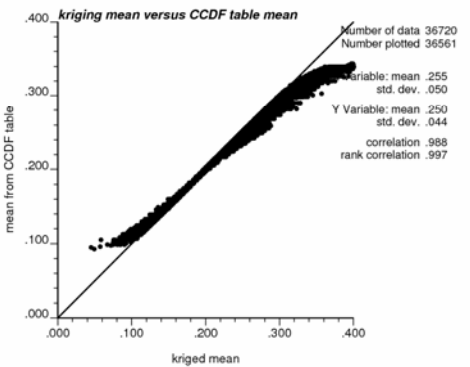
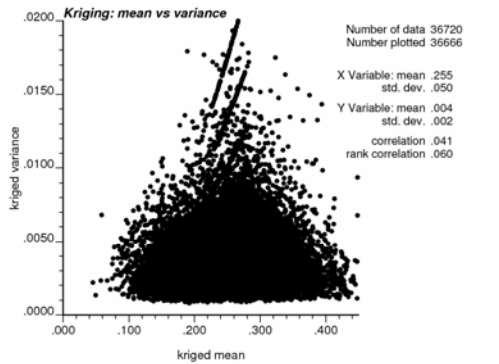
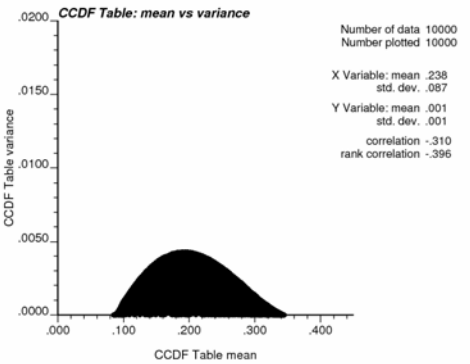
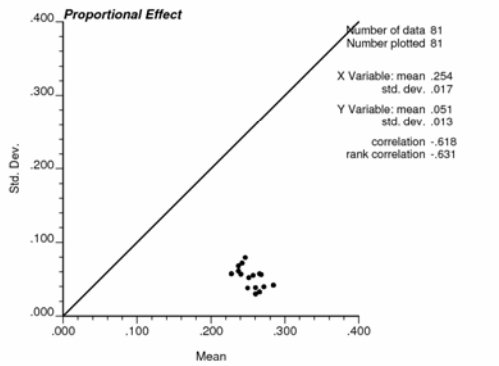
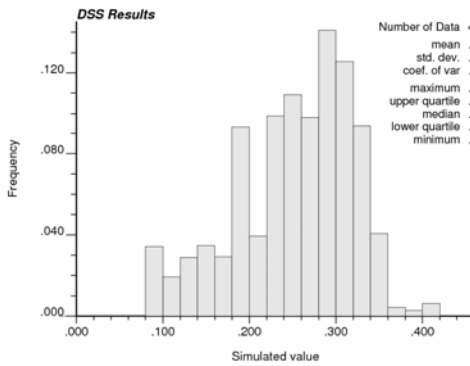
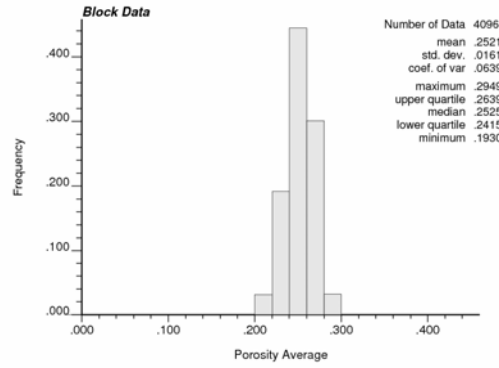
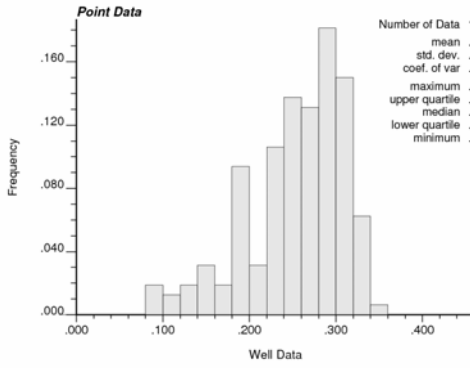


Figure 7-14: The CCDF lookup-table method results with a global distribution (top row). The proportional effect is not clear (second right). The CCDF table of means and variances does not cover all the kriging mean and variances (third row). The results of matching means and variances are shown in the bottom row.

7.5 A Large Example

The exact downscaling technique can be implemented in four steps: 1) data assembly; 2) variogram modeling; 3) exact downscaling using kriging or DSS approach; 4) checking the results.

7.5.1 Data assembly

Block data can be obtained from Bayesian updating results. It should cover the entire interested area for fine scale modeling. Well data are very important. The block and well data should be checked to ensure their consistency.

In this example, the interested area is about 4 sections, that is, approximately 3200m by 3200m. The porosity block data is taken from a large 2-D prior model at a scale of 50m by 50m for a 10m layer. The map and histogram of the block data are shown in Figure 7-15. There are 16 wells in the study area with log data. The locations of the 16 wells and the histogram of the well porosity data are shown in Figure 7-16. The mean of well data is close to the mean of block data. The variance of well data is larger the block data.

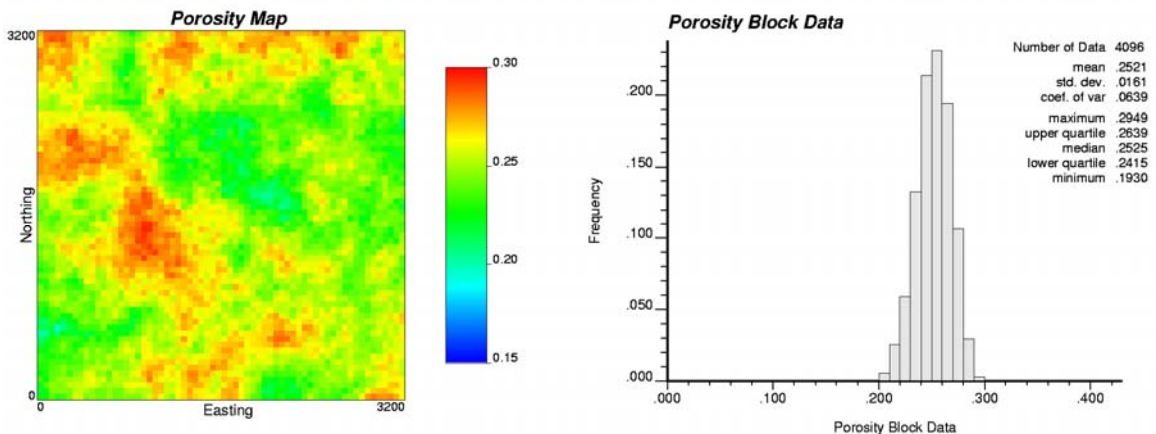


Figure 7-15: 2-D map of porosity block data at a scale of 50m x 50m x 10 m.

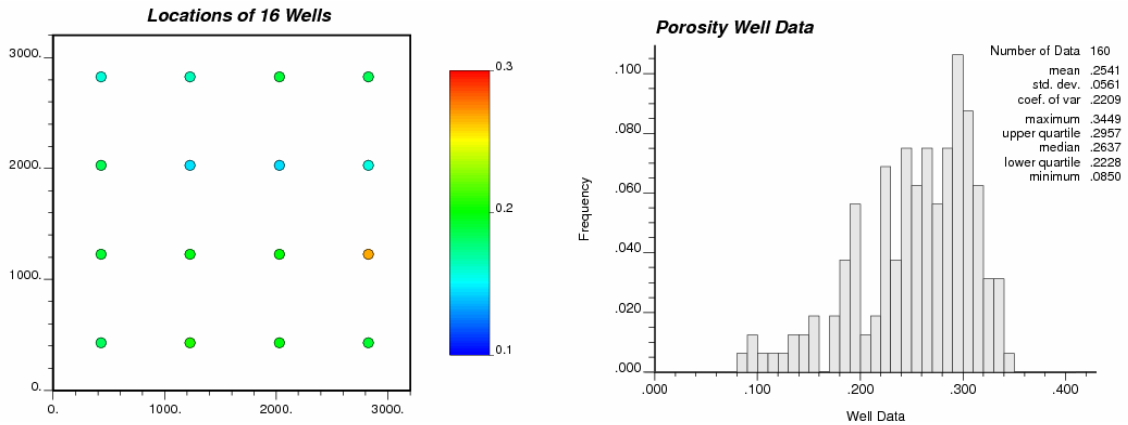


Figure 7-16: The location map of the 16 wells with the color scale showing porosity in fraction and the histogram of the well log porosity in the right.

7.5.2 Variogram modeling

Variogram should be calculated from the point data. If there is not enough point data available, the variogram model used for Bayesian updating of the 2-D mapping can be used. An omnidirectional horizontal variogram and a vertical variogram are calculated from the well log data, and are shown in Figure 7-17.

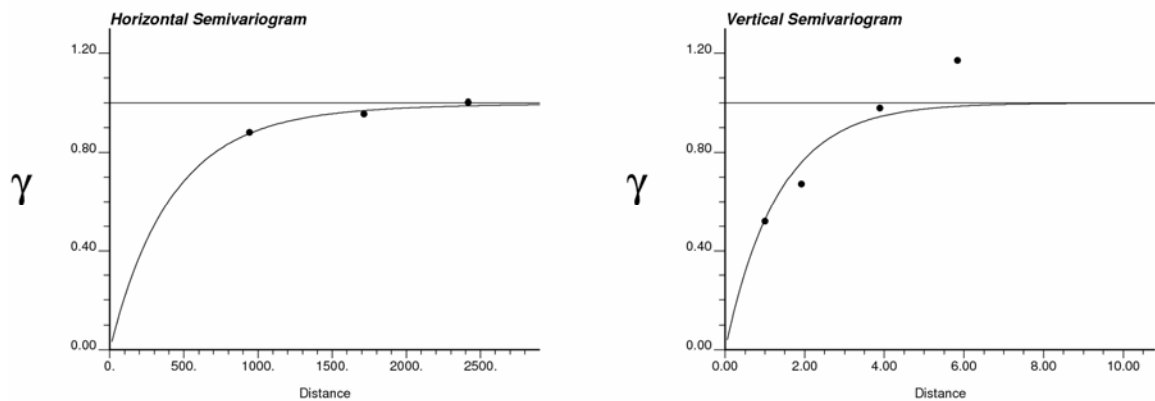


Figure 7-17: An omnidirectional horizontal variogram (left) and a vertical variogram (right).

7.5.3 Exact downscaling

The 2-D block data is extended to a 3-D model using both the EDDK and EDDSS methods. The block data are downscaled in the vertical direction to generate a 3-D model at scale of 50m by 50m by 1m. The 3-D porosity model from EDDK is shown in Figures Figure 7-18 to Figure 7-20. And the 3-D porosity model from EDDSS is shown in Figure 7-21 to Figure 7-23. The map of block porosity (top left) and all odd numbered x-y view slices of the 3-D model are shown together. The dashed lines in the block porosity map indicate the locations of the x-z and y-z cross sections. The x-z and y-z cross sections of the 3-D Model are shown in Figure 7-20 and Figure 7-23. The dashed lines in the x-z and y-z cross sections indicate the wells. The well data are reproduced. And the horizontal continuity is clearly shown in the cross sections. EDDSS realization has more variation than the EDDK result.

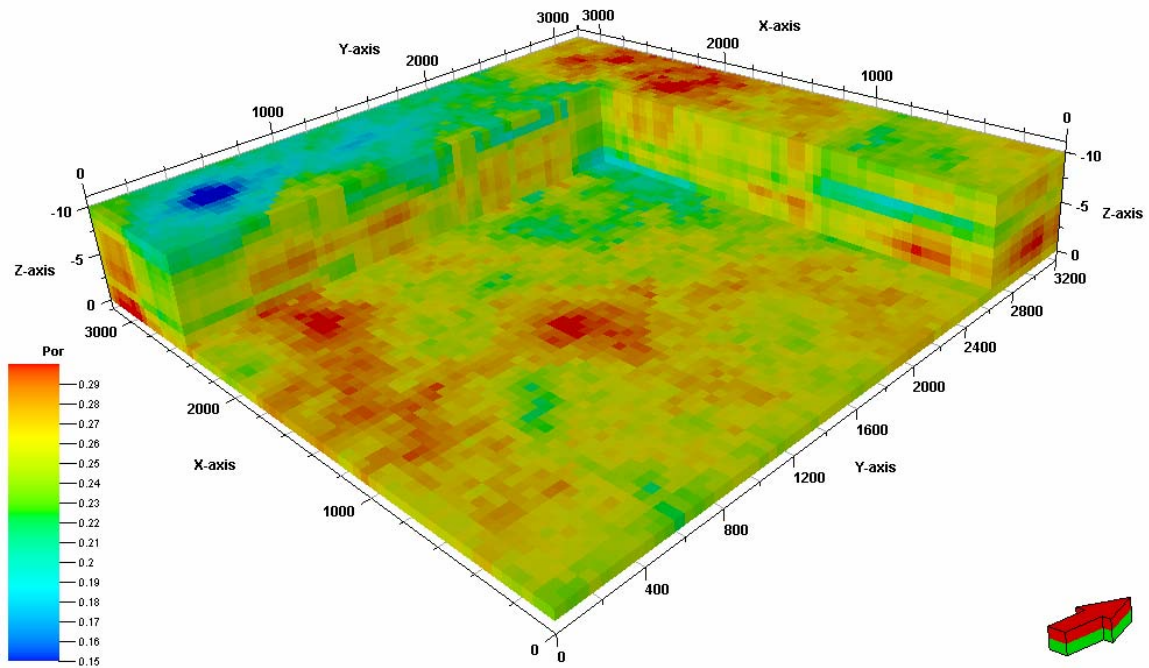


Figure 7-18: The 3-D porosity model from EDDK, the porosity is in fraction and the arrow is pointing to north.

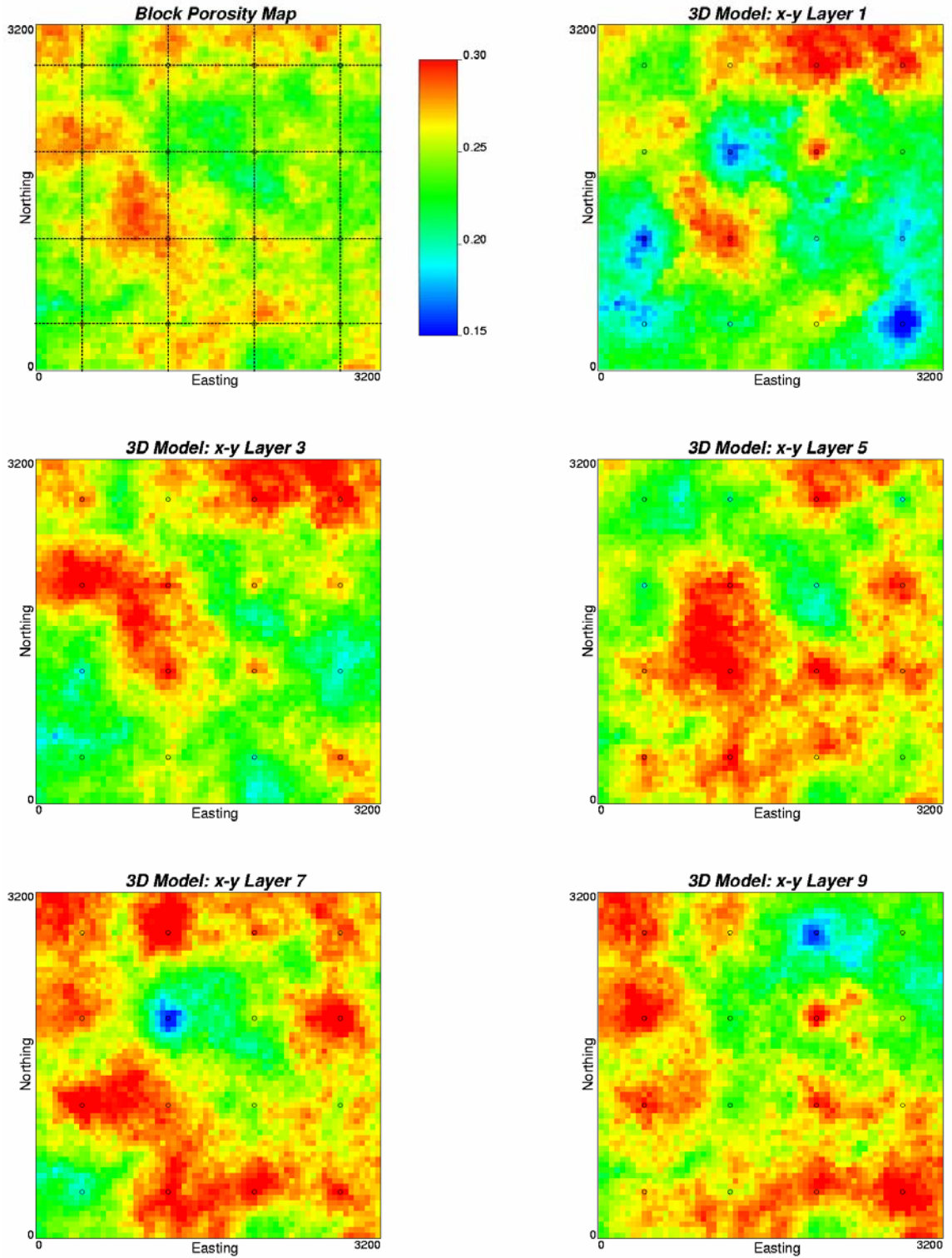


Figure 7-19: The 2-D porosity map and all odd numbered x-y view slices of the 3-D model from EDDK. The 3-D porosity is at the scale of 50 x 50 x 1m. The dashed lines in the porosity map (the top left) indicate the locations of the x-z and y-z cross sections, the porosity is in fraction.

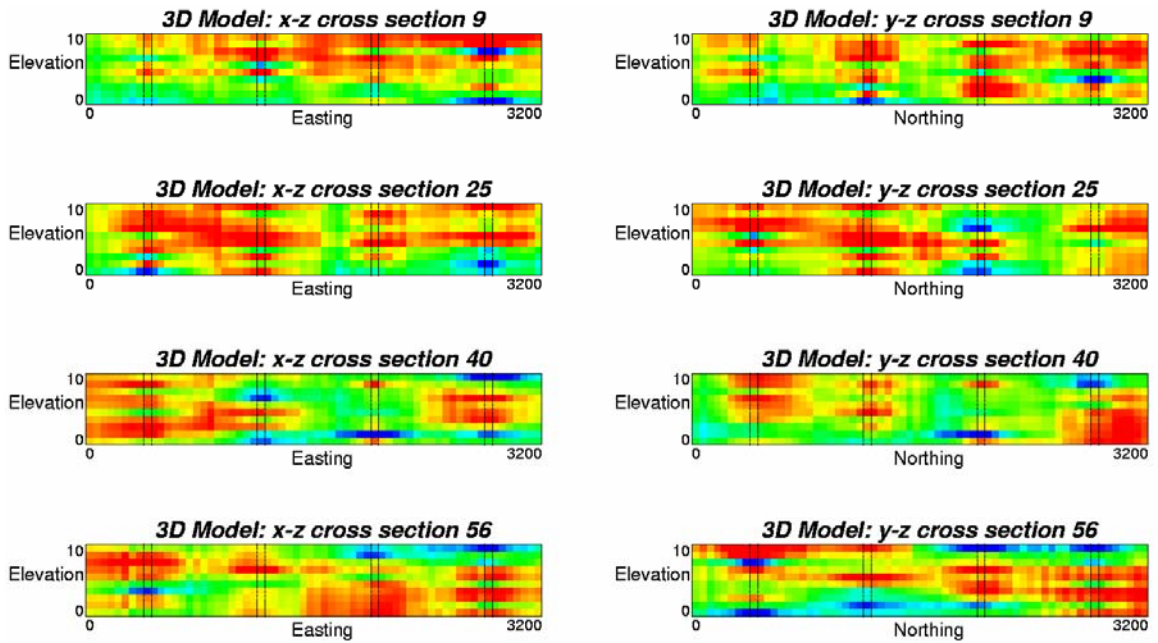


Figure 7-20: The x-z and y-z cross sections of the 3-D porosity model from EDDK. The 3-D porosity is at scale of 50x50x1m. The dashed lines in the x-z and y-z cross sections indicate the wells. The horizontal continuity matches the well data.

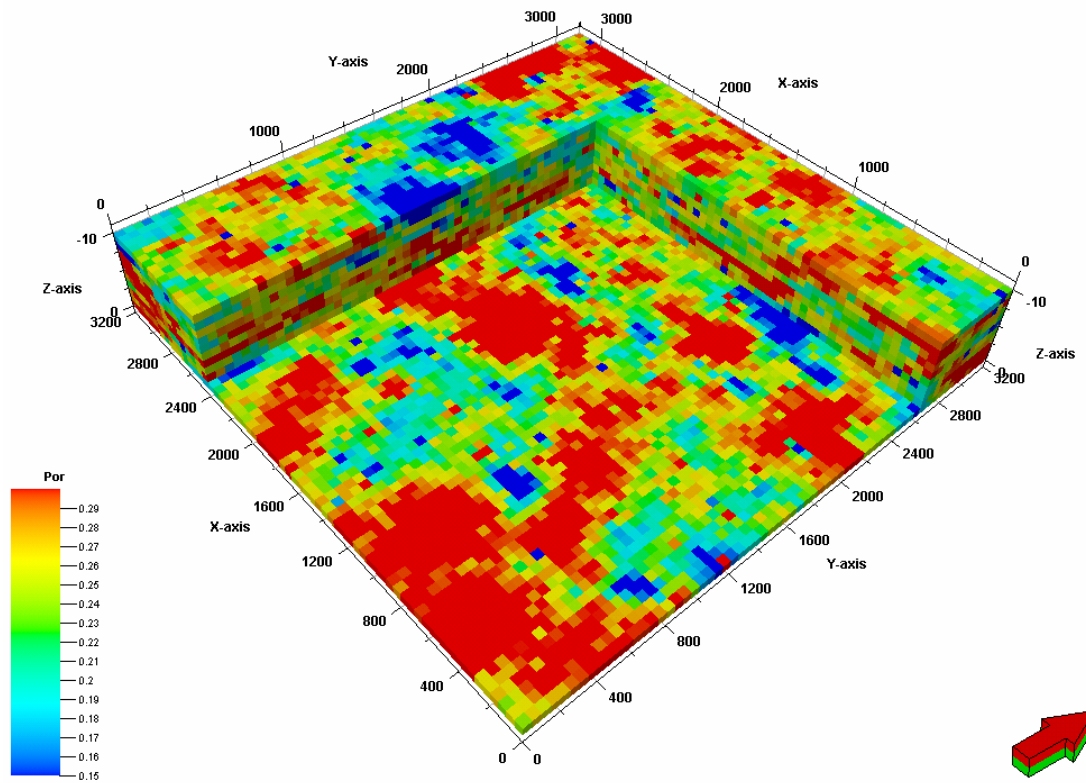


Figure 7-21: A 3-D porosity realization from EDDSS, the porosity is in fraction and the arrow is pointing to north.

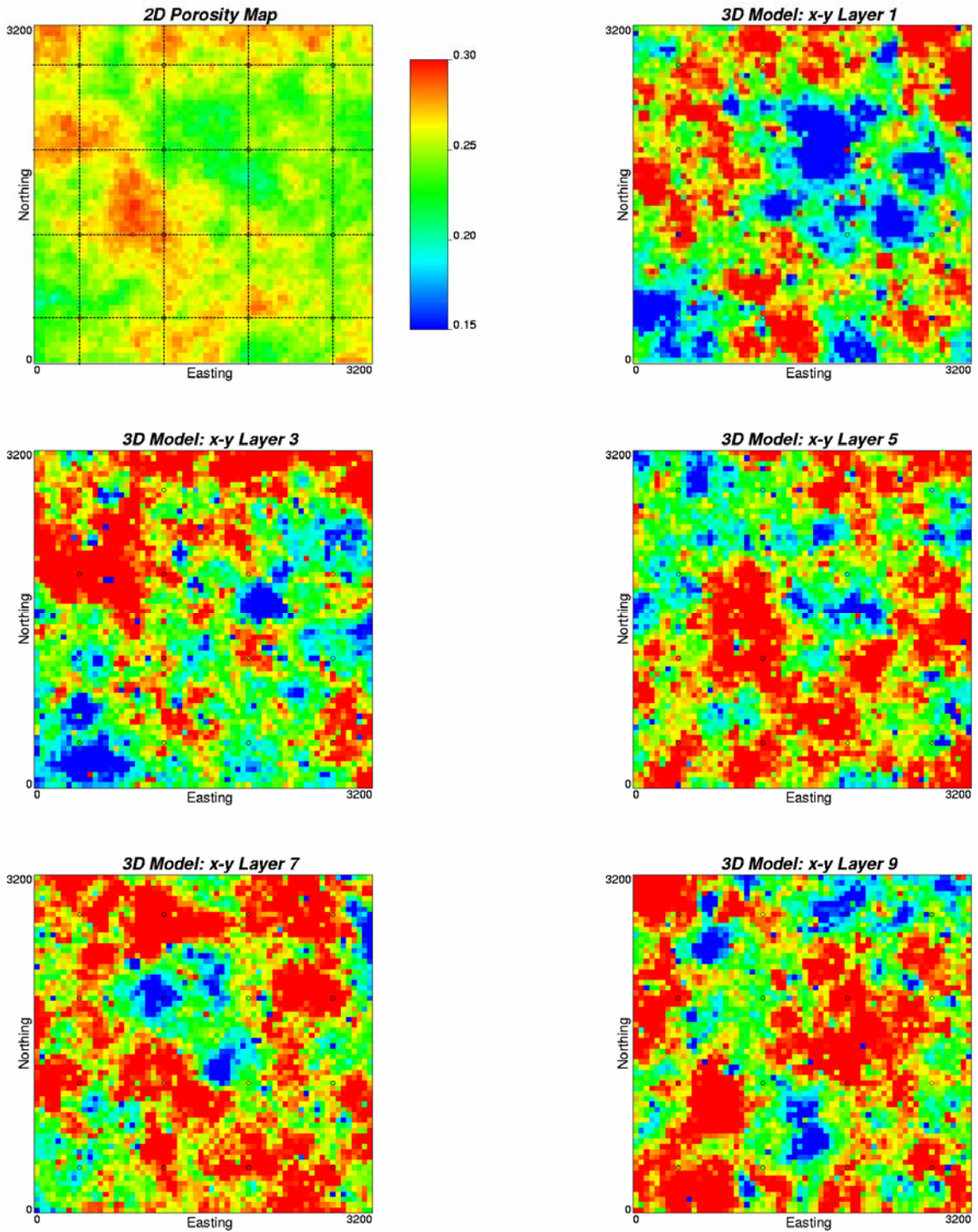


Figure 7-22: The 2-D porosity map and all odd numbered x-y view slices of the 3-D model from EDDSS. The 3-D porosity is at the scale of 50 x 50 x 1m. The dashed lines in the porosity map (the top left) indicate the locations of the x-z and y-z cross sections.

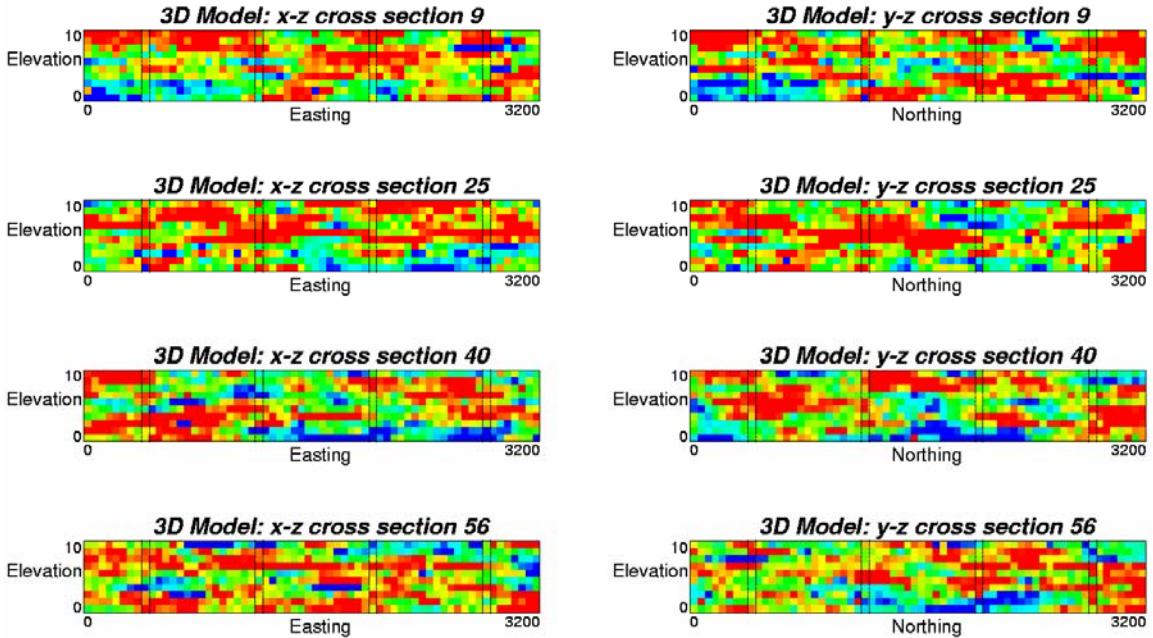


Figure 7-23: The x-z and y-z cross sections of the 3-D porosity model from EDDSS. The 3-D porosity is at scale of 50x50x1m. The dashed lines in the x-z and y-z cross sections indicate the wells. The horizontal continuity matches the well data.

7.5.4 Checking results

The 3-D model is converted back to a 2-D model using the arithmetic average of each column. The results are plotted together with the original 2-D porosity map and the cross plot of the two grids in Figure 7-24. After downscaling to a 3-D model and upscaling back to a 2-D model, the new 2-D map is exactly the same as the original map. The consistency between the two models confirms that the scaling method is exact.

The histogram of the downscaled porosity is shown in Figure 7-25. It shows that the mean is same as the mean of block data (Figure 7-15), and the maximum and minimum values are same as the point data (Figure 7-16). Because kriging estimates are smooth, a standard deviation of 0.0282 falls between the block data (0.0161) and the point data (0.0561). The variance of the EDDSS realization is close to the point data variance.

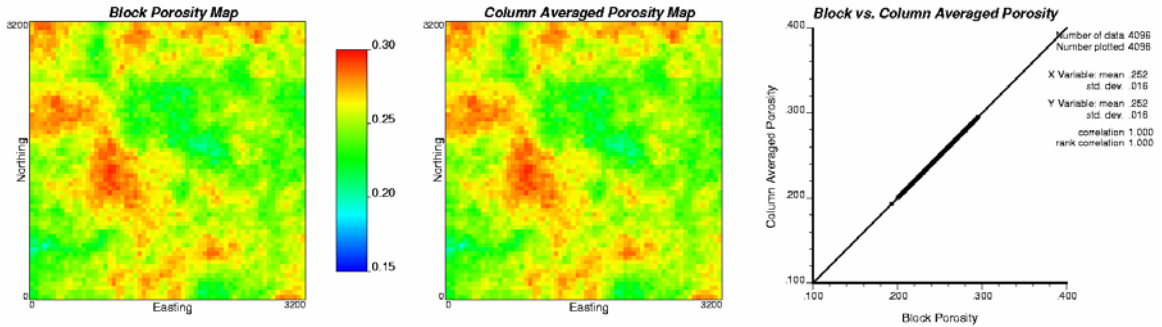


Figure 7-24: The block 2-D porosity map (left), the map of the column averaged porosity from the 3D model (middle), and the cross plot of the two grids (right) indicates the exactness. The porosity is in fraction.

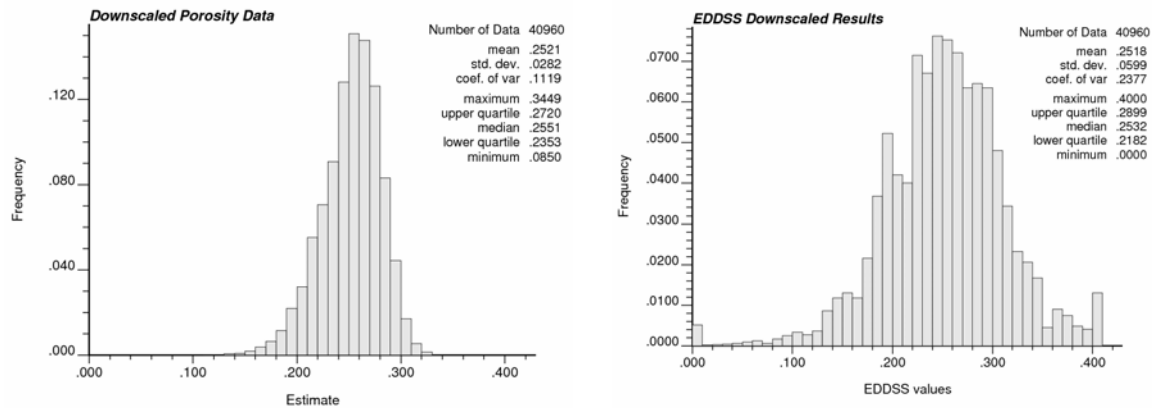


Figure 7-25: The histograms of the fine scale porosity estimated from EDDK (left) and simulated from EDDSS (right). The means are close to the input well data mean (Figure 7-16). The standard derivation of EDDK is small because of the kriging smoothness.

7.6 Comparison between Exact Downscaling and Approximate Downscaling Methods

Approximate downscaling is always possible with geostatistical methods: co-kriging, collocated co-kriging, and using the block data as locally varying mean can be used to construct fine scale 3-D model with larger scale data. A comparison of the 3-D models constructed by exact downscaling method and approximate downscaling method is conducted to show the difference in flow simulation results made by the downscaling methods.

A synthetic dataset was created based on some 2-D large scale models generated from the Surmont lease. The geostatistical 2-D realizations were constructed over 100s of square kilometers at an areal resolution of 100m square. After selecting the locations of SAGD well pairs, a small area (800m by 200m) around a particular SAGD well pair was extracted from the 2-D models and downscaled areally to 20m by 2m. Then, the EDDSS and an approximate downscaling method were used to extend the 2-D model to 3-D models. The approximate downscaling was using SGS with block data as locally varying mean. The 3-D models were used in the thermal simulator, CMG Stars, for flow simulation around a pair of horizontal wells. The 3-D models and flow simulation results were compared.

The 2-D porosity data used as block data are shown in a map and a histogram in Figure 7-26. The location map of the 8 delineation wells in the study area and the histogram of well data are also shown in Figure 7-26.

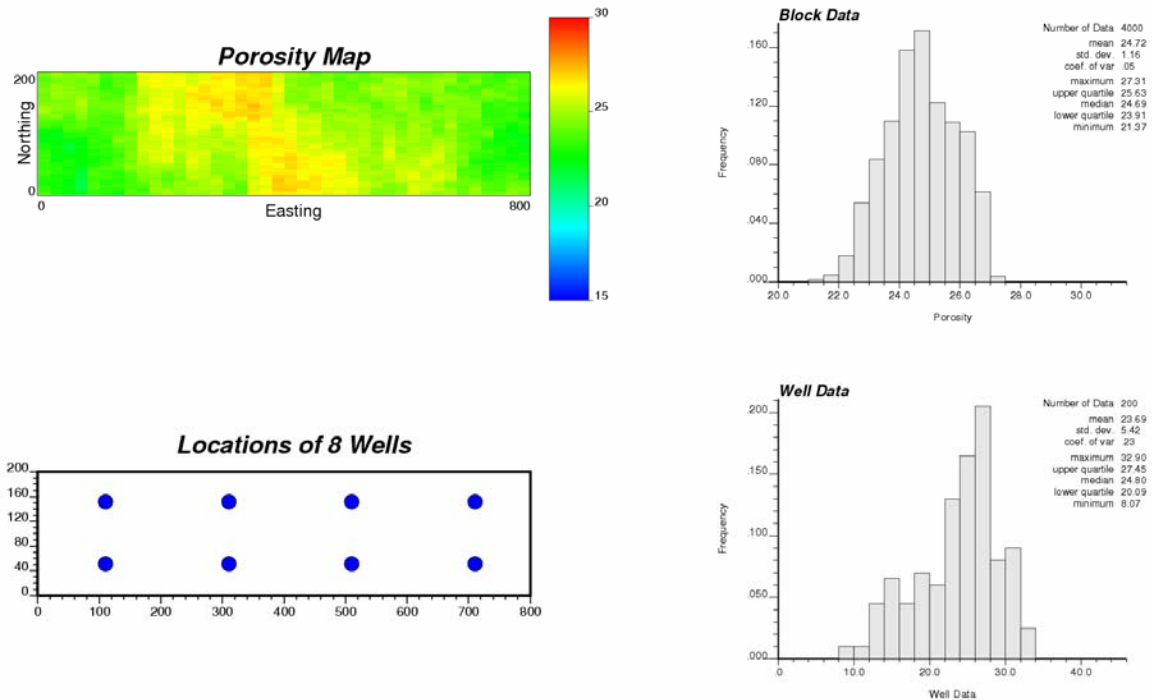


Figure 7-26: The porosity block data (top) and well data (bottom) used for downscaling. The porosity is in percentage.

The EDDSS was used to downscale the block data to a vertical resolution of 2 m from a total thickness of 100 m. The results are shown in Figure 7-27. The first row illustrates plane views of the 3-D model at the layers of 20 and 40. The remaining images show different slices of the 3-D model in y-z and x-z cross sections. The heterogeneity at the fine scale clearly presents in the cross sections.

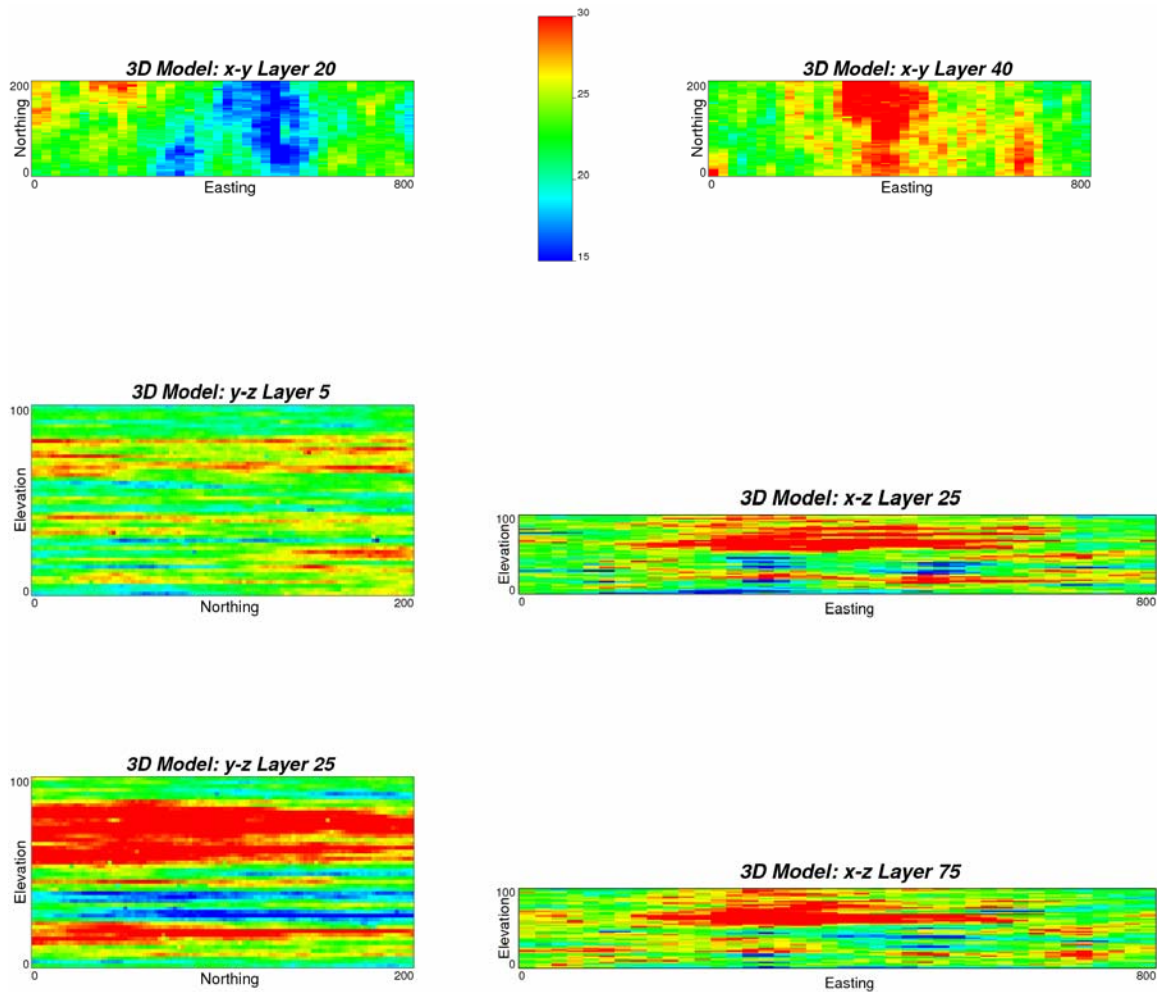


Figure 7-27: The exact downscaling results: 3-D porosity model in plane view (first row), y-z (left) and x-z (right) cross sections. The porosity is in percentage.

An approximate downscaling method was used to generate a 3-D model from the 2-D block data. Sequential Gaussian simulation was performed using the well data, and the block data were input into the simulation as the locally varying mean (Deutsch and Journel, 1998). The results are shown in Figure 7-28.

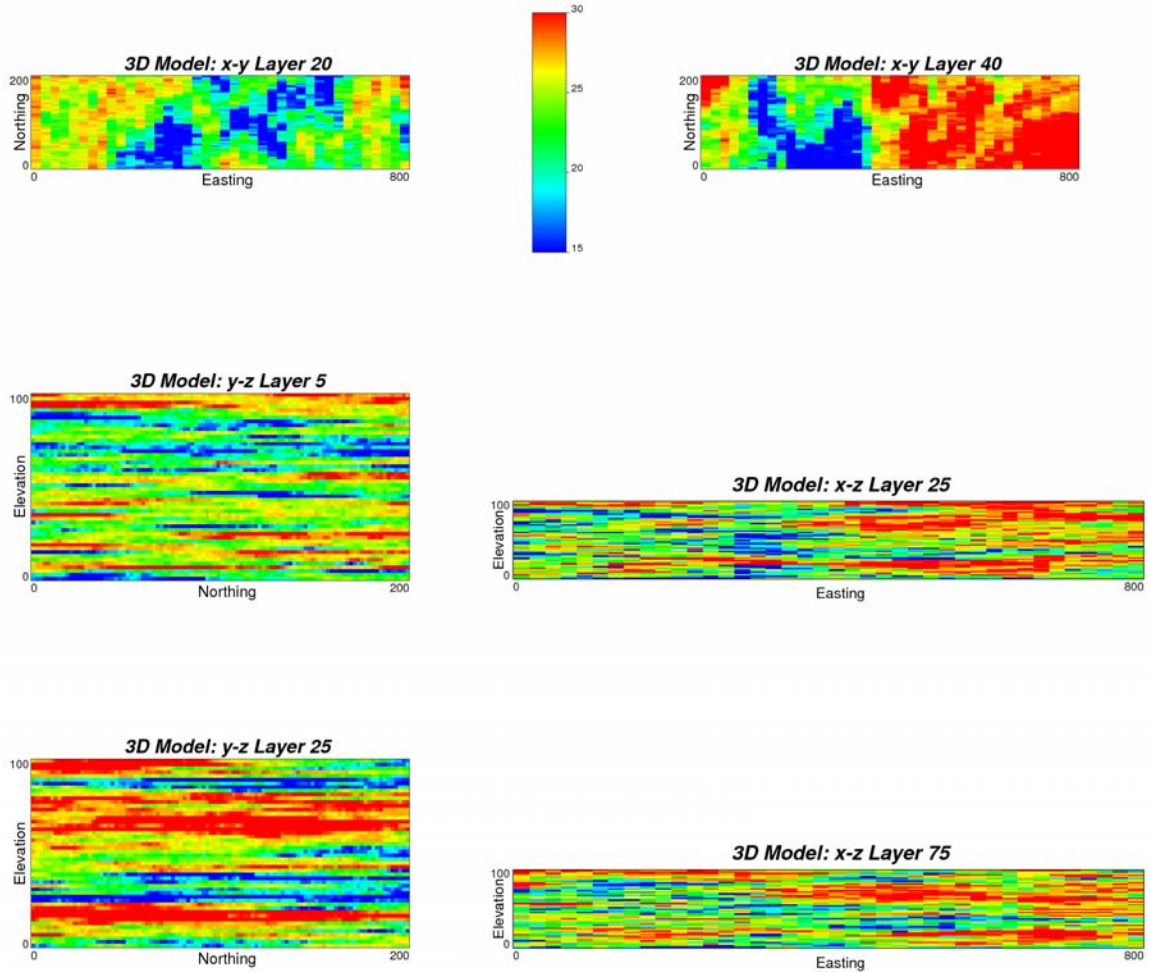


Figure 7-28: The approximate downscaling results in plane view (first row), y-z (left) and x-z (right) cross sections. The porosity is in percentage.

Both 3-D models were converted back to 2-D maps using the arithmetic averaging of each column. The results are plotted and shown together with the original 2-D porosity map in Figure 7-29. The averaged porosity map from the exact downscaled model is identical to the original 2-D map; but the average porosity map from the approximate downscaled model is quite different. The cross plots of column averages versus block data for the approximate downscaling method and the exact downscaling method are shown in Figure 7-30. The fine scale 3-D model generated with the approximate downscaling method is inconsistent with the initial coarse scale model; however, the model from the exact downscaling method matches exactly. A few points off the 45° line are caused by numerical instabilities in the matrix solutions.

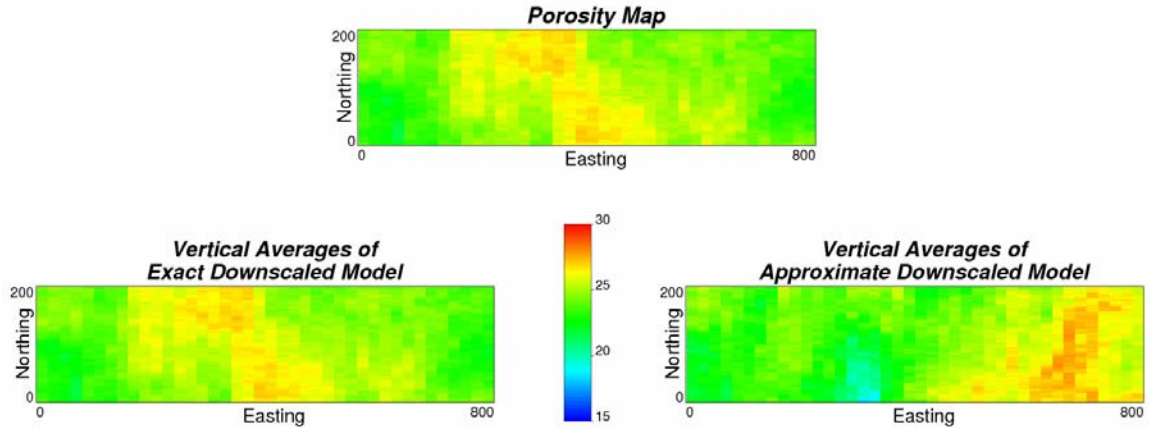


Figure 7-29: The map of original porosity block data (top), the map of vertically averaged porosity from the exact downscaled 3-D model (left) and the map of vertically averaged porosity from the approximate downscaled 3-D model (right). The porosity is in percentage.

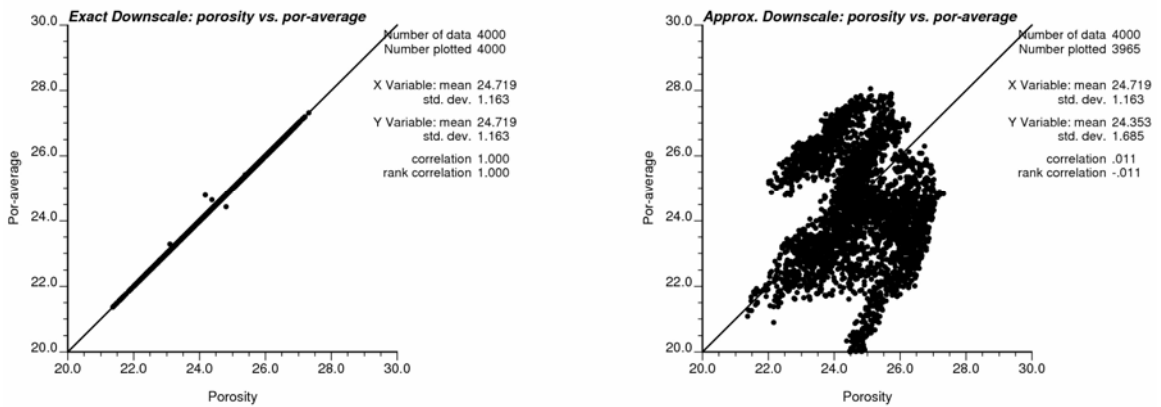


Figure 7-30: The cross plots of porosity block data vs. block average of fine scale model for the exact downscaling method (left) and the approximate downscaling method (right)

Flow simulations of a SAGD well pair using the 3-D models were conducted. The results are shown in Figures 31 and 32. There is a large difference between the results using the two downscaling methods. The steam chambers developed after 5 years of steam injection indicate a much larger chamber for the exact downscaled model than the approximate downscaled model. The nearly double-sized steam chamber results in a nearly doubled oil production for the exact downscaled model (Figure 7-32). With more steam injection required to develop the steam chamber, the approximate downscaled model indicates a higher cumulative steam oil ratio (CSOR) than the exact downscaled

model (Figure 7-31). This will not always be the case of course, but this shows the sensitivity of the results to the downscaling methodology.

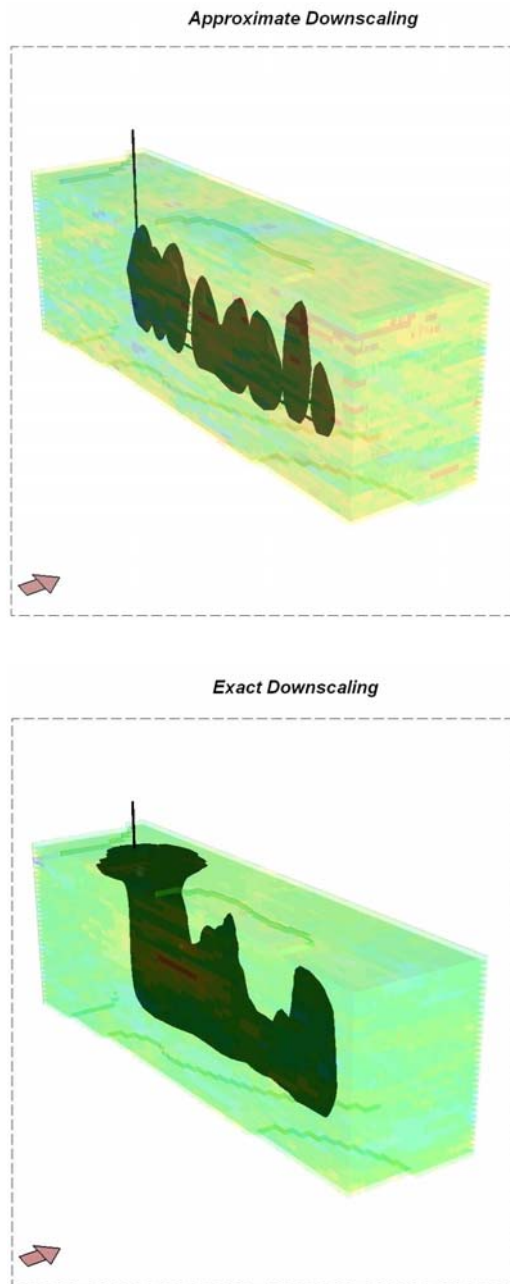


Figure 7-31: The steam chambers after 5 years of steam injection. The model by exact downscaling (bottom) developed a nearly double-sized steam chamber than the approximate downscaled model (top).

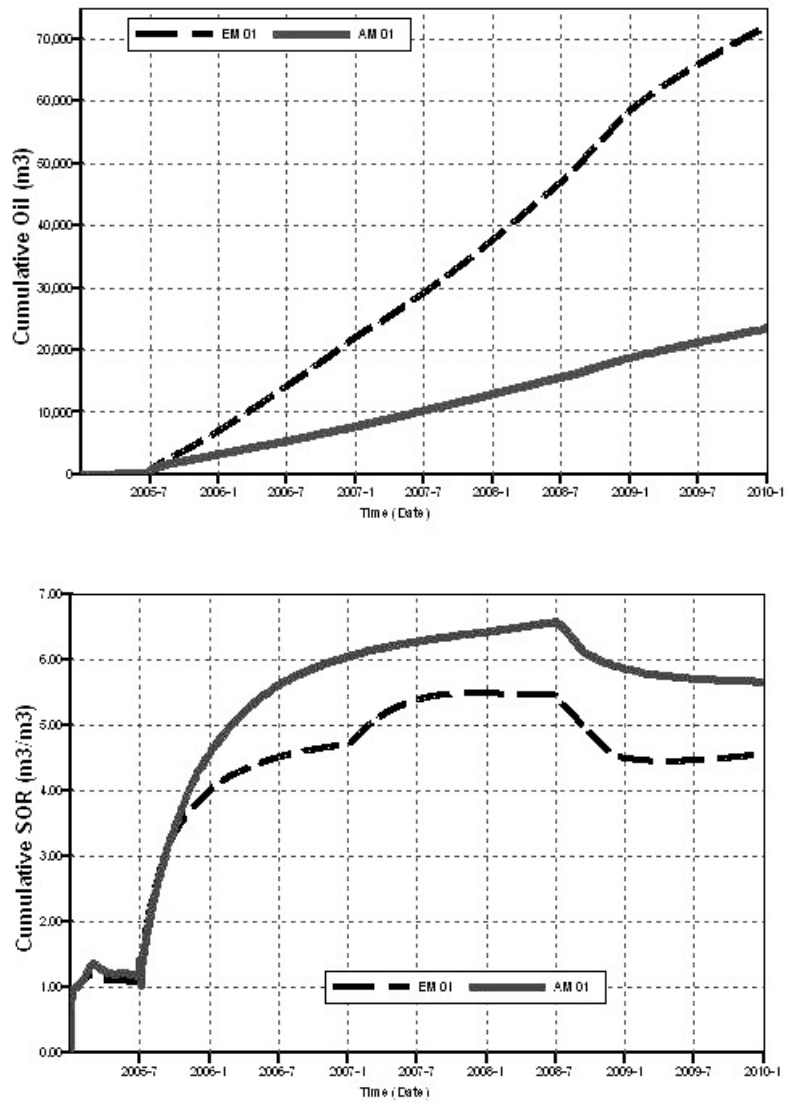


Figure 7-32: The results of flow simulation using the models generated by the two methods: the top plot is the cumulative oil production curves, and the bottom plot is the cumulative steam oil ratio (CSOR) curves. The gray solid line is for the approximate downscaling method, and the black dashed line is for the exact downscaling method.

It is clear that using different downscaling methods to generate fine scale models has a large impact on the flow simulation results. Using a fine scale model that exactly matches the initial coarse model would give us more confidence in the model.

CHAPTER 8

CASE STUDY: RESERVOIR MODELING IN THE SURMONT LEASE

The Surmont lease is located about 60 kilometers southeast of Fort McMurray, Alberta, Canada (Figure 8-1). It is one of the biggest leases in the Athabasca Oil Sands. The Surmont lease is about 6 townships (larger than 500 km², see Figure 8-2). The McMurray formation at Surmont contains thick early Cretaceous bitumen-saturated sands. Because the oil sands deposits are too deep to mine, the advanced heavy oil recovery technology, Steam Assisted Gravity Drainage (SAGD) process is used to extract them. The bitumen recovery project is operated jointly by ConocoPhillips Canada Ltd. and Total. Construction of the facilities and development drilling started in 2004. Commercial production of Phase one is expected to begin in 2007.



Figure 8-1: The location of the Surmont lease in the map of Alberta, Canada.

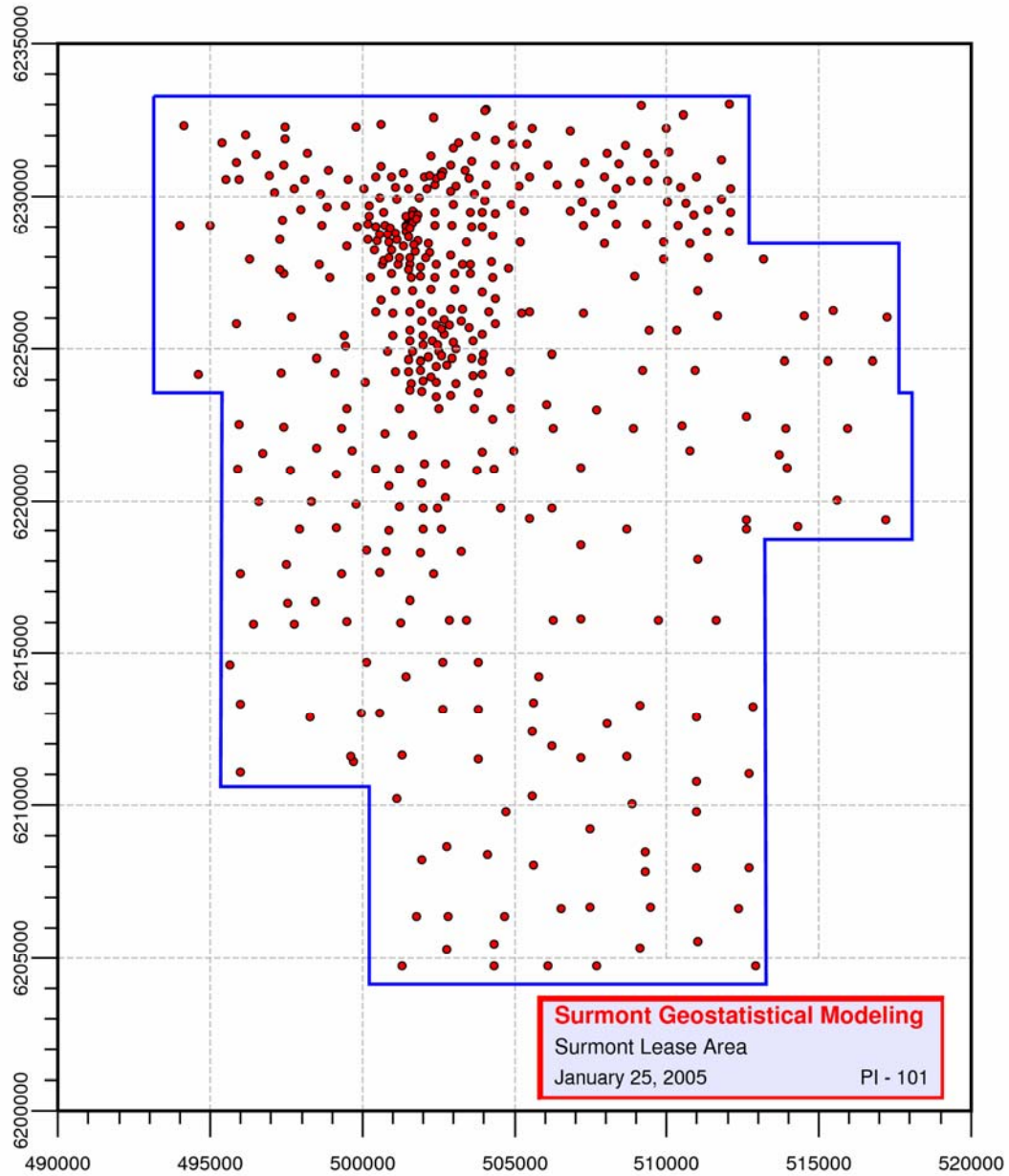


Figure 8-2: The Surmont lease map with delineation well locations, the map units are in meters.

Reservoir characterization in the Surmont lease has been conducted by using geostatistical modeling techniques. There are three major parts: (1) 2-D mapping of reservoir parameters with local uncertainty assessment to better understand the subsurface formation, (2) resource estimation and global uncertainty assessment to serve for reservoir planning and development, (3) fine scale 3-D model of a small area, such as Pad area, for well placement and flow simulation.

Detailed 3-D models of heterogeneity are useful. They provide numerical models that are consistent with the small scale well data, measures of connectivity and visualizations that appear realistic. The challenge of 3-D models in the context of our problem is twofold: (1) the size of the models, and (2) the requirement for realistic summaries of reservoir quality at each location. The lease area is more than 500 km², the thickness is on the order of 100m, there are more than 10 variables of interest and we would need 100 or more realizations to represent uncertainty. More than 20 billion numbers would need to be routinely manipulated to understand Surmont at a relatively coarse discretization of 50m x 50m x 1m.

The second challenge is more subtle. Reservoir management decisions depend in many factors such as the thickness of good quality reservoir, presence of top or bottom water, structure of the base reservoir and geological variability. These factors are, for the most part, areal summaries of the reservoir. They can be reliably calculated from the well data; however, they are not as reliably estimated from 3-D models. High resolution geostatistical models do not reproduce all of the complex geological features and trends. This challenge is addressed by research.

In summary, the advantages of using 2-D geostatistical modeling include (1) good estimates of reservoir quality consistent with available well data, (2) uncertainty at each location, (3) simple and fast modeling of variables required for decision making, (4) exact downscaling to construct fine scale 3-D models when and where needed. Thus, 2-D geostatistical modeling using Bayesian updating techniques is conducted for the Surmont Lease.

Several reservoir parameters are important. The thickness of net pay or net continuous bitumen thickness (NCB) is related to the height of an anticipated steam chamber. The bulk oil weight (BOW) measures the fraction of the bitumen mass to the total rock mass. The porosity (ϕ) and oil saturation (S_o) over the net continuous bitumen are related to the recoverable bitumen by the SAGD process. An important feature of many areas of the McMurray formation is the presence of top water and top gas that can provide a sink for the injected steam and adversely affect recovery. These upper units are

referred to as thief zones for the injected steam. Each project and company identifies different critical parameters. The typical project will involve predicting 20 to 30 variables at each 2-D location. Only a few variables will be described in this chapter. Most of the data is derived from well logs and core data.

The available data variables are divided into two types: primary variables that we must predict and secondary variables that are established from geophysical interpretation or geological trend mapping. Secondary variables are used to constrain the prediction of primary variables away from the well data. The secondary variables are often structural variables. Three structural surfaces are used: (1) the bottom surface of the McMurray formation (BSM), (2) the top surface of the McMurray formation (TSM), and (3) the Wabiskaw-McMurray surface (WMS), which is a maximum flooding surface above the McMurray formation. These structural data are usually quite reliable because of their lateral continuity and they are derived from a variety of data sources (well and seismic data). These three variables and the calculated gross thickness (GTM) of the McMurray formation are treated as secondary variables for the 2-D modeling.

Because the lease-wide results are considered confidential, only a small area of the Surmont Lease is used to demonstrate the 2-D modeling.

8.1. 2-D Mapping with Bayesian Updating

Five types of maps are generated for each reservoir parameter. The *trend* map is used to reveal the large scale trend in each parameter. The *prior* map is the kriging map of each parameter after being transformed to a Gaussian variable. These two maps are created for understanding each parameter independently. A correlation matrix plots the correlation between the variables. Based on the correlations, the *likelihood* map is created with the secondary data. The correlation matrix and the likelihood map provide information for understanding the correlation between the variables. Then, the Bayesian updating approach is applied to merge the prior models and likelihood models. This approach is similar to collocated cokriging, and is implemented in Gaussian space. The updated model contains the information from well data and from secondary data. The

updated map shows the results of Bayesian updating in the Gaussian space. The updated Gaussian distributions must be back transformed to real units and are often summarized by the *final* maps, which are the P₁₀/P₅₀/P₉₀ maps of each parameter or the probability maps of these reservoir quality parameters at certain threshold.

8.1.1. Trend maps

The trend map is used to provide the overall trend of each variable in the entire study area. This map is created by simple kriging with a variogram designed to reveal large scale features. Usually, a long range variogram (1/3 of the domain size) with modest nugget effect (30%) is used. All reservoir parameters are mapped with this trend variogram. As an example, the trend maps of the NCB and BOW are shown in Figure 8-3. Some high value zones are shown in the left of the study area for NCB.

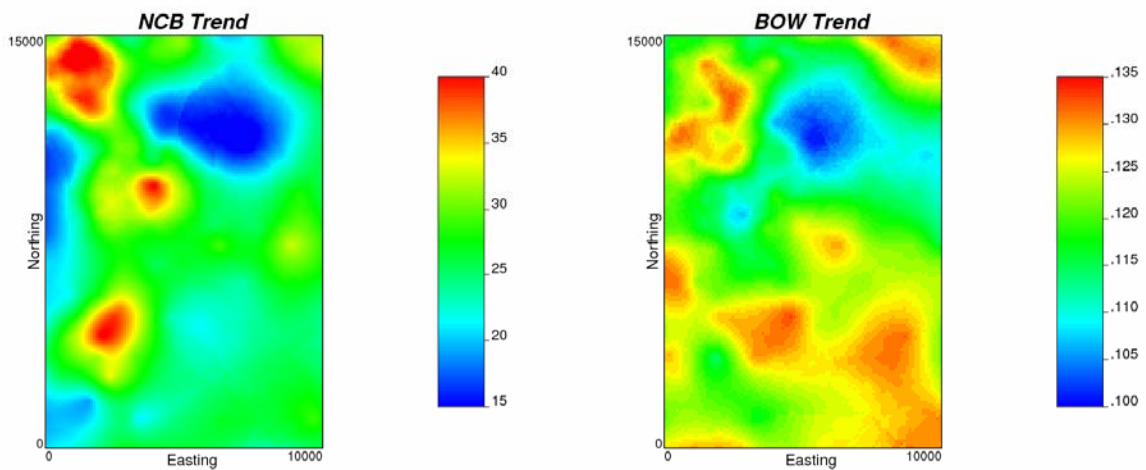


Figure 8-3: The trend maps of NCB in meters and BOW in fraction.

8.1.2. Prior maps

The prior model is also created by kriging but with the data in Gaussian space and the variogram calculated and fit from the well data. Variogram maps are helpful to find the direction of continuity in each parameter. Then, the directional variograms are calculated. The experimental variograms are modeled using a semi-automatic variogram fitting algorithm. The variogram and the model of the NCB are shown in Figure 8-4.

Kriging was then performed using these variogram models and the normal score data. The prior model generates an uncertainty distribution at each location. The uncertainty is a normal distribution with kriged mean and variance. The prior map for the NCB and BOW are shown in Figures 8-7 and 8-8. They look similar to their trend maps but have more detailed small scale features. The values on these maps are only conditional to surrounding data of the same type; we still must consider the secondary data. If the prior maps do not show the large scale trend features from the trend maps, then kriging with a local mean is considered to impose the large scale trend values.

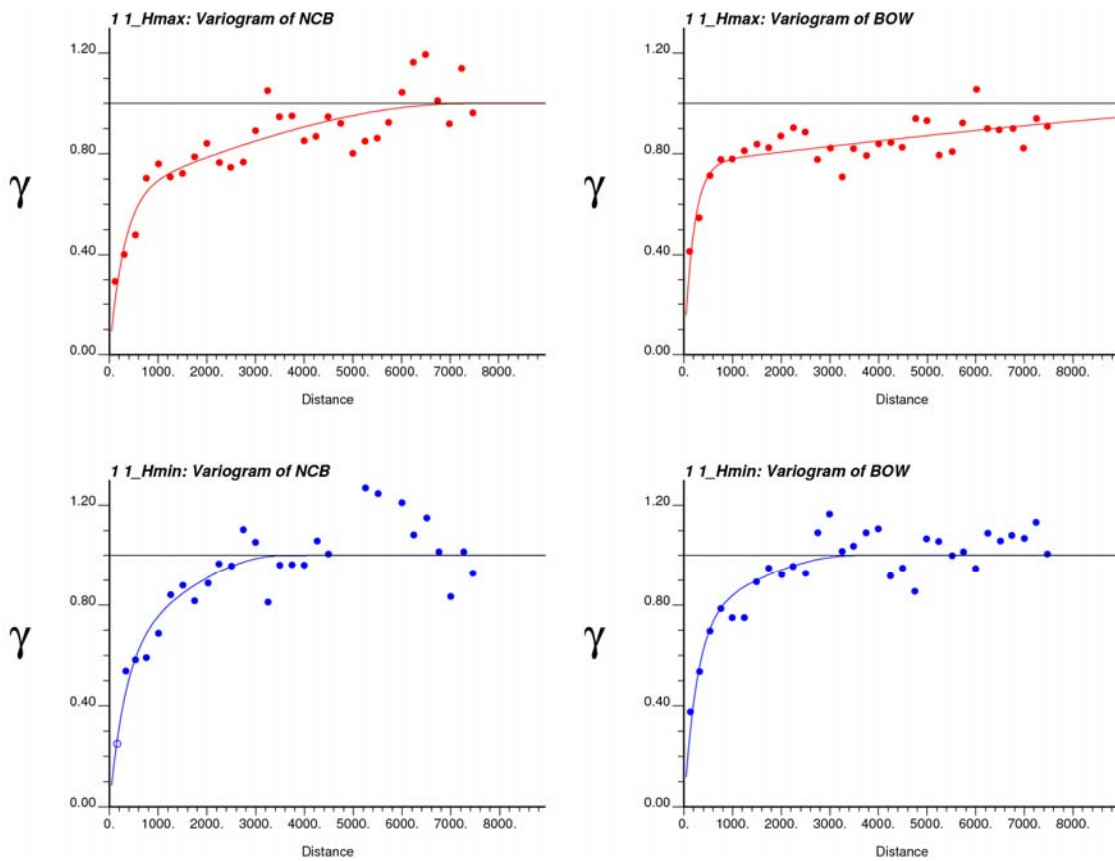


Figure 8-4: Directional variograms and fitted models for NCB (left) and BOW (right).

8.1.3. Correlation matrix and likelihood maps

A cross plot of each pair of the variables is plotted to check the data and determine the correlation between each the pair of variables. Data that fall outside of a trend with

the other data should be reviewed and perhaps eliminated to obtain a more representative correlation between the variables. Particular attention is paid to the three characteristic non-Gaussian features of (1) non-linear relationship, (2) heteroscedastic variability, that is, changing variability of one variable as another variable changes, and (3) constraint features where one variable is constrained by other. The correlation coefficients are summarized and shown in a correlation matrix (Figure 8-5).

Sw	-0.09	-0.13	-0.15	0.04	-0.03	-0.51	-0.23	1.00
Phi	0.10	0.20	0.21	0.00	0.26	0.87	1.00	-0.23
BOW	0.18	0.27	0.29	-0.06	0.32	1.00	0.87	-0.51
NCB	-0.04	0.41	0.43	0.29	1.00	0.32	0.26	-0.03
GTM	-0.86	-0.09	-0.08	1.00	0.29	-0.06	0.00	0.04
WMS	0.55	0.97	1.00	-0.08	0.43	0.29	0.21	-0.15
TSM	0.56	1.00	0.97	-0.09	0.41	0.27	0.20	-0.13
BSM	1.00	0.56	0.55	-0.86	-0.04	0.18	0.10	-0.09
	BSM	TSM	WMS	GTM	NCB	BOW	Phi	Sw

Figure 8-5: The correlation matrix of the 8 variables

With the secondary data and the correlations between a primary reservoir variable and the secondary variables, we can calculate the likelihood for each reservoir variable. The four variables used for the secondary data are shown in Figure 8-6. The likelihood model provides a conditional distribution of each variable at each location conditional to collocated data of other types. The likelihood results are mapped to show the information from the secondary data. The likelihood maps of NCB and BOW are shown in Figures 8-7 and 8-8.

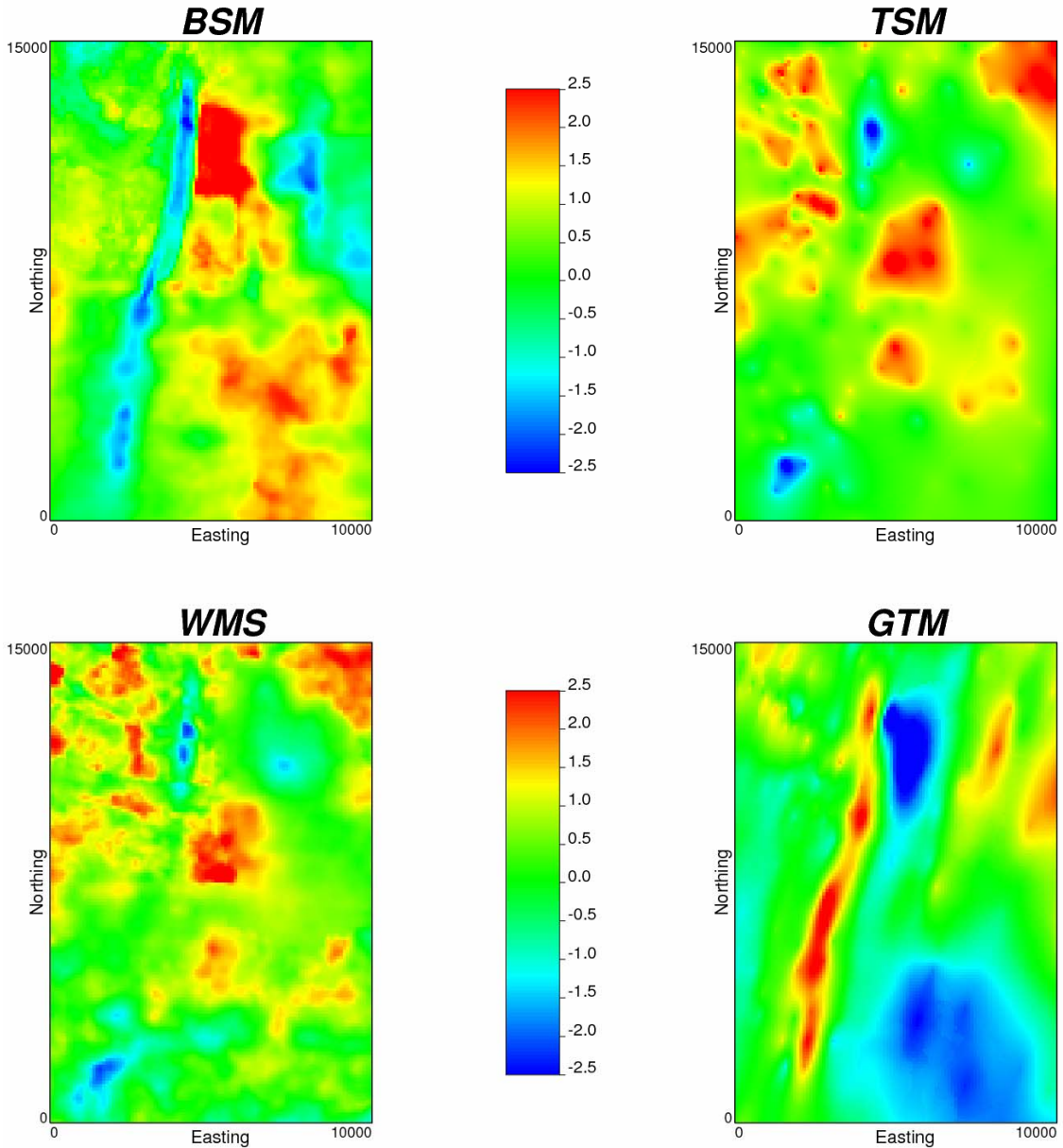


Figure 8-6: The maps of the four secondary variables in Gaussian units.

8.1.4. Updated maps and final maps

Bayesian updating is used to merge the prior models and likelihood models. The resulting model is called the updated model. The uncertainty of each parameter at each location is generated from the information of well data and the secondary data. The uncertainty distribution is also a nonstandard normal distribution with updated mean and

variance. The updated map shows the updated means in Gaussian space. The updated maps of NCB and BOW are shown in Figures 8-7 and 8-8.

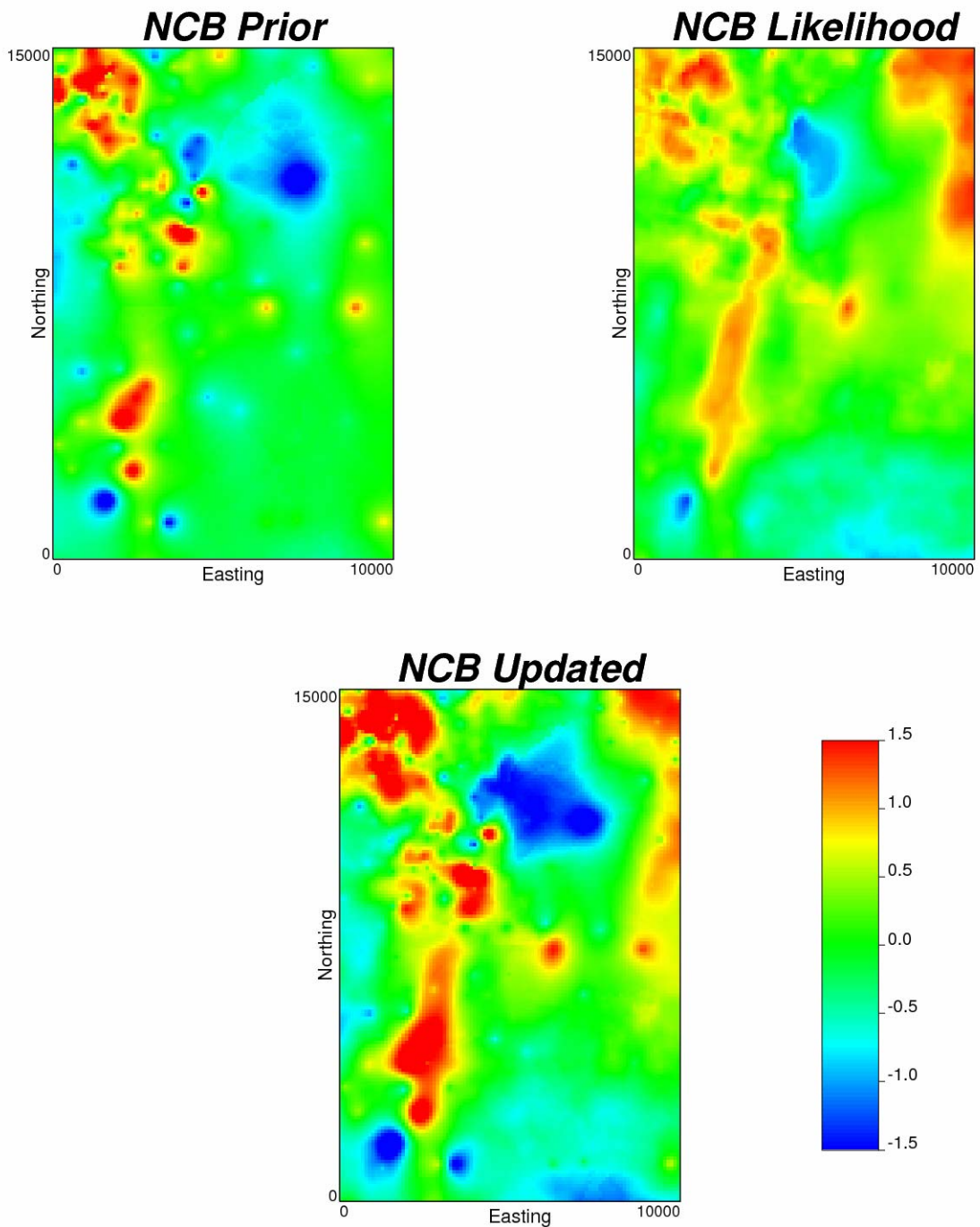


Figure 8-7: The prior (top left), likelihood (top right) and updated maps (bottom) of NCB in Gaussian units.

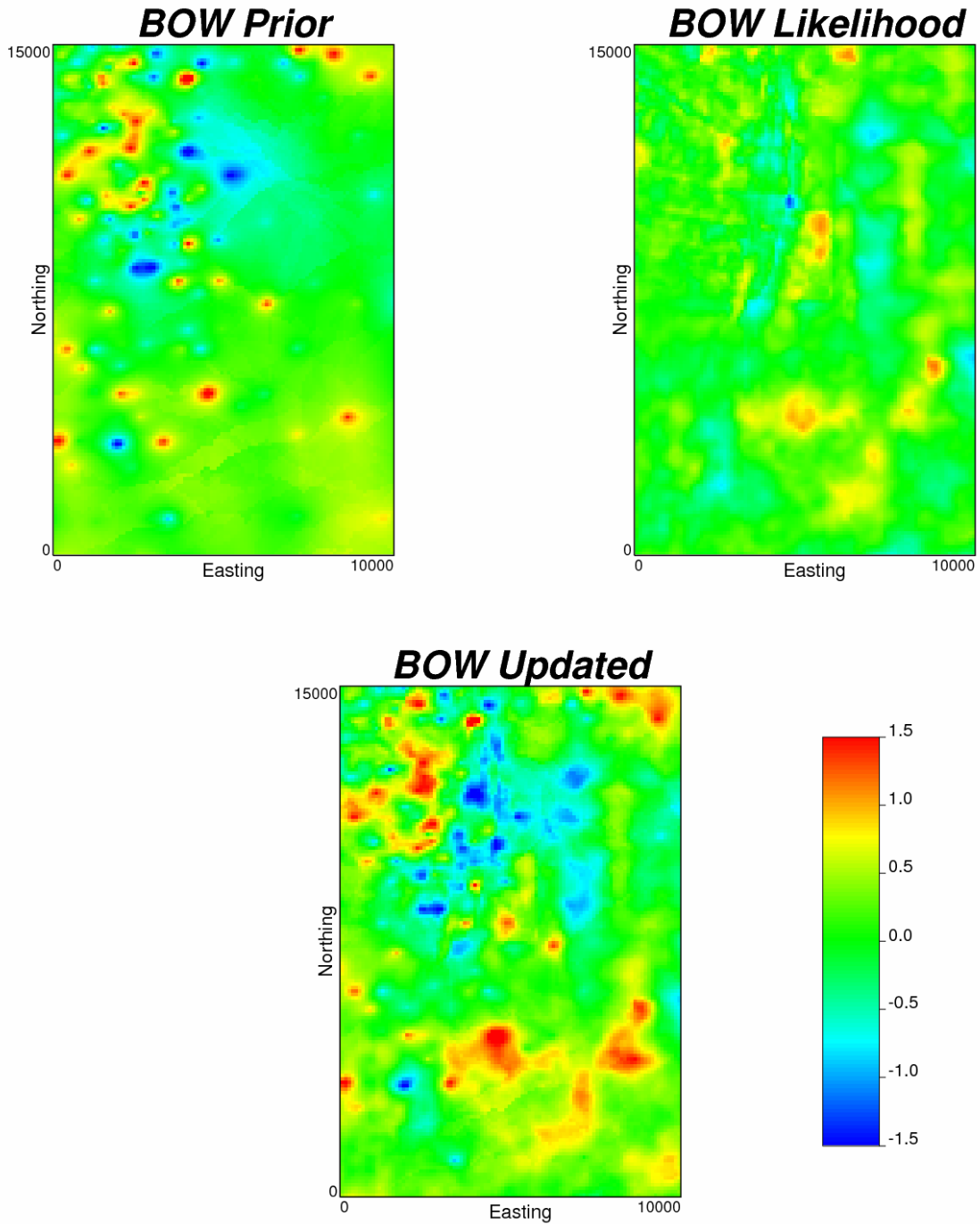


Figure 8-8: The prior (top left), likelihood (top right) and updated maps (bottom) of BOW in Gaussian units.

The updated distributions are transformed to real units to show the best estimate and the uncertainty at each location in real values. These features are summarized by P10, P50 and P90 values. The map of P50 values provides the median of each reservoir

parameter at each location. The map of P10 values can be used to identify the high value areas. The map of P90 values can be used to identify the low valued areas.

All variables are predicted. The maps of local P10, P50 and P90 values for NCB are shown in Figure 8-9. The green color in the P10 map shows where there is a 90% chance to have more than 25m of net continuous bitumen. The blue color in the P90 map shows where there is a 90% chance to be less than 20m of net continuous bitumen.

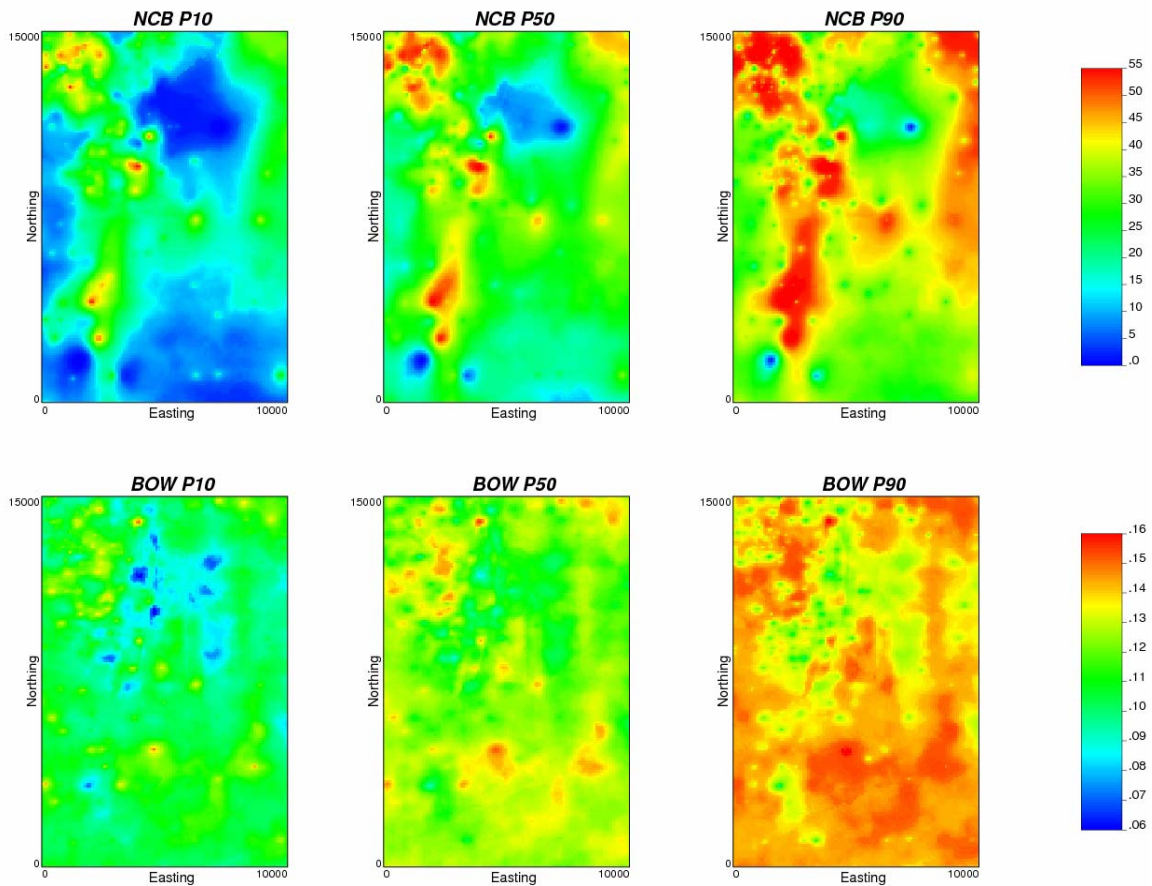


Figure 8-9: Maps summarizing uncertainty in NCB in meters (top row) and BOW in fraction (bottom row). The P10 low values are shown on the left, the P50 values are shown in the middle and the P90 high values are shown on the right.

8.1.5. Model validation

Cross validation is used to estimate the variables at locations where we know the true value. All well locations were used. Likelihood calculations and updating were

performed. Cross validation was performed with the Gaussian transforms of the original variables. The results were back transformed to original units. The uncertainty models were checked with accuracy plots. Figure 8-10 shows the accuracy plots of the NCB and BOW; the model for NCB is accurate and precise.

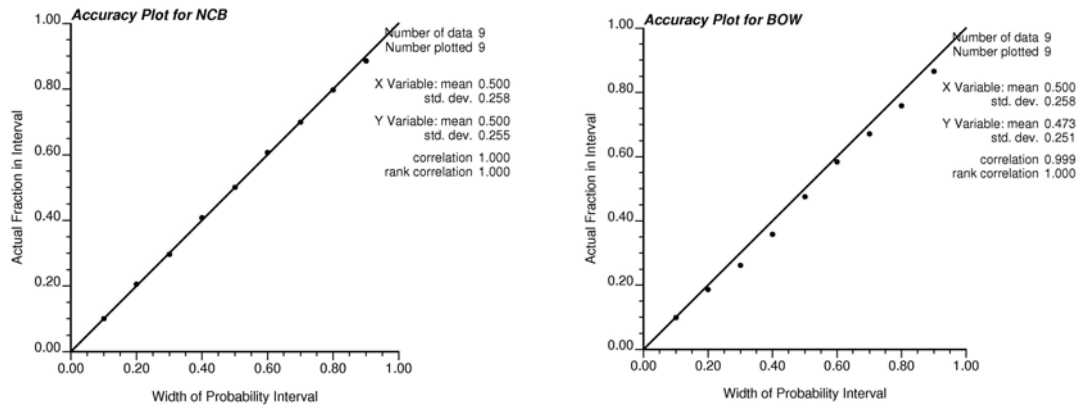


Figure 8-10: The accuracy plots of cross validation results for NCB and BOW.

A number of wells were drilled after these models were constructed. The goodness of the probabilistic estimates can be checked and compared to the new drilled wells. The results are shown in Figure 8-11. The model for NCB worked out extremely well.

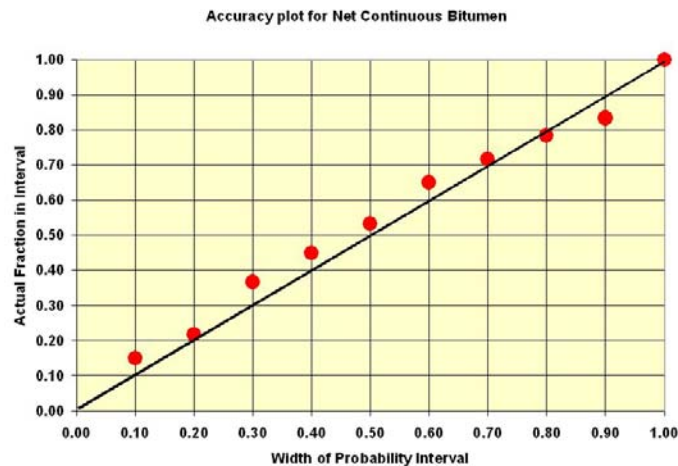


Figure 8-11: Accuracy plot of 2-D model validating with new wells of 2004.

The fairness of the probability values, that is, a good accuracy plot is not enough for good probabilistic predictions. The width or variance of the local distributions must also be narrow for good distributions.

8.2. Global Resources Assessment

Accurate estimation of the in-situ resource range and associated risks is important for reservoir management planning and development. There was an interest in the recoverable bitumen resource by SAGD and the original oil in place for SAGD (SAGD OOIP) in the Surmont lease and other arbitrarily large areas. We refer to these large areas as “global” to distinguish them from the “local” small 100m by 100m areas calculated in the 2-D models. The global SAGD OOIP was mostly affected by the net continuous bitumen thickness (NCB) and the presence of steam thief zones. A threshold of NCB=18m was considered as the minimum thickness for the economic recovery of bitumen with the current SAGD technology. When the presence of a certain thief zone is present, a minimum of 30m NCB is considered for SAGD to be economically successful. A lower 10m NCB cutoff was also considered to include the resource that could be used for future development when more advanced bitumen recovery technology becomes available. The global SAGD OOIP was calculated with different NCB cutoffs and for different thief zone types.

The calculation of SAGD OOIP and thief zone (TZ) type required six correlated variables: net continuous bitumen (NCB), net porosity (ϕ), net water saturation (S_w), thief zone protection factor (TZPF), effective water thickness (EWT), and effective gas thickness (EGT). These variables had been analyzed as part of 2-D geostatistical studies.

$$\text{SAGD OOIP} = \text{NCB} \cdot \phi \cdot (1 - S_w)$$

$$\text{TZ type} = 1, \text{ if } \text{TZPF} \geq 5 \text{ m or } (\text{EWT} = 0 \text{ m and } \text{EGT} = 0 \text{ m})$$

$$= 2, \text{ if } (0.8 \text{ m} > \text{EWT} > 0\text{m}) \text{ or } (\text{EWT} = 0 \text{ m and } \text{EGT} > 0 \text{ m})$$

$$= 3, \text{ if } \text{EWT} \geq 0.8 \text{ m}$$

The SAGD OOIP variable must be multiplied by area to get a volume. The uncertainty in global SAGD OOIP was a concern to the Surmont Team. It was calculated using the Bayesian updated 2-D models. An estimate of global SAGD OOIP from prior information alone was also interesting. The logic and calculations used to assess

uncertainty and to obtain the estimate over large regions of the Surmont lease are summarized as follows.

8.2.1. Uncertainty in global SAGD OOIP

Uncertainty of small 100 m by 100 m areas or the incrementally larger LSD areas are captured very well by the 2-D models as indicated by the model validation results. Assessing uncertainty over larger scales, however, requires a different approach. Calculation of uncertainty from a local uncertainty measure to a regional or global uncertainty measure requires consideration of the spatial correlation within the region/domain because the assumption of independence between the smaller scale areas will drastically understate uncertainty at a large scale. The methodology presented in Chapter 5 was used. The key steps are (1) construct local distributions of uncertainty (done already); (2) generate spatially correlated probability values; (3) draw values for all variables at all locations and keep them together as a realization (the spatial and multivariate simulation).

The reporting of uncertainty for an arbitrary volume required six proportions (in turquoise color in the table below): the proportion/probability of each of the three thief zone types and the proportion/probability of being above 10, 18, and 30 m NCB. Each of the six proportions was characterized by a distribution of uncertainty. Uncertainty was summarized by three values: a P10, P50, and P90. These were shown in the turquoise boxes in the table below. Further, there was a distribution of uncertainty in the SAGD OOIP with no constraint on the thief zone type and no constraint on the net continuous bitumen (the bright yellow color square in the table below). There were six distributions of SAGD OOIP uncertainty for the three different thief zone types (no constraint on net continuous bitumen) and the three different NCB cutoffs (no constraint on thief zone type), which are shown in the pale yellow squares in the table below.

There were nine distributions of uncertainty in the SAGD OOIP for all combinations of the three thief zone types and the three NCB cutoffs (shown in the tan color in the table below). These distributions of uncertainty had P10, P50, and P90 values for SAGD

OOIP, as well as P10, P50, and P90 values for the proportion of values within the NCB/TZ class (shown in turquoise boxes above the tan boxes below).

Uncertainty for an Arbitrary Volume		Thief Zone Type			
		No Constraint	TZ1	TZ2	TZ3
			P ₁₀ / P ₅₀ / P ₉₀	P ₁₀ / P ₅₀ / P ₉₀	P ₁₀ / P ₅₀ / P ₉₀
NCB Cutoff	No Constraint	P ₁₀ / P ₅₀ / P ₉₀	P ₁₀ / P ₅₀ / P ₉₀	P ₁₀ / P ₅₀ / P ₉₀	P ₁₀ / P ₅₀ / P ₉₀
	NCB > 10	P ₁₀ / P ₅₀ / P ₉₀	P ₁₀ / P ₅₀ / P ₉₀	P ₁₀ / P ₅₀ / P ₉₀	P ₁₀ / P ₅₀ / P ₉₀
			P ₁₀ / P ₅₀ / P ₉₀	P ₁₀ / P ₅₀ / P ₉₀	P ₁₀ / P ₅₀ / P ₉₀
	NCB > 18	P ₁₀ / P ₅₀ / P ₉₀	P ₁₀ / P ₅₀ / P ₉₀	P ₁₀ / P ₅₀ / P ₉₀	P ₁₀ / P ₅₀ / P ₉₀
			P ₁₀ / P ₅₀ / P ₉₀	P ₁₀ / P ₅₀ / P ₉₀	P ₁₀ / P ₅₀ / P ₉₀
	NCB > 30	P ₁₀ / P ₅₀ / P ₉₀	P ₁₀ / P ₅₀ / P ₉₀	P ₁₀ / P ₅₀ / P ₉₀	P ₁₀ / P ₅₀ / P ₉₀
P ₁₀ / P ₅₀ / P ₉₀			P ₁₀ / P ₅₀ / P ₉₀	P ₁₀ / P ₅₀ / P ₉₀	

In summary, 3+3+9=15 distributions of proportions (three numbers each) and 1+3+3+3•3=16 distributions of SAGD OOIP uncertainty (three numbers each) were used to report the uncertainty for an arbitrary volume: 93 numbers in all. Uncertainty was tabulated according to the format shown above.

The underlying models of uncertainty were created at a 100m by 100m areal scale. Uncertainty at this scale is dominated by the spacing of nearby wells and the available secondary data variables. This uncertainty can be straightforwardly scaled up to the LSD scale (about 400m x 400m) by arithmetic averaging under an assumption that the values are highly correlated over a 400m scale.

The uncertainty at the 100m or LSD scale was represented by distributions of uncertainty in all of the variables including net continuous bitumen (NCB), net porosity (ϕ), net water saturation (Sw), thief zone protection factor (TZPF), effective water thickness (EWT), and effective gas thickness (EGT). The uncertainty in each of these variables does not give uncertainty in SAGD OOIP or TZ type. The correlation between these variables and the spatial correlation within the region/domain must be taken into account.

Accounting for the correlation between NCB, ϕ ,..., and EGT was done with simulation. Multiple realizations (L=100) of the six variables were drawn accounting for the correlation between the variables and the spatial correlation within the region/domain (see purple shaded squares in the table below). Then, with each set of six numbers the

SAGD OOIP and TZ type were calculated (see yellow squares on the right). The results were analyzed to fill in the uncertainty table.

Realization #	NCB	ϕ	S_w	TZPF	EWT	EGT	SAGD OOIP	TZ Type
1								
2								
3								
...								
L								

There are a number of simulation techniques in use throughout statistics and geostatistics. The LU method (named after the Cholesky LU matrix decomposition method) has been around for a long time and is suitable when the problem is small. For example, consider assessing uncertainty in the SAGD OOIP and TZ type at a particular location, that is, filling in a table as shown above.

The use of the LU method to simulate multiple dependent variables is straightforward. Only the correlation matrix between the six variables was required, and a set of correlated normal scores was required to account for the spatial correlation of the variables. The latter requirement was satisfied by generating unconditional realizations using sequential Gaussian simulation for each of the six variables.

The simulated variables were then used to calculate the corresponding SAGD OOIP and TZ type at each location. This was performed for multiple realizations and the uncertainty was assessed. The resulting distributions of uncertainty are shown in Table 8-1.

Uncertainty depends on the amount of local well data, the secondary data variables and the modeling approach and parameters. We have observed a consistent decrease in uncertainty as additional delineation wells are drilled.

Uncertainty for Lease Area			Thief Zone Type			
			No Constraint	TZ1	TZ2	TZ3
NCB Cutoff	No Constraint		0.864 / 1.000 / 1.156	0.392 / 0.418 / 0.445	0.214 / 0.228 / 0.243	0.329 / 0.353 / 0.382
	NCB > 10	0.652 / 0.715 / 0.784	0.834 / 0.974 / 1.134	0.336 / 0.382 / 0.438	0.111 / 0.129 / 0.153	0.413 / 0.479 / 0.569
	NCB > 18	0.535 / 0.602 / 0.689	0.761 / 0.908 / 1.073	0.238 / 0.258 / 0.282	0.110 / 0.127 / 0.150	0.295 / 0.328 / 0.361
	NCB > 30	0.294 / 0.365 / 0.446	0.527 / 0.663 / 0.827	0.324 / 0.371 / 0.429	0.099 / 0.118 / 0.141	0.408 / 0.475 / 0.566
				0.196 / 0.219 / 0.249	0.069 / 0.082 / 0.103	0.263 / 0.300 / 0.338
				0.299 / 0.348 / 0.410	0.075 / 0.091 / 0.116	0.389 / 0.459 / 0.551
				0.119 / 0.142 / 0.172	0.014 / 0.020 / 0.030	0.163 / 0.200 / 0.246
				0.219 / 0.271 / 0.333	0.021 / 0.030 / 0.045	0.284 / 0.357 / 0.455

Total No. Blocks = 55483

Table 8-1: The Surmont Lease resource estimation and uncertainty assessment: the blue shaded boxes are proportions and the others are barrels – standardized to “1.000” for the lease.

8.3. Fine Scale 3-D Models

Fine scale 3-D models are required for well placement and flow simulations. A half-pad area is selected for 3-D modeling. The model area is 1,400m by 1,000m, and there are six wells in the area (top left in Figure 8-12).

The structure of the model is bounded by two stratigraphic surfaces (Figure 8-13). The WabMcM is a maximum flooding surface at the top and the DevUnc is an unconformity surface at the bottom. The vertical stratigraphic coordinates of the model are set to be “parallel to top”. The maximum distance between the two surfaces are 91m. The 2-D averages of wells are calculated at the maximum distance. The histogram of the 2-D well data is shown in Figure 8-12. The Bayesian updating technique is used to generate 2-D porosity and water saturation at scale of 50m by 50m. Simulation realizations are generated by using Bayesian updating with P-field simulation. The realization#1 (middle left in Figure 8-12) is used for exact downscaling to construct 3-D fine scale models. The histogram of the block data is shown in Figure 8-12.

The target grid resolution of the 3-D model is 10 x 10 x 1m. We can directly downscale the 2-D porosity data, but it will time consuming. Instead, the 2-D porosity is first downscaled aerially to 10m by 10m, and then the downscaled 2-D results are downscaled vertically to construct the 3-D model.

The first downscaling results are shown at the bottom of Figure 8-12. The histogram is reasonably reproduced. It has more high and low values than the block data.

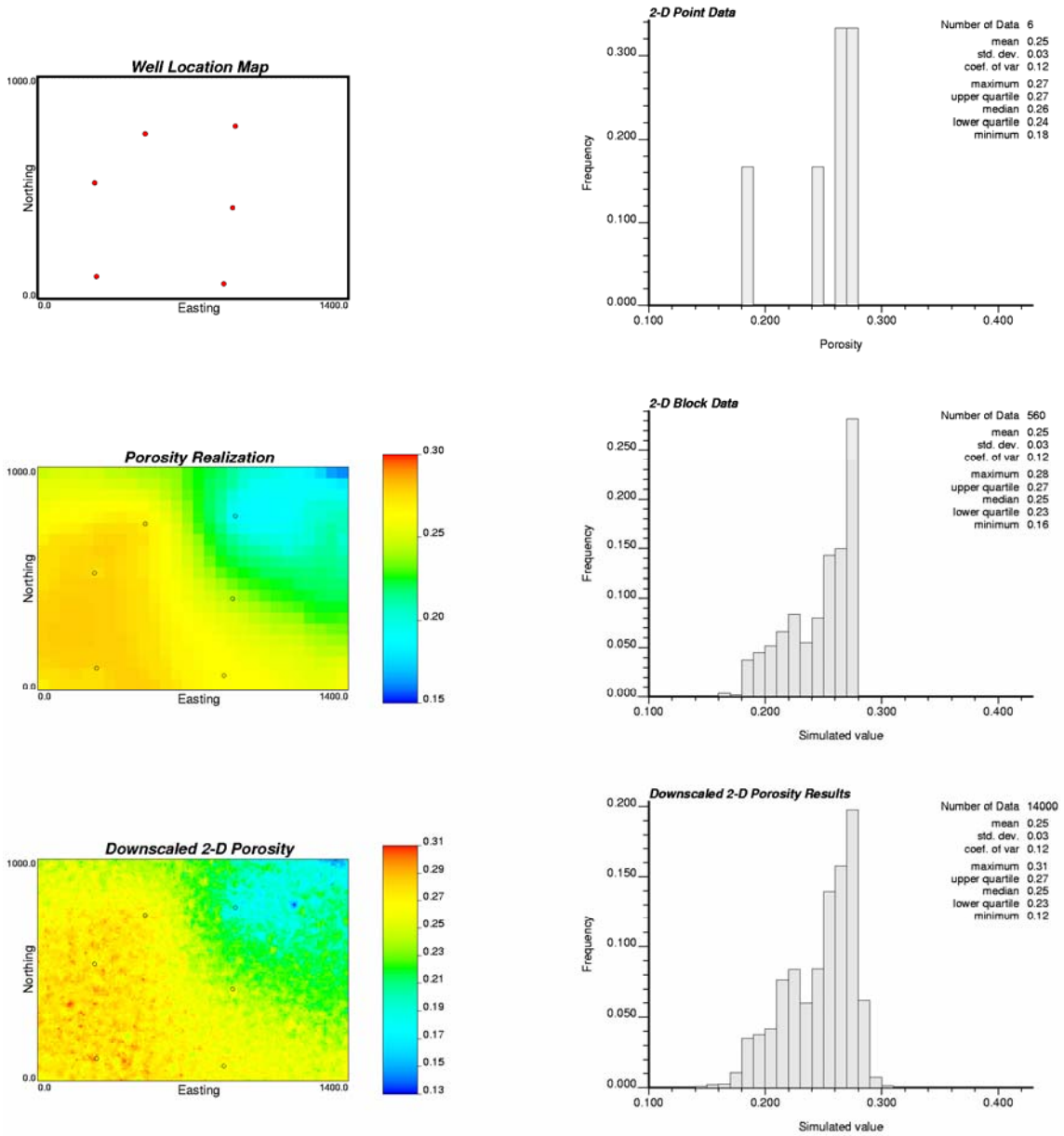


Figure 8-12: The Bayesian updating with P-Field simulation realization#1(middle left) is exact downscaled from 50m by 50m to 10m by 10m (bottom left). The histograms of point data (top right), block data (middle right), and downscaled values are shown on the right.

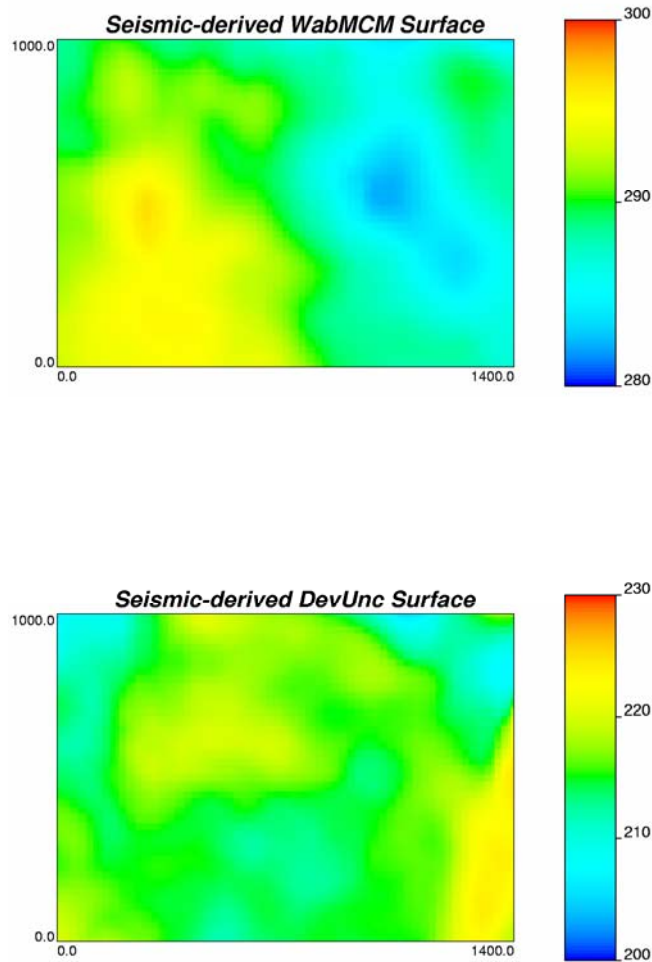


Figure 8-13: The stratigraphic surfaces used for the 3-D modeling: WabMcM is the top surface, and DevUnc is the bottom surface in meters.

The second downscaling is performed using the 2-D porosity data and the well data from the six wells. The histograms of the point data (top left), block data (top right), and 3-D downscaled values (bottom) are shown in Figure 8-14. The histogram of the downscaled results is a combination of the histograms of point and block data.

The simulated results are converted back to the regular coordinates and clipped with the two structural surfaces. The final model of 3-D porosity realization #1 is shown in Figure 8-15. The model has a grid resolution of 10 x 10m areally and 1m vertically. The field spans 1,400m, 1,000m and 91m in the Easting, Northing and Elevation directions, respectively. The vertical direction is exaggerated by 5 times.

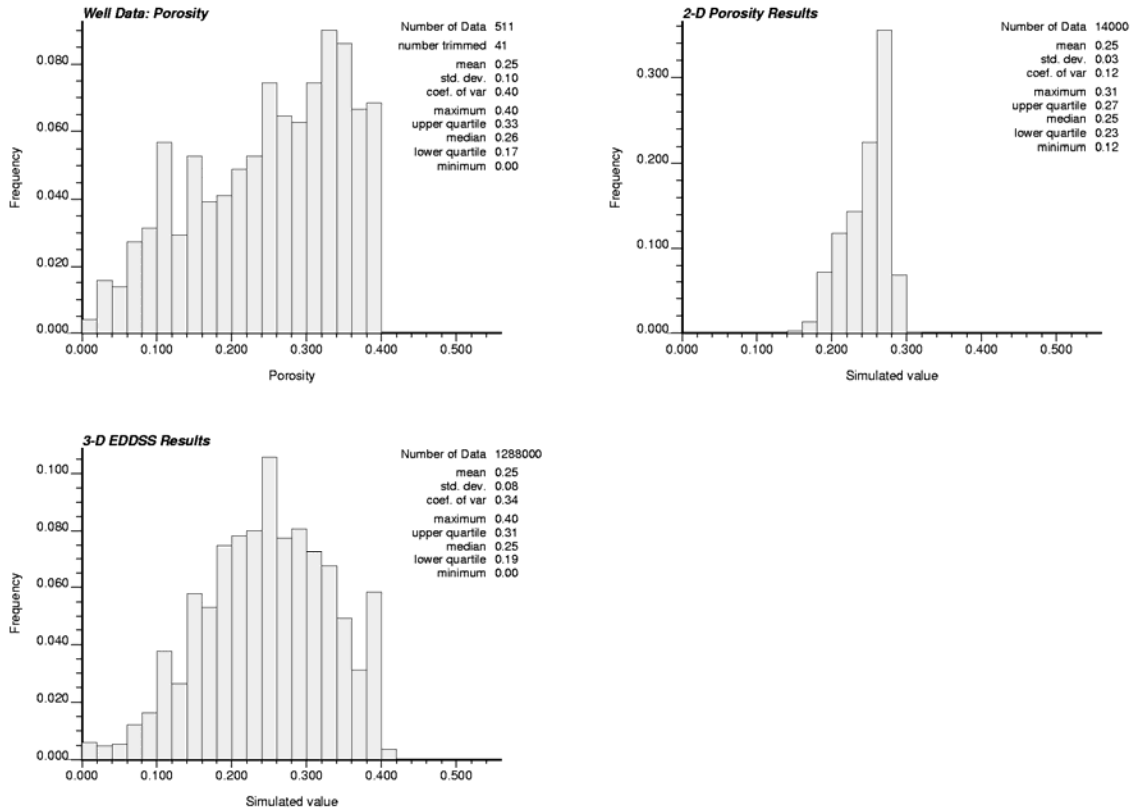


Figure 8-14: The histograms of point data (top left), block data (top right), and 3-D downscaled values (bottom).

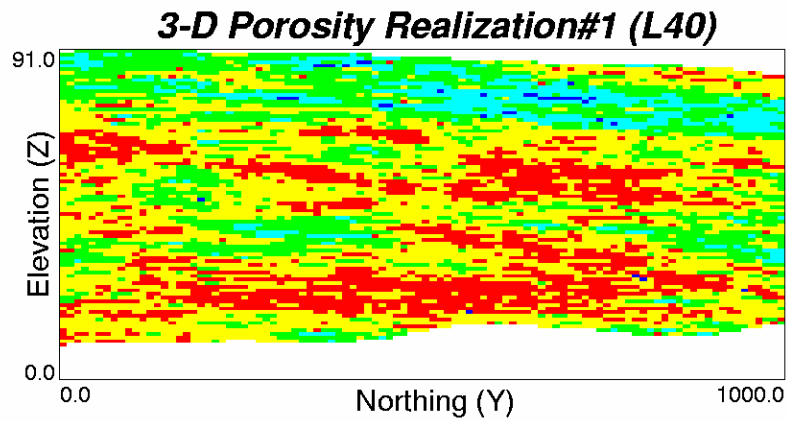
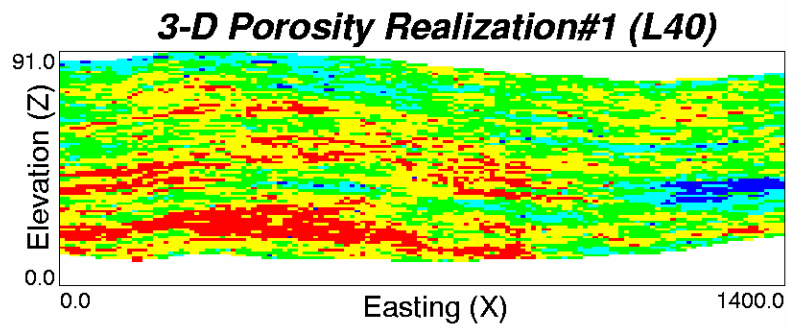
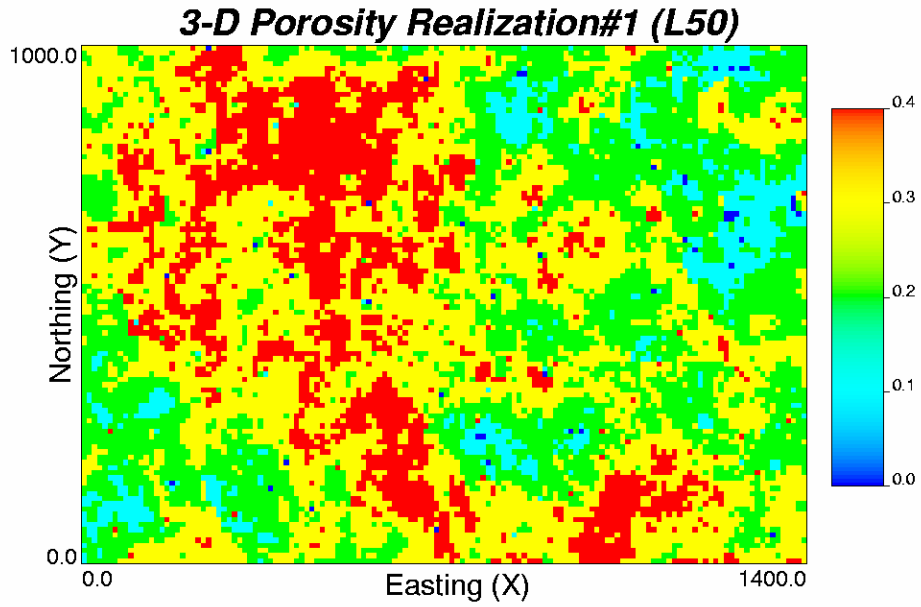


Figure 8-15: The 3-D porosity realization #1. The model has a grid resolution of 10 x 10m areally and 1m vertically. The field spans 1,400m, 1,000m and 91m in the Easting, Northing and Elevation directions, respectively. The vertical direction is exaggerated by 5 times.

CHAPTER 9

CONCLUSIONS AND RECOMMENDATIONS

Reservoir modeling can be improved in many ways. Two important ways are: (1) integrating different types of data to improve estimation and reduce uncertainty between wells, (2) keeping reservoir models consistent at different scales to avoid bias in scaling. Based on some practical projects conducted in Canada's heavy oil reservoirs, a scale consistent reservoir modeling scenario was developed to build reservoir models from multiple data integration and to ensure the models at different scales are consistent with each other. The scenario consists of three major steps: (1) construct field scale reservoir models over the entire lease area by integrating multivariate information from all available data; a Gaussian-based Bayesian updating technique can be used with local uncertainty assessment; (2) perform petroleum resource estimation with the global uncertainty assessment from the field scale reservoir model generated in step 1; the spatial/multivariate simulation approach can be used to account for the spatial and multivariate correlations among the local uncertainties; (3) construct fine scale 3-D models of heterogeneity that are consistent with the field scale model and well data. Exact downscaling techniques can be used to ensure the field scale model can be exactly reproduced. Summaries and recommendations for each step are presented below.

9.1 Large Scale Modeling

In Canadian heavy oil reservoirs, it is common that a variety of data are available for reservoir modeling. These data include core and log data, seismic attributes, and conceptual geological models. Data scales, reliability, coverage and availability must be taken into account in integrating these data into a numerical reservoir model. Constructing a large scale model using multiscale data is relatively easy. All small scale data can be upscaled to the model scale. Then, the Gaussian-based Bayesian updating

technique can be used to integrate these data: well data are used as primary data, and seismic data, structural surfaces, geological information are used as secondary data. The Bayesian updating technique decomposes the collocated cokriging estimate into two models: prior and likelihood. The prior model is built from well data, and the likelihood model is built from all secondary information. The definition of prior and likelihood could be reversed with a different interpretation. The prior model is then updated with the likelihood model to build the final posterior or updated model that accounts for all the information.

Uncertainty assessment is based on the multivariate Gaussian assumption in the technique. The multivariate Gaussian model permits local uncertainty distributions to be fully defined by a mean and variance. The kriging-based technique provides mean and variance for all of the three models: prior, likelihood, and updated. Thus, the local uncertainty of each model can be reviewed. The updated uncertainty always has the smallest variance. The multivariate Gaussian model requires all data be transformed into a Gaussian distribution at the beginning, and the updated distribution is back transformed into the original units at the end to give the local uncertainty distributions. The local uncertainty distributions provide valuable information for selecting SAGD Pad areas or the area of interest.

There is an implicit assumption of stationarity in all geostatistical techniques. The spatial statistical parameters are assumed to be constant over the entire model area. Reservoir parameters normally show some non-stationary features over a large area. Locally varying features should be considered in the large scale modeling. An enhanced (or non-stationary) Bayesian updating technique is developed to account for the locally varying correlations and data quality. The local correlation coefficient is calculated from all of the data weighted based on their distance from the location of interest. The quality of the secondary data is accounted for to improve the accuracy of the local uncertainties. The locally varying histogram and variogram should also be considered in the Bayesian updating approach. Further research on this is required.

Simulation realizations are required for building fine scale models. Simulation with Bayesian updating can be performed sequentially or using a P-field simulation approach. The P-field simulation with Bayesian Updating is recommended because of computational efficiency and the consistency between the local uncertainties and the simulation realizations. P-field simulation may cause some minor problems but they are considered negligible.

9.2 Global Resource Uncertainty Assessment

Global resource uncertainty can be assessed based on the local uncertainties from the large scale models. Petroleum resource is generally calculated from multiple variables over a lease area or any large area. The local uncertainties of these variables are spatially and multivariately correlated. The joint uncertainties require a combined P-field and LU simulation approach. Probability fields are generated from the spatial correlations of the variables; the multivariate correlations are introduced into the probabilities by LU simulation. These probabilities allow to draw simultaneously all the simulated values from all the local conditional distributions established in the Bayesian updating. The global uncertainty in a petroleum resource can be easily assembled from the multiple correlated simulation realizations. The global uncertainty is consistent with the local uncertainties in the large scale model.

P-field simulation may cause a slight non-stationarity in the variogram structure of the simulated values: the continuity near conditioning data is slightly overstated (Srivastava, 1992). The spatial structures are approximately reproduced by considering the joint correlations. These effects on global uncertainty are considered negligible. A sequential simulation approach can be used to remove the effects, but it would require recalculating all of the conditional distributions in a random path using previously simulated values. It is not guaranteed that the global uncertainty will be consistent with the local uncertainties from the Bayesian updating. Applying LU simulation to multivariately correlate the probability fields will also affect the variogram structures of the simulated values. If the variables are highly correlated, their variogram structures are

similar so that the effect is small. If the variables are highly non-correlated, the effect is also small. However, the effect on the variables with a moderate correlation coefficient may be big. Further research to quantify the effect could be necessary.

The spatial/multivariate simulation approach also relies on stationarity and multivariate Gaussianity. The locally varying features can also be applied. The locally varying correlation can be used for LU simulation; the probability field can be generated from locally varying variogram. Subdividing the area is an alternative when geology indicates a strong non-stationarity in the model area. The sources of uncertainty need to be understood separately.

The uncertainties in the input statistical parameters such as mean, variance, variogram and correlation coefficient are not considered in both local and global uncertainties. They may have significant influence on the uncertainty model. Spatial bootstrap can be used to assess the uncertainties in some statistical parameters (Deutsch, 2004). Further research is needed for incorporating these uncertainties into Bayesian updating technique and the spatial/multivariate simulation approach.

9.3 Exact Downscaling Technique

Detailed fine scale 3-D model can be generated by exact downscaling of the large scale model in the area of interest. The exact downscaling technique is using point scale data and a large scale model to construct a fine scale model at the model scale. Volume-averaged variances are used to account for the different supports among the block, model and point values. The exact downscaling with direct simple block kriging and direct sequential simulation approaches have been proved to reproduce exactly the large scale model.

In the direct simple block kriging approach, the kriging weights assigned to the point data and nearby block data are sometimes positive in estimating some cells and are negative in estimating other cells in a block. Eventually, their influences on all of cells in the block are canceled out. Only the weights of the collocated block can not be canceled

out. The sum of the weights is always equal to the discretization number of the block so that the block value is always exactly reproduced. In the direct sequential simulation approach, the influence of the collocated block becomes significant in the last few cells, and the weights of previously simulated cells in the block become negative. In the last cell, the collocated block screens out all the data outside of the block; and the difference between the weight of the collocated block and the weights of all previously simulated cells is 1 so that the block value is always exactly reproduced.

Without the multivariate Gaussian model, the direct simple block kriging and sequential simulation approaches require additional process to determine the local distributions. The CCDF lookup table method can provide local uncertainty for EDDSS. But it does not reproduce the global histogram when it is highly skewed. The final histogram always falls between the normal distribution and the input distribution because of the central limit theory. There are some post processes that can exactly reproduce the input histogram but they remove the variability or uncertainty caused by ergodic fluctuations (Deutsch, 2005). The proportional effect should also be accounted for in direct sequential simulation. The proportional effect may not be fully described by a simple linear function. Local variances can be over-modified; this makes it difficult to reproduce the global variance. Further research is needed for a better characterization of the proportional effect. Histogram reproduction and proportional effect are long-term research topic for direct sequential simulation.

An unstructured grid can be downscaled into fine scale regular grid by using locally varying block discretization number. These numbers have to be consistently used in the calculation of volume-averaged covariances. Large discretization numbers will require a significant computational time and may reduce the accuracy of the EDDSS results. Optimized methods for volume-averaged covariance calculation and kriging system solver are needed for improved performance.

A stronger stationary assumption is required for the exact downscaling approaches. The linear scale relationship is assumed constant over the entire model volume. Although

constructing a fine scale 3-D models for a small area do not need to explicitly account for an areal trend. A vertical trend is almost always required to construct 3-D model from 2-D maps. One idea is to use the vertical trend as locally varying mean in the EDDSS approach. Subdividing the formation into multiple stratigraphic units is an alternative. It will require 2-D mapping in each stratigraphic unit, and then exact downscaling to construct the 3-D model.

Exact downscaling of facies proportions is feasible with EDDSS. Order correlation must be applied during the simulation process to ensure all the simulated facies proportions sum to one. The correction affects the simulated values but not the linear scale relationship in EDDSS because the scale relationship is enforced in the last cell. The order correlation will not be needed in the last cell because the simulated facies proportions will sum to one if the block facies proportions can be exactly reproduced.

Overall, the scale consistent modeling scenario can improve the accuracy of reservoir description by considering multiscale data integration and consistency of models at different scales. The application in the Surmont oil sands reservoir shows a great applicability for reservoir characterization.

BIBLIOGRAPHY

- Alabert, F. G.: "The Practice of Fast Conditional Simulations through the LU Decomposition of the Covariance Matrix," *Mathematical Geology*, 19(5), p. 369-386. 1987.
- Behrens, R.A., Macleod, M.K., Tran, T.T. and Alimi, A.O.: "Incorporating Seismic Attribute Maps in 3D Reservoir Models," *SPE Reservoir Evaluation & Engineering*, p. 122-126, April 1998.
- Besag, J.: "On the Statistical Analysis of Dirty Pictures," *J. R. Statist. Soc. B.*, 48, p. 259-302, 1986.
- Bourgault, G.: "Using Non-Gaussian Distributions in Geostatistical Simulations," *Mathematical Geology*, 29(3), p. 315-334, 1997.
- Butler, R.M.: "*Thermal Recovery of Oil and Bitumen*," Prentice Hall, 1991.
- Cardwell, W.T., and Parsons, R.L.: "Average Permeabilities of Heterogeneous Oil Sands," *Trans. Am. Inst. Mining Met. Pet. Eng.* 160:34-42, 1945.
- Caers, J.: "Adding Local Accuracy to Direct Sequential Simulation," *Mathematical Geology*, 32(7), 815-850, 2000.
- Coll, C., Jing, X.D. and Muggeridge, A.H.: "Integration of Core and Log Information to Improve the Representation of Small/Medium-Scale Heterogeneity," SPE 56804 presented at the SPE Annual Technical Conference and Exhibition, October 1999.
- Deutsch, C.V., Srinivasan, S. and Mo, Y.: "Geostatistical Reservoir Modeling Accounting for Precision and Scale of Seismic Data," SPE 36497 presented at the 1996 SPE Annual Technical Conference and Exhibition, October, 1996.
- Deutsch, C.V. and Journel, A.G.: "*GSLIB: Geostatistical software library and user's guide*," 2nd edition, Oxford University Press, New York, 1998.
- Deutsch, C.V., Tran, T.T., and Xie, Y-L.: "An Approach to Ensure Histogram Reproduction in Direct Sequential Simulation," Centre for Computational Geostatistics Annual Report Three, University of Alberta, 2001.

- Deutsch, C.V.: “*Geostatistical Reservoir Modeling*,” Oxford University Press, New York, 2002.
- Deutsch, C.V.: “A Statistical Resampling Program for Correlated Data: Spatial_Bootstrap,” Centre for Computational Geostatistics Annual Report Six, University of Alberta, 2004.
- Deutsch, C. V. and Zanon, S.: “Direct Prediction of Reservoir Performance with Bayesian Updating Under a Multivariate Gaussian Model,” Paper presented at the Petroleum Society’s 5th Canadian International Petroleum Conference (55th Annual Technical Meeting), Calgary, Alberta, 2004.
- Deutsch, C.V.: “A New *trans* Program for Histogram and Trend Reproduction,” Centre for Computational Geostatistics Annual Report Seven, University of Alberta, 2005.
- Deutsch, C. V., Ren, W., and Leuangthong, O.: “Joint Uncertainty Assessment with a Combined Bayesian Updating/LU/P-Field Approach,” paper presented at *IAMG 2005*, 6 pages, 2005.
- Deutsch, C.V.: “What in the Reservoir is Geostatistics Good for?” *Journal of Canadian Petroleum Technology*, 12 pages, May 2006.
- Doyen, P. M.: “Porosity from Seismic Data: A Geostatistical Approach,” *Geophysics*, 53(11), 1988.
- Doyen, P.M., Den Boer, L.D., and Pilley, W.R.: “Seismic Porosity Mapping in the Ekofisk Field Using a New Form of Collocated Cokriging,” Society of Petroleum Engineers, SPE 36498 presented at the SPE Annual Technical Conference and Exhibition, 1996.
- Doyen, P.M., Psaila, D.E., Den Boer, L.D. and Jans, D.: “Reconciling Data at Seismic and Well Log Scales in 3-D Earth Modeling,” SPE 38698 presented at the SPE Annual Technical Conference and Exhibition, October 1997.
- Fang, J.H., Chen, H.C. Visscher, P.B.: “Reservoir Characterization via Geostatistical and Fractal Simulations,” SPE 25525 presented at the SPE Annual Technical Conference and Exhibition, 1992.
- Frykman, P. and Deutsch, C.V.: “Geostatistical Scaling Laws Applied to Core and Log Data,” SPE 56822 presented at the SPE Annual Technical Conference and Exhibition, October 1999.

- Gorell, S. B.: "Creating 3-D Reservoir Models Using Areal Geostatistical Techniques Combined with Vertical Well Data," SPE 29670 presented at the SPE Annual Technical Conference and Exhibition, 1995.
- Goovaerts, P.: "*Geostatistics for Natural Resources Evaluation*," Oxford University Press, New York, 1997.
- Haldorsen, H. H.: "Simulator Parameter Assignment and the Problem of Scale in Reservoir Engineering," pp 293-340. In: Lake, L.W. and Carroll, H.B. (eds.), *Reservoir Characterization*, Academic Press, 1986.
- Hardy, H. B.: "*Fractals in Reservoir Engineering*," World Scientific Publishing, Singapore, 1994.
- Hewett, T.A.: "Fractal Distributions of Reservoir Heterogeneity and Their Influence on Fluid Transport," SPE 15386 presented at the SPE Annual Technical Conference and Exhibition, October 1986.
- Hewett, T.A. and Behrens, R.A.: "Conditional Simulation of Reservoir Heterogeneity with Fractals," *SPE Formation Evaluation*, 217, *Trans.*, AIME, 289, September 1990.
- Isaaks, E. H. and Srivastava, R. M.: "*Introduction to Applied Geostatistics*," Oxford University Press, New York, USA, 1989.
- Johnston, D.H.: "Chapter 1 Reservoir Management Introduction," p. 1-5. In R.E. Sheriff, *Reservoir Geophysics*, Society of Exploration Geophysicists, Tulsa, OK, 1992.
- Journel, A.G. and Huijbregts, Ch. J.: "*Mining Geostatistics*," Academic Press, 1978.
- Journel, A.G.: "Geostatistics for Reservoir Characterization," SPE 20750 presented at the SPE Annual Technical Conference and Exhibition, 1990.
- Journel, A.G.: "Modeling Uncertainty: Some Conceptual Thoughts," In Dimitrakopoulos (ed.) *Geostatistics for the Next Century*, Kluwer Academic Publishers, 1994.
- Journel, A.G., Xu, W.: "Posterior Identification of Histogram Conditional to Local Data," *Mathematical Geology*, 26(6), 323-359, 1994.

- Journel, A.G.: "Conditioning Geostatistical Operations to Nonlinear Volume Averages," *Mathematical Geology*, 31(8), 932-953, 1999.
- Kelkar, M. and Perez, G.: "*Applied Geostatistics for Reservoir Characterization*," Society of Petroleum Engineers Inc., Richardson, Texas, USA, 2002.
- Kupfersberger, H., Deutsch, C.V. and Journel, A.G.: "Deriving Constrains on Small-Scale Variograms due to Variograms of Large-Scale Data," *Mathematical Geology*, 30, 1998.
- Kentnell, D.J., Bloom, L.M. and Comber, G.A.: "Improvements in Grade Tonnage Curve Prediction via Sequential Gaussian Fractal Simulation," *Mathematical Geology*, 31(3), 1999.
- Lake, L.W.: "The Origins of Anisotropy," *Journal of Petroleum Technology*, April, 1988.
- Lasseter, T. J., Waggoner, J.R. and Lake, L.W.: "Reservoir Heterogeneities and Their Influence on Ultimate Recovery," pp. 545-560. In: Lake, L.W. and Carroll, H.B. (eds.), *Reservoir Characterization*, Academic Press, 1986.
- Laurence R. L. and Rachel T. N.: "Fundamentals of Geophysical Interpretation," Geophysical Monograph Series, No. 13, *Society of Exploration Geophysicists*, 2004.
- Leuangthong, O.: "The Promises and Pitfalls of Direct Simulation," Centre for Computational Geostatistics Report Seven, University of Alberta, Edmonton, Alberta, 2005.
- Manchuk, J., Leuangthong, O. and Deutsch, C.V.: "A New Approach to Direct Sequential Simulation that Accounts for the Proportional Effect: Direct Lognormal Simulation," Centre for Computational Geostatistics Report Seven, University of Alberta, Edmonton, Alberta, 2005.
- McCullagh, P. and Nelder J. A.: "*Generalized Linear Models*," 2nd edition, Chapman and Hall, London, 1989.
- McLennan, J. and Deutsch, C.V.: "*Guide to SAGD Reservoir Characterization Using Geostatistics*," a guide book published in Centre for Computational Geostatistics, University of Alberta, Edmonton, Alberta, 2003.

- Nowak, M.S. and Srivastava, R.M.: "A Geological Conditional Simulation Algorithm that Exactly Honours a Predefined Grade-Tonnage Curve," In. Baafi, E.Y., schofield, N.A., Proceedings of the *Geostatistics Wollongong 96*, Vol. 2. Kluwer Academic Publishers, Dordrecht, Netherlands, p. 669-682, 1997.
- Oz, B., Deutsch, C.V., Tran, T.T. and Xie, Y.: "DSSIM-HR: A Fortran 90 Program for Direct Sequential Simulation with Histogram Reproduction," *Computers & Geosciences*, vol. 29, p. 39-51, 2003
- Phan, V. and Horne, R.H.: "Fluvial Channel Parameter Estimation Constrained to Static, Production, and 4D Seismic Data," SPE 77518 presented at the SPE Annual Technical Conference and Exhibition, 2002.
- Pyrzcz, M.J. and Deutsch, C.V.: "Building Blocks for Direct Sequential Simulation on Unstrured Grids," Centre for Computational Geostatistics Report Four, Edmonton, Alberta, 2002.
- Ren, W., Leuangthong, O., and Deutsch, C.V.: "*Surmont Geostatistical Modeling Project Report One*," University of Alberta. Edmonton, Alberta, 2004a.
- Ren, W., Cunha, L.B., and Deutsch, C.V.: "Preservation of Multiple Point Structure when Conditioning by Kriging," *Geostatistics Banff 2004*, Proceedings of the Seventh International Geostatistics Congress, September 2004.
- Ren, W., Leuangthong, O., and Deutsch, C.V.: "Geostatistical Reservoir Characterization of McMurray Formation by 2-D Modeling," Centre for Computational Geostatistics Report Six, Edmonton, Alberta, 2004b.
- Ren, W., McLennan, J., Leuangthong, O., and Deutsch, C.V.: "Reservoir Characterization of McMurray Formation by 2-D Geostatistical Modeling," extended abstract in *AAPG 2005*, 6 pages, 2005a.
- Ren, W., Leuangthong, O., and Deutsch, C. V.: "Global Resource Uncertainty Using a Spatial/Multivariate Decomposition Approach," Paper presented at the Petroleum Society's 6th Canadian International Petroleum Conference (56th Annual Technical Meeting), Calgary, Alberta, 2005b.
- Ren, W., McLennan, J., Cunha, L.B., and Deutsch, C.V.: "An Exact Downscaling Methodology in Presence of Heterogeneity: Application to The Athabasca Oilsands," paper presented in *SPE ITOHOS 2005*, Calgary, November 2005c.

- Ren, W., and Deutsch, C.V.: "Exact Downscaling in Geostatistical Modeling," Centre for Computational Geostatistics Report Seven, Edmonton, Alberta, 2005.
- Ren, W., McLennan, J., Leuangthong, O., and Deutsch, C.V.: "Reservoir Characterization of McMurray Formation by 2-D Geostatistical Modeling," *Natural Resources Research*, 2006a.
- Ren, W., and Deutsch, C.V.: "Bayesian Updating with Local Varying Correlation," Centre for Computational Geostatistics Report Eight, Edmonton, Alberta, 2006b.
- Ren, W., Deutsch, C.V., Garner, D., Wheeler, T.J., Richey, J.F., and Mus, E.: "Quantifying Resources for the Surmont Lease with 2D Mapping and Multivariate Statistics," SPE 102094 presented at the SPE Annual Technical Conference and Exhibition, October 2006c.
- Reza, Z.: "*Some Aspects of Production Data Integration in Reservoir Modeling*," PhD Thesis, University of Alberta, Edmonton, Canada, 2003.
- Satter, A., Varnon, J.E. and Hoang, M.T.: "Integrated Reservoir Management," *Journal of Petroleum Technology*, 1994.
- Sheriff, R.E.: "Petrophysical and Geophysical Background Basic Petrophysics and Geophysics," pp. 37-49. In R.E. Sheriff, *Reservoir Geophysics*, Society of Exploration Geophysicists, Tulsa, OK, 1992.
- Soares, A.: "Direct Sequential Simulation and Cosimulation," *Mathematical Geology* 33(8), 911-926, 2001.
- Srivastava, R.M.: "An Overview of Stochastic Methods for Reservoir Characterization," pp. 3-16. In: Yarus, J.M. and R.L. Chambers (eds.), *Stochastic Modeling and Geostatistics: principles, methods and case studies*, Vol. 3 of AAPG Computer Applications in Geology, 1994.
- Srivastava, R.M.: "The Visualization of Spatial Uncertainty," pp. 339-345. In: Yarus, J.M. and R.L. Chambers (ed.), *Stochastic Modeling and Geostatistics: principles, methods and case studies*, Vol. 3 of AAPG Computer Applications in Geology, 1994.
- Srivastava, R. M.: "Reservoir Characterization with Probability Field Simulation," *SPE Formation Evaluation*, 7(4), pp. 927-937, 1992.

- Stein, A., J. Brouwer, and J. Bouma: "Methods for Comparing Spatial Variability Patterns of Millet Yield and Soil Data," *Soil Science Society of America Journal* 61, pp. 861-870, 1997.
- Tran, T.T., Wen, X.H. and Behrens, R.A.: "Efficient Conditioning of 3D Fine-Scale Reservoir Model To Multiphase Production Data Using Streamline-Based Coarse-Scale Inversion and Geostatistical Downscaling," SPE 56518 presented at the SPE Annual Technical Conference and Exhibition, October 1999.
- Tran T.T., Deutsch, C.V. and Xie, Y.: "Direct Geostatistical Simulation with Multiscale Well, Seismic, and Production Data," SPE 71323 presented at the SPE Annual Technical Conference and Exhibition, 2001.
- Tamhane, D., Wang, L. and Wong, P.M.: "The Role of Geology in Stochastic Reservoir Modeling: The Future Trends," SPE 54307 presented at the 1999 SPE Asia Pacific Oil and Gas Conference and Exhibition, April 1999.
- Xu, W., Tran, T.T., Srivastava, R.M. and Journel, A.G.: "Integrating Seismic Data in Reservoir Modeling: the Collocated Cokriging Alternative," SPE 24742 presented at the 67th Annual Technical Conference and Exhibition, 1992.
- Yang, C. T., Chopra, A. K., Chu, J., Huang, X. and Kelkar, M. G.: "Integrated Geostatistical Reservoir Description Using Petrophysical, Geological, and seismic data for Yacheng 13-1 Gas Field," SPE 30566 presented at the SPE Annual Technical Conference and Exhibition, October 1996.
- Yao, T. and Journel, A.G.: "Integrating Seismic Attribute Maps and Well Logs for Porosity Modeling in a West Texas Carbonate Reservoir: Addressing the Scale and Precision Problem," *Journal of Petroleum Science and Engineering*, 28, 2000.
- Yeten, B. and Gumrah, F.: "The Use of Fractal Geostatistics and Artificial Neural Networks for Carbonate Reservoir Characterization," *Transport in porous media*, 41, pp. 173-195, 2000.
- Waggoner, J.R.: "4D Seismic: Synergy, Not Just Integration, of Geophysics and Engineering," SPE 50665 presented at the SPE European Petroleum Conference, October 1998.
- Weber, K.J.: "How Heterogeneity Affects Oil Recovery", pp 487-544. In: Lake, L.W. and Carroll, H.B. (eds.), *Reservoir Characterization*, Academic Press, Inc. 1986.

Wen, X.H., Deutsch, C.V., Cullick, A.S. and Reza, Z.A., “*Integration of Production Data in Generating Reservoir Models*,” Centre for Computational Geostatistics, University of Alberta, Edmonton, Canada, 2005.

Zanon, S., Nguyen, H. and Deutsch, C.V.: “Power Law Averaging Revisited,” Centre for Computational Geostatistics Report Four, University of Alberta, Edmonton, Canada, 2002.

Zanon, S.: “*Advanced Aspects of Sequential Gaussian Simulation*,” M.Sc. Thesis, University of Alberta, Edmonton, Canada, 2004.

Zwicky, R.W. and Eade, J.R.: “The Tar Sands Core Analysis Versus Log Analysis Controversy - Does It Really Matter?” *Canadian Well Logging Society Formation Evaluation Symposium*, 6th, Calgary, 1977

APPENDIX

DOCUMENTATION

GSLIB software package (Deutsch and Journel, 1998) is used for the preparation of the thesis. There are some new GSLIB-type FORTRAN programs created for the techniques developed in the thesis, including the P-field simulation with Bayesian Updating, calculation of LVC, ACD, and the exact downscaling EDDSS, and EDSK. This appendix only documents the two main programs created for the exact downscaling techniques. The theory and implementation are described in Chapters 6 and 7. The source codes are not listed because of length considerations.

The first program **EDSK** is for the exact downscaling with direct block kriging. There is a build-in option on how many block data are used for the block kriging. The program takes in block data and point data, and generates models at the point scale. The discretization levels between the block and point scales need to be specified exactly. The variogram model at the point scale is required. The second program **EDDSS** is for the exact downscaling with direct sequential simulation. The histogram reproduction and proportional effect correction are build-in functions. The program takes in block data and point data, and generates models at the model scale. The discretization levels need be specified exactly for between the block and the model scales, and between the model and the point scales. The variogram model is required at the point scale.

Parameters for EDSK

```

line      START OF PARAMETERS:
1         Block.dat                - file with data
2         1                        - columns for grid
3         32  25  50                - nx,xmn,xsiz
4         16  825  50               - ny,ymn,ysiz
5         1  5  100                 - nz,zmn,zsiz
6         wells.dat                 - file with data
7         0  1  2  3  4             - columns for DH,X,Y,Z,var
8         -1.0  1.0e21              - trimming limits
9         2                          - debugging level: 0,1,2,3
10        edsk.dbg                  - file for debugging output
11        edsk.out                  - file for kriged output
12        4  4  1                   - x,y and z block discretization
13        1                          - Multiple blocks types
14        1  32                      - min, max data for kriging
15        0                          - max per octant (0-> not used)
16        160  160  10.              - maximum search radii
17        0.0  0.0  0.0             - angles for search ellipsoid
18        0                          - global mean
19        1  0.0                     - nst, nugget effect
20        2  1.0  0.  0.  0.         - it,cc,ang1,ang2,ang3
21        100.0  100.0  2.5          - a hmax,a hmin,a vert

```

Figure A-1: An example parameter file for EDSK.

Figure A-1 presents an example of the parameter file for **EDSK**. The input block data are specified on **Lines 1 and 2**. The grid definition is given on **Lines 3 to 5**. The GSLIB grid is centre-node regular grid and positive upward in the vertical direction. The point data are specified on **Lines 6 to 8**. Debugging level, debugging file, and output file are specified on **Lines 9 and 11**. The discretization numbers in three directions is given on **Line 12**. The model scale is assumed at the point data scale. **Line 13** gives the option for multiple block types: 1 is for the collocated block only; 2 is for the collocated plus direct connected blocks (total 5 blocks); 3 is for the 5 blocks plus corner connected blocks (total 9 blocks). The standard GSLIB conventions are followed (Deutsch and Journal, 1998). **Line 14** gives the minimum and maximum number of original data that should be used to kriging a grid node. If there are fewer than minimum data points, the global mean is used directly for the node. **Line 15** gives the number of original data to use per octant. If this parameter is set less than or equal to 0, then it is not used; otherwise, the data is partitioned into octants and the closest number of data in each octant is retained for the simulation of a grid node. **Line 16** gives the search radii in the maximum horizontal direction, minimum horizontal direction, and vertical direction of the search ellipsoid that defined on **Line 17**. **Line 18** gives the global mean that should be

the mean of block data, otherwise, it is replaced. **Line 19** gives the number of semi-variogram structures and the isotropic nugget constant. For each of the **nst** nested structures one must define **it**, the type of structure; **cc**, the *c* parameter; **ang1,ang2,ang3**, the angles defining the geometric anisotropy; **aa_hmax**, the maximum horizontal range; **aa_hmin**, the minimum horizontal range; and **aa_vert**, the vertical range.

```

Parameters for EDDSS
*****

line   START OF PARAMETERS:
1      2D-eddss.out           - file with large scale block data
2      1                      - columns for grid
3      140   502105   10      - nx,xmn,xsiz
4      100   6228955   10     - ny,ymn,ysiz
5      1     46       92     - nz,zmn,zsiz
6      1     1       92     - block discretization in x,y and z
7      1     1       1     - model cell discretization in x,y and z
8      PAD0-TT.dat           - file with point data
9      2 3 5 7 0            - columns for X,Y,Z,var,wt
10     -1.0      1.0e21      - trimming limits
11     0                      - debugging level: 0,1,2,3
12     eddss.dbg            - file for debugging output
13     eddss.out           - file for kriged output
14     1                      - number of realizations
15     1                      - histogram reproduction method (0=no,1=yes)
16     100   100   50      - if 1: mean,variance,quantile discretization
17     3.5     1.0        - limit for mean and stdev in CCDF Table
18     0                      - need mean and variance? (0=no,1=yes)
19     mean-var.out        - if yes, the output file name
20     0                      - consider ref. dist (0=no, 1=yes)
21     refdist.dat        - file with ref. dist distribution
22     4     0              - columns for vr and wt
23     -1    1     0        - prop eff:0=no;1=yes,slope,intercept
24     0.0   0.40          - zmin, zmax (possible range of data values)
25     696699             - random number seed
26     0     8             - min and max original data for sim
27     12                - number of simulated nodes to use
28     0                      - maximum data per octant (0=not used)
29     850   450   15.     - maximum search radii
30     0.0   0.0   0.0     - angles for search ellipsoid
31     800   800   21      - size of covariance lookup table
32     25                - global mean
33     2     0.0          - nst, nugget effect
34     2     0.512   0.   0.   0. - it,cc,ang1,ang2,ang3
35     367.0  367.0  5.55   - a hmax,a hmin,a vert
36     1     0.488   0.   0.   0. - it,cc,ang1,ang2,ang3
37     1420.0 1420.0 62.1   - a hmax,a hmin,a vert

```

Figure A-2: An example parameter file for EDDSS.

Figure A-2 presents an example of the parameter file for **EDDSS**. The block data are specified on **Lines 1 and 2**. The grid in standard **GSLIB** conventions is specified on **Lines 3 to 5**. The discretization numbers between the block and model scales in x, y, and z directions are given on **Line 6**. The discretization numbers between the model and point scales in three directions are given on **Line 7**. The point data are specified on **Lines 8 to 10**. Debugging level, debugging file, and simulation output file are specified on **Lines 11**

and 13. The number of simulation realizations is specified on **Line 14.** **Lines 15 to 19** specify the option on histogram reproduction. The CCDF look-up table method has been described in Section 7.4. The discretization numbers of mean, variance for the look-up table, and the discretization numbers of quantiles for building each CCDF are specified on **Line 16.** The limits of possible Gaussian mean and variance are given on **Line 17.** The range of mean is defined between negative and positive limit, and the range of the variance is defined between 0 and the limit. Lines 18 and 19 gives the option of an output file contains kriged mean and variance and selected mean and variance from the CCDF look-up table at each node. **Lines 20 to 22** give the option of a reference distribution of point data if there is not sufficient point data available. **Line 23** gives the option of correcting kriged variance for proportional effect. The slope and intercept of the linear relationship between the local mean and local variance at the model scale are specified. **Line 24** specifies the limits of data values.

The standard GSLIB conventions are followed. **Line 25** gives the random number seed (a large odd integer). **Line 26** gives the minimum and maximum number of original data that should be used to simulate a grid node. **Line 27** gives the maximum number of previously simulated values that should be used to simulate a grid node. **Line 28** gives the number of original data to use per octant. **Line 29** gives the search radii in the maximum horizontal direction, minimum horizontal direction, and vertical direction of the search ellipsoid that defined on **Line 30.** **Line 31** defines the size of the covariance look-up table that serve to reduce the computing time on covariance calculation. **Line 32** gives the global mean that should be the mean of block data. **Lines below 33** define the semi-variogram at the point scale.